Geophysical Characterisation of the Groundwater-Surface Water Interface

Lancaster University

Paul McLachlan

This thesis is submitted for the degree of Doctor of Philosophy on September 2019

Lancaster Environment Centre

Declaration

This thesis has not been submitted in support of an application for another degree at this or any other university. It is the result of my own work and includes nothing that is the outcome of work done in collaboration except where specifically indicated. Many of the ideas in this thesis were the product of discussion with my supervisors Professor Andrew Binley and Professor Jonathan Chambers.

Paul McLachlan

B.Sc. (Hons)

Excerpts of this thesis have been published/submitted in the following academic publications:

McLachlan, P., Chambers, J., Uhlemann, S. and Binley, A. (2017), Geophysical characterisation of the groundwater–surface water interface, Advances in Water Resources, 109, 302–319.

McLachlan, P., Chambers, J., Uhlemann, S. Sorensen, J., and Binley, A. (*in review*), Electrical resistivity monitoring of river-groundwater interactions in a chalk river and neighbouring riparian zone, Near Surface Geophysics.

McLachlan, P., Chambers, J., Uhlemann, S. and Binley, A. (*in review*), Assessing electrical resistivity and induced polarisation characterisation of riverbed sediments, Journal of Applied Geophysics

Authorship statement:

PM = Paul McLachlan, AB = Andrew Binley, JC = Jonatthan Chambers, SU = Sebastian Uhlemann.

Chapter 1 was written by PM and comments were provided by AB.

Chapter 2 was written by PM, comments were provided by AB, JC, and SU, the manuscript was also reviewed for publication in Advances in Water Resources.

Chapter 3 was written by PM, comments were provided by AB and JC.

Chapter 4 was written by PM, comments were provided by AB and JC. A number of discussions were had with Guillaume Blanchy about the development of the R functions for modelling of EMI data.

Chapter 5 was written by PM, comments were provided by AB and JC. Majority of data was collected with assistance from Michael Tso and Tao Min. Additional data provided by JC and James Sorensen.

Chapter 6 was written by PM, comments were provided by AB, SU, and JC. Data was collected with assistance from Youliang Zhang, Michael Tso.

Chapter 7 was written by PM, comments were provided by AB, James Sorensen, SU, and JC. Field work was conducted with assistance from SU and Cornelia Inauen. The manuscript was also reviewed for publication in Near Surface Geophysics.

Chapter 8 was written by PM, comments were provided by AB.

Abstract

The groundwater-surface water (GW-SW) interface has received interest due to its active role in governing GW-SW exchanges, and its implications for environmental health at reach to catchment scales. This thesis advances geophysical methods for characterising the GW-SW interface; in addition it has broader implications for general hydrogeophysics. Three key areas are explored: (1) electromagnetic induction (EMI) characterisation of a riparian wetland, (2) field and laboratory induced polarisation (IP) methods to assess biogeochemical properties of a riverbed, and (3) time-lapse electrical resistivity imaging (ERI) monitoring of a river and neighbouring riparian zone.

Advances in EMI instruments and inversion methods are such that there is interest in using EMI to obtain electrical conductivity models. The ability of EMI methods to resolve hydrogeological properties is assessed here. An inversion algorithm was developed to obtain models of sharply, and smoothly, varying conductivity. It was demonstrated that data collected at 1 m elevation ought to be inverted using a Maxwell based forward model, as opposed to a cumulative sensitivity forward model. Additionally, it was found that measurement noise has more influence on the convergence of inversions for data collected at greater elevations. In comparison, raw EMI data were used to resolve peat depth of the wetland (RMSE=18%) and correlated well with peat hydraulic conductivity (R^2=0.8). These findings demonstrate that in many cases use of inversion methods is unnecessary; this also simplifies data collection as calibration of EMI data is therefore unimportant.

Links between induced polarisation (IP) and hydrologically/biogeochemically relevant properties have been shown in the laboratory. In this work, riverbed sediments are characterised using lab and field based IP methods, and measurements of grain size, cation exchange capacity and surface area. Contrasts of riverbed sediments could be resolved using lab IP; additionally, relationships to surface area matched published studies. Electrical contrasts were more significant at frequencies higher than those typically used in the field; this indicates the benefit of using multi-frequency field IP devices. It was not possible to resolve electrical contrasts with the field data because of complications, such as erroneous fixing of river resistivity and the influence of micro-topography. This work highlights the necessity of forward modelling to confirm results of aquatic ERI surveys.

Time-lapse ERI was used to resolve GW-SW exchanges on a GW dependent Chalk river. Correlation analysis was used to identify areas of the subsurface that exhibited similar hydrological patterns. Despite development of an inversion workflow to account for a changing stage, resistivity patterns in the riverbed were too extreme to be attributed to dynamics in the riverbed and were attributed to inversion artefacts. It was, however, possible to reveal the complex interplay of changing GW levels, biological activity, precipitation and vegetation cutting, and its influence on

the riparian zone. This study highlighted how correlation statistics could be used to summarise large ERI data sets and reveal complex patterns and improve conceptual understanding of site hydrology.

Contents

1 Thesis Structure and Aims

1.1 Introduction

The groundwater-surface water (GW-SW) interface has received particular interest due to its active role in governing GW-SW exchanges and its implications for environmental health at reach to catchment scales. Resolving properties and processes of the GW-SW interface is of critical importance, for instance, characterisation of structural heterogeneity exerts a strong influence on the spatial heterogeneity of interactions and associated residence times. Furthermore, textural properties, including cation exchange capacity and surface area, influence the biogeochemical potential of the GW-SW interface and govern its ability to transform nutrients and pollutants. In addition to spatial heterogeneity, exchanges across the GW-SW interface can be highly dynamic as a result of relative changes in river and GW levels. In recent years, there has been increased interest in the use of geophysical methods for characterising the GW-SW interface.

This thesis comprises a total of six principal chapters; Chapter 2 provides an overview of the interest in characterisation of the groundwater-surface water (GW-SW) interface and a discussion of numerous relevant geophysical studies. Chapter 3 comprises a detailed overview of electrical methods in addition to several functions suitable for processing and inverting geoelectrical data. Chapter 4 includes an overview of electromagnetic induction (EMI) methods in addition to several functions suitable for processing and inverting EMI data. The latter three of the six chapters focus on three distinct, predominantly field based, investigations; Chapter 5 deals with hydrogeological characterisation of the Boxford Wetland, UK, using EMI methods, Chapter 6 deals with the use of field and lab based induced polarisation (IP) methods to characterise the riverbed properties of the River Leith, UK, and Chapter 7 deals with using time-lapse electrical resistivity imaging (ERI) to characterise dynamic processes in the River Lambourn and adjacent Boxford Wetland, UK. In addition, a discussion chapter, Chapter 8, is included to assess whether the thesis aims were met and to provide future directions.

1.2 Thesis Aims

The six main chapters are written such that they are coherent in isolation. Although this means that there is inevitable overlap between chapters, this has been kept to a minimum and similar explanations are typically presented from different angles to reiterate concepts without repetition. Furthermore, although consistent abbreviations are used throughout, they are defined in each

chapter as they appear in the text. Nonetheless, the six chapters operate as coherent piece of work in order to address the following principal research questions:

1. **How best can EMI methods be used to reveal subsurface structure; what is gained from inverting EMI data as opposed to direct use of raw measurements?**

   In recent years there has been increased applications involving inversion of EMI data. However, despite this, there are still a number of important issues to address; for instance, although a number of inversion algorithms that implement Maxwell-based forward models exist, the cumulative sensitivity forward model is still commonly used. Moreover, the necessity of device calibration is unclear, with some authors advocating that it is essential, whereas other authors do not. Perhaps the most important aspect to consider is if models of electrical conductivity obtained from inversion of EMI data offer enhanced characterisation over the direct use of raw measurements. For instance, whereas inversion of EMI data is fairly novel, raw EMI measurements have had a long history of validated application.

   To address these issues, an inversion algorithm was developed to model EMI data, and in addition to several functions to process EMI data, all of which are discussed in Chapter 4. The performance of Maxwell based and cumulative sensitivity based forward models is also assessed in Chapter 4, for the case where EMI devices are operated at ground level and at 1 m elevation, in addition to characterising the effect of errors on the inversion process. In Chapter 5 the ability of inverted and raw EMI data to provide information about the subsurface structure is compared with an extensive intrusive data of peat depths.

2. **Are electrical properties observed at the laboratory scale resolvable at the field scale and what implications this has for obtaining quantitative information at field scale?**

   In comparison to laboratory based IP methods, the application of IP methods at field scale is rare. Furthermore, despite the fact that a number of properties relevant to the GW-SW interface being highly correlated to electrical properties, applications in aquatic environments are even rarer. To address the above question, laboratory based IP measurements were conducted on intrusively obtained riverbed samples to characterise their electrical properties over a range of frequencies. In addition, measurements of the grain size distribution, cation exchange capacity and surface area were measured using standard laboratory practices. Field surveys of IP were then used to assess whether

properties observed in the laboratory could be resolved in the field, and synthetic examples were used to assess issues of aquatic based electrical surveys. Whilst the laboratory, field and synthetic data are discussed in Chapter 7, it is also important to note that inversion of field and synthetic data was facilitated through several ERI and IP modelling tools that were developed; these tools are discussed in Chapter 3.

3. **Can ERI be used to reveal lateral and vertical GW-SW exchange between in riverbeds and riparian zones?**

Time-lapse ERI is commonly used to characterise changes in subsurface hydrological processes, given that signals associated with lithological properties can be assumed constant and changes can be attributed to changes in saturation, pore water conductivity and temperature. To address this research aim, a time-lapse ERI array was installed laterally across a riverbed and robust methods of error quantification were used in order to assess its ability to characterise lateral and vertical river exchanges, see Chapter 7. In addition, as with Chapter 6, the work presented in Chapter 7 relies on the modelling tools presented in Chapter 3.

1.3 Thesis Structure

The content of each chapter is summarised as follows:

Chapter 2 provides an outline of the GW-SW interface, before providing an overview of commonly used geophysical methods. Three principal areas of geophysical characterisation of the GW-SW interface are then considered: (1) structural characterisation, (2) mapping zones of GW-SW connectivity, (3) revealing dynamic processes. The various strengths, challenges and areas of interest for geophysical research are then discussed. It is important to note that this chapter was published in its entirety (McLachlan et al., 2017), and as a result reiterates points mentioned in the justifications of why the research was necessary.

Chapter 3 provides an extensive overview of ERI and IP methods; moreover it outlines a series of R functions that were written to serve as a wrapper to facilitate inversion of geoelectrical data using R2 and cR2. R2 and cR2 are robust inversion algorithms for forward and inverse modelling of resistivity and complex resistivity data (see http://www.es.lancs.ac.uk/people/amb/Freeware/R2/R2.htm). In addition to providing a description of the code structure, several examples are used to highlight several aspects of geoelectrical characterisation. Specifically, a synthetic example demonstrating the difference between data collected using dipole-dipole and Wenner measurement sequences is presented, followed by

another synthetic example demonstrating the effect of fixing different regions with the inversion (this is particularly relevant for modelling electrical data acquired in rivers, Chapters 6 and 7). Finally, an example highlighting the data processing and error modelling capabilities of the functions is provided for a field IP data set collected at an archaeological site in Lancaster, UK.

Chapter 4 comprises a description of EMI methods and provides the background for a series of R functions used to process and model EMI data. In addition to providing a description of the code structure, several examples are used to highlight issues involved in subsurface characterisation using EMI methods. For instance, comparisons between using the cumulative sensitivity forward model and a Maxwell based forward model are made, and implications of noise for cases where an EMI device is operated at 0 and 1 m elevation are discussed.

Chapter 5 is concerned with the use of EMI methods to characterise a riparian wetland. In this work an extensive set of intrusively derived peat depths were used to assess the performance of EMI methods. Methods involving the use of raw EMI measurements and EMI inversion were tested. Furthermore, the influence of data calibration and the effect of treating the subsurface as two and three-layer cases were investigated. In addition to peat depths, correlation between organic matter content, pore water conductivity and hydraulic conductivity were also investigated.

Chapter 6 investigates the ability of laboratory and field based IP methods to characterise the biogeochemical properties of riverbed sediments. Samples of the riverbed were obtained intrusively and characterised using laboratory based IP and measurements of cation exchange capacity, grain size distribution and surface area. Field IP was also used to assess whether the electrical properties observed in the laboratory could be observed at field scales. Following this, a number of synthetic modelling examples were used to explore pitfalls of aquatic electrical imaging.

Chapter 7 is concerned with using time-lapse ERI to characterise interactions between a GW fed river and the subsurface. Specifically, the ability of time-lapse ERI to resolve GW-SW exchanges was investigated. Data were modelled using a workflow to allow for appropriate treatment of the dynamic river level using both independent and difference inversions. Furthermore, a method for characterising time-lapse errors in the difference inversion was implemented. A detailed discussion explaining the interactions occurring in the riparian zone is also included.

Chapter 8 summarises the principal findings of the work included in this thesis, addresses if the research aims were met and provides some recommendations for future research.

2 Geophysical Characterisation of the Groundwater-Surface Water Interface

2.1 Introduction

It is widely recognised that groundwater (GW) and surface water (SW) form a continuum and are not isolated components (Winter et al., 1998; Malard et al., 2002; Sophocleous, 2002). GW-SW interactions have significant implications for water quantity, water quality, and health of aquatic ecosystems, at site to catchment scales (Winter et al., 1976; Stanford and Ward, 1993; Findlay, 1995; Boulton et al., 1998, 2010; Buss et al., 2009; Harvey and Gooseff, 2015). For instance, contaminated GW discharge can degrade streams, lakes, deltas and wetlands, and associated habitats; conversely, GW discharge may also supply vital nutrients and act as a thermal buffer to maintain ecological functions (Power et al., 1999; Brunke and Gonser, 1997; Hayashi and Rosenberry, 2002; Marzadri et al., 2013a, 2013b). Over-abstraction of GW can also result in the redistribution or disappearance of SW resources (Winter et al., 1998), and in coastal regions, the contamination of fresh water aquifers (Ingham et al., 2006).

The transition zone between SW environments and GW systems, the GW-SW interface, is important as it governs the exchange of water, nutrients, and pollutants (Kalbus et al., 2006; Buss et al., 2009; Fleckenstein et al., 2010; Lin et al., 2010; Lansdown et al., 2015). Despite conceptually representing an interface, the term GW-SW interface is commonly used to describe alluvial sediments proximal to SW bodies, e.g. streambeds, lake-beds, riparian zones, and flood plains. Therefore, it typically has vertical extents of up to several metres and horizontal extents in the order of hundreds of metres. It is important to note that here the term GW-SW interface is not synonymous with the hyporheic zone (HZ). The HZs definition can be ambiguous and is discipline dependent (Stanford and Ward, 1988; Triska et al., 1989; Tonina and Buffngton, 2009; Boulton et al., 2010; Ward, 2016; Hester et al., 2017); it is perhaps best described as the region of the GW-SW interface that occurs non-continuously in both space and time, and permits the mixing of both GW and SW (e.g. Gooseff, 2010). Therefore, its presence is not as ubiquitous as commonly assumed and mixing is actually often limited to narrow zones (Hester et al., 2013, 2017). The physical

dimensions of the hyporheic zone are also difficult to define; however, the majority of HZ studies focus on lateral scales of < 10 m and vertical scales of < 1 m (Ward, 2016).

There are numerous established methods that exist for characterisation of the GW-SW interface (e.g. see Cook and Herczeg, 2000; Stonestrom and Constantz, 2003; Bridge et al., 2005; Greswell et al., 2005; Kalbus et al., 2006; Rosenberry and LaBaugh, 2008; Fleckenstein et al., 2010). However, despite providing direct measurements, use of piezometers, seepage meters, and boreholes may be limited by site conditions, environmental protection, or installation costs. In this way information may be spatially limited and unrepresentative. Conversely, tracer experiments (e.g. Findlay et al., 1993; Triska et al., 1993; Harvey et al., 1996; Harvey and Fuller, 1998; González-Pinzón et al., 2015; Xie et al., 2016) provide information that is averaged over larger volumes and therefore may fail to characterise spatial heterogeneity, e.g. identifying low mobility and high mobility zones in the subsurface (Singha et al., 2008).

In the past two decades, near surface geophysics has been increasingly used in characterisation of the GW-SW interface, in addition to other environmental applications (Binley et al., 2015; Parsekian et al., 2015; Singha et al., 2015). Geophysical techniques are sensitive to geophysical properties of the subsurface and hence act as proxies for geological, hydrological, and biogeochemical parameters. It is important to note that while advances in geophysical instruments and subsequent modelling have allowed for more reliable data interpretation, geophysical data can still be ambiguous, and often special consideration is required for the deployment of geophysical tools in different settings. Nonetheless, geophysical tools offer the unprecedented opportunity to characterise subsurface parameters at vertical scales of centimetres to hundreds of metres, horizontal scales of metres to hundreds of metres, and temporal resolutions of minutes to hours. Furthermore, given that multi-disciplinary research has been essential in GW-SW interface research (Newbold et al., 1982; Bencala, 1984; Valett et al., 1993; Sophocleous, 2002; Wojnar et al., 2013; Ward, 2016), the wider application of geophysical tools would be beneficial.

This review focuses on various geophysical tools relevant to characterising properties and processes of the GW-SW interface. In this review, the GW-SW interface and GW-SW interactions are first considered, common geophysical approaches are outlined, various geophysical applications are then reviewed, and finally, avenues of future research are discussed. Although important in governing zones of GW-SW interaction, more general geophysical studies investigating properties of the bedrock aquifers are not included here, but have been the subject of a number of reviews (e.g. Rubin and Hubbard, 2005; Linde et al., 2006; Singha et al., 2007;

Holliger, 2008; Hubbard and Linde, 2011; Binley et al., 2015; Singha et al., 2015; Boaga, 2017). However, large scale airborne geophysical studies, which typically sense to depths of tens to hundreds of metres, are considered as they have the potential to provide a large scale context for processes occurring across the GW-SW interface. Moreover, these applications fit well into the requirement that GW-SW interactions ought to be considered at catchment scales (Kaika, 2003; Hering et al., 2010; Buss et al., 2009; Harvey and Gooseff, 2015).

2.2 The Groundwater-Surface Water Interface

The GW-SW interface is subjected to exchanges spanning multiple spatial scales (Tóth, 1963; Woessner, 2000). At large scales, GW flow paths are principally influenced by hydrostatic forces arising from topography and geology, and occur on scales of metres to hundreds of kilometres (Tóth, 1963; Freeze and Witherspoon, 1967; Winter et al., 1998). On smaller scales, flow paths originating in the SW may temporarily enter the subsurface and allow for GW-SW mixing. These flow paths are commonly referred to as hyporheic exchange flows (HEFs) and are principally governed by geomorphological features (Elliot and Brooks, 1997; Käser et al., 2009; Boano et al., 2014; Hester et al., 2017). HEFs are generally reported to be driven by hydrodynamic forces induced by sand dunes, and cobbles at millimetre to centimetre scales or by hydrostatic forces generated by pool-riffle sequences, sediment bars, meanders, and riparian zones at metres to tens of metres (Harvey et al., 1996; Woessner, 2000; Lautz and Siegel, 2006; Tonina and Buffngton, 2007, 2009; Käser et al., 2009, 2013; Stonedahl et al., 2010, 2013; Boano et al., 2014). In this way, hydrological pathways are typically viewed as being nested within in each other, Fig. 2.1. In reality, this distinction is somewhat arbitrary as HEFs have been stated to occur laterally over hundreds of metres (Boano et al., 2014). Ideally, the point at which the water originating from SW more closely resembles the GW, following GW-SW mixing, is the point at which it becomes groundwater recharge regardless of where and when it returns to the surface.
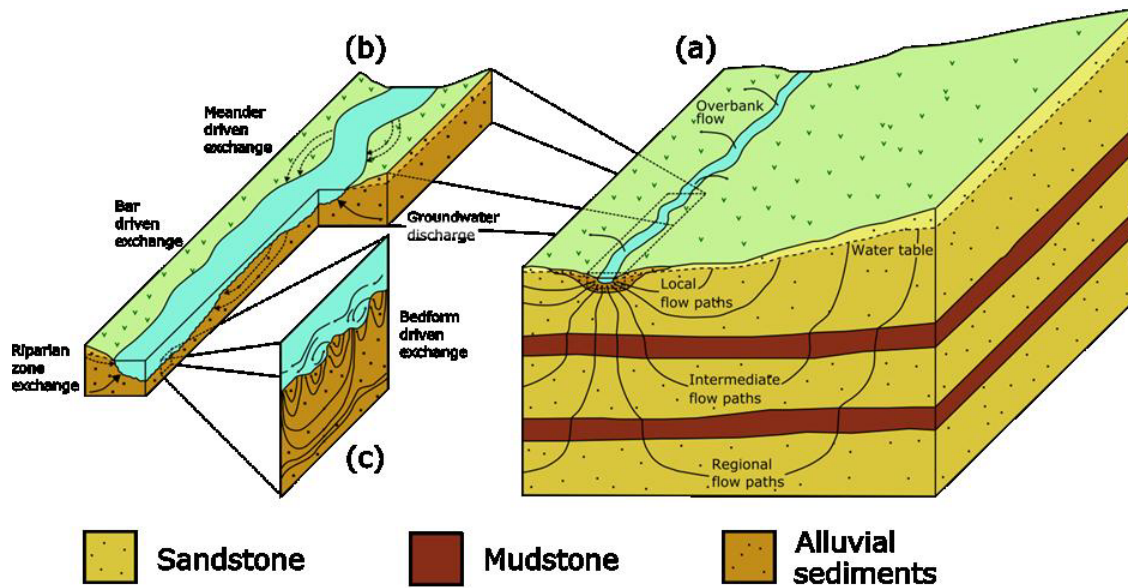
Figure 2.1: (a) Various scales of groundwater flow paths and their relation to (b) macro-scale and (c) micro-scale exchanges in a river and neighbouring riparian zone (after Tóth, 1963; Winter et al., 1998; Stonedahl et al., 2010).

The GW-SW interface is also influenced by temporal variability across scales of milliseconds to years. For instance, turbulent flow in rivers can drive GW-SW mixing within several millimetres of the sediment-water interface on timescales of milliseconds to seconds (Menichino and Hester, 2014; Chandler et al., 2016). On larger time scales, periodic variations in precipitation, snowmelt, evapotranspiration, and flood pulses can modify, or reverse, GW-SW interactions (Boano et al., 2008; Loheide and Lundquist, 2009; Wondzell et al., 2010; Larsen et al., 2014; Zimmer and Lautz; 2014; Dudley-Southern and Binley, 2015; Malzone et al., 2016; Schmadel et al., 2016). GW-SW interactions can also be influenced by waves and tides (Harvey et al., 1987; King et al., 2009; Bianchin et al., 2011), or driven by density contrasts (Musgrave and Reeburgh, 1982; Webster et al., 1996; Boano et al., 2009).

Properties and processes of the GW-SW interface are therefore highly spatially and temporally variable. Lithological heterogeneity in alluvial deposits cans influence permeability, dispersivity, subsurface residence times, and zones of GW-SW exchange. Bedrock aquifers can also dictate whether interactions are localised (e.g. in fractured or karstic settings) or distributed (e.g. in clastic aquifers), and consequently they influence hydrological and biogeochemical conditions at the GW-SW interface (Nagorski and Moore, 1999; Gandy et al., 2007; Kennedy et al., 2009). Temporal

variability in hydrostatic forces can influence locations and timings of GW-SW interactions, the interactions of GW and HEFs, and consequently biogeochemical reactions (Boano et al., 2014). Biogeochemical properties, such as cation exchange capacity, redox gradients, and thermal gradients, have long been known to be important (e.g. Bencala et al., 1984; von Gunten et al., 1991; Winter et al., 1998; Power et al., 1999) but are highly variable, making it difficult to predict pollutant attenuation and nutrient cycling. Furthermore, there have been a limited number of investigations into HZ and GW-SW interface processes across different orders of streams, and their relevance to the catchment (e.g. Gomez-Velez and Harvey, 2014; Kiel and Cardenas, 2014; Marzadri et al., 2017). Therefore, field methods that provide spatially and temporally complete data sets about geological, hydrological, and biogeochemical information at site to catchment scales are required (Buss et al., 2009; Boano et al., 2014; Harvey and Gooseff, 2015; Ward et al., 2016; Hester et al., 2017).

2.3 Geophysical Approaches

The general premise of geophysics is to obtain information about the geophysical properties of the subsurface to infer information about geological, hydrological, and biogeochemical properties (Binley et al., 2015). Geophysical properties can be interpreted using petrophysical models, calibration with other methodologies (both non-geophysical and geophysical), and analysis of temporally distributed data sets of dynamic processes. Geophysical techniques considered here are electrical resistivity (ER), induced polarisation (IP), self-potential (SP), electromagnetic induction (EMI), ground penetrating radar (GPR), and seismic methods (Table 1). Furthermore, forward, inverse, and petrophysical modelling are also briefly discussed due to their importance in data interpretation. Fundamental geophysical theory (e.g. Telford et al., 2010) is beyond the scope of this section, and instead focus is given to the basic principles of field and modelling techniques. Applications of temperature sensing in GW-SW interface studies are also beyond the scope of this review (e.g. Stonestrom and Constantz, 2003; Irvine and Lautz, 2015; Hare et al., 2015; Irvine et al., 2016; Wilson et al., 2016).

Table 2.1: Commonly used field based geophysical methods including their typical applications, spatial sensitivities and acquisition times.

Geophysical Technique	Geophysical property	Hydrogeological properties	Typical investigation depths	Typical acquisition time for 100 m transect
Electrical Resistivity	Electrical Resistivity/ Conductivity	Water content, clay content, pore water conductivity, porosity, lithology	Metres to tens of metres	Tens of minutes
Induced Polarisation	Electrical Resistivity/ Conductivity and Chargeability	Water content, clay content, surface area, hydraulic conductivity, pore water conductivity, porosity, lithology	Metres to tens of metres	Tens of minutes to hours
Spectral Induced Polarisation	Resistivity/ Conductivity and Chargeability (with frequency dependency)	Water content, clay content, surface area, hydraulic conductivity, pore water conductivity, porosity, lithology	Metres to tens of metres	Tens of minutes to hours
Self-Potential	Electrical potential	Hydrological flux, hydraulic conductivity, redox gradients	Metres	Seconds to minutes
Electromagnetic Induction	Electrical conductivity/ resistivity	Water content, clay content, salinity	Metres to 100s of metres	Seconds to minutes
Ground Penetrating Radar	Dielectric permittivity, electrical conductivity	Water content, porosity, stratigraphy	metres to tens of metres	Seconds to tens of minutes
Seismic	Bulk density, elastic moduli	Porosity, lithology	metres to tens of metres	Tens of minutes

Electrical Resistivity

ER methods are used to determine subsurface electrical resistivity by injecting low frequency (<1 kHz) electrical currents into the ground with two current electrodes and measuring the resultant voltage between two or more potential electrodes (Binley, 2015). ER methods are typically minimally invasive as they commonly involve placing stainless steel electrodes several centimetres into the subsurface, however, in some cases borehole ER is used for enhanced characterisation (e.g. Slater et al., 1997; Crook et al., 2008; Wilkinson et al., 2010; Coscia et al., 2011, 2012). In environmental applications the ER signal is typically dependent on the characteristics of the pore water and grain-fluid interface (Glover, 2015). Modern ER instruments are capable of systematically using different combinations of electrodes arranged in lines or grids to image the subsurface in 2D or 3D surveys (Loke et al., 2013). These types of surveys are often referred to as ER imaging (ERI) or ER tomography (ERT). In addition to 2D and 3D surveys, temporally distributed measurements can be used to monitor dynamic processes (e.g. Ward et al., 2010a; Johnson et al., 2012; Uhlemann et al., 2016).

Induced Polarisation

IP methods are effectively an extension of ER methods and use low frequency (< 1 kHz) currents to assess the capacitive properties of the subsurface (Binley, 2015). The IP signal typically arises due to the temporary accumulation of ions in porous media following the injection of an electric current (Kemna et al., 2012). Whereas the ER signal is dependent on the properties of both the pore fluid and the porous media, the IP signal is more closely associated with the properties of the grain-fluid interface (Revil et al., 2012). IP can therefore provide information about lithological properties with less influence from pore water conductivity (Vinegar and Waxman, 1984; Kemna et al., 2000; Lesmes and Frye 2001; Weller et al., 2013; Glover, 2015). As with ER methods, IP measurements can be made using two current electrodes and two potential electrodes. Modern multichannel systems permit the use of multiple potential dipoles simultaneously in addition to recording the full waveform of the IP signal. Induced polarisation can be conducted in either the time or the frequency domain (Revil et al., 2012). Time domain IP methods involve injecting a direct electrical current between the current electrodes before abruptly switching it off and measuring the voltage decay over a specific time interval between the potential electrodes. Frequency domain IP involves injecting alternating electrical currents and measuring the impedance and the phase lag of the current and voltage waves. Frequency domain IP methods can also be carried out using multiple frequencies to assess the frequency dependent impedance and phase shift between injected current and measured voltage, this is typically referred to as spectral IP (SIP).

Self-Potential

Unlike ER and IP methods, SP methods are passive in that they measure naturally occurring voltages within the subsurface (Jackson, 2015). The SP method is relatively simple in that voltages can be measured using non-polarising electrodes and a high impedance voltmeter (Minsley et al., 2007). Non-polarising electrodes are required to minimise polarisation at the electrode surface and a high impedance voltmeter is required to avoid current leakage in the voltmeter (Revil et al., 2012). Under natural conditions the SP signals arise from electro-kinetic, electrochemical and thermoelectric effects (Wynn and Sherwood, 1986; Revil et al., 2012; Jackson, 2015). The electro-kinetic effect, or streaming potential, arises from the advective transfer of excess charges through porous materials (Rizzo et al., 2004). The electrochemical effect originates from the presence of ion and electron concentration gradients, such as those resulting from redox conditions (Sato and Mooney, 1960; Revil et al., 2010). The thermoelectric effect is caused by the differential thermal diffusion of ions in pore fluid, and electrons and donor ions in porous media (Wynn and Sherwood, 1986).

Electromagnetic Induction

Whereas ER, IP, and SP use low frequency (< 1 kHz) electrical currents, electromagnetic methods (e.g. EMI and GPR) use higher frequency signals to induce electromagnetic effects in the subsurface. EMI instruments operate in either the frequency domain (FDEMI) or the time domain (TDEMI) and use primary and secondary coils to determine subsurface electrical conductivity and magnetic susceptibility (Everett and Meju, 2005; Fitterman, 2015). In FDEMI systems a primary current with a specific angular frequency is generated in the primary coil; this induces a primary magnetic field that is out-of-phase with the initial current. The primary magnetic field creates an electromagnetic force that induces eddy currents in the subsurface and a consequent secondary magnetic field. The secondary magnetic field is detected by the secondary coil and is used to infer information about in phase and out-of-phase components of the subsurface electromagnetic properties. In TDEMI systems, a current is typically passed around the primary coil before it is abruptly switched off. This current generates a primary magnetic field which induces an electromagnetic force, both of which are in-phase with the primary current. The electromagnetic force generates eddy currents that decay by ohmic dissipation following termination of the primary current. The decay of the eddy currents produces a secondary magnetic field and its rate of change through time is measured by the secondary coil to infer subsurface conductivity (Nabighian and Macnae, 1991). Modern FDEMI instruments contain multiple secondary coils and can be used to detect information from several depths simultaneously. EMI systems have advantages over electrical methods in that they do not require contact with the sub surface, allowing for easier usage in waterborne or airborne surveys (e.g. Butler et al., 2004; Binley et al., 2013; Harrington et al., 2014).

Ground Penetrating Radar

As with EMI, GPR methods use electromagnetic signals to assess subsurface properties. However, the frequencies used in GPR are higher (10 MHz to 2 GHz), such that the signal travels by wave propagation, rather than by diffusion. In GPR systems a high frequency signal is emitted into the subsurface via a transmitter antenna before it travels to the receiver antenna, e.g. by reflection from an interface of contrasting electrical properties (Huisman et al., 2003; Annan, 2005; van der Kruk, 2015). The amplitudes and travel times of the returning waves are then used to determine dielectric properties and locate boundaries in the subsurface. Field studies often involve time domain GPR systems and typically use frequencies between 50 and 500 MHz. Frequency domain systems are also available, and in some cases using wider bandwidth permits more accurate modelling of the subsurface (Lambot et al., 2004, 2006). The depth of penetration of the signal is dependent upon the electrical conductivity of the subsurface and the frequencies used. Due to frequency dependent

attenuation mechanisms, higher frequencies do not penetrate to as great depths but permit higher resolution images. Furthermore, highly electrically conductive environments may attenuate the signal and reduce the penetration depth.

Seismic Methods

Seismic methods operate similarly to GPR but use the propagation of acoustic energy to infer information about the mechanical properties of the subsurface (Steeples, 2005; Schmitt, 2015). Seismic surveys are classified as reflection, refraction, or surface methods. Reflection methods rely on reflected energy from boundaries between media with different seismic velocities, refractive surveys rely on refractive waves that curve as they move through velocity gradients and surface methods rely on boundary waves that propagate along the surface. For all methods, signals are recorded using geophones and for reflection and refraction methods, a source (e.g. sledgehammers, explosives or weight drops) is required to create seismic waves. Although sources can also be used for surface methods, passive sources can also be used (e.g. Louie et al., 2001). See Rabbel (2010) for a comprehensive review of near surface reflection and refraction applications.

Geophysical Modelling

Forward modelling is used to calculate the data that would theoretically be observed for a given distribution of geophysical properties. The underlying principles of geophysical methods are generally well understood, so the creation of synthetic data sets from a model of geophysical properties is relatively straight forward (Binley, 2015). Forward modelling serves two key purposes: (1) to aid survey design and (2) to assist in inversion and interpretation of data. For instance, different geophysical methods and measurement schemes have different strengths and weaknesses. Therefore, by making reasonable estimates of the subsurface properties the usefulness of a geophysical technique can be assessed prior to its deployment (Terry et al., 2017). Forward modelling may also be useful in guiding interpretation of unusual features; moreover, prior to sufficient computational power, geophysical data were often interpreted by comparing data with forward models, such as ER sounding curves (Loke et al., 2013).

Inverse modelling is the process of determining the distribution of subsurface geophysical properties based on observed geophysical data and any prior information. The principles of geophysical inversion are beyond the scope of this paper but information can be found elsewhere (e.g. Aster et al., 2005; Tarantola, 2005; Menke, 2012; Linde et al., 2015). The majority of inverse problems are ill-posed in that there can be an infinite number of solutions for one geophysical data set. In order to constrain the inversions, regularisation may be used to introduce assumptions to prevent over fitting of data and stabilise solutions, e.g. lateral smoothing in stratified deposits (Constable et al., 1987; Tarantola, 2005). Moreover, uncertainty can further be reduced by carrying

out joint or coupled inversions. In hydrogeophysics, joint inversions involve incorporation of various geophysical and hydrogeological data sets (e.g. Linde et al., 2006; Herckenrath et al., 2013), while coupled inversions model geophysical data within the bounds of prior hydrological models (e.g. Hinnell et al., 2010; Huisman et al., 2010).

In order to be of use in hydrogeology, geophysical models are often interpreted in terms of geological, hydrological, or biogeochemical parameters. Although geophysical data can be interpreted qualitatively (e.g. by looking at resistivity patterns), by monitoring dynamic processes (Johnson et al., 2012; Singha et al., 2015), or through combination with other methods (e.g. Day-Lewis and Lane, 2004; Moysey et al., 2005; Huisman et al., 2010; Miller et al., 2014), petrophysical relationships are commonly used.

Petrophysical and pedological relations can be used in joint inversions to relate two independent geophysical methods (e.g. Hoversten et al., 2006; Zhang and Revil, 2015) or after geophysical inversion to translate geophysical data. Although mechanistic petrophysical models exist (e.g. Leroy and Revil, 2009; Montaron, 2009; Revil et al., 2012), the majority of models used are semi-empirical or empirical. For instance, models have been developed to relate electrical conductivity and porosity (Archie et al., 1942; Waxman and Smits, 1968), to link water content with dielectric permittivity (Topp et al., 1980), and to interpret IP responses with surface area, grain size, and permeability (Vinegar and Waxman, 1984; Börner and Schön, 1991; Slater and Lesmes, 2002; Binley et al., 2005; Slater et al., 2007; Weller et al., 2013, 2015a, 2015b, 2015c). It is also important to note that electrical conductivity is also linked to temperature, and as a result, ERI monitoring studies are often corrected for temperature (e.g. Brunet et al., 2010; Chambers et al., 2014a; Uhlemann et al., 2016).

2.4 Geophysical Characterisation of GW-SW Interactions

Geophysical applications to characterise properties and processes at the GW-SW interface can be split into three principal areas: (1) characterising subsurface structure, (2) mapping zones of GW-SW connectivity, and (3) monitoring hydrological processes. Whereas structural characterisation and GW-SW exchange mapping have included studies at site and catchment scales, monitoring dynamic processes has been conducted solely at site scales. In this section various geophysical applications relevant to characterising the GW-SW interface are discussed. The majority of studies

have focused on freshwater streams and rivers; however, studies have also been conducted in wetlands, deltas, and lakes.

2.4.1 Structural Characterisation

Structural characterisation is essential as the structure governs hydrological properties and subsequent processes. Although minimally intrusive, calibration of geophysics with intrusive methodologies is often required to interpret geophysical information (e.g. Zhou et al., 2000; Chambers et al., 2014b). Also, in some cases, borehole methods involving ERT, IP, GPR, or seismic methods may be used for increased resolution of the deeper subsurface (e.g. Slater et al., 1997; Huisman et al., 2003; Kemna et al., 2004; Crook et al., 2008; Dorn et al., 2011). Nonetheless, geophysical methods provide a level of resolution that would be unachievable through the use of point measurements alone.

Small Scale Structural Characterisation

Several applications have used geophysics to characterise subsurface structure at the Hanford Nuclear Site (Washington, US) to assess pollution pathways to the Columbia River (Johnson et al., 2015). For example, Slater et al. (2010) used waterborne ERI and IP surveys to determine the contact depth of a high permeability unit and low permeability sections of the underlying unit. Depressions in the contact interface were interpreted to be palaeo-channels, and were shown to be areas of GW discharge by using distributed temperature sensing. Land based IP surveys were also conducted at the site and were effective in revealing contrasts between the two units and locating palaeo-channels (Mwakanyamale et al., 2012). The locations of these palaeo-channels were also in agreement with later studies that used temporally distributed ERI to monitor GW-SW interactions (Johnson et al., 2012; Wallin et al., 2013), as discussed in Section 4.3. Also at the Hanford Site, Williams et al. (2012a-d) used seismic surveys over several tens of kilometres to interpolate the sandstone-basalt interface between boreholes. They identified significant lows in the contact and determined additional potential pollution pathways to the Columbia River.

A number of geophysical studies have also been conducted at a riparian wetland (Boxford, UK). Crook et al. (2008) used surface and down borehole ER methods to reveal geological boundaries beneath the neighbouring River Lambourn. In the wetland, Chambers et al. (2014b) used ERI, soil probing, and borehole data to characterise the 3D structure of the subsurface. They identified different superficial deposits, determined the depth to the chalk bedrock, and identified the weathering profile within the chalk, all of which are likely to have important hydrological implications, Fig. 2.2. Loke et al. (2015) compared a standard ERI Wenner array and an optimised array, and found that the optimised array was able to locate geological interfaces with greater

accuracy. In another study, surface GPR revealed that the gravels subdivide into a lower section of chalky gravels and an upper section of coarse flint gravel (Newell et al., 2015). The study also found that gravels below a depth of 2 m were relatively structureless, whereas the shallower gravels displayed potential point bar lateral accretion surfaces in association with the peat channels, which are likely to have further implication for hydrology of the site.
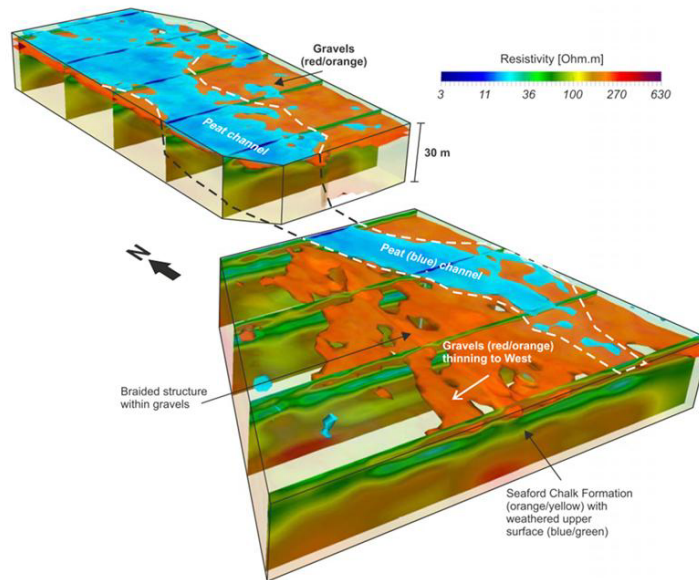
Figure 2.2: 3D resistivity model of the Boxford riparian wetland. Solid volumes are shown for regions with resistivities of less than 50 ohm.m in blue, peat, and with resistivities greater than 150 ohm.m in orange, gravel (Chambers et al., 2014b).

Geophysics has also been employed successfully for site scale structural characterisation in a variety of other settings. Crook et al. (2008) used ERI to evaluate the structure and volume of alluvial deposits in Oregon (US), highlighting how it could be used to provide valuable information to model biogeochemical exchange. In comparison, Mermillod-Blondin et al. (2015) characterised alluvial structure using GPR in the Rhone River (Lyon, France). They identified two lithofacies, and installed piezometers to monitor hydraulic heads and temperature changes. Samples were also taken to assess water chemistry, sedimentology, and bacterial and invertebrate assemblages. They found that HEFs were faster in the cobble/gravel facies than the gravel/sand facies, and that faster flow led to a greater delivery of organic carbon and an increase in microbial activity. Revil et al. (2005) demonstrated how ERI can be used to determine the 3D geometry of a palaeo-channel and showed that SP can be used to determine preferential flow paths (Camargue, France). Several studies have also indicated how multiple geophysical techniques can be used to more accurately

characterise the subsurface structure (e.g. Gallardo and Meju, 2004; Günther and Rucker, 2006; Jafar-Gardomi and Binley, 2013). For instance Doetsch et al. (2012a) and Zhou et al. (2014) were able to improve structural characterisation at the Thur River, Switzerland by structurally guiding ERI inversion with GPR data.

As well as constraining geological boundaries, geophysics has been used to enhance the spatial extent of hydrogeological information. For example, Doro et al. (2013) correlated ERI with slug and pumping tests at the River Steinlach, Germany and Miller et al. (2014) used ERI and permeameters at several alluvial floodplains in Oklahoma, US. Although the majority of structural studies provide static images of the system, SW systems, particularly rivers, are characterised by dynamic erosional and depositional patterns. This dynamic nature is known to have important hydrological and biogeochemical implications for processes in the GW-SW interface (Elliot and Brooks, 1997; Packman and MacKay, 2003). Toran et al. (2012) used ERI to determine changes in sedimentation following installation of a restoration structure, however the dynamic nature of riverbeds is more widely studied in civil engineering where scouring may lead to undermining of bridge foundations (Anderson et al., 2007). Several methods (e.g. echo sounding, intrusive measurements, bulk electrical conductivity probes) have been used to assess changes in channel bed geometry (Prendergast and Gavin, 2014). However, GPR and seismic methods have been particularly useful as they can provide information about the channel geometry and sediment structure beneath the sediment-water interface without the need for intrusive measurements (Webb et al., 2000; Prendergast and Gavin, 2014).

Large Scale Structural Characterisation
Large scale structural characterisation has typically used airborne TDEMI (AEM) in association with other data sets. Harrington et al. (2014) used AEM, geological maps, and environmental tracers to infer aquifer architecture beneath a large river in north-western Australia at the catchment scale, Fig. 2.3. They postulated zones of GW discharge which could be useful in targeting sites for future investigation. AEM has also been used alongside geological mapping data to reveal sedimentary structures and faults (Jørgensen et al., 2012), with ERI to reveal geological variability in deltaic deposits (Meier et al., 2014), with borehole data to identify hydro-facies in glacial deposits (He et al., 2014), with seismic methods to identify the bedrock-superficial interface (Oldenborger et al., 2016), and with hydrogeological modelling to aid in predicting nitrate reduction at catchment scales (Refsgaard et al., 2014). Although AEM dominates regional scale geophysical surveys, other techniques have also been used. Froese et al. (2005) used ERI and GPR at 20-40 km intervals, along with lithological descriptions of bank cuttings to characterise alluvial deposits along a 1000 km reach of the Yukon River (North America), and Ball et al. (2006) used waterborne ERI and geological borehole data to characterise leakage potential in the Interstate and

Tristate Canals (US). Columbero et al. (2014) also used waterborne ERI surveys to characterise the subsurface structure of a glacial lake (NW Italy). They identified an area where lacustrine silts had reduced thickness, and found that this region coincided with anomalous SP signals. They tentatively suggested that SP could be used to locate zones of GW discharge.
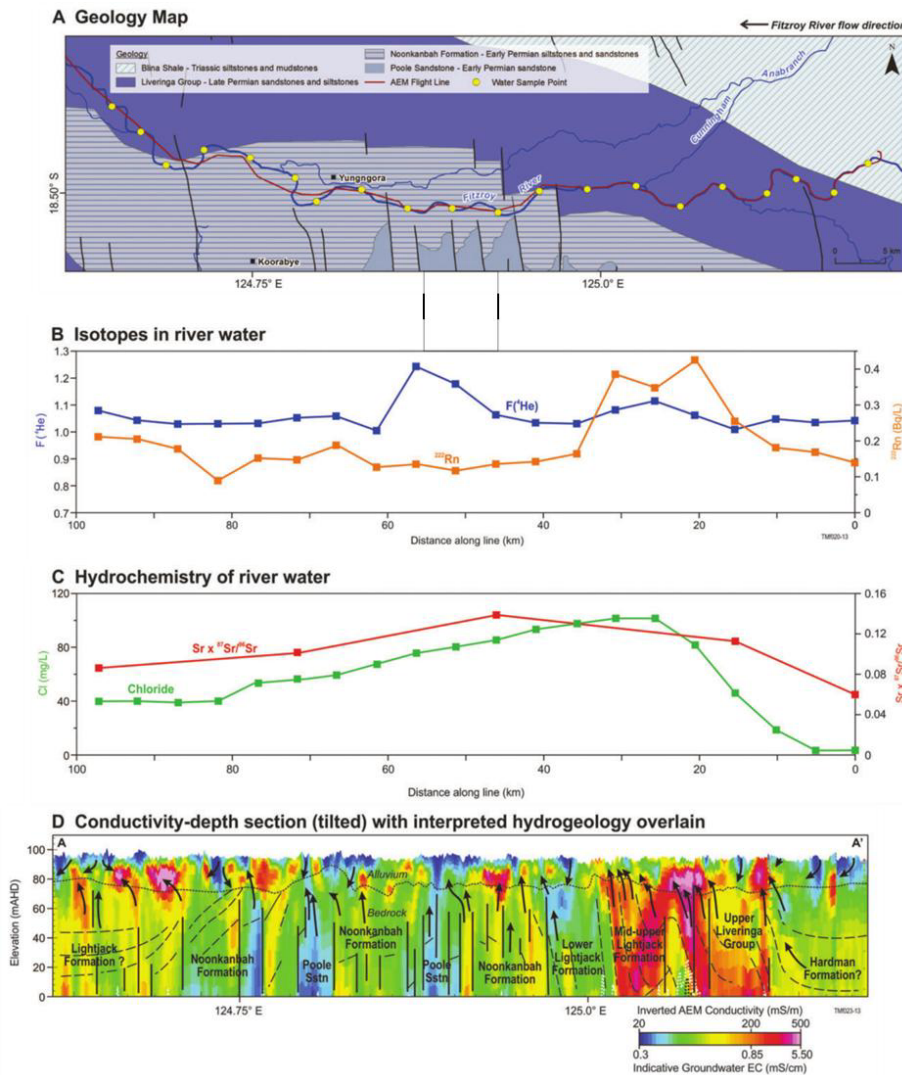
Figure 2.3: Combined plot showing (A) river water sample locations and AEM survey line with respect to basement geology, (B) isotope data, (C) chemical data, and (D) an inverted conductivity-depth section with litho-stratigraphic interpretation. Solid black lines in (A) and (D) represent faults, dashed lines and arrows in (D) represent lithological boundaries and groundwater flow directions. The conductivity-depth section is vertically exaggerated with a V:H ratio of 1:100 (Harrington et al., 2014).

30

2.4.2 Mapping Zones of Groundwater-Surface Water Exchange

A principal consequence of structural heterogeneity is that it generates variability in GW-SW connectivity. Identification of zones of enhanced GW-SW connectivity is important for informing water management and locating areas of potential environmental significance (Buss et al., 2009; Binley et al., 2013). Methods for assessing spatial variability in GW-SW exchange (e.g. seepage meters and piezometers) can be labour-intensive to install. Several geophysical applications have demonstrated how geophysics can exploit the contrasts in electrical and thermal properties of SW and GW to identify areas of GW-SW interaction at site to catchment scales more quickly. In this way geophysics can be used as a reconnaissance tool for qualitatively identifying important areas for further study or as an additional data source to extrapolate information between traditional measurements.

Local Scale Mapping of Groundwater-Surface Water Interactions

Although contrasts in the electrical properties of GW and SW are relatively small (e.g. between 10 and 150 mS/m) in freshwater environments, several geophysical studies have been successful in revealing areas of GW-SW exchange. For instance, Mansoor et al. (2006, 2007) used waterborne ERI to detect locations of elevated pore water conductivities within an urban wetland which arose due to leaching from marginal landfill sites during rainfall events. Nyquist et al. (2008) mapped locations of GW-SW exchange within a stream section at metre-scale resolution by comparing 2D ERI sections collected at high and low stage. Differences in the inverted models were interpreted as zones of GW-SW exchange; these zones correlated with the thinning of a clay layer located beneath a carbonate aquifer and the overlying alluvium. FDEMI methods have also been used to reveal contrasts in electrical conductivity and locate zones of GW-SW connectivity. Butler et al. (2004) used FDEMI and seismic methods to locate a clay aquitard and the extent of a clay window recharge zone. Binley et al. (2013) used waterborne FDEMI surveys alongside piezometric data and chemical sampling (Heppell et al., 2014) to reveal spatial variability in GW discharge. Areas of high electrical conductivity were correlated with upwelling of more solute-rich GW, while areas of low electrical conductivity coincided with areas exhibiting horizontal hydraulic gradients, Fig. 2.4.
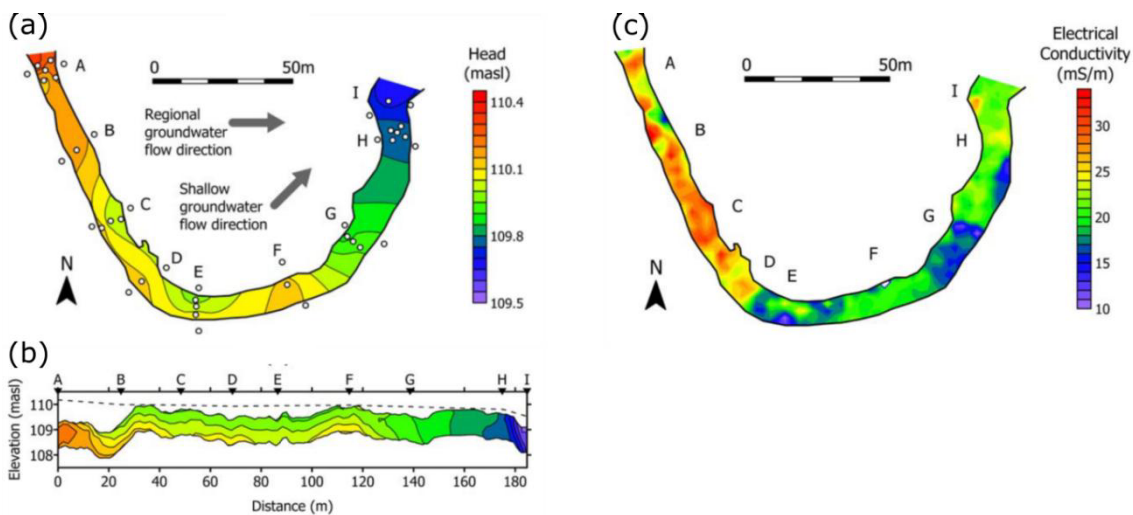
Figure 2.4: Comparison of interpolated hydraulic heads obtained from piezometers and electrical conductivity obtained from waterborne EMI survey. (a) Horizontal profile obtained from 100 cm deep piezometers. Symbols show measurement locations. (b) Vertical profile obtained from 20, 50, and 100 cm deep piezometers. The dashed line shows measured stage profile. (c) Map of riverbed electrical conductivity obtained from Geonics EM38. Hydraulic heads are shown in masl (meters above mean sea level) (after Binley et al., 2013).

Contrasts in electrical conductivity have also been used in coastal environments where the contrasts can be much larger. For instance, Zarroca et al. (2014) used ERI methods in association with piezometric and natural tracer data in a coastal wetland. They were able to identify zones of focused upwelling and distinguish between local and regional GW flow paths, and detect the intrusion of seawater which converged in the wetland. Kinnear et al. (2013) demonstrated that FDEMI could be used to map lateral variability in electrical conductivity. They found that fresh GW discharge in the brackish Ringkøbing Fjord (Denmark) was constrained to the shoreline and demonstrated the potential for geophysical techniques to aid in assessing water budgets over larger areas.

Catchment Scale Groundwater-Surface Water Connectivity Mapping

Similarly to structural characterisation, there have been several applications to map GW-SW connectivity at larger scales (hundreds of metres to tens of kilometres). Paine (2003) used field based FDEMI to determine ranges in electrical conductivity and AEM to locate salinisation sources, in addition to assessing lateral extent and intensity of salinisation, by developing relationships from borehole water samples in northern Texas (US). In the Venice Lagoon (Italy), Viezzoli et al. (2010) used AEM to assess saltwater intrusion in the coastal aquifer and to

characterise the transition between fresh water saturated sediments and overlying saltwater saturated sediments beneath the lagoon. Kirkegaard et al. (2011) used AEM in the Ringkøbing Fjord (Denmark) finding that buried valleys beneath the lagoon were characterised by high salinity waters while some areas of the lagoon were characterised by fresher waters. ERI has also been used to map locations of GW-SW discharge. Kelly et al. (2009) used a towed waterborne ERI array and tracer data to differentiate between local and regional GW discharge along a 50 km river reach in South East Australia.

2.4.3 Monitoring Groundwater-Surface Water Interactions

In addition to using contrasts in the geophysical properties of GW and SW to map areas of exchange, geophysical techniques have been used to monitor and quantify processes of the GW-SW interface at local scales (metres to tens of metres). Aside from heat tracing methods, geophysical monitoring studies have almost exclusively involved ERI. However, Christiansen et al. (2011) demonstrated how time-lapse gravity measurements can be used to assess river-riparian zone exchanges. ERI methods are somewhat analogous to monitoring wells in tracer experiments in that changes in resistivity are used to infer changes in hydrological properties or conditions (e.g. saturation or pore water conductivity). ERI can be used to image the entire region immediately beneath an electrode array. This means that low mobility zones, which are likely to be important in biogeochemical cycling given the long residence times, can also be detected (Singha et al., 2008; Toran et al., 2013b).

Temporally distributed ERI surveys have been used at the Hanford Site (US) to monitor inland water intrusion in relation to changes in river stage and to detect high and low mobility zones in the riparian zone (Johnson et al., 2012; Wallin et al., 2013). They used time-series and time-frequency analysis to reveal the timing and location of GW-SW interactions. Cardenas and Markowski (2011) imaged a flood cycle in a dam-regulated river, finding that the HZ was laterally discontinuous and varied with time. In addition to surface electrodes, cross borehole ERI has been used to increase sensitivity at depths and locate areas of high and low permeability by monitoring 3D hydrological processes within the riparian zone of the Thur River, Switzerland (Coscia et al., 2011, 2012). At the Boxford riparian wetland, Uhlemann et al. (2016) found that peat exhibited a two-layer behaviour separated by an intermittent clay layer; the upper layer showed a reduction in resistivity during the summer due to increased pore water conductivity and the lower layer exhibited an increase in resistivity during the winter months due to the reception of resistive GW.

Studies in fresh water environments have also used salt tracers to artificially induce electrical conductivity contrasts. For instance, Ward et al. (2010a) estimated the relative areas of the HZ by

comparing a pre-injection ERI model with subsequent post-injection ERI models, Fig. 2.5. More recently, Ward et al. (2013) monitored changes in the HZ finding that hydraulic gradients parallel and perpendicular to the valley gradient had minimal influence on HZ extent and that the HZ extent increased with decreasing vertical gradients away from the stream. Similarly, Toran et al. (2013a) found that persistence of the saline tracer was more dependent on thickness and grain size rather than on the presence of restoration structures. Recently, Clemence et al. (2017) used a 3D array to obtain 7 m × 1 m × 1 m resistivity images of the subsurface following the injection of a tracer into the subsurface and note the importance of accurate characterisation of stage level for inverse modelling.

ERI and salt tracer studies have also been used to monitor processes in the riparian zone. To investigate the importance of voids in the riparian zone Menichino et al. (2014) created an artificial macro-pore and monitored intra-meander flow using ERI. They found that their open macro-pore enabled more solute transport and increased solute tailing, both of which are likely to be important in hydrological and biogeochemical processes. Whereas Doetsch et al. (2012b) used a 3D ERI monitoring array to estimate riparian zone infiltration velocities and found agreement with monitoring well data.

Similar to mapping zones of exchange, the natural conductivity contrasts in coastal environments can be used to monitor GW-SW interaction processes. Swarzenski et al. (2007) investigated bidirectional exchange between a coastal aquifer and sea water using ERI, electromagnetic seepage meters, and geochemical tracers. They found that the tide strongly influenced hydraulic gradients such that during high tides GW discharge was reversed and seawater infiltrated into the coastal aquifer. In a similar experiment, Henderson et al. (2010) found that their ERI also indicated suppressed GW discharge, whereas temperature measurements indicated GW discharge continued at high tide. Their sensitivity modelling indicated that during high tide electrical current was preferentially focused in the conductive SW and that consequently, the resistive GW could not be easily resolved. This demonstrates the issue that methods may be limited in certain environments, it therefore highlights the importance of forward modelling to realise the sensitivity of geophysical data.
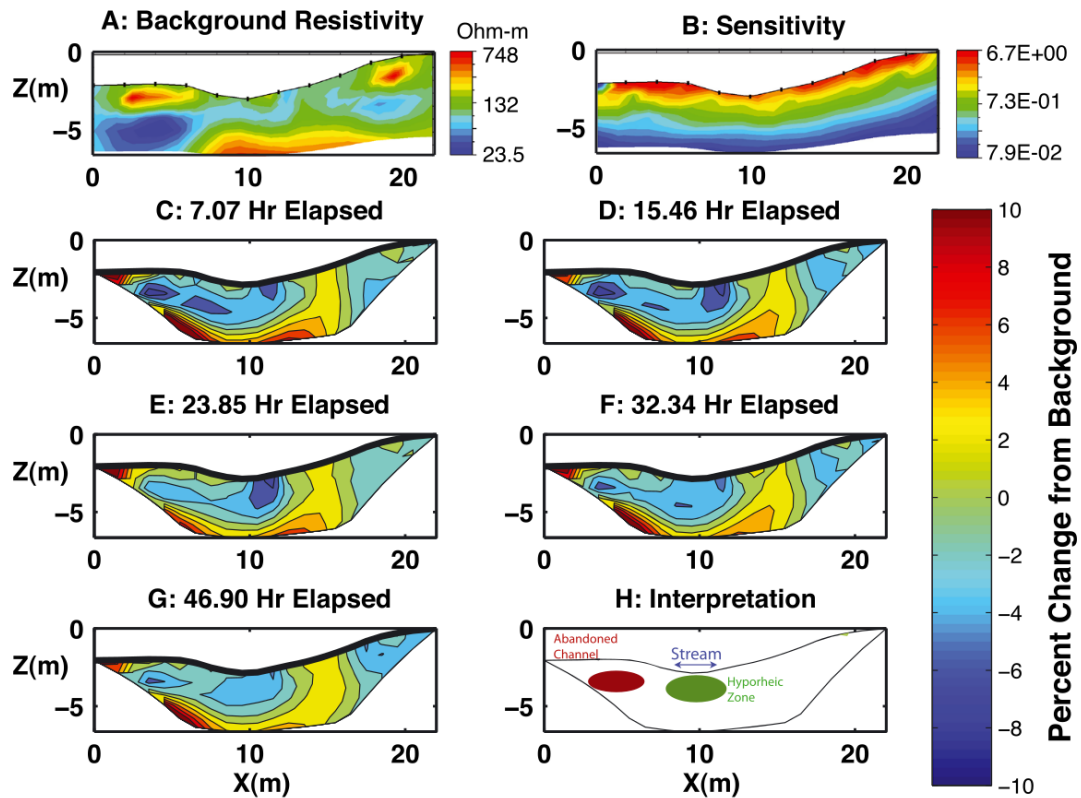
Figure 2.5: Electrical resistivity imaging of solute transport in subsurface of a stream during a 21-hour injection. Transects run perpendicular to the stream, with flow direction out of the page. (A) Pre-injection electrical resistivity model. (B) Model sensitivity as a function of physical location. (C-G) Time-lapse ERI results, at time elapsed after beginning the conservative solute injection. Colour indicates percentage change in bulk resistivity from background conditions. (H) Interpretation of resistivity images. Resistive feature in pre-injection model is interpreted to be an abandoned cobble bed (Ward et al. 2010a).

2.5 Discussion

Geophysical techniques have successfully provided information about processes and properties relevant to the GW-SW interface, with research focusing on three key areas: (1) characterising structure, (2) mapping zones of GW-SW interaction, and (3) monitoring dynamic processes. However, studies of properties and processes in the GW-SW interface would benefit from continued geophysical input, for which there are several avenues of potential research. In this section the strengths, challenges, and recent developments in geophysical techniques are discussed alongside opportunities for the future.

2.5.1 Strengths of Geophysics

It is convenient to organise geophysical techniques into more general themes to consider their strengths as tools to: (1) guide more focused investigations, (2) supplement other data sets, and (3) monitor dynamic processes. These strengths are also apparent in other fields of near surface geophysics (e.g. Singha et al., 2015; Binley et al., 2015; Parsekian et al., 2015). Their presence highlights the scope of geophysics for studies concerned with the GW-SW interface and more general environmental applications.

Reconnaissance Tools

Often the usefulness of data can only be appreciated following the instrumentation of a site. By targeting specific sites based on preliminary geophysical investigations it may be possible to save resources and obtain more representative and useful information. In addition, at catchment scales the decision to select a particular site may be purely incidental to land access and prior instrumentation. At local scales FDEMI (e.g. Butler et al., 2004; Binley et al., 2013) and ERI (e.g. Mansoor and Slater, 2007; Nyquist et al., 2008) have been shown to be capable of identifying zones of hydrological interest. Additionally, geophysics has also been used to locate areas of biogeochemical interest. For example, Uhlemann et al. (2017) used ERI to guide biogeochemical and hydrological sampling of an arsenic contaminated aquifer in Cambodia (see also Richards et al., 2017) by characterising its sedimentological setting. In this way, geophysics can also be used to improve the confidence that intrusive data are representative or appropriate for characterisation of the site.

Additionally, geophysics has also been used as a reconnaissance tool at catchment scales; AEM has been used for locating palaeo-channels (Worrall et al., 1999; Abraham et al., 2012) and areas of GW-SW connectivity (Jørgensen et al., 2012; Harrington et al., 2014). As noted by Kruse (2013), there is significant potential for combining remote sensing data with aerial and land based geophysics. These methods are highly complementary given that remote sensing data and typically sensitive to the surface and/or shallow subsurface (< 1 m) whereas geophysical techniques may be sensitive up to depths of several tens or hundreds of metres (Parsekian et al., 2015). Geophysics and remote sensing have been combined in permafrost studies, for instance AEM (Pastick et al., 2013) and ground based ERI and GPR (Yoshikawa and Hinzman, 2003) were used alongside remote sensing data to assess the thickness and distribution of permafrost. Approaches such as those employed by Wilson et al. (2016), whereby lakes were prioritised based on their geological setting before thermal imagery was analysed, could be enhanced by inclusion of geophysical data. The combination of remote sensing data and geophysics would be useful in linking surface and

subsurface properties and would be a powerful tool in GW-SW interaction studies. Furthermore, these applications could provide additional constraints for catchment scale considerations of HEFs (e.g. Kiel and Cardenas, 2014; Gomez-Velez and Harvey, 2014).

Supplementing Other Data Sets

Geophysical measurements that are sensitive to geological, hydrological or biogeochemical properties can be used to reduce interpolation uncertainty and increase the spatial coverage of information. The combination of methods has additional advantages in that by combining different data sources, poor sensitivity and other methodological limitations can be reduced. Combining data sets is common in GW-SW interface research. For instance, González-Pinzón et al. (2015) combined centimetre scale probes with chemical tracers, piezometers, fibre optic distributed temperature sensing, temperature sensors, and ERI to improve conceptual understanding of a river reach at several scales. The development of integrated and standardised approaches may also be beneficial for generating common data sets through use of 'out of the box' tools . This would allow comparison of field sites and improve conceptual models. For example, a table of tried and tested methods for a several types of environments could be generated; however, it is important to note that field sites may require specific tools. Multi-method approaches are similarly used in hydrogeophysical research to combine geophysical techniques with hydrological and geophysical techniques (e.g. Moyse et al., 2005; Hinnel et al., 2010). The grouping of traditional and geophysical applications can improve the spatial extent of available information across a range of scales and improve the quantitative interpretation of geophysical data. To date, most geophysical studies of the GW-SW interface have focused on characterising the geological structure. Future applications should endeavour to extract information about the hydrological and biogeochemical properties of the subsurface.

Monitoring Dynamic Processes

Processes occurring at the GW-SW interface can be highly dynamic. It can be difficult to characterise these processes with traditional methods as they can interrupt processes and continuous measurements may not be possible. In this review, the ability of ERI to characterise dynamic processes has been demonstrated (e.g. Ward et al., 2010a; Johnson et al., 2012; Wallin et al., 2013). These strengths are also highlighted in related fields where ERI and IP have been used to monitor contaminant transport, biological activity and biogeochemical processes (e.g. Michot et al., 2003; Garre et al., 2011; Slater and Atekwana, 2009; Johnson et al., 2010; Flores-Orozco et al., 2011; Chen et al., 2009; Singha et al., 2015). It is anticipated that knowledge from these fields could be applied to characterisation of the GW-SW inter face. In addition, temporally distributed surveys of other geophysical methods may be beneficial, for example, FDEMI could be used to ex tend the information obtained in ERI monitoring studies and temporally distributed GPR, or

seismic, surveys could be used to better characterise the dynamic nature of riverbed geomorphology.

2.5.2 Challenges of Geophysics

Despite the progress made by geophysics, it is also important to appreciate the challenges of geophysical methods. These are related to geophysics in general and are on-going issues in geophysical research. The principal challenges of geophysical techniques are that: (1) measurement and modelling uncertainty, (2) site specific considerations are often needed, and (3) geophysics needs to be processed and modelled for quantitative interpretation. These limitations greatly contribute to the reluctance to adopt geophysical techniques in environmental studies. Here these challenges are discussed briefly, but it is anticipated that by addressing the issues more thoroughly, application of geophysics in environmental sensing will become more common.

Measurement and Modelling Uncertainty

Geophysical data and modelling methods can be uncertain. For instance, despite the broad recognition of errors in geophysical measurements, they can be poorly dealt with and as a result, incorrect interpretations of geophysical data can be made (Binley et al., 2015). For instance, GPR and EMI survey devices often need to be corrected for instrument drift (Jacob and Hermance, 2004; De Smedt et al., 2016), and error weighting of data needs to be appropriate in geophysical measurements to prevent over fitting of data Particular interest regarding this has been given to errors in ERI data. Typically, stacked or reciprocal measurements are used to assess the quality of measurements and weight them appropriately in inverse modelling (Binley, 2015; Singha et al., 2015). Stacked errors are obtained from consecutive repeat measurements for each current injection, and reciprocal errors are obtained by reversing the measurement sequence and conducting a secondary survey. Reciprocal measurements are typically viewed as being more robust, as stacked measurements may underestimate measurement error (Tso et al., 2017).

However, it should be noted that if the process of interest is occurring faster than a direct and reciprocal measurement scheme, then reciprocal errors may not be so useful (e.g. Ward et al., 2010a). Additionally, some studies have also looked at assessing the value of information within geophysical images in order to assess how reliable geophysical models are (e.g. Oldenburg and Li, 1999; Daily et al., 2005). For instance, Oldenburg and Li (1999) use a depth of investigation method to assess the vertical reliability of ER and IP models. More recently, Jafar-Gardomi and Binley (2013) investigated the information content of combined ERI, FDEMI and GPR data sets, and Nenna and Knight (2013) assessed the benefit of adding geophysical data to assess the

38

maintenance of a coastal aquifer. Methods similar to these could assist in determining the value of data assimilation and help to aid in survey design.

Site Specific Considerations

In all applications, it is important to consider the target, scale of interest and the likely subsurface properties in order to return the most beneficial information. For instance, larger electrode spacing in ERI and IP or lower frequencies in GPR surveys will permit characterisation to deeper depths, but will sacrifice resolution (Binley et al., 2015; van der Kruk, 2015). Forward modelling tools such as Terry et al. (2017) can help to guide survey design based on the targets of interest and the expected subsurface properties. In some cases, geophysical surveys may also be optimised; for example, in ERI electrode number, position and measurement geometry can be designed to improve spatial resolution whilst removing unnecessary measurements and consequently reducing measurement time (Wilkinson et al., 2006, 2012; Loke et al., 2015).

It is useful to briefly note some considerations necessary to applications in SW bodies. The water column can be problematic as it can create current focusing effects in methods influenced by electrical conductivity. For instance, in in-stream ERI surveys, the depth of investigation required; the river level, and electrical conductivity of river water should be taken into consideration when deciding the electrode spacing; furthermore consideration of whether use floating arrays or bed electrodes is also important (Snyder et al., 2002). These measurements can also aid in interpretation of data (e.g. Slater et al., 2010; Binley et al., 2013). However, it should be noted that additional constraints make it more difficult to solve inverse problems, and errors in measurements of water depth or in-stream electrical conductivity may generate significant inversion artefacts (Day-Lewis et al., 2006). ERI studies in SW bodies have involved static arrays (Nyquist et al., 2008; Crook et al., 2008) and towed arrays (e.g. Kelly et al., 2009; Slater et al., 2010). The latter methodology has benefits in that it can improve survey productivity; however, it precludes error quantification (Slater et al., 2010) and requires various electrode spacings to improve vertical resolution (Allen, 2007). In addition to resolution and methodology considerations, some geophysical applications may not be appropriate for the setting. For example, the use of salt tracers and ERI may be prohibited in ecologically sensitive areas, or GPR signals may be attenuated in highly electrically conductive areas.

Extracting Quantitative Information

Recovering quantitative information from geophysics is a major challenge and has been the subject of numerous reviews (e.g. Rubin and Hubbard, 2005; Singha et al., 2007; 2015; Loke et al., 2013). Hydrogeological information can be extracted from geophysical data by using petrophysical relationships, interpreting time-lapse data and through combination with other techniques.

Petrophysical models are commonly used due to their simplicity; however, their usage can be problematic. As noted by Singha et al. (2015) translation of geophysical images with poorly resolved heterogeneity or inversion artefacts will be erroneous, the support volumes of geophysical and hydrological parameters are often different, meaning conversions can be poor, and the resolution of geophysical images can be spatially and temporally variable such that petrophysical transformations may be inconsistent. Geophysical information can also be interpreted temporally without the need for petrophysical transformations. Johnson et al. (2012) and Wallin et al. (2013) used time-series and time-frequency analyses of the Columbia River stage and ERI to reveal preferential pathways, whereas Ward et al. (2010b) demonstrated that temporal moments of ER and solute transport data were well correlated for diffusive transport in the HZ. Geophysical data may also be interpreted from the combination with other techniques. For example, calibrating geophysical and hydrological data at point scale and estimating the correlation at field scale (Day-Lewis and Lane, 2004), by using changes in geophysical properties to calibrate hydrological models (e.g. Binley et al., 2002), or by coupled (e.g. Hinnel et al., 2010) and joint inversions (Kowalsky et al., 2005; Johnson et al., 2009).

As noted, many applications to characterise the structure of the GW-SW interface (i.e. static surveys) have revealed geometry of geological deposits. Future applications should aim to characterise properties such as permeability, surface area, and cation exchange capacity. Although petrophysical models are often used to translate static geophysical data following inversion, there has been recent resurgence of interest in joint inversions. Joint inversions use petrophysical relations to link multiple geophysical data sets with each other, or with hydrological data sets. They have demonstrated significant potential in recovering hydrological properties (Kowalsky et al., 2005; Johnson et al., 2009; Jardani et al., 2013; Soueid-Ahmed et al., 2014, 2016) and are a promising direction for quantitative interpretation of geophysical surveys of the GW-SW interface. However, these methods are rarely routinely employed given the different sensitivities from different geophysical methods and site specificity.

2.5.3 Recent Developments in Geophysical Applications

Since the advent of hydrogeophysics during the 1990s (Binley, 2015), geophysical techniques have evolved from their traditional exploratory usage to being capable of characterisation of hydrological states and dynamic processes. Additionally, in more recent years the field of biogeophysics, which aims to relate the biological processes and modifications of the subsurface to geophysical properties, has emerged (Atekwana and Slater, 2009). Biogeophysical applications have typically involved characterising reactive conditions (e.g. Naudet et al., 2003; Sassen et al.,

2012; Chen et al., 2013), detecting biogeochemical by products (e.g. Slater and Binley, 2006; Comas et al., 2007; 2014; Parsekian et al., 2011), detecting changes to physical structure as a result of microbial activity (e.g. Williams et al., 2005; Slater et al., 2008), or monitoring plant-water interactions (e.g. Michot et al., 2003; Shanahan et al., 2015). In addition, the usage of unmanned vehicles in environmental research has vastly increased and it is expected that automated deployment of miniaturised geophysical devices could become common in future years. In this section developments in: (1) electrical resistivity monitoring, (2) induced polarisation, (3) self-potential, (4) multi-coil electromagnetic induction, and (5) unmanned vehicles, and their potential application to answer current needs in GW-SW interface characterisation are discussed.

Electrical Resistivity Monitoring

ERI is one of the most commonly and widely applied geophysical methods. There has been significant interest in developing low power, automated instruments for long term monitoring (e.g. Daily et al., 2004; Kuras et al., 2009; Ogilvy et al., 2009; Chambers et al., 2015). These instruments have the potential to provide spatially extensive data sets with high spatial and temporal resolution. Moreover, instruments can also transmit data to high performance computers to allow for real time monitoring of subsurface processes (Singha et al., 2015). For instance, computational advances in inversion schemes, e.g. image differencing to avoid regularisation in the time dimension (Wallin et al., 2013) or parameterisation based on the physics of plume shape evolution (e.g. Miled and Miller, 2007; Pidlisecky et al., 2011), are promising tools for extracting hydrological information from ERI monitoring data. As noted, time-lapse ERI to monitor processes in the HZ typically do not use reciprocal measurements as a more robust estimate of error as acquisition times are perhaps too long for revealing the processes of interest. ERI acquisition times could be reduced using multichannel systems, optimised electrode arrays (e.g. Wilkinson et al., 2012), or shorter current injection. However, it should be noted that use of short injection times could result in unreliable measurements of resistivity (Binley, 2015). Also, although most studies have been conducted over periods of several hours, longer ERI monitoring studies such as that of Uhlemann et al. (2016) could be used to aid in revealing seasonal variation in GW upwelling or river-riparian zone interactions.

Induced Polarisation

Despite being less commonly used than ERI, many modern ERI instruments are also capable of IP measurements. Although ERI is more robust in that it has higher signal-to-noise ratios, the IP signal is more closely related to geological characteristics and petrophysical relationships exist for relating IP signal to surface area, permeability and cation exchange (Vinegar and Waxman, 1984; Börner and Schön, 1991; Slater et al., 2007; Revil et al., 2012; Weller and Slater, 2015). These properties have clear relevance to the GW-SW interface, however, IP studies of the GW-SW

interface have been limited (e.g. Slater et al., 2010; Mwakanyamale et al., 2012). The limited application, in comparison to ERI, is probably due to the complexity associated with analysis of data. Nonetheless, it is anticipated that IP would be beneficial in revealing variability in permeability, surface area and cation exchange capacity, and potentially biogeochemical processes (e.g. Flores-Orozco et al., 2011; Chen et al., 2009; 2013), at the GW-SW interface.

Self-Potential

Similar to IP, usage of SP in GW-SW interaction studies has been less frequent; however, there are several possible applications. The SP signal arises from electro-kinetic, electrochemical, and thermoelectric sources. SP has been used to characterise hydraulic properties during pumping tests (Rizzo et al., 2004; Revil et al., 2008; Soueid Ahmed et al., 2014, 2016), through palaeo-channels (Revil et al., 2005), through fractures (Wishart et al., 2006, 2008), and in arctic hill slopes (Voytek et al., 2016). Applications in GW-SW interface research could involve assessing the spatial and temporal variability of GW discharge (e.g. Colombero et al., 2014) or HEFs, or characterising hydraulic conductivity. However, perhaps the most intriguing use of SP at the GW-SW interface would be to characterise the variability in redox conditions. SP has been used to extend the spatial coverage of redox measurements obtained from monitoring wells associated with a contaminant plume at the Entressen Landfill in France, Fig. 2.6 (see Naudet et al., 2003, 2004; Arora et al., 2007; Linde and Revil, 2007). Naudet et al. (2004) removed the electro-kinetic contribution using piezometric head data and found that the SP signal and redox potential values showed good correlation ($R^2 = 0.85$). It is, however, important to note the differentiation of SP sources may be more complex in the GW-SW interface, and the electro-kinetic effect may dominate the signal. Any work involving SP would need to account for all sources of the SP signal appropriately in addition to adequate understanding of redox chemistry.
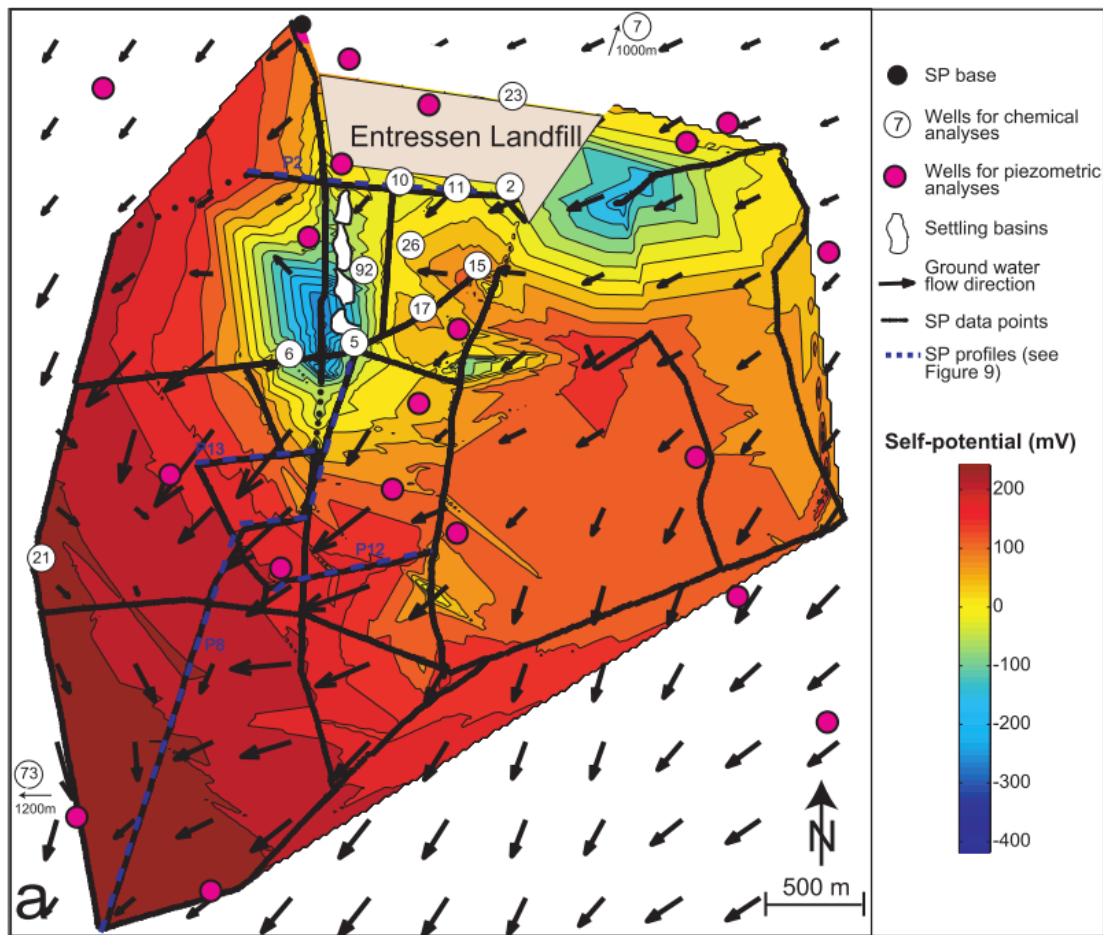
Figure 2.6: Map of self-potential obtained by linear interpolation of measurements made at 10 m resolution in first 2 km from landfill site and 20 m elsewhere. Hydraulic gradients obtained from piezometers (Naudet et al., 2004).

Multi-Coil Electromagnetic Induction

In recent years, FDEMI instruments have been increasingly used in hydrological investigations due to their improved reliability and stability (Boaga, 2017). Furthermore, FDEMI methods have the advantage over ERI in that they do not require contact with the ground and can therefore be more productive. Modern FDEMI instruments contain multiple coils and are able to provide information about vertical variability in addition to lateral variability. They therefore make it possible to extend the application of FDEMI beyond qualitative mapping of GW-SW interactions (e.g. Butler et al., 2004; Binley et al., 2013; Kinnear et al., 2013). In addition, as noted recently by Christiansen et al. (2016), the majority of studies present apparent electrical conductivity, e.g. without appropriate data processing or inverse modelling. Advances in data filtering and inversion schemes, such as EM4Soil (EMTOMO, 2013), Aarhus Workbench (Christiansen et al., 2016) or FEMIC (Elwaseif et

43

al., 2017), permit more accurate modelling of subsurface conductivity structure and may lead to more reliable subsurface characterisation using FDEMI.

Furthermore, temporally distributed FDEMI surveys similar to Robinson et al. (2012), Shanahan et al. (2015) and Huang et al. (2017) could prove useful in GW-SW interface characterisation. For instance, FDEMI instruments could be used to investigate diurnal dynamics of salt water wedges in coastal environments or seasonal changes in GW upwelling, provided there are substantial contrasts in the electrical conductivity of GW and SW. It is important, however, to note that some authors (e.g. Lavoué et al., 2010) argue for the need to calibrate FDEMI with ERI, this may be particularly true in time-lapse measurements where ambient conditions, or the operator, may influence the readings obtained.

Unmanned Vehicles

Given the significant increase in the availability and application of automated ground based, waterborne and aerial technology in many aspects of environmental sensing, the translation to geophysical sensing is inevitable. Automated aerial, terrestrial, and waterborne vehicles would offer the capability for precise and repeatable data collection. Unmanned aerial vehicles (UAVs) have the ability to fly at lower elevations (∼30 m) than typical aircraft, and are therefore able to provide high-resolution data sets without sacrificing productivity. Geophysical applications using automated vehicles have predominantly involved magnetic mapping to locate man-made features (Stoll, 2013; Phelps et al., 2014). Automated vehicles may also be able to simultaneously process and contour data, and transmit information in real time (Phelps et al., 2014). Furthermore, automated systems could be programmed in such a way that anomalous regions are resurveyed in higher resolution automatically.

The majority of unmanned aerial vehicles are small (< 25 kg) and are limited to lightweight instruments; however, larger vehicles capable of carrying heavier payloads are available (Whitehead et al., 2014a, 2014b). It can be envisaged that miniaturisation (or weight reduction) of geophysical tools, and the increasing pay loads of UAVs, could allow for increased collection of automated aerial geophysical data. However, non-aerial geophysical applications could easily be adapted to use automated vehicles; for instance, roving surveys using plate electrodes for ERI (Christensen and Sørensen, 1998), large scale FDEMI surveys (Christiansen et al., 2016) or waterborne surveys (Kelly et al., 2009; Binley et al., 2013; Colombero et al., 2014) would not be difficult to automate and may aid in collection of data across larger scale, e.g. to investigate parameters at catchment scales.

2.6 Summary

Geophysical tools have clear application in revealing geological, hydrological and biogeochemical heterogeneity at the GW-SW interface. Geophysical tools are highly complementary to traditional tools as they are sensitive to regions of the subsurface that are not always reachable by direct measurements. The majority of geophysical applications have focused on characterising subsurface structure, revealing spatial variability in GW-SW interactions and imaging hydrological processes. Data sets obtained from these field studies have significant potential to improve characterisation and modelling of parameters at the GW-SW interface. Over the last 20 years, geophysical methods have grown to be powerful tools in hydrogeological research, in part due to the view that geophysical tools are used to aid hydrogeological problems alongside traditional methods. Geophysics provides valuable practical tools for assessing many unknowns of the GW-SW interface. Moreover, although caution in quantitative interpretation of geophysical data is warranted, attempts at improving uncertainty quantification, inversion routines and translating data are on-going. Efforts to provide solutions to these issues can only continue to improve confidence in geophysics so that its potential can be more widely appreciated and applied across a variety of scales. In recent years, there has been significant development in techniques and methodologies in parallel research areas, some of which would enhance the information obtained in studies of the GW-SW interface. Continued integration of geophysical methods would be beneficial in characterising hydrological and biogeochemical heterogeneity in the GW-SW interface and understanding the implications for water quality and ecological health.

3 Processing and Modelling Electrical Resistivity and Induced Polarisation Data

3.1 Introduction

Electrical resistivity (ER) and induced polarisation (IP) methods have a long history, predominantly in resource exploration. More recently, advances in techniques, and growing interest in the dependency of geoelectrical properties on several hydrological properties, have led to a wide range of hydrogeophysical applications. For instance, ER is strongly linked to porosity, saturation and pore water conductivity. In comparison, IP methods, which are effectively an extension of ER methods, are more closely linked to electrical characteristics of the grain surface, as opposed to the pore space. ER methods have been used to characterise geological structure (e.g. Rayner et al., 2007; Hirsch et al., 2008; Chambers et al., 2014), and to image hydrological processes (e.g. Ward et al., 2010; Uhlemann et al., 2016; Mary et al., 2019). IP methods have been used to characterise geological structure (e.g. Slater et al., 2010; Mwakanyamale, 2012), image microbial processes (Saneiyan et al., 2018), and characterise hydraulic conductivity in both the field (e.g. Hördt et al., 2007; Benoit et al., 2018) and laboratory (e.g. Slater et al., 2007).

Initially, ER methods focused on qualitative determination of lateral and vertical variation in electrical properties. For instance, early hydrogeophysical work included Zhody and Jackson (1969) who used sounding methods to look for deep groundwater in Hawaii. However, early quantitative use of sounding methods have also included sounding curves to produce 1D models of electrical resistivity or developing empirical relationships by combing ER and hydrogeological methods (e.g. Sir Niwas and Singhal, 1985). Furthermore, sounding techniques are still widely used today, particularly in developing countries or where the target of interest is deep (e.g. Chandra et al., 2012; Ekwe et al., 2012; Khalil, 2010). Profiling methods are also used today, particularly in archaeological studies (e.g. Gaffney, 2008) and in waterborne surveys (e.g. Ball et al., 2006) to reveal lateral variations in resistivity. The development of multi-electrode and multi-channel ER and IP devices is such that permit the simultaneous collection of sounding and profiling data can be

automated. This coupled with robust inversion algorithms, is such that the majority of applications nowadays may be referred to as geoelectrical imaging.

Inversion methods are used to iteratively model a subsurface distribution of geoelectrical properties that match observed ER and IP. In the majority of cases, electrodes placed on the surface are used to characterise the distribution of geoelectrical properties in the subsurface. The obtained model of geoelectrical properties is dependent upon the spatial sensitivity of the measurements, model and measurement errors and, of course, the electrical properties of the subsurface. By utilising different electrode geometries, and adequately accounting for model and measurement errors, the image resolution can be improved. The past three decades have seen a number of significant improvements such that the application of 2D, 3D and time-lapse imaging is increasingly common; consequently, geoelectrical methods are a fundamental tool for hydrogeophysicists.

In this chapter an overview of the basic principles behind ER and IP are discussed, including data acquisition and inverse modelling. Several R based functions used in this thesis to facilitate inversion through R2 and cR2 are then presented. R2 and cR2 are well-tested codes for inversion of ER and IP data that have been used in a wide variety of applications (e.g. Terry et al., 2017; de Sosa et al., 2018; Cheng et al., 2019). These inversion algorithms lack a graphical user interface but use several text documents as an input; the R functions described here provide a means to generate these input files in order to facilitate the inversion process. In addition, these functions deal with processing and error modelling of data, generation of triangular meshes via Gmsh (Geuzaine and Remacle, 2009), and plotting of inversion results. Some capabilities of these functions, and the R2 and cR2 inversion algorithms, are presented to demonstrate necessary steps in processing and modelling field data, and generating and modelling synthetic data. Specifically, three case studies are presented: (1) a comparison of Wenner and dipole-dipole measurement geometries using forward and inverse modelling, (2) the effect of modifying regularisation within the inversion for a synthetic case, and (3) the processing and error modelling of field IP data prior to inversion.

3.2 Electrical Resistivity and Induced Polarisation

3.2.1 Background

Electrical methods typically involve using two current electrodes to inject a current into the ground and another set of two electrodes to measure the resulting potential difference. Resistivity methods commonly use a DC source to obtain a transfer resistance from Ohm's Law ($R = V_P/I$), where V_P is the primary voltage and I is the current, Fig. 3.1. Stainless steel is generally the electrode material of choice, as it is durable, does not typically suffer from changes in electrical contact due to

corrosion, and is relatively cheap. However, other electrode materials have also been used, including graphite, porous pots, and platinum (e.g. LaBreque and Daily, 2008; Kuras et al., 2015). It is important to note that often a background voltage (self-potential) may be observed but can be easily removed as a result of the shape of the injected waveform, Fig. 3.1a. DC surveys typically involve frequencies of 0.5 to 2 Hz and a use switched square wave to minimise electrode polarisation and consequent erroneous measurements, Fig. 3.1a. Typically, on-off time for the injected current is around 0.5-1 s; it is important to note here that where significant capacitive properties exist in the subsurface, longer injection times may be required to ensure that the V_P is reached, Fig. 3.1b.
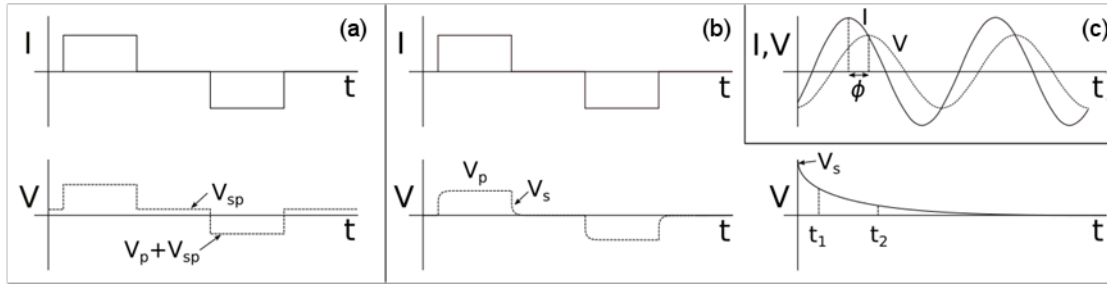
Figure 3.1: Injected currents and observed voltages in: (a) DC resistivity, (b) TDIP, and (c) FDIP.

The charge-up effect before V_P is reached is exploitable and forms the basis of the IP method. As with ER measurements, IP measurements are typically made by injecting a current using an electrode pair and measuring the electrical potential across another electrode pair. This charge-up effect is also reciprocated by a decay following cessation of a DC source, where the voltage drops immediately to a secondary voltage before decaying to the background potential, Fig. 3.1b. Siegel (1959) defined the V_S/V_P ratio as the apparent chargeability to provide a measurement of the capacitive effect of subsurface polarisable bodies; however, difficulty in obtaining V_S is such that the integral chargeability is commonly used. The integral chargeability, M_a, is given by:

$$M_a = \frac{1}{t_2 - t_1} \frac{1}{V_P} \int_{t1}^{t2} V(t)\, dt, \tag{3.1}$$

where, t_1 to t_2 is the time interval of the measurement and the integral is obtained through sampling of the voltage at discrete times between t_1 and t_2, Fig. 3.1b. The integral chargeability is dependent on the timing and duration of sampling window; furthermore if the off time is too short the signal may not have decayed fully before the next cycle leading to errors in subsequent measurements. When using a DC source this method is commonly referred to as time-domain IP (TDIP); however,

the capacitive effects of the subsurface can also be determined using an AC source. When an AC source is used the method is often referred to as frequency domain IP (FDIP). In FDIP, the phenomena can be expressed as a complex resistivity comprising a real component obtained from the ratio of peak voltage and peak current, and an imaginary component is obtained from the difference between voltage and current (expressed as a phase angle, φ, Fig. 3.1c). Thus, the measured potentials are complex values containing information about the resistivity and polarisation of the subsurface.

In the field, FDIP instruments typically use frequencies between 0.5 and 25 Hz, measurements made at lower frequencies can be time-consuming whereas measurements made at higher frequencies may be subject to inductive coupling effects. FDIP measurements made in the laboratory are less limited and frequencies between 1 mHz and 1000 Hz are commonly used. Furthermore, recently there has been work to develop correctional procedures to extend characterisation beyond 1000 Hz (e.g. Wang et al., 2019). Laboratory applications are often concerned with the behaviour of materials across a broad range of frequencies and are consequently referred to as spectral IP (SIP) methods. Several laboratory-based SIP studies have focussed on linking the spectra of and the hydrological properties and electrical properties (e.g. Slater et al., 2007).

3.2.2 Electrode Geometry

ER measurements can be expressed as either transfer resistances or as apparent resistivities. The latter is effectively the resistivity of a homogenous earth that would provide the same transfer resistance as measured. That is to say that for a homogenous earth the measured apparent resistivity would match the resistivity of the subsurface, regardless of the electrode geometry. In reality the subsurface is heterogeneous, nonetheless apparent resistivities are perhaps more meaningful as a unit as they give a direct indication of the bulk or average subsurface resistivity in the vicinity of the electrodes. The relationship between transfer resistance, R, and apparent resistivity, ρ_a, is determined by the geometric factor, k:

$$\rho_a = kR.$$
(3.2)

The geometric factor is governed by the positions of four electrodes used to make the measurement. Different array geometries have different sensitivity patterns such that they will have different apparent resistivities for the same heterogeneous subsurface; common geometries are displayed in Fig. 3.2. For instance, Wenner measurements have poor depth sensitivity but are good at resolving lateral contrasts, whereas dipole-dipole measurements have a greater depth of

investigation but a lower lateral sensitivity. Unlike the apparent resistivity, integral chargeability and phase angle are extrinsic properties uninfluenced by a geometric factor. In addition, phase angles can be approximated, for a reference frequency, from chargeability via a linear relation, i.e. $\varphi = cM$, where c is typically in the range of -1 to -1.5 and depends on the measurement windows used. The benefit of this assumption is that TDIP data can easily be expressed as an apparent complex resistivity and modelled using complex resistivity algorithms.
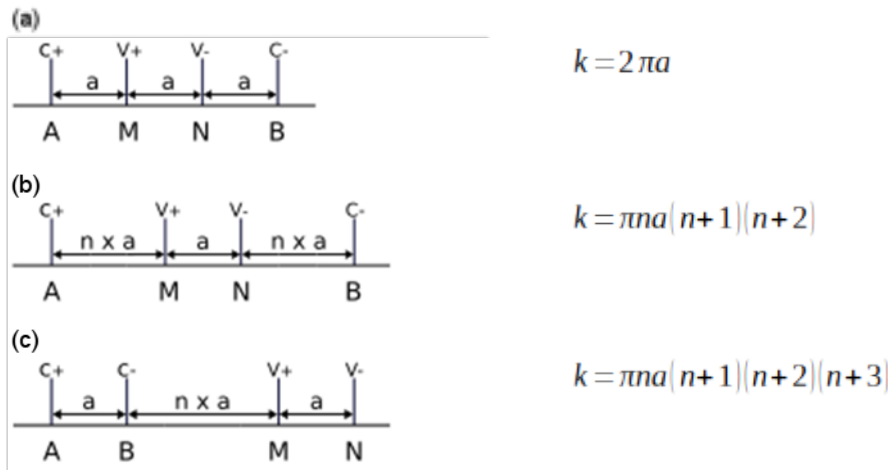
Figure 3.2: Common measurement arrays and their geometric factors: (a) Wenner, (b) Schlumberger, and (c) dipole-dipole.

3.2.3 Measurement Errors

ER and IP measurements conducted in the field can be influenced by a number of sources of errors. In order to interpret field results these errors must be understood and adequately characterised. One common source of error is the high contact resistances between electrodes and the ground, however it is generally simple to fix this issue (e.g. by using salt water or bentonite clay), furthermore, the majority of modern ER and IP instruments provide estimates of contact resistance. Naturally occurring self-potential could also be a source of error, this is particularly true if they are highly erratic and variable in time, however the majority of instruments provide automatic filters and thus such effects are generally not a problem.

IP measurements are particularly prone to measurement errors, and as a result, additional care is often required to reduce the error. For instance, whilst it is true that for ER measurements made with large geometric factors, the operator needs to be aware that the observed voltages are not at

the limits of instrument resolution; this issue is more problematic in TDIP given that the voltage decay needs to be recorded. Consequently, required voltages in TDIP surveys tend to be higher than in DC resistivity surveys. As with ER, IP measurements can be made with stainless steel electrodes, however many authors (e.g. Zhou and Dahlin, 2003; Zarif et al., 2018) have advocated the use of non-polarising electrodes to improve data quality. Furthermore, due to inductive and capacitive coupling that can occur, dipole-dipole measurements are generally preferred over other array types given that potential and current electrodes are not nested.

There are several ways to characterise error in geoelectrical data, for instance, the majority of modern devices permit measurement stacking and typically provide a measurement error associated with stacking. However, as demonstrated by Tso et al. (2017), errors derived from measurement stacking can be too conservative and it is the best practice to record reciprocal data sets whereby the survey is repeated with voltage and current pairs swapped. Robust error quantification is essential in data inversion in order to weight data properly in the inversion process and to prevent over or under-fitting of data.

Although it is generally accepted that reciprocal measurements provide the best estimate of error for ER measurements, they double survey time and can therefore be unappealing. Furthermore, the longer injection times for TDIP is such that collecting reciprocal data sets for TDIP can be extremely time-consuming. Moreover, although the validity of reciprocity in ER methods is accepted, it has been showing that the result is largely dependent upon injected current (Zadorozhnaya et al., 2008). Flores-Orozco et al. (2016) proposed a method of TDIP filtering whereby IP data quality is assessed on the decay of the IP curve alone, and reciprocal measurements are not required. This method looks for the classical decay curve and rejects measurements that do not conform to this shape; however, as pointed out by Dahlin and Loke (2015) and Dahlin et al. (2018) it may be possible under a number of scenarios to get atypical decay curves.

3.2.4 Traditional Electrical Resistivity Methods

Traditionally, ER surveys were conducted in profiling or sounding modes. Profiling methods use constant electrode separations and obtain information about the lateral variability in electrical resistivity. Conversely, in sounding surveys, the centre point remains fixed and the electrode separation is progressively increased to allow for deeper signal penetration. Whereas profiling methods have focussed on revealing lateral contrasts in apparent electrical resistivity, type curves were widely used to manually interpret sounding data. Following from this, type curves were superseded by 1D inversion techniques (Ghosh, 1971) where a forward model was used to generate

theoretical measurements based on a given 1D model of electrical resistivity and inversion algorithms were used to obtain a distribution of resistivity which best explained the observed measurements.

A major limitation of sounding methods is the assumption of no lateral resistivity changes and they are therefore inaccurate in areas with significant lateral heterogeneity. In order to characterise lateral changes in addition to vertical changes, profiling and sounding surveys were conducted in order to produce 2D pseudo-sections (e.g. Ward, 1990). Furthermore, although quantitative modelling was achieved, it required manual adjustments of a forward model and was laborious, meaning such work was rare (e.g. Hohmann et al., 1982). Nonetheless, these early attempts at inversions obtained from sounding measurements and surveys to acquire both sounding and profiling methods were fundamental in developing ER and IP methods, and underpin modern techniques.

3.2.5 Modern Electrical Resistivity Methods

Developments in multi-electrode geoelectrical imaging equipment significantly improved the potential to reveal vertical and lateral variability in electrical properties. Multi-electrode systems first appeared commercially in the late 1980's (Griffiths et al., 1990) and permitted the utilisation of different electrodes within an array to access different areas of the subsurface using multiple electrode configurations. In this way, the simultaneous collection of sounding and profiling data is essentially automated. Furthermore, these systems provide multichannel capabilities that allow potential measurements on a number of electrode pairs simultaneously to significantly reduce acquisition time.

Typically, arrays comprising different combinations, and electrode separations, of the geometries displayed in Fig. 3.2 are used. In addition to standard measurements there has been work on optimising electrode arrays. These efforts are concerned with automating the process of finding the optimum set of electrodes array configurations. For example, the 'Compare R' method by Wilkinson et al. (2006) and subsequent work by Loke et al. (2014) and Uhlemann et al. (2018) have been used to improve resolution of the subsurface whilst using fewer electrodes in both 2D and 3D applications, compared to standard array geometries.

As mentioned, ER and IP measurements do not provide a direct measure of the geoelectrical properties of the subsurface. In order to allow for quantitative interpretation of measurements, appropriate modelling tools are required. As with the 1D curve matching methods used for

electrical soundings, inverse methods can be used to obtain a model of geoelectrical properties that best describes the observed data. Formulation of the inverse problem requires that the expected measurements for a given geoelectrical distribution be known. This is achieved via the forward model. For DC resistivity the forward model can be expressed as:

$$\nabla \left[\frac{1}{\rho(x,y,z)} \nabla V_p(x,y,z) \right] = -I\delta(x_s),$$ (3.3)

The potential at any point on the surface or within a surface can then be determined from a given resistivity distribution. For the case of 2D and 3D variation in resistivity, equation 3.3 can be modified, as shown by Binley and Kemna (2005). Furthermore, equation 3.3 (and 2D and 3D variants) can be expressed in terms of voltage and resistivity as complex variables, allowing the modelling of complex resistivity for IP investigations. Additionally, the forward model for TDIP is not considered here but can be found in Binley and Kemna (2005).

Since equation 3.3 (and 2D and 3D variants) cannot be solved analytically for the general case with any given variation in resistivity, grid-based methods (typically finite difference or finite element) are used to approximate the solution. Given the geometrical flexibility of the finite element method, it is commonly used in ERT and IP inversion, including R2 and cR2. For such methods, the subsurface is divided into numerous finite elements. By using a sufficiently fine mesh and appropriate boundary conditions, accurate solutions for the potential over complicated distributions of geoelectrical properties can be determined. For more details see Binley and Kemna (2005).

Whereas the forward model is used to calculate a set of theoretical measurements for a given distribution of geoelectrical properties, the inverse model aims to provide a distribution of geoelectrical properties given a set of measurements. In applying inverse methods, unknown parameters (e.g. resistivities) are designated for cells within a mesh. Such cells are geometrically defined as the finite elements or clusters of finite elements. The majority of inversion algorithms are based on a least squares fit between data and model parameters; the data misfit, , can be expressed as:

$$\phi_d = \| W_d(d - F(m)) \|^2,$$ (3.4)

where d are the data (e.g. measured transfer resistances), is the forward model estimates for parameter set m (typically the logarithm of resistivity), represents a data weighting matrix, which comprises the reciprocal error of each measurement and forward modelling error. Many initial

attempts to minimise using automated curve matching procedures (e.g. Barker, 1992; Zohdy, 1989) resulted in slow convergence, or divergence, of the solution. As the subsurface is ultimately represented by a fine mesh of parameters, the number of unknowns significantly outweighs the number of known geoelectrical properties, and hence the problem is underdetermined. To address this, spatial regularisation is commonly applied. Constable et al. (1987) proposed a method whereby the smoothest model that is consistent with the data is determined. Their approach utilises a spatial regularisation in order to ensure a stable and unique solution:

$$\phi = \phi_d + \alpha\phi_m, \tag{3.5}$$

where, α is the misfit between the modelled resistivity and some reference resistivity and determines the magnitude of the model misfit used . Model misfit is given by:

$$\phi_m = \| W_m \left(m - m_{ref} \right) \|^2, \tag{3.6}$$

where is a model weighting and is an optional reference model, e.g. for time-lapse modelling. The matrix ensures regularisation of the parameter values, effectively adding a dependency of parameters to adjacent values.

There are a number of inversion algorithms for ER and IP modelling, for example Res2DInv (e.g. Loke and Barker, 1996) the Aarhus Workbench (Auken et al., 2014), PyGIMLi (Gunther and Rucker, 2006; Rucker et al., 2006) and, R2 and cR2 (Binley and Kemna, 2005). In this thesis, R2 and cR2 were utilised because of their flexibility and ease of use. R2 is a finite element-based ER inverse code based on the approach briefly described above. The cR2 code is a complex formulation of R2 for IP applications. R2 and cR2 have been widely used for 2D inversion of ERT and IP data, respectively (e.g. Mares et al., 2016, Whalley et al., 2017; Terry et al., 2017). R2 and cR2 require several text documents: a 'protocol.dat' file containing measurement information, an 'R2.in' or 'cR2.in' file containing inversion parameters, and a 'mesh.dat' file containing details about a finite element mesh. To improve modelling capability for the applications within this thesis, a number of R functions were developed for R2 and cR2. It is common practice to process data in different ways, try different inversion parameters and assess different meshes; however manual generation of these input files is time-consuming. Furthermore, the development of functions to facilitate inversion was essential to test different forward model scenarios and automate tasks such as the generation of different meshes for time-lapse data (e.g. to account for river stage, see Chapter 7).

3.3 Code Structure

The functions rely mostly on base R functions but make use of ViridisLite (Garnier et al., 2018), akima (Gebhardt, 2016), and deldir (Turner, 2019) for plotting. The functions are compatible with R2 (v3.3) and cR2 (v2.0) and use Gmsh (Geuzaine and Remacle, 2009) to generate triangular meshes. The functions, their description and their required input parameters are displayed in Appendix 1. The structure of the code is summarised below and the general workflow is displayed in Fig. 3.3.

The functions follow the basic workflow for both inverse and forward modelling. For inverse problems, a data file containing columns of A, B, M and N positions, resistances and phase angles (if cR2 is to be used) is required. Alternatively, for TDIP data, a file containing columns of A, B, M and N positions, resistance, apparent chargeability, and chargeabilites at each time interval is required; the *filt.decay.curves()* function is then used to remove noisy decay curves (see Section 3.4.3). The *pair.meas()* function is used to pair the measurements and calculate averages and errors for each quadrupole; alternatively, for time-lapse difference inversions, the *pair.time.lapse.meas()* function computes an error appropriate for difference inversions (see Chapter 7). The *err.mod()* can be used to fit an error model for standard (e.g. for non-time-lapse data), before *write.protocol.dat()* is used to write the measurements and their corresponding errors to a 'protocol.dat' file. Alternatively, if no reciprocal data are available, *write.protocol.dat()* can be used directly; however, as no weights will be present in the 'protocol.dat' file, weights need to be specified in the 'R2.in' or 'cR2.in' using *write.R2.in()* or *write.cR2.in()*, respectively. A triangular mesh must then be generated using *write.mesh.dat()*, which writes the necessary input files, executes Gmsh and converts it into R2 and cR2 compatible formats using *msh.to.dat()*. Following generation of the 'protocol.dat' and 'mesh.dat' files, 'R2.in' or 'cR2.in' files are created using *write.R2.in()* or *write.cR2.in()* where a number of inversion parameters can be set. Functions *run.R2.exe()* or *run.cR2.exe()* are then used to run either the R2 or cR2 executable and invert the data.

For forward modelling, *write.seq.dat()* can be used to generate a dipole-dipole, Wenner or Schlumberger array and write it to a 'protocol.dat' file. A mesh is then generated using *write.mesh.dat()*. Generally, synthetic data should be generated on a fine mesh and then be inverted on a coarser mesh, as is the procedure here. Following mesh generation, *write.res0.dat()* can be used to write the model from which data are to be generated. This function requires the input of a list of zones. Each zone comprises a list of x and y coordinates, a resistivity, and a phase angle (if cR2 is being used). The *write.res0.dat()* function uses the nested function *in.zone()*, which uses a ray casting algorithm to determine if the element centre is in or out of the zone. After the creation of 'protocol.dat' and 'res0.dat', *write.R2.in()* or *write.cR2.in()* is used to specify that the problem

type is a forward problem. As with inverse modelling, *run.R2.exe()* or *run.cR2.exe()* is then used to generate synthetic data. The function *return.synth.data()* combines *write.res0.dat()*, *write.R2.in()* or *write.cR2.in()*, and *run.R2.exe()* or *run.cR2.exe()* to create a data frame of synthetic data. Noise can be added to the synthetic data using *add.noise()* before the data are inverted.

The *write.mesh.dat()* is key to inverse and forward model problems, and requires some additional explanation. The mesh dimensions are based on the electrode positions and require the input of characteristic length 1, characteristic length 2, and a depth of investigation. The mesh generated has a fine region close to the electrodes and a coarse region beyond. The x dimensions of the fine region are defined by the average spacing of the electrodes; for instance the x coordinates range from 5 electrode spacings before the position of the first electrode and 5 electrode spacings beyond the position of the last electrode, the y coordinate limits are determined from the elevations of the first and last electrodes and the depth of investigation. The size of elements in the fine region are then determined from characteristic length 1, and the elements in the coarse region are determined from characteristic length 2.

In addition to functions facilitating data processing and inversion, several functions were written to plot data; all plot functions require a xyz data frame and details of the electrode positions. The *pretty.tri()* function plots a colour map where the x and y coordinates are interpolated into Thiessen polygons using the deldir package (Turner, 2019). Alternatively *pretty.scatter()* uses a xyz data frame to plot a coloured scatter plot. It is often convenient to plot raw data as a pseudo-section using *plot.pseudo()* where a transect of apparent resistivity data can be plotted with a pseudo-depth determined by the separation of electrodes, a pseudo-section can be plotted using. For all plots the viridis colour scale is used as default.
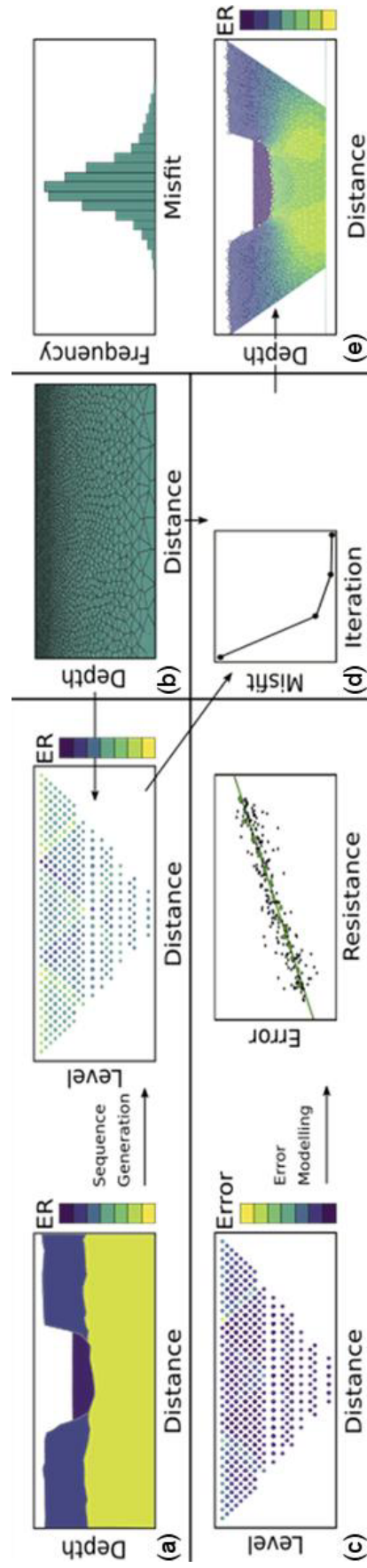
Figure 3.3: Schematic showing workflow of R functions: (a) generation and corruption of synthetic data, (b) mesh generation, (c) filtering and error modelling of field data, (d) inversion, and (e) plotting inversion results.

3.4 Modelling Examples

3.4.1 Assessing Different Array Types

To demonstrate the capabilities of generating synthetic data from different array types, the first case involves two inclined resistive units separated by an inclined conductive unit, Fig. 3.4a. In many cases, it may be necessary to test different array types to understand the limits of the method and understand which array performs best. In this example, synthetic data for dipole-dipole and Schlumberger arrays are generated, corrupted with noise, and inverted. These arrays were chosen as they are the most commonly used measurement sequences in geoelectrical imaging. Moreover whilst optimised arrays exist (e.g. Wilkinson et al., 2006) the benefit of these sequences is that they can be used directly. The dipole-dipole array comprises 4838 measurements whereas the Schlumberger array comprises 4550 measurements. Moreover to avoid any biases, synthetic data was generate using a mesh with finer elements than the mesh used for the inversion,

The script used in Case 1 is shown in Appendix 1, Fig. 11.1. In summary, first a data frame of electrode positions is created comprising columns stating the x and y coordinates, and a column stating that the electrodes are surface electrodes. A 'mesh.dat' file is then generated using *write.mesh.dat()* based on the positions of the electrodes. For forward modelling different zones of the mesh need to be assigned different resistivity values. To do this a nested list of x and y coordinates and the resistivity value are created. The *write.seq()* function is used to write a 'protocol.dat' file for dipole-dipole and Schlumberger sequences. The *return.synth.data()* uses *write.res.dat()* to assign the elements a resistivity value depending on if the element centre lies inside or outwith a zone, before using *write.R2.in()* and *run.R2.exe()* to generate synthetic data. Elements within zone 1 are assigned a resistivity of 800 ohm.m, elements within zone 2 are assigned a resistivity of 1200 ohm.m, the central zone is assigned a background resistivity of 200 ohm.m, and synthetic data are then corrupted with 2% normally distributed errors and written to a 'protocol.dat' file prior to inversion. A new mesh is then generated and a new 'R2.in' file is created; following the inversion, the synthetic model and two inverted models are plotted using triangular polygons.
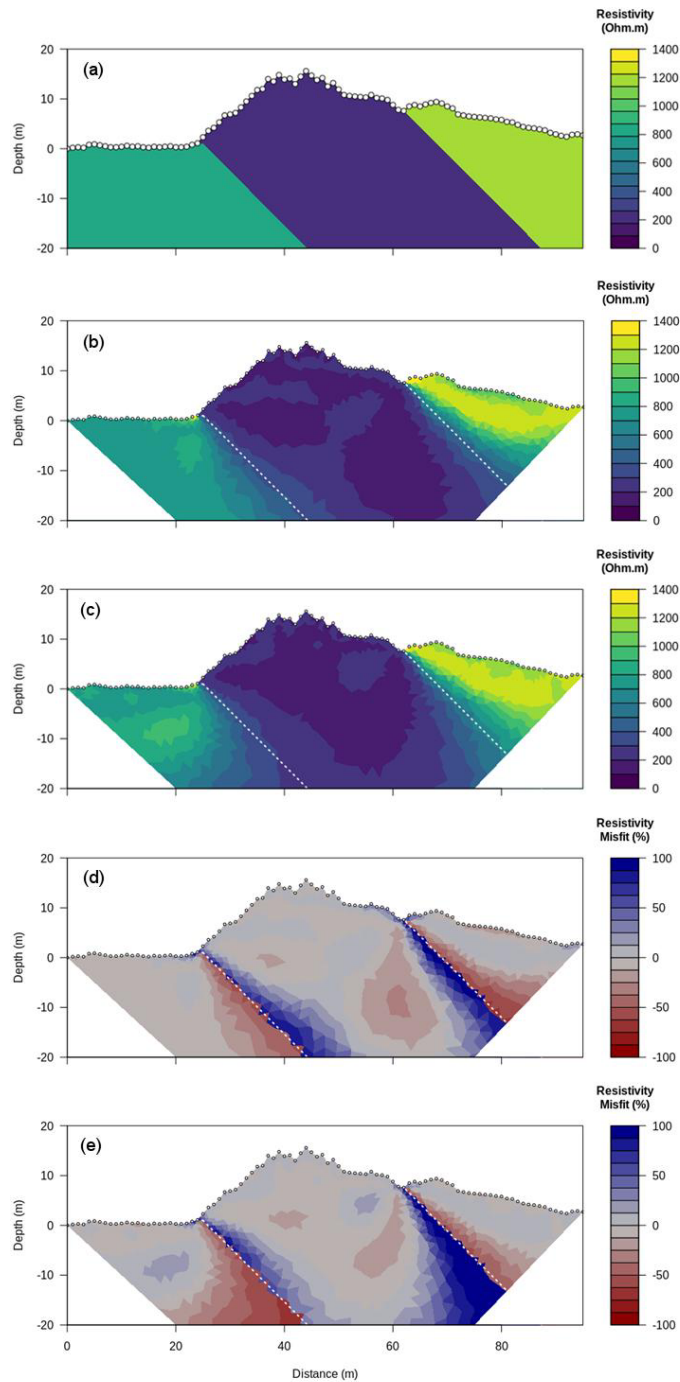
Figure 3.4: (a) Model for Case 1 comprising three sloping layers: underlying layer with resistivity of 800 ohm.m, an intermediate layer with resistivity of 200 ohm.m and an overlying layer with resistivity of 1200 ohm.m. (b) and (c) show inversion of data generated for a dipole-dipole, and a Schlumberger array. Resistivity misfit as a percentage between models (a) and (b), and (a) and (c) are shown in (d) and (e), respectively. White circles indicate electrode positions.

It can be seen that synthetic data obtained using both Schlumberger and dipole-dipole arrays (Fig. 3.4b and c) provide distributions of resistivity that match the synthetic model well, especially near the surface. However, to reveal areas where the inverted resistivity does not match the resistivity of the synthetic model, the differences can be calculated and expressed as a percentage change from the synthetic model (Fig. 3.4d and e). By looking at the percentage differences, it is more evident that the inverted synthetic data mismatch is the highest along the boundaries, which is to be expected given the regularisation. It can also be seen that the model obtained from the dipole-dipole survey has better depth resolution. Nevertheless, the majority of regions are resolved with an accuracy of +/- 10% for both array geometries.

3.4.2 Blocking and Fixing Zones

In Case 1 it was observed that regularisation across the boundary led to large differences between resistivities in the synthetic model and the inverted model. R2 (and cR2) can be configured to prevent smoothing across boundaries, provided that the boundaries known. For example, if seismic data revealing a sharp geological boundary was available for Case 1, the mesh could be discretised into different regions to prevent smoothing across lithological boundaries. Another example, particularly relevant to this thesis, is in the context of rivers, where there should be an abrupt difference in the resistivity of the river and of the riverbed. Furthermore, R2 and cR2 permit the fixing of element values. For example, if the resistivity of the river is known, it can be fixed in the inversion to improve resolution of the riverbed. To demonstrate the capabilities of blocking and fixing regions (i.e. to prevent smoothing across boundaries or to fix electrical properties) of the inverse models, a synthetic scenario representing a river is generated. Case 2 comprises an upper layer with a resistivity of 50 ohm.m underlain by a more resistive layer with a value of 200 ohm.m and a river with resistivity of 20 ohm.m, see Fig. 3.5a. In this example, the effects of allowing smoothing across the river-sediment interface, preventing smoothing across the interface, and fixing the river to an observed resistivity value are considered.
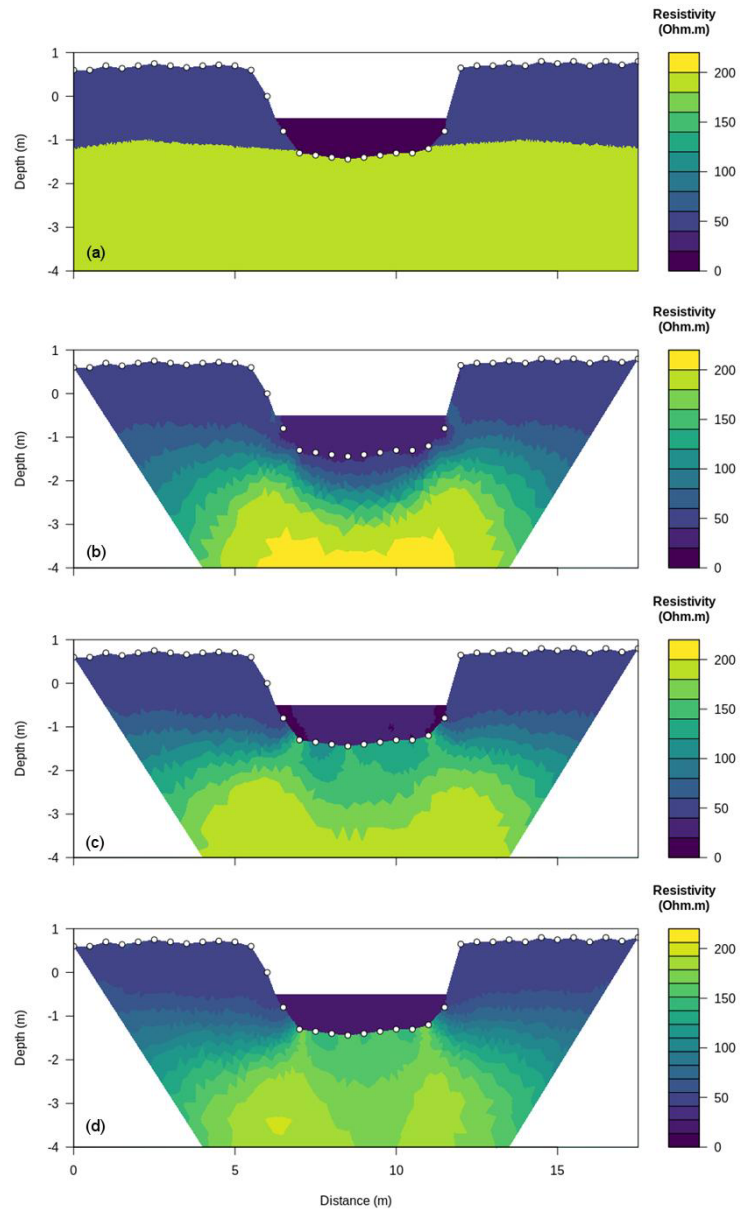
Figure 3.5: (a) Model for Case 2 with upper layer electrical resistivity of 50 ohm.m, a lower layer with resistivity of 200 ohm.m and a river with resistivity of 20 ohm.m. (b) shows inversion of data for the case when regularisation across the river-riverbed interface is permitted. (c) shows inversion of data for the cases when regularisation across the interface is bloacked. (d) shows inversion of data for when the river resistivity is fixed at 20 ohm.m. White circles indicate electrode positions.

The steps for Case 2 are shown in Appendix 1, Fig 11.2, however, the flow is summarised as follows. Initially, electrode positions are assigned, and electrodes occurring on the riverbed are stated as being buried; in this case, rows in column 3 are labelled 'true' if on the surface and 'false' if on the riverbed. A mesh file is generated as before except in this case topographic points for

where the river meets the banks are included. Two zones are then defined, the first describes the subsurface stratigraphy and the second captures the boundary of the river. A 'protocol.dat' file is written for a dipole-dipole sequence and then synthetic data are generated before being corrupted with noise. A new mesh is then generated for each of the three cases. For the first case, this mesh is left unmodified to permit smoothing across the river-sediment interface during inversion. For the second case the mesh is modified to prevent smoothing. Finally, for the third case, the value of the river zone is fixed at 20 ohm.m. The synthetic model is then plotted along with the three inverse models, details about the river elevation and additional topographical points are included in the plot function to blank appropriate regions. If two zones overlap, elements will be assigned the value of the second zone in the list.

It can be seen that allowing regularisation across the boundary results in the resistivity in the immediate vicinity of the river being underestimated (Fig. 3.5b). Interestingly, although fixing the resistivity of the river improves the image of the subsurface (Fig. 3.5d), a similar effect is also achieved simply preventing regularisation across the boundary (Fig. 3.5c). The same is not true for longitudinal surveys, see Chapter 6.

3.4.3 Processing and Inversion of Induced Polarisation Data

To demonstrate the data processing and error modelling capabilities, we use an IP data set collected from a former Roman port (Quay Meadow, Lancaster, UK), see Fig. 3.6. Prior electromagnetic induction surveys at this site revealed an 8 x 40 m conductive anomaly running perpendicularly to the original position of the River Lune, i.e. prior to land reclamation. To further investigate the likely nature of this anomaly, an IP survey was conducted to determine if the conductive anomaly was related to metallic waste, a more clay rich soil or a difference in pore water conductivity. Data were collected using an Iris Instruments Syscal Pro with a dipole-dipole array, 48 electrodes and an electrode spacing of 0.5 m; the plots produced in this example are displayed in Fig. 3.7.

Figure 3.6: Location of the IP array in relation to the Lancaster Castle Field site, transect is located on Quay Meadow by a red line. Maps taken from Edina DigiMap.

The steps taken to produce the plots in Fig. 3.7 are shown in Appendix 1 (Fig. 11.3). To begin with a triangular mesh is generated for an electrode array with flat topography and equally spaced electrodes. IP data are then processed, the file consists of the electrode positions, the measured transfer resistance, apparent chargeability and the chargeabilities measured at each time interval. The IP data is then filtered based on their decay curves. To do this a log-linear relationship is fitted for each decay curve and an R^2 is computed, following this data with relationship with an R^2 value above a threshold value is removed (see Fig. 3.7a and b).

In addition, if the relationship crosses the time axis before t_2, or data values are negative they are also removed. However, it is noted that negative apparent chargeabilities and non-characteristic decay curves (e.g. Dahlin and Loke, 2015; Dahlin, 2018) are not necessarily invalid. On the contrary, provided the majority of apparent chargeabilites are positive and display characteristic decay curves, these filtering methods are assumed appropriate. It is also important to note that Flores-Orozco et al. (2016) advocates for a more supervised approach involving manual checking of each decay curve. This enables them to keep decay curves where only one or two windows are characterised by poor quality; however here it is assumed that so long as the majority of data are kept the differences in approach should not matter substantially.
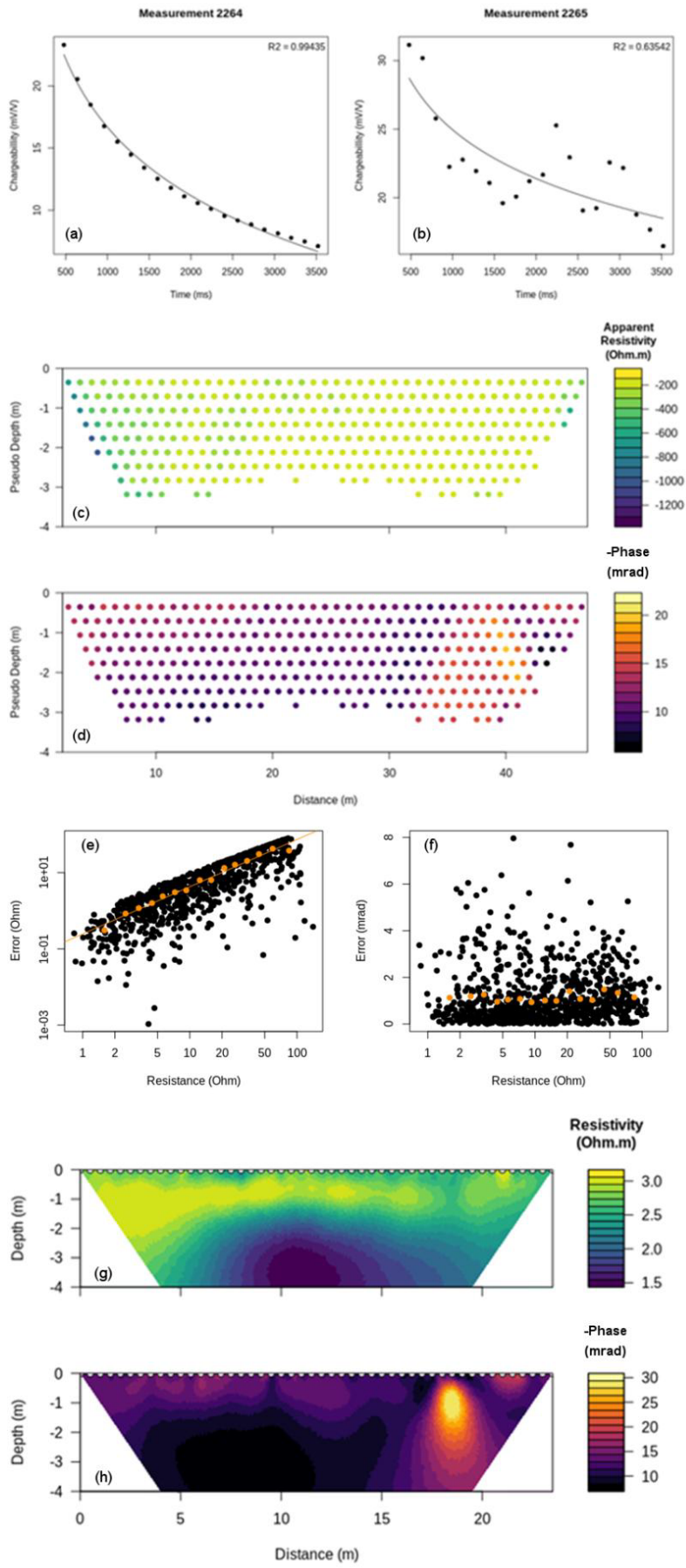
Figure 3.7: Plots for Case 3, (a) acceptable decay curve, (b) rejected decay curve, (c) apparent resistivity pseudo-section, (d) phase pseudo-section, (e) resistance errors, (f) phase errors, (g) inverted resistivity model, and (h) inverted phase model.

The decay curve filter function outputs a data frame with A, B, M and N electrode positions, resistance and phase (apparent chargeability is converted using a default value of $c = -1$, where $\varphi = cM$). Direct and reciprocal measurements are then paired, measurements without reciprocal pairs are rejected and mean and error values are calculated for resistances and phase angles. Pseudo-sections of the data can be plotted so that outliers can be identified visually and removed if need be before error models are fitted to the data. For resistance error analysis, the relationship between average resistance and resistance error is fitted using a linear model, a power law model or a mixed effects model (e.g. Tso et al., 2017); the former two involves the binning of data (Fig. 3.7e). For phase error analysis, the relationship between average resistance and phase error is fitted using a power law fit or a parabola fitted in log-linear space (Fig. 3.7f). Data are written to a 'protocol.dat' file with modelled errors, before the 'cR2.in' file is generated and cR2.exe is called to perform the inversion. Plots of the triangular polygons are then plotted for the resistivity and phase values.

As with the preliminary electromagnetic surveys, the conductive anomaly can be seen in the centre of the Fig. 3.7g, starting at about 2 m depth. The phase angle plot (Fig. 3.7h) indicates that this feature has comparatively lower phase angle, suggesting that the conductive anomaly is related to the pore water, either more saturated or a higher conductivity, as opposed to the presence of clay or metal. A high phase anomaly is revealed at an x position of 18 m and a depth of 1 m. This feature is not so well displayed in the resistivity section and likely represents a small metallic feature, e.g. utility cables. Future investigations could focus on intrusive work to determine the nature of this low resistivity, low phase feature, perhaps it represents an in-filled channel inlet at the Roman Port.

3.5 Summary

The general principles of the ER and IP methods have been described, including the use of inverse modelling. A number of R scripts have been developed to assist application of the R2 and cR2 codes used within the thesis. These functions aid in the creation of the necessary input files for R2 and cR2 inversion and significantly simplify the work required to prepare these files. The workflow follows a classical approach of data input, error modelling and inversion. Methods to run forward scenarios to assess the ability, or more importantly the inability, of certain arrays to resolve information about the geoelectrical structure of the subsurface is important. Furthermore, the functions are written in an accessible language, making it easy to follow and allows for easy addition of more features.

4 Processing and Modelling Electromagnetic Induction Data

4.1 Introduction

Frequency domain electromagnetic induction (EMI) methods use phenomena governed by Maxwell's equations to provide information about the electrical conductivity (EC) of the subsurface. Given that EC is the reciprocal of electrical resistivity, EMI methods provide comparable information to electrical resistivity methods. However, they do not require direct coupling to the ground and are consequently more productive than standard electrical resistivity imaging surveys. EMI measurements are typically expressed as apparent electrical conductivities (ECa) and have a long history of being used to reveal spatial patterns in a number of hydrologically important parameters such as soil salinity (e.g. Corwin, 2008), soil moisture (e.g. Corwin and Rhoades, 1982; Williams and Baker, 1982; Sherlock and McDonnell, 2003), and soil texture (Triantafilis and Lesch, 2005), see Table 4.1. Furthermore, some studies have used repeated (e.g. time-lapse) measurements of ECa to reveal temporal patterns in addition to spatial patterns, e.g. for water content (Robinson et al., 2011; Martini et al., 2017).

Table 4.1: Applications of Electromagnetic Induction Methods to reveal spatial and temporal patterns in hydrological and geological properties.

Application	Reference
Moisture content	Robinson et al., 2011; Martini et al., 2017, Brosten et al. (2011), Comas et al. (2004), Cassiani et al. (2012), Corwin and Rhoades (1982), Corwin (2008), Doolittle and Brevick (2014), Williams and Baker (1982), Sudduth et al. (2001)
Soil salinity	Paine (2003), Corwin (2008), Diaz and Herrero (1992), Corwin and Lesch (2005), Hatch et al. (2006)
Water table depth	Sherlock and McDonnell (2003), Doolittle et al. (2012), Shanahan et al. (2014), Robinson et al. (2008), Schumann and Zaman (2003), Buchanan and Triantafilis (2009)
Carbon content	Martinez et al. (2009), Bechtold et al. (2013)
Clay content	Triantafilis et al. (2001), Triantafilis and Lesch (2005)

In addition to ECa mapping, the development of multi-frequency and multi-coil instruments has enabled the possibility of inversion of EMI measurements to provide quantitative models of depth specific EC. For instance, by obtaining multiple EMI measurements with different sensitivity patterns, a model of EC can be obtained. However, as with all geophysical inverse problems, the inherent ill-posedness and non-uniqueness of solutions requires the introduction of regularisation or constraints (e.g. Constable et al., 1987; Trantola, 2005) to produce models of smoothly or sharply varying EC, see Fig. 4.1. Furthermore, measurements are highly correlated and therefore not truly independent. The inversion can be formulated as an optimisation problem where the objective function is some measure of misfit between measured and modelled data. The majority of inversion algorithms use a 1D forward model based on either the linear cumulative sensitivity (CS) forward model proposed by McNeill (1980) or non-linear full solution (FS) forward models based on Maxwell's equations (e.g. Wait, 1982; Frischknecht et al., 1987). Moreover, in some EMI inversion software (e.g. EM4Soil and the Aarhus Workbench) lateral constraints can be used to encourage laterally smoothed images using a 1D forward model, which is typically called quasi-2D/3D inversion.
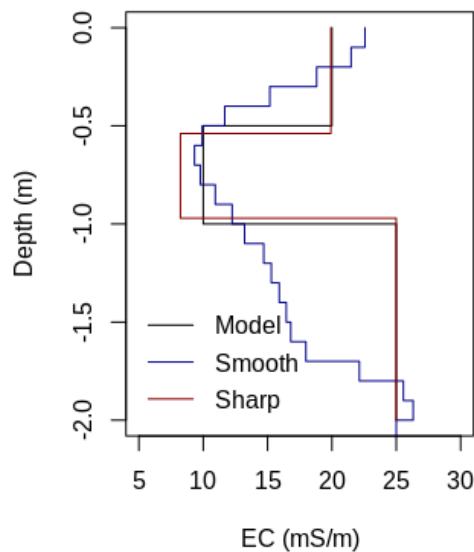
Figure 4.1: Comparison of smooth and sharp inversion models of data obtained from a model of sharply varying electrical conductivity.

As with EMI mapping, applications using inverted EMI data have also been diverse (Table 4.2). Applications typically focus on using an inversion based on either the CS or a FS forward model to produce regularised, smoothly varying, models of EC with fixed depths or sharply varying models of EC where layer depths are also a parameter. Whereas regularised models are useful in areas

where there is a smoothly varying property of interest, e.g. water content, this may be less appropriate in areas with abrupt changes in EC, e.g. lithologically stratified environments, see Fig. 4.1. However, it is important to note that regularised inversions can also be used alongside edge detection techniques to determine lithological boundaries (e.g. Fredriksen et al., 2017).

Table 4.2: Applications of electromagnetic induction methods using inversion algorithms to produce quantitative conductivity models.

Application	Author	Regularisation	Forward model
Lithology	Von Hebel et al. (2014)	Sharp	FS
Lithology	Fredriksen et al., (2019)	Smooth	FS
Water content	Whalley et al. (2016)	Smooth	CS
Water content	Haung et al. (2016)	Smooth	CS
Lithology	Saey et al. (2015)	Smooth	CS and FS
Lithology	Christiensen et al. (2015)	Smooth	FS
Hydraulic conductivity	Brosten et al. (2011)	Smooth	CS
Organic carbon	Haung et al. (2017)	Smooth	CS and FS
Lithology	Mester et al. (2011)	Sharp	CS and FS

Whereas regularised solutions permit the resolution of multilayer models, sharp inversions with no smoothing between layers will be limited to fewer layers and may require bounds to encourage logical solutions. Furthermore, because individual measurements are not independent, the problem with six measurements and five parameters (e.g. three ECs and two depths) is not an over-determined problem. Some examples of inverse algorithms to produce sharp models of EC include Mester et al. (2011) who used a combined global and local search to obtain two-layer models, with no regularisation, von Hebel et al. (2013) expanded on this work to provide three-layer models of EC using the Shuffled Complex Evolution (SCE) algorithm of Duan et al. (1993). This method required EC bounds which are defined by half the lowest measured ECa and double the highest measured ECa when the device is operated at ground level. Although it can be adapted for when the device is operated above ground, these constraints are fairly conservative and only work well for relatively homogenous sites. For instance, they are inappropriate for the examples presented in Section 4.4, which are representative of the riparian wetland considered in Chapter 5.

The attractiveness and frequent use of the CS forward model stem from its simplicity and computational efficiency over the FS forward model. However, its use requires several specific assumptions about instrument operation for a given ground EC. In many cases these assumptions may be invalid even in fairly non-extreme environments, for instance, Beamish (2011) proposes that they are only valid in low EC environments (< 12 mS/m). Furthermore, the commonly used ECa values in qualitative mapping studies are typically derived under the same assumptions and therefore may not give the most reliable approximation of subsurface EC. However, the comprehensibility of ECa as a measurement is such that several authors have attempted to obtain ECa via different methods (e.g. Andrade et al. 2015).

In this chapter the theoretical background of EMI measurements is summarised, including the necessary assumptions behind the ECa measurement proposed by McNeill (1980) and the CS forward model. A FS forward model is also discussed before various proposed methods for obtaining a more reliable ECa are discussed. Following this, an outline of R based functions used in this thesis is presented. Specifically, functions to process, forward model, inverse model, and plot EMI data are included. Two synthetic cases are then discussed to highlight the scope of some of the code and explore two fundamental aspects of the EMI inversion problem. The performance of the CS inversion and the influence of measurement error on the FS inversion, which have not been investigated in detail, are assessed. Although functions to produce regularised inverse models are included here, it is important to note that the focus of this work was to develop an inversion algorithm for modelling of data from a riparian wetland; hence the emphasis was on producing sharp images of the subsurface.

4.2 Electromagnetic Induction Background

EMI devices operate by passing an alternating current through a transmitter coil to generate a primary electromagnetic field (H_P). This time-varying primary electromagnetic field interacts with the subsurface to induce eddy currents which in turn generate a secondary electromagnetic field (H_S). H_P and H_S are then recorded by the receiver coil, see Fig. 4.2. The ratio of H_S and H_P is expressed as a complex number with an in-phase component (P) and an out-of-phase, or quadrature, component (Q). H_S/H_P is dependent on both the instrument set up (e.g. operating frequency, coil separation and coil orientation) and subsurface conditions (e.g. magnetic, conductive and dielectric properties). At the low frequencies used (< 15 kHz) only magnetic and conductive contributions are important; however, given that the majority of environmental applications are non-magnetic, the magnetic permeability of the subsurface is often assumed to be equal to that of free space ($\mu_0 = 1.257 \times 10^{-8}$ H/m).
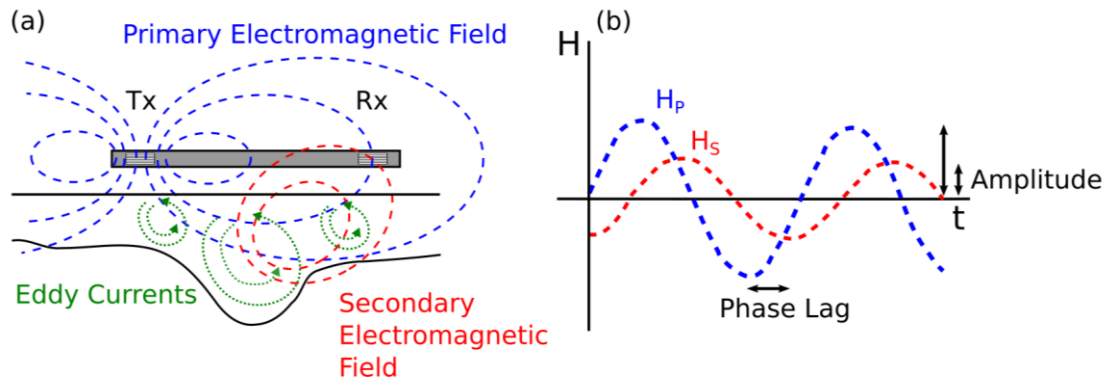
Figure 4.2: Schematic of the principle behind the EMI method showing the interaction of the primary (Hp) and secondary electromagnetic fields (Hs) arising from a conductive layer in the subsurface.

For any given ground conditions, the obtained H_S/H_P is dependent upon the separation distance between the transmitter and receiver coil, the operation frequency and the orientation of coils. The most commonly used orientations are referred to as coplanar loops in which both the transmitter and receiver coils are orientated either horizontally (HCP) or vertically (VCP) with respect to ground. In addition, many devices are multi-coil or multi-frequency, meaning that measurements with different sensitivity ranges can be obtained by the same instrument which can then be used for inverse modelling. For instance, the GF Instruments Explorer unit, from here on referred to as the GF Explorer, operates at 10 kHz, has three receiver coils, with different separations, and can be used in either VCP or HCP mode. This means that a total of six measurements can be obtained (3 for each orientation of the coils). The GF Explorer, and majority of other instruments, expresses their measured values as apparent electrical conductivity (ECa). This term was introduced by McNeill (1980) to provide a more comprehensible measurement with the same units as EC, S/m. McNeill (1980) derived a linear relation from analytical solutions describing the Q value obtained from a homogenous ground. The relationship therefore links the Q value of an assumed homogenous subsurface volume to an ECa. This relationship requires that the device is laid on the ground and that the induction number (β) is low (β << 1). As a result it is commonly referred to as the low induction number (LIN) approximation and is given by:

$$\sigma_a = \frac{4}{\omega\mu_0 s^2} Q,$$

(4.1)

70

where ω is the angular frequency and s is the coil separation. The dimensionless induction number which increases for increasing ground EC is given by

$$\beta = s\left(\frac{2}{\omega\mu_0\sigma}\right)^{0.5}.$$

(4.2)

For the GF Explorer and a ground EC of 100 mS/m the induction numbers for the coils with separations of 1.48, 2.82 and 4.49 m are 0.093, 0.177 and 0.282, respectively. Although these lie well within the threshold proposed by McNeill (1980) other values of < 0.3 (Wait, 1962) and < 0.02 (Frischknecht, 1987) have also been proposed for LIN approximations to be valid. The majority of manufacturers state that their devices operate under LIN conditions and use the LIN approximation to convert Q to ECa. It is important to note here although the GF Explorer is also said to operate at LIN conditions, the device is calibrated using the manufacturer's own calibration. They provide two calibrations, one for operating the device at 0 m and the other at 1 m. Both of these calibrations are done by taking measurements over ground of known EC and fitting a linear relationship. Therefore, measurements obtained whilst operating the device at 1 m should be roughly comparable as those observed if the device were at 0 m. From here on, the ECa obtained under the LIN approximation will be referred to as LIN-ECa, whereas the ECa obtained from the GF Instruments will be termed GF-ECa. A comparison of LIN-ECa and GF-ECa are shown in Fig. 4.3.
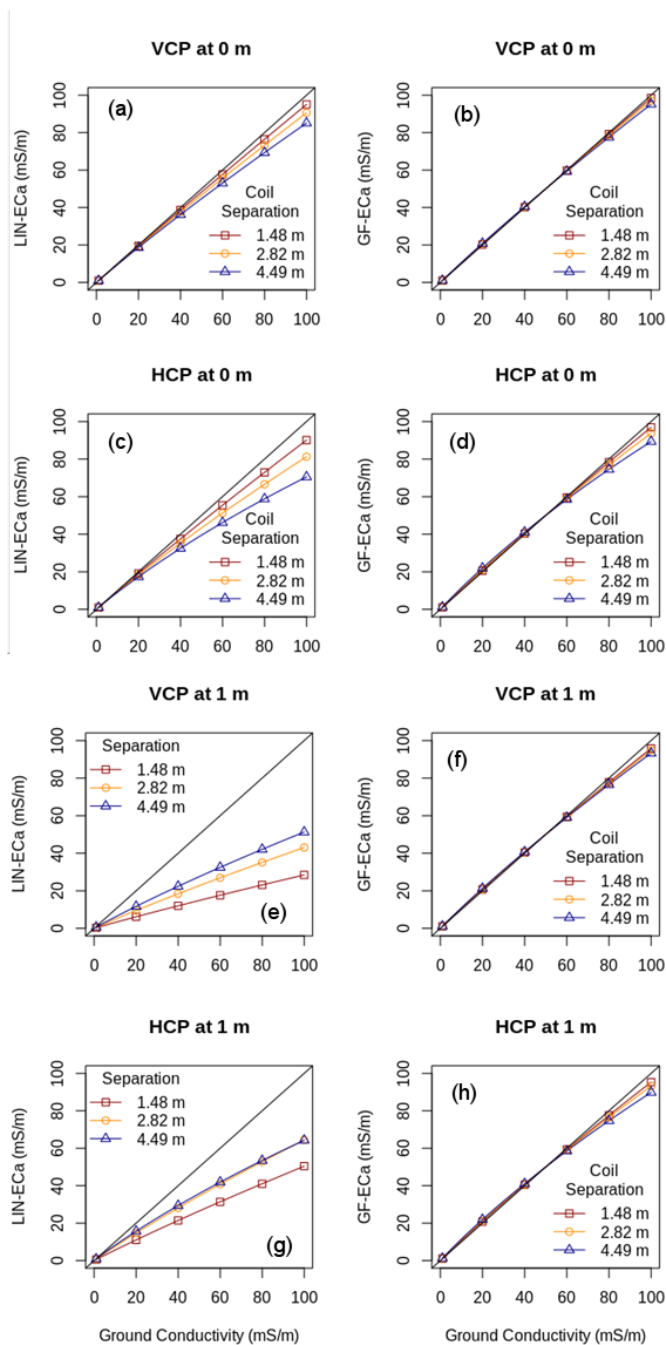
Figure 4.3: Modelled apparent electrical conductivities (ECa) for the GF Instrument Explorer device above a homogenous ground using different calibrations for different operation heights: (a) ECa obtained using low induction number approximation (LIN-ECa) with device at 0 m with coils in vertical coplanar (VCP) orientation, (b) ECa obtained using GF calibration (GF-ECa) with device at 0 m with coils in VCP orientation, (c) LIN-ECa for device at 0 m with coils in horizontal coplanar (HCP) orientation, (d) GF-ECa for device at 0

72

m with coils in HCP orientation, (e) LIN-ECa for device at 1 m with coils in VCP orientation, (f) GF-ECa for device at 1 m with coils in HCP orientation, (g) LIN-ECa for device at 1 m with coils in HCP orientation, and (h) GF-ECa for device at 1 m with coils in HCP orientation.

Ideally, ECa values should line on the 1:1 line for a homogenous ground when operated at ground level (0 m). It can be seen that as the ground EC increases the LIN-ECa deviates from the 1:1 line. In comparison the GF-ECa obtained when the device is operated at the ground level lies closer to the 1:1 line, it does however deviate at higher EC. It is evident from these plots that although the link between Q and ECa using the LIN approximation and the GF calibration is assumed linear, it is not. The same deviation can be observed when the device is operated at 1 m; however the LIN-ECa deviates further from the 1:1 line than the GF-ECa lies. In reality the ECa should be lower when operated at 1 m elevation due to the air layer between the ground and the device. However, the purpose of the 1 m GF-ECa calibration is to provide an ECa measurement more similar to that if the device was operated at ground level. The benefit of this is that the device will give values that are more representative of the ground. Nonetheless, this calibration needs to be considered when inverting data; for instance, to use the FS forward model data needs to be expressed as Q values, meaning that converting ECa measurements obtained using the GF calibration at 1 m via the LIN approximation will lead to erroneous inverse models.

In addition to the LIN approximation, McNeill (1980) provided functions to describe the relative contribution of material below a specific depth to the ECa when a device operates under LIN conditions. These CS functions assume that the response of the device is linearly related to the EC structure of the subsurface, i.e. the EC structure does not influence instrument sensitivity. The CS responses for VCP and HCP orientations are as follows:

$$R_{VCP}(z) = (4z^2 + 1)^{0.5} - 2z, \tag{4.3}$$

$$R_{HCP}(z) = (4z^2 + 1)^{(-0.5)}, \tag{4.4}$$

where z is the depth normalized by the coil separation, s. From these equations the sensitivities for different coil orientations and separations are apparent (Fig. 4.4). It can be seen that measurements made with coils in the VCP orientation are more sensitive to the shallow subsurface and HCP measurements are sensitive to deeper depths. These functions are commonly used by manufacturers to provide information about the depth sensitivity of their instruments. For the GF Explorer, this is

quoted as the depth above which 70% of the signal comes from, which is in line with the rule of thumb that states VCP measurements have an effective depth of 0.75 times the coil separation and 1.5 times for HCP measurements.
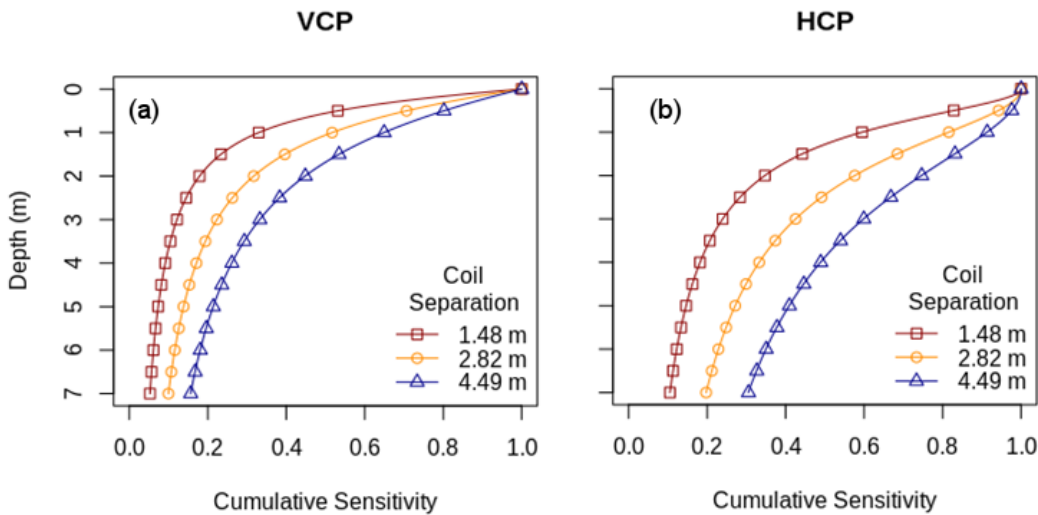
Figure 4.4: Cumulative sensitivity patterns for the GF Instruments Explorer when operated at ground level in both coil orientation modes.

These approximations proposed by McNeill (1980) have been fundamental in advancing the EMI methods, both in qualitative mapping and quantitative modelling of EC data. As noted previously, despite the availability of inversion algorithms based on the FS forward model, the use of CS forward model in EMI applications is still fairly common. This is largely due to their simplicity and speed in the inversion process compared to FS forward solutions. For instance, for regularised inversions where depths are not parameters, the linear nature of the CS forward model means that they can be solved in one iteration. However, in many cases, these LIN assumptions are invalid and can lead to inaccurate measurements. For example, when ground EC is high, when there is strong heterogeneity in the subsurface EC, or when the device is not operated at ground level. Furthermore, Andrade et al. (2016) showed that under fairly typical field conditions, LIN assumptions can lead to significant errors, and Beamish (2011) suggested that LIN assumptions are only appropriate in environments with EC of less than 12 mS/m.

In order to calculate the true response, in terms of H_S/H_P, of the ground for a given measurement setup, a FS forward model must be used. The model used relies on the assumption that

electromagnetic fields propagate only due to conduction currents, which is valid at low-frequencies ($< 10^5$ Hz). The Maxell-based full solution is provided by Wait (1982) and can be used to determine the response of an EMI instrument over a 1D layered earth comprising N layers:

$$\left(\frac{H_S}{H_P}\right)_{VCP} = -s^2 \int_0^\infty R_0 J_1(s\lambda)\, d\lambda, \tag{4.5}$$

$$\left(\frac{H_S}{H_P}\right)_{HCP} = -s^3 \int_0^\infty R_0 J_0(s\lambda)\lambda^2 d\lambda, \tag{4.6}$$

where J_0 and J_1 are Bessel functions of zero and first order, respectively, and R_0 is the reflection factor, which is dependent on the thicknesses and EC of each layer. The reflection factor can be calculated at the interface between the air and the first layer. It can be obtained recursively from layer N, given that layer N and beyond is assumed homogenous and therefore $R_{N+1} = 0$, and the following:

$$R_n = \frac{\dfrac{\Gamma_n - \Gamma_{n+1}}{\Gamma_n + \Gamma_{n+1}} + R_{n+1} e^{-2\Gamma_{n+1}h_{n+1}}}{1 + \dfrac{\Gamma_n - \Gamma_{n+1}}{\Gamma_n + \Gamma_{n+1}} e^{-2\Gamma_{n+1}h_{n+1}}}, \tag{4.7}$$

where, and h_n and σ_n are the thickness and the EC of the nth layer. R_0 is obtained by assuming the EC of layer 0 is 0 S/m to reflect the air. The integrals in equations 4.6 and 4.7 can be calculated by linear filtering using weights provided by Guptasarma and Singh (1997). Furthermore, the response for instruments operated at 1 m can be modelled by including a layer with a thickness of 1 m and an EC of 0 S/m.

In addition to providing a more accurate forward model for inverse modelling, several authors have used FS forward models to provide more representative ECa values when LIN assumptions are invalid. Typically, methods either focus on the Q value, as with the LIN approximation, or use both the P and Q components to obtain an ECa. Methods using Q values include Huang and Fraser (2002) who used Q values obtained at two different frequencies to estimate ECa above a strongly magnetic subsurface. Alternatively, Andrade et al. (2016) proposed minimising the difference between measured Q values and predicted Q values obtained from a homogenous half-space EC. This method can be used for any measurement height; however, it requires initiation using the LIN approximation and as a result may provide ambiguous or erroneous results at high induction

numbers. Alternatively, Beamish (2011) proposes a procedure based on the device properties and operation height to correct ECa values obtained using the LIN approximation. Methods which use both the P and Q values include Huang and Won (2000) who used multi-frequency EMI instruments operated at ground level based on both EC and magnetic susceptibility half-space models. Additionally, Guillemoteau et al. (2015) minimised the differences between the modelled and measured H_s/H_p responses to estimate EC for instruments operated at 0 m. He et al. (2017) developed a translation algorithm that features fast computation speed, high accuracy, and insensitivity to instrument elevation. However, given the requirement for accurate and stable P measurements, which is often not the case (De Smedt et al., 2016; Delefortrie et al., 2014), methods using P values can be problematic. In this work the method proposed by Andrade et al. (2016) is used; to distinguish it from LIN-ECa and GF-ECa, it is referred to as Andrade-ECa in the preceding text. The Andrade-ECa values for the GF Explorer operated at 1 m above a homogenous ground is shown in Fig. 4.5; note that when the device is operated at 0 m, Andrade-ECa will fall on the 1:1 line for a homogenous ground.
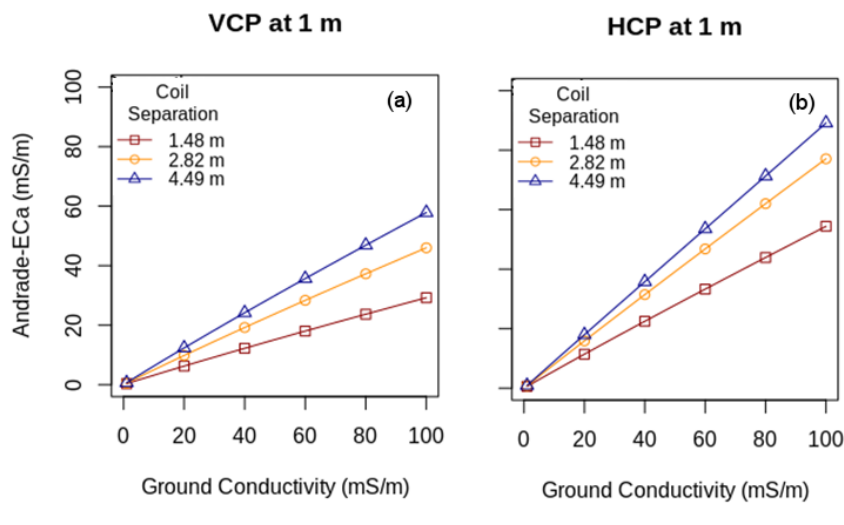
Figure 4.5: Expected Andrade-ECa for GF Instruments Explorer when device is operated at 1 m in VCP and HCP modes.

4.3 Code Structure

The functions developed rely mostly on base R packages, but make use of sceua (*Skøien* et al., 2014) for minimisation of an objective function, and ViridisLite (Garnier et al., 2018) and akima (Gebhardt, 2016) for plotting. Furthermore, for the Hankel transfor*m,* weights provided by

Guptasarma and Singh (1997) are used. These functions follow a basic workflow for processing, calibrating, inverting, and plotting field data and modelling synthetic data, e.g. for feasibility studies and survey design, see Fig. 4.6. Functions are separated into different groups based on their purpose; details about the necessary parameters for each function can be found in Appendix 2. The function groups are discussed in more detail in the following sections.

4.3.1 Data Tools

Data tools are used to process, filter and calibrate data. The first function *filt.data.emi()* is for filtering data collected in a continuous roaming mode. The deviation of neighbouring measurements is calculated, and noisy data are replaced by values interpolated from preceding and succeeding measurements. Additionally, data are binned into bins with equally spaced ECa and P values; bins containing data below a given percentage threshold, i.e. outlier data, are then removed. The *run.ave()* function can be used to average sequential measurements and smooth data. The *plot.cross.over.points()* function can be used to build an error model; measurements made at the same location, and separated by a given time lag, are used to calculate measurement error. Much of the work concerning inversion of EMI data advocates for calibration of EMI measurements (Lavoué et al., 2010; von Hebel et al., 2013) in order to improve inversion convergence and increase model confidence. Several methods exist for calibration, including sounding elevation (e.g. Tan et al., 2017), soil sampling (e.g. Moghadas et al. 2012) and calibration using models derived from electrical resistivity imaging (ERI) (e.g. Lavoué et al., 2010). In this work calibration can be done using a model of electrical resistivity from an ERI transect by *calibrate.emi()* and by the elevation method using *calibrate.emi2()*.

4.3.2 Apparent Conductivity-Quadrature Conversion Tools

ECa-Q conversion tools are used to convert between ECa and Q. *GF.eca.to.Q()* converts Q to GF-ECa using the linear calibration used by GF Instruments, whereas *eca1.to.Q()* uses the LIN approximation. There are three functions for converting Q to ECa: *Q.to.eca1()* which uses the LIN approximation; *Q.to.eca2()* which uses the Andrade et al. (2016) minimisation method using a Q value obtained from a FS forward model equations 4.5 and 4.6 for a homogenous half-space EC; and *Q.to.eca3()* which uses the Andrade et al. (2016) minimisation method and a Q value obtained from the analytical equations of McNeill (1980) for a homogenous half-space EC. *Q.to.eca3()* is favoured in the FS forward model based inverse solutions because of its computational advantage in comparison to *Q.to.eca2()*.
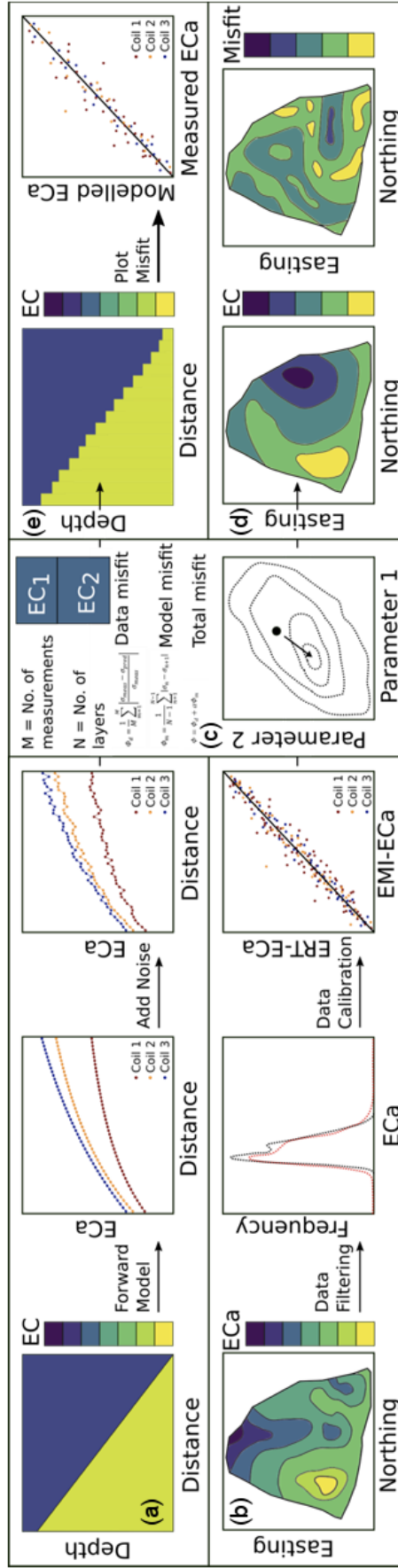
Figure 4.6: Schematic showing the work flow used in the functions: (a) details the generation and noise corruption of synthetic data, (b) shows the filtering and calibration of EMI data, (c) inversion of data, (d) plotting inverse results of field surveys.

78

4.3.3 Forward Model Tools

Forward model functions are used to return the theoretical response of a given instrument setup and a given EC distribution. They are therefore used in the inversion to test the suitability of a given model in relation to the observed measurements, and generate synthetic data. The *fwd.eca.cs()* function provides the forward model based on the CS functions (equations 4.3 and 4.4) and requires input of: the EC of each layer in mS/m; the starting depth of each layer (the first layer will start at 0 m, the ground level); the separation and orientation of each coil in the measurement setup; the operation height. The *fwd.eca.fs1()* function calculates the forward response in terms of Q values for a given model using the FS forward model (equations 4.5 and 4.6) and converts it to LIN-ECa values using *Q.to.eca1()*; it requires the same input as *fwd.eca.cs()* in addition to the operating frequency of the device. Similarly, *fwd.eca.fs2()* and *fwd.eca.fs3()* obtain Q values and convert them to Andrade-ECa values using *Q.eca2()* and *Q.eca3()*, respectively.

4.3.4 Inverse Tools

A total of twelve inversion algorithms were written, the first set of four use fwd.eca.cs(), the second set of four use *fwd.eca.fs3()* and third set of four use *return.Q()* to calculate the response of the model. Each set of four functions follow the same basic pattern. Functions *inv.eca.cs2.1()*, *inv.eca.fs3.1()* and *inv.Q1()* invert data for a vector of depths using a regularisation term to ensure a smoothly varying model of EC. Functions *inv.eca.cs2.2()*, *inv.eca.fs3.2()* and *inv.Q2()* aim to find the best two-layer model with a sharp EC contrast. Functions *inv.eca.cs2.3()*, *inv.eca.fs3.3()* and *inv.Q3()* use a Monte-Carlo type approach to return a sharply varying multilayer model by randomly selecting fixed depths and solving the EC for those depths then ranking models by misfit and taking the model with the lowest misfit as the best one. Functions *inv.Q5()* etc., use a Shuffled Complex Evolution algorithm to obtain a multi-layer model of sharply varying EC. The methods using the Monte-Carlo type approach are clearly more computationally expensive as they solve the inverse problem a number of times; however they provide consistently reliable results without getting stuck in local misfit minima. All of these algorithms seek to minimise the difference between observed values and predicted values, the data misfit (Φ_d), in addition the model misfit (Φ_m) which can be used to characterise the variation of EC in the model. The Φ_d and Φ_m can be calculated using the L1 or the L2 norm. The L1 norm is concerned with absolute differences and is defined for data and model misfit as follows:

$$\Phi_d = \frac{1}{N}\sum_{n=1}^{N}\left|d - f(m)\right|,$$

(4.8)

$$\Phi_m = \frac{1}{M} \sum_{m=1}^{M-1} \left| EC_m - EC_{m+1} \right|, \qquad (4.9)$$

where N is the number of measurements, d is the observed values and *f(m)* is the values predicted from the forward model, *M* is the number of layers and EC_m is the electrical conductivity of layer m. In comparison the L2 norm is concerned with the square of the differences and is used as follows:

$$\Phi_d = \frac{1}{N} \sum_{n=1}^{N} \left(d - f(m) \right)^2, \qquad (4.10)$$

$$\Phi_m = \frac{1}{M} \sum_{m=1}^{M-1} \left(EC_m - EC_{m+1} \right)^2, \qquad (4.11)$$

The L1 norm is implemented as the default method as it is not significantly influenced by outlier data. The misfit calculations use the L1 norm which uses the magnitude differences as opposed to the squared differences used in the L2 norm; although methods to account for error in the inversion were investigated, using the L1 norm gives satisfactory results without the need for error terms. Regardless, the total misfit is calculated as follows:

$$\Phi = \Phi_d + \alpha \Phi_m, \qquad (4.12)$$

where α is a smoothing parameter determining the influence of Φ_m on the total misfit which is essential in the fixed depth inversions but optional in the sharp inversions. The objective function can be minimized using the optim package which has a selection of solvers: Nelder-Mead (Nelder and Mead, 1965), conjugate gradient (Fletcher and Reeves, 1964), and L-BFGS-B (Byrd et al., 1995). Alternatively, the sceua() package can be used which uses shuffled complex evolution (Duan, 1993) to find the parameter values that best fit the data. For both the L-BFGS-B and shuffled complex evolution methods, model bounds need to be supplied to constrain the parameter space. The above described inversion functions require input of a single set of measurements, e.g. measurements made at a single location. As the majority of applications involve measurements at multiple locations functions requiring the input of multiple measurement sets are also included, and have *all.* as a prefix to the above described inverse functions (e.g. *inv.eca.fs3.1()* becomes *all.inv.eca.fs3.1()*) Moreover, the computational demand of large surveys is such that these

functions make use of the base R parallel package to distribute calculations over multiple cores and reduce computation time.

4.3.5 Plotting Tools

Several plotting functions are also included to plot raw data and inversion results. Contour maps or coloured scatter plots of raw measurements and inversion results can be plotted using *pretty.cont()* or *pretty.scatter()*, respectively. Both functions require the input of an xyz data frame, and *pretty.cont()* requires an additional parameter to crop contouring to prevent it significantly over extend into locations with no data. Inverted models can also be plotted using the *pretty.quad()*, which requires a data frame consisting of the x and y positions, the elevation, the inverted EC and the depths of each layer. The function will parse the data frame to produce a linear transect with cells of quadrilateral polygons coloured according to the EC. The *pretty.start()* function is used to plot starting models taking zones as the region.

4.4 Synthetic Examples

To highlight some of the capabilities of the above described functions and investigate some of the issues surrounding the inversion of EMI data, several synthetic cases were designed using the properties of the GF Explorer. Firstly, the performance of the CS forward model is assessed by generating data using the FS forward model and converting them into Andrade-ECa values. It could be argued that ECa values provided via another method be used in the inversion for the CS forward model; however, it is taken that Andrade-ECa offer the best relation to Q values and hence are the most appropriate. Andrade-ECa values are generated to simulate the GF Explorer being operated at both ground level and at 1 m elevation. In the second case, the effect of noise on the GF Explorer being operated at ground level and 1 m elevation using a FS forward model is assessed. In both cases, a simple two-layer structure is generated comprising a first layer with EC of 30 mS/m and second layer of 5 mS/m, i.e. broadly comparable to the conditions of the peat and gravel layers found in the Boxford Wetland, as discussed in Chapter 5. In both synthetic cases, data are generated and inverted using 1D forward models, although it could be argued that a 2D/3D forward model is better for describing the system, here the interest was in comparing between FS and CS and the influence of noise on the 1D forward model.

4.4.1 Synthetic Modelling Case 1

The model for Case 1 comprises a 30 mS/m overlying 5 mS/m layer with the boundary starts at 0.2 m depth at the 0 m position and trends at a constant slope to 2 m depth at the 47.5 m position, Fig. 4.7a. The workflow is shown in Appendix 2 (Fig. 12.1); however, to summarize, synthetic data are

generated for both 0 m and 1 m elevations using the FS and by converting Q values into Andrade-ECa. Data are then inverted using *inv.eca.cs2.3()* and *inv.eca.fs3.3()*, before being plotted.

Figure 4.7: (a) Model for Case 1 with upper layer conductivity of 30 mS/m and lower layer conductivity of 5 mS/m, and a sloping interface trending from 0.2 m depth at 0 m and 2 m depth at 47.5 m. (b) and (c) inversion of data collected at 0 m inverted with the CS forward model and a FS model, respsectively. (d) and (e) inversion of data collected at 1 m inverted with the CS forward model and a FS model

To begin with, the functions are imported into the working environment; two empty data frames consisting of 48 rows and 9 columns are then created to store the synthetic data. A sequence of x positions with 1 metre spacing is generated and the depth assuming a constant slope from (0, -0.2)

to (47.5, -2) is obtained by linear interpolation. The coil separations and coil orientations of the six measurements obtainable by the GF Instruments Explorer are then assigned as a variable. A loop is then used to generate synthetic data for each position along the transect for a model with an upper layer EC of 30 mS/m and a lower layer EC of 5 mS/m for both 0 m and 1 m elevations. Synthetic data are stored in the previously generated data frames. Data are then inverted using *all.inv.eca.cs2.3()* and *all.inv.eca.fs3.3()* for both synthetic data frames. The interface is between the two-layers is then stored as a list so that it can be read and plotted using *pretty.quad()*. The inverse models are then plotted, including the interface line, using the default viridis colour scheme with the y scale limits set to -2 and 0, the z scale limits set to 0 and 40, and the bin number set to 10.

It can be seen from Fig. 4.7b that when operated at ground level the CS function performs just as well as the FS forward model. In contrast, when the data are generated for an elevated device, the accuracy of the CS forward model decreases as the depth of the interface increases. For instance, at the 30 m position of the transect, the modelled depth is 0.7 m greater than the model depth. Furthermore, it underestimates the expected EC. On the other hand, the FS forward model performs better when the device is operated at 1 m as opposed to when it is operated at the ground level. This is perhaps due to increased depth penetration of device signal when elevated above the ground as noted by some authors (e.g. Andrade et al., 2018). However, the overall signal becomes smaller than when operated at higher elevations above ground level, meaning that noise is more detrimental to measurements made at higher elevations..

4.4.2 Synthetic Modelling Case 2

In Case 2, the influence of noise on the FS inversion is investigated. As with Case 1, ECs of the upper and lower layers are set to 30 and 5 mS/m, respectively. However, in this Case with an undulating interface with depths ranging from 0.5 to 0.8 m is used, Fig. 4.8. The code to generate Fig. 4.8 is shown in Appendix 2, Fig. 12.2. Firstly, synthetic data are generated for elevated and non-elevated operation; then an additional data set with noise is generated for each elevation; after that, results are inverted using *fs.eca.3.3()* before being plotted.
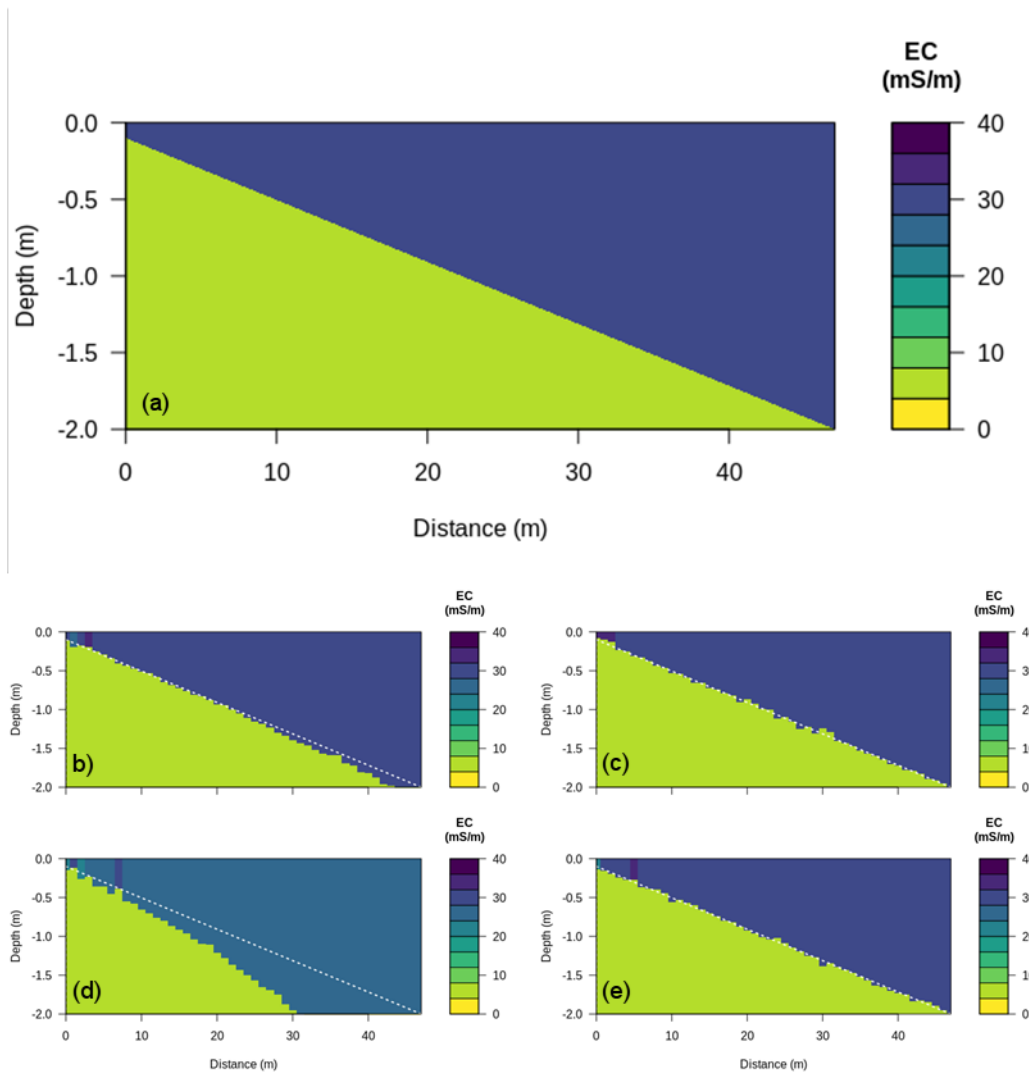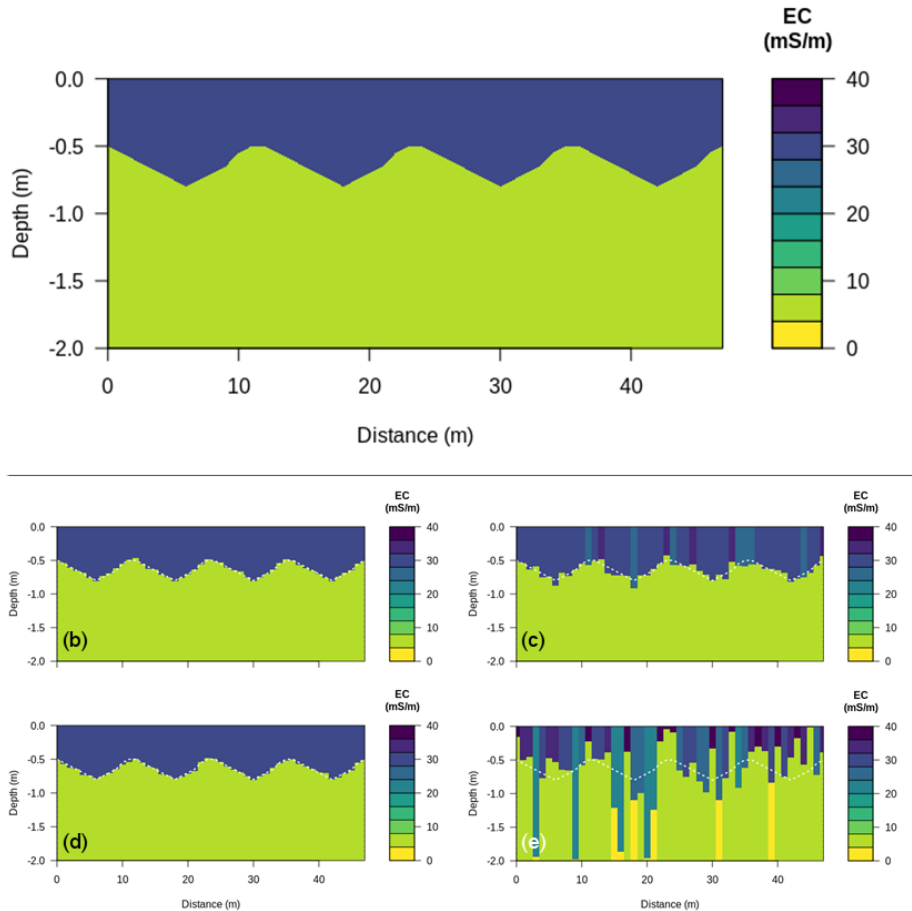
Figure 4.8: (a) Model for Case 2 with upper layer conductivity of 30 mS/m and lower layer conductivity of 5 mS/m, and an undulating interface.

Firstly, functions are imported; four empty data frames with 48 rows and 9 columns are then created to store the synthetic data. The x and y positions are assigned as a variable. The coil separations and orientations of the six measurements obtainable by the Explorer are also assigned as variables. A loop is then used to generate synthetic data for each position along the length of the model at 0 m elevation; data are corrupted with 2% normally distributed noise. The same is done for the device being operated at 1 m elevation; synthetic data with and without noise are then stored in the previously generated data frames. Data are then inverted using *all.inv.eca.fs3.3()* for all synthetic data sets. The interface between the two-layers is stored as a list so that it can be read and plotted using *pretty.quad()*. The inverse models are plotted, including the interface line, using the default viridis colour scheme with the y scale limits set to -2 and 0, the z scale limits set to 0 and 40, and the bin number set to 10.

It can be seen that when the device is operated at ground level the inverted model is reasonable for both scenarios where no noise and 2% noise is added. When the device is operated at 1 m elevation the inversion returns a reasonable model for no noise; but with 2% noise, the inverted model fails to match the model from which the data were generated for most locations. It does, however, perform well at some points but the misfits at these locations are not superior to the misfit at the other locations. Hence it would be impossible to know their truthfulness in a real (field) case. Furthermore, introduction of a lateral smoothing parameter would not improve the model, for the same reason.

4.5 Errors Due to Instrument Elevation

To explore this problem further synthetic data were generated for a model comprising a 1 m thick 30 mS/m upper layer and a 5 mS/m lower layer for the GF Explorer operated at both 0 m and 1 m. To begin with, 50,000 models were generated with a fixed layer 2 EC of 5 mS/m, a random layer 1 EC between 15 and 45 mS/m and a random layer 1 thickness between 0 and 2 m. The forward model response of these 50,000 random models was calculated using *fwd.eca.fs3()* for 0 and 1 m cases and the total misfit (equation 4.8) was calculated as a percentage. This process was then repeated with the fixing of layer 1 EC at 30 mS/m, and the values of layer 2 EC and layer 1 depth were obtained the ranges of 0 to 10 mS/m and 0 to 2 m, respectively. The process was repeated again for the case where layer thickness was fixed at 1 m and layer 1 and layer 2 EC had values of between 15 and 45 mS/m, and 0 to 10 mS/m, respectively. The parameter space and corresponding misfits are shown in Fig. 4.9.

It is immediately evident that when the device is operated at the ground level, the area of the 5% misfit contour is smaller, indicating that the solution is more stable. Although it is true that this is only one instance of adding errors, the percentage errors added are the same for both cases. Furthermore, it is evident from Fig. 4.9b and 4.9d that the inversion performs more poorly when operated at 1 m elevation. It can be seen for the case when the device is operated at 0 m *fs.eca.3.3()* obtains a model close to the synthetic model but not for the elevated case. It can, however, be seen that when one of the parameters is fixed, the model with the best misfit, of the 50,000 random models, is close to the synthetic model. Therefore, in cases where the device must be operated at 1 m it may be possible to resolve reliable images of a simple two-layer subsurface if additional information is provided; for example, when there are intrusive or ground penetrating radar data to constrain the boundary, or an accurate estimate of one of the layer EC values. For instance, for the latter it may be reasonable to assume a constant EC value for layer 2, for example if it is a unit

without significant clay portions, but with homogenous porosity and well mixed pore water, e.g. a gravel.
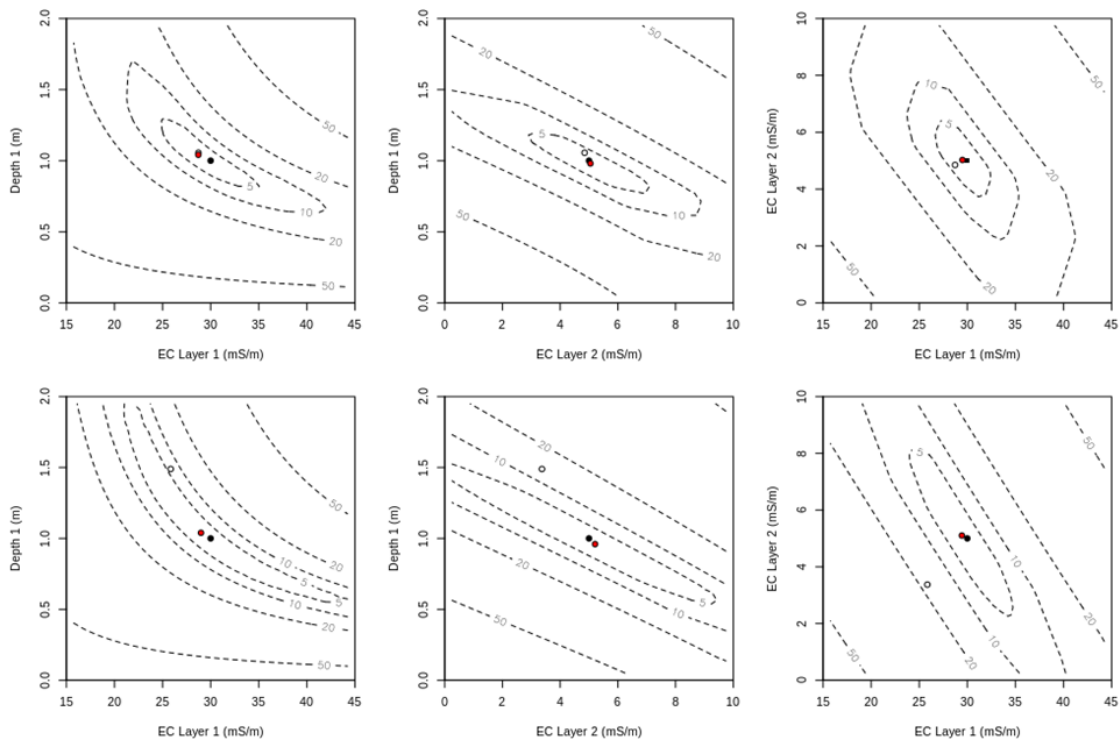
Figure 4.9: Parameter space for a synthetic model comprising a 1 m thick upper layer with an EC of 30 mS/m and a lower layer with an EC of 5 mS/m. The black circle refers to the synthetic model, the red circle is the best model of the 50,000 randomly generated models, and the white circle is the results of inv.fs.3.3(). (a) and (d) show the parameter space when layer 2 EC is fixed at 5 mS/m for 0 m and 1 m cases, respectively. (b) and (e) show the parameter space when the layer 1 EC is fixed at 30 mS/m for 0 m and 1 m cases, respectively. (c) and (f) show the parameter space when layer 1 thickness is fixed at 1 m for 0 m and 1 m cases, respectively.

It is shown that even small errors can significantly reduce the capabilities of EMI measurements when operated at 1 m. It is therefore important to consider some of the sources of error in EMI measurements, e.g. some inevitable error associated with operation of the device. However, additional sources may arise from changing temperature or different users. It is still possible to account for these errors by using a drift station (i.e. a location where measurements are repeated during the survey) or calibrating measurements. Another important source of error is the incorrect orientation of coils, the incorrect height, or the inclination of the device relative to the ground so that it is no longer parallel. These issues are fairly common in areas where the use of a cart or

frame may be impractical and the device must be operated by carrying it. In such a case, the device may rotate about the long axis or the device may become inclined due to user imbalance or the presence of slopes on the field site. Whilst these factors cannot be investigated with the presented 1D forward model, the effect of erroneous height can be investigated. Fig. 4.10 shows the difference in Andrade-ECa values for the GF Explorer at 1 and 0.9 m, normalised by the values when the device is operated at 1m and expressed as a percentage.
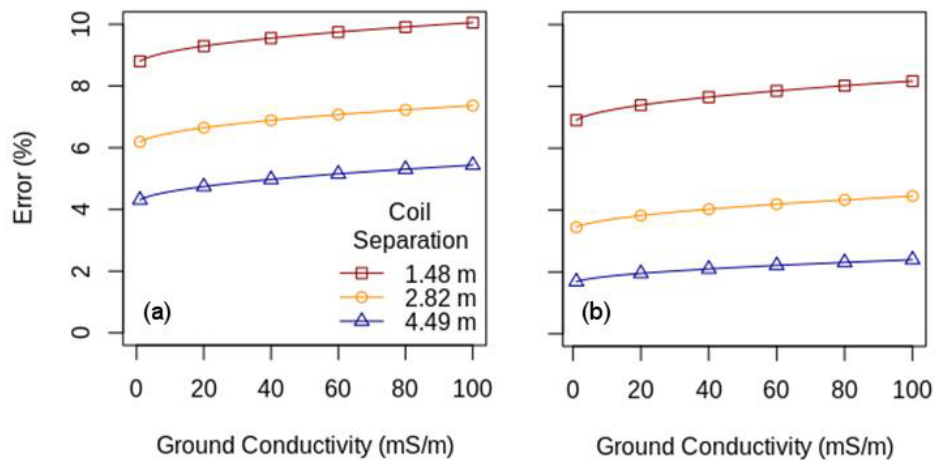
Figure 4.10: Errors of Andrade-ECa values if the device is operated at 0.9 m as opposed to 1 m when device is operated in (a) VCP and (b) HCP modes.

It is evident that the shallower the depth of investigation the larger the error that arises from incorrect elevation. For instance, for the 1.48 m coil separation when the GF Explorer is operated in VCP mode the value of ECa obtained at 0.9 m will be ~9% higher than the value obtained when the device is operated at 1 m. This is important to consider in the EMI inversion. Furthermore, although this may not have significant impact of ECa mapping, it may be relevant for time-lapse studies depending on the expected magnitude of changes in ECa.

4.6 Concluding Remarks

The applications of EMI devices for ECa mapping are diverse; the validity of ECa derived by the LIN has been questioned by a number of authors who propose alternative methods to obtain ECa values from the imaginary component of the ratio between the primary and secondary electromagnetic fields. However, in the majority of cases, these ECa mapping studies are concerned with developing linear regressions between ECa and the property of interest and given

that the EC values typically do not vary over multiple orders of magnitude at most field sites, LIN-ECa, or indeed any ECa value obtained assuming a linear relation, is more than adequate.

Despite the availability of open source forward models, including this one, the application of inversions using the CS forward model is frequent. Although for the cases investigated here, this appears valid when the device is operated at ground level, the CS forward model should not be used for elevated surveys. Furthermore, it should be noted that the validity of the CS forward model was only tested here for low conductivity environments and is likely that this would break down at higher electrical conductivities.

Although the FS forward model is favourable for elevated scenarios, small measurement errors can lead to significant errors in the inversion process. Although this instability can be mitigated for simple two-layer models by fixing one of the parameters, it was not fully investigated for more complex models. Perhaps inclusion of additional measurements with different sensitivities or an improved objective function that appropriately deals with measurement errors could be implemented.

It was also demonstrated that significant errors can arise from erroneous device elevations. Ideally, instruments should be operated at, or close to, ground level on a sledge or cart. Use of a sledge or cart would also mitigate errors associated with erroneous orientation or inclination of the device; although these were not investigated it is anticipated that they would have similar significant effects on the inversion.

5 Revealing the Hydrogeological Structure of a Riparian Wetland Using Electromagnetic Induction Methods

5.1 Introduction

Characterisation of wetlands is important for assessing their role in the exchange of water, nutrients, and pollutants between surface water (SW) and groundwater (GW) systems. Wetlands play a crucial role in maintaining ecosystem health throughout the catchment and are often sites of considerable biodiversity. Furthermore, despite contributing to approximately 2–6% of the Earth's land surface (Kayranli et al., 2009) wetlands contain 20–25% of the organic carbon within soil (Gorham, 1995). Moreover, due to the anaerobic degradation of organic matter occurring in most wetlands, it has been estimated that they contribute 20–40% of current global methane emissions (Bloom et al., 2010), and explain 70% of annual variations in atmospheric methane concentrations (Bridgham et al., 2013). In addition, wetlands are likely to be threatened by climate change, e.g. changes in base flow, flooding events, water quality, and heat stress are likely to modify their function (Gorham 1995; Erwin, 2009). Consequently, wetlands are protected by environmental legislation, including the European Union Water Framework Directive and Habitats Directive, and the US Clean Water Act.

Until the mid-1970s the importance of wetlands was generally overlooked and they were often modified to permit alternative land use. For instance, wetlands were commonly replaced by agricultural fields, and commercial or residential developments. However, there has since been a significant effort in restoring, maintaining, and managing wetlands. Adequate management requires appropriate wetland characterisation; conventionally this is achieved through lithological sampling or installation of piezometers (e.g. Grapes et al., 2005; Allen et al., 2010). However, these methods typically have limited spatial coverage and in some cases may be environmentally prohibited. The past 30 years has seen many developments in the field of near surface geophysics (Binley et al., 2015; McLachlan et al., 2017). The majority of geophysical applications to characterise wetlands

have used electrical resistivity imaging (ERI) given the dependency of resistivity on lithology, pore water conductivity, and saturation. For example, ERI has been used to characterise both dynamic processes (Musgrave and Binley, 2011; Zarroca et al., 2014; Uhlemann et al., 2016) and geological structure (Chambers et al., 2014; Miller et al., 2014; Sonkamble et al., 2019) of wetlands.

Given the sensitivity of frequency domain electromagnetic induction (EMI) methods to electrical conductivity, the inverse of electrical resistivity, they provide a useful tool in wetland characterisation. Furthermore, given that EMI devices do not require direct coupling with the ground they are typically more productive than ERI methods. In recent years, the development of multi-coil and multi-frequency instruments is such that EMI measurements can be translated into quantitative models of conductivity using inverse methods. EMI inversions have been used to characterise stratigraphy (e.g. Saey et al., 2014; von Hebel et al., 2015; Frederiksen et al., 2017), organic matter content (e.g. Huang et al., 2017), and hydraulic conductivity (e.g. Brosten et al., 2011), all of which are important properties of wetlands. It is also important to note that EMI methods have had a long history of using raw measurements to obtain similar information (e.g. Sudduth et al., 2005; 2010; 2013).

The purpose of this work is to assess the ability of EMI methods to characterise a riparian wetland. The field site was previously characterised extensively using ERI and intrusive sampling (Chambers et al., 2014), and comprises superficial peat and gravel deposits overlying chalk bedrock. The ability of raw EMI data and inverted EMI data to characterise the depth to peat-gravel interface, the organic matter content of the peat, and the pore water conductivity and the hydraulic conductivity of the peat and gravel is assessed. Specifically, the following questions are investigated: (1) 'Are properties of the wetland best correlated with raw or inverted EMI data?', (2) 'How many intrusive observations are required to build a robust #linear regression linking peat depth and raw EMI data?', (3) 'What are some of the implications associated with data collection when the device is operated at 1 m elevation?', (4) 'Is data calibration necessary prior to inversion?', and (5) 'What is the best approach for obtaining reliable models of conductivity from EMI inversions?'.

5.2 Electromagnetic Induction

5.2.1 Background

EMI devices operate by passing an alternating current through a transmitter coil to generate a primary electromagnetic field. This primary electromagnetic field induces eddy currents in the

subsurface which then generate a secondary electromagnetic field. The interference of the primary and secondary electromagnetic fields is measured by a receiver coil. The ratio of the primary and secondary fields has an in-phase and an out-of-phase, or quadrature, component. The quadrature component is typically of most interest as it is dependent on conductivity, whereas the in-phase component is more closely related to magnetic properties which are often negligible in environmental applications. However, it is important to note that the in-phase component is also related to conductivity, and hence still may contain some useful information.

The sensitivity patterns of EMI instruments are dependent upon the orientation of transmitting and receiving coils, the separation distance between the coils, the frequency of the alternating current, and the subsurface conductivity. The majority of devices typically utilise a combination of multiple frequencies, coil separations or coil orientations to obtain measurements with different sensitivity patterns. For instance, the GF Instruments Explorer (Brno, Czech Republic), the instrument used in this study and hereafter referred to as the GF Explorer, has three receiver coils meaning that three measurements can be obtained simultaneously. In addition, the GF Explorer can be operated in vertical (VCP) and horizontal coplanar (HCP) modes meaning that a total of six measurements can be obtained. From hereafter, the six measurements are referred to as VCP1, VCP2 and VCP3, ranging from the shortest to longest coil separation when operated in the VCP mode, and HCP1, HCP2 and HCP3 when operated in HCP mode.

The observed quadrature is typically expressed as an apparent conductivity; i.e. the conductivity of a homogenous subsurface with an equivalent quadrature value. Apparent conductivity is expressed in mS/m, the same units as conductivity, and hence offers a more comprehensible unit than quadrature. The linear low induction number (LIN) approximation is commonly used to convert quadrature values to apparent conductivity values (McNeill, 1980). However, it is important to note that the GF Explorer is calibrated using a linear manufacturer calibration based on their test site and therefore data must be dealt with accordingly, prior to inversion.

5.2.2 Maxwell Based Forward Model

The EMI forward model is based on Maxwell's equations and relies on the assumption that electromagnetic fields propagate due to conduction currents, which is valid at low frequencies ($< 10^5$ Hz). The solution, provided by Wait (1982), can be used to determine the response of an EMI instrument over a 1D layered subsurface:

$$\left(\frac{H_S}{H_P} \right)_{VCP} = -s^2 \int_0^\infty R_0 J_1(s\lambda) \, d\lambda, \tag{5.1}$$

$$\left(\frac{H_S}{H_P}\right)_{HCP} = -s^3 \int_0^\infty R_0 J_0(s\lambda)\lambda^2 d\lambda , \qquad (5.2)$$

where s is the coil separation, J_0 and J_1 are Bessel functions of zero and first order, respectively. R_0 is the reflection factor, which is dependent on the thicknesses and conductivity of each layer from ground level to layer N, the deepest layer. Given that layer N is assumed infinite with a homogenous conductivity, and consequently, it can be calculated recursively:

$$R_n = \frac{\frac{\Gamma_n - \Gamma_{n+1}}{\Gamma_n + \Gamma_{n+1}} + R_{n+1} e^{-2\Gamma_{n+1}h_{n+1}}}{1 + \frac{\Gamma_n - \Gamma_{n+1}}{\Gamma_n + \Gamma_{n+1}} e^{-2\Gamma_{n+1}h_{n+1}}} , \qquad (5.3)$$

where , and h_n and σ_n are the thickness and conductivity of the nth layer, respectively. The integrals in equations can be calculated by linear filtering, using weights provided by Guptasarma and Singh (1997). Furthermore, the response for instruments operated at 1 m above ground level can be modelled by including a layer of thickness 1 m and a conductivity of 0 S/m.

5.2.3 Inversion of Electromagnetic Induction Data

As with other geophysical inverse problems, the EMI inverse problem is under-determined. This is typically addressed by introducing a regularisation term to penalise abrupt changes in conductivity of sequential layers and produce models of smoothly varying conductivity. Given the stratified nature of the field site, it is expected that changes in conductivity will be more abrupt. As with the use of regularisation, unique solutions can also be encouraged by constraining the model to a small number of discrete layers. Furthermore, whereas regularised algorithms may use a series of fixed depths where the inversion algorithm is only solved for layer conductivity, limiting the number of layers allows depths to be included as parameters. However, if no regularisation is to be used, the number of parameters should not outweigh the number of measurements. For instance, the six measurements obtained by the GF Explorer cannot be used to obtain a four layer model as it will have seven parameters. Furthermore, given the correlation of EMI measurements it may still be that simpler problems are still under-determined.

In this work, 1D inverse modelling of data was conducted by optimising the difference between observed EMI data and predicted EMI data for a given set of model parameters using equations 5.1 and 5.2. The data misfit,, was calculated using the normalised L1 norm:

$$\Phi_d = \frac{1}{N} \sum_{n=1}^{N} |d - f(m)|,$$

(5.4)

where *d* is the EMI data, *f(m)* is the forward model response of a given model and *M* is the number of measurements. The L_1 norm is used as it is less influenced by outlier data; furthermore, it was found to be more robust than methods aiming to account for the error of EMI data. Several methods for minimising equation 5.4 were attempted, firstly by using Nelder-Mead (Nelder and Mead, 1965) and conjugate gradient (Hestenes and Stiefel, 1952) methods with the optim package of the R stats package (R Core Team, 2013). However, these attempts were susceptible to convergence on local minima, especially when a three-layer model was specified and the EMI data was for the elevated at 1 m case. A second method was designed whereby depth values were 1000 models were selected randomly and fixed so that the inverse problem could be solved solely for conductivity before each model was ranked by its total misfit. This method gave consistent results and had the added benefit that the model confidence could be easily assessed; however, it was computationally demanding and largely impractical.

Given the challenges noted above, the shuffled complex evolution (SCE) algorithm (Duan et al., 1993), as implemented by von Hebel et al. (2014), was used to minimise equation 5.4. The SCE is an evolutionary algorithm method that combines the simplex procedure of Nelder and Mead (1965) with controlled random search of Price (1987) and the competitive evolution of Holland (1987) alongside the concept of complex shuffling. It can be implemented in R via the rtop package (Skoien, 2014). The algorithm operates by creating multiple complexes to explore different regions, or local areas, of the whole parameter space simultaneously. In this way several promising regions of the parameter space can be investigated and evolved individually with the competitive complex evolution algorithm, such that the inversion is not as susceptible to convergence on local minima. Individual complexes are then shuffled to obtain the parameter set which best describes the objective function (Muttil and Jayawardena, 2008). The SCE algorithm requires boundaries for the parameters; von Hebel et al. (2014) proposed that conductivity boundaries be determined by two times the maximum value of apparent conductivity and half of the minimum apparent conductivity for their survey conducted near ground level. Although this can be adapted for the case where the device is operated at 1 m elevation, it was found to be too conservative at the field site, hence limits of 0 to 100 mS/m are used as bounds for the conductivity of each layer.

To test the reliability of the inversion scheme and the ability of measurements with the same device properties as the GF Instruments Explorer to characterise the expected conductivities of the wetland, synthetic data were generated for two-layer and three-layer models using equations 5.1 and 5.2. In all cases the lowest layer was assumed to extend to an infinite depth. The two-layer model comprises a 0.8 m thick layer with a conductivity of 30 mS/m overlaying a layer with a conductivity of 7.5 mS/m. The three-layer model comprises a 0.8 m thick layer with a conductivity of 30 mS/m overlaying a 2 m thick layer with a conductivity of 7.5 mS/m, overlying a layer with a conductivity of 20 mS/m. Data were generated for the cases where the device is operated at 0 and 1 m elevation, and in one case, data were then corrupted by adding 2% normally distributed noise, Fig. 5.1. The depth limits used for layer one were 0 and 2 m in the two- and three-layer cases, and the depth limits for layer two were 2-5 m for layer 2 in the three-layer case. The conductivity limits for all layers were set as 0 to 70 mS/m.
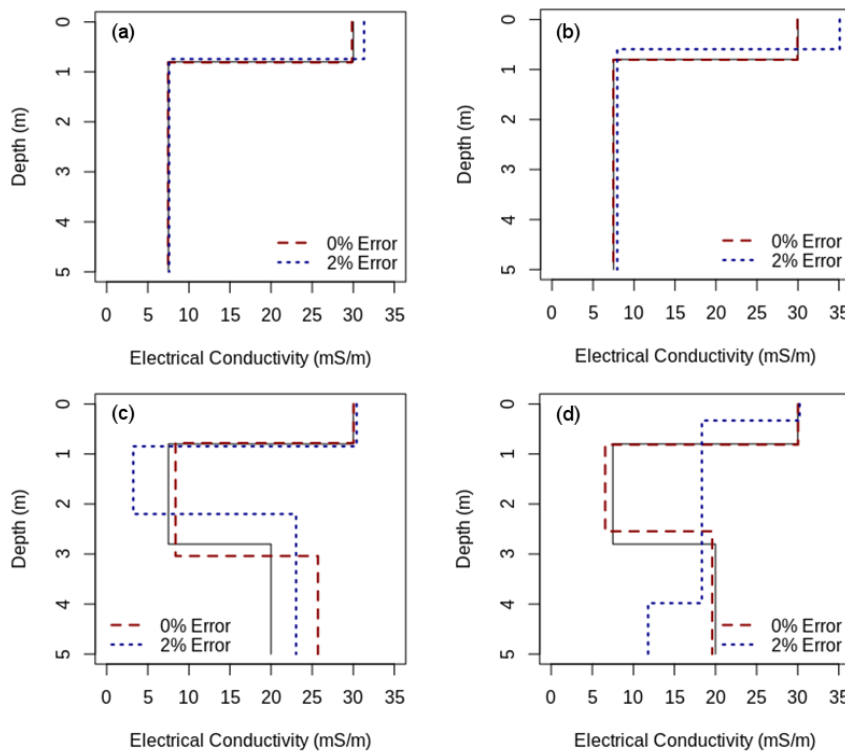

Figure 5.1: Model inversion of synthetic data with no noise and 2% noise for two-layer model when device is operated at (a) 0 m and (b) 1 m, and three-layer model when device is operated at (c) 0 m and (d) 1 m.

For the two-layer model the depth of layer one and the conductivities of each layer are well resolved for data with and without error. In comparison, the three-layer model is better resolved for the error free elevated case, perhaps due the modification of sensitivity patterns as a result of operating the device at 1 m (e.g. Andrade et al., 2018), this could be investigated by computing the contrasting sensitivity patterns for the given subsurface conductivity distribution and the elevation of the device. When noise is added to the elevated case it can be seen that inverse model is poorly resolved. To explore this further, data were generated for a two-layer case with a 0.8 m thick upper layer with a conductivity of 30 mS/m and an infinitely thick lower layer with conductivity of 7.5 mS/m. Synthetic data were generated for the specifications of the GF Explorer operated at 0 m, 0.5 m, and 1 m and then corrupted with 2% Gaussian noise. Corruption of the data was repeated 500 times to produce 500 sets of synthetic data for each elevation, data were then inverted to obtain a two-layer model with depth constraints of 0 to 2 m. The difference between the parameters of the synthetic model and the parameters of the inverted model are presented Fig. 5.2.

The effect of 2% error can clearly be seen for different operation elevations, for instance the layer 1 depth, and conductivities of layer 1 and layer 2 are clearly best resolved when the device is operated at 0 m. As the height of the device is increased the distribution of the absolute differences between parameters in the synthetic data and parameters obtained from the inversion become wider. Also, although the mean depth of layer 1 in the inverted models matches the synthetic model for the case where data were generated for 0 m elevation, the mean depths of layer 1 become progressively deeper for increasing device elevation. This is an effect of the boundary condition that dictates that the minimum depth of layer 1 must exceed 0 m. Although this effect does not shift the mean conductivity of layer 1 obtained for each elevation, the mean conductivity of layer 2 can be seen to progressively decrease for increasing elevation to account for the overestimated depth. Given that at the field site the dense vegetation requires the device to be operated at 1 m, it is important to assess data quality when inverting field data.
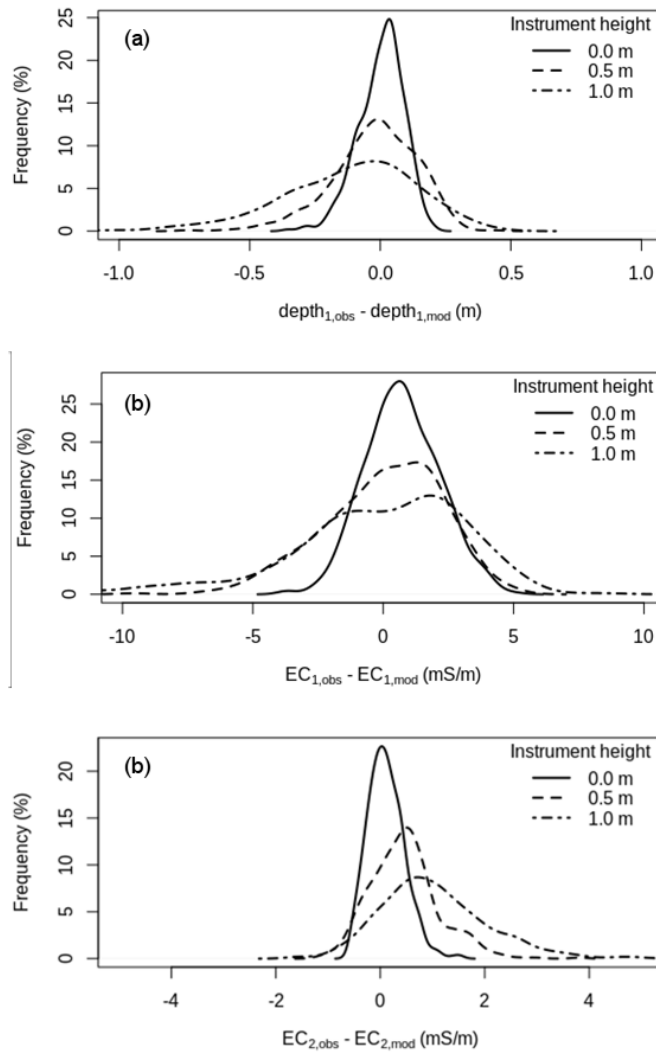
Figure 5.2: Effect of 2% error on results of inversion when device is operated at different elevations. Distributions of the difference between the synthetic model and inverted model values for (a) layer 1 depth, (b) layer 1 conductivity and, (c) layer 2 conductivity for the GF Explorer operated at 0 m, 0.5 m, and 1 m.

5.3 Materials and Methods

5.3.1 Study Site

The Boxford wetland study site, is a riparian wetland located on the River Lambourn, adjacent to the town of Boxford, Berkshire, UK. The River Lambourn and its associated wetlands comprise some of the least impacted chalk river systems in Britain; furthermore, the Boxford Wetland is a designated Site of Special Scientific Interest (SSSI) and a Special Area of Conservation (SAC)

owing to the habitat it provides for aquatic and terrestrial fauna and flora. The wetland is dissected into a north and a south meadow by the Westbrook Channel and is well instrumented with a number of piezometers screened within the peat, gravel, and chalk, see Fig. 5.3.
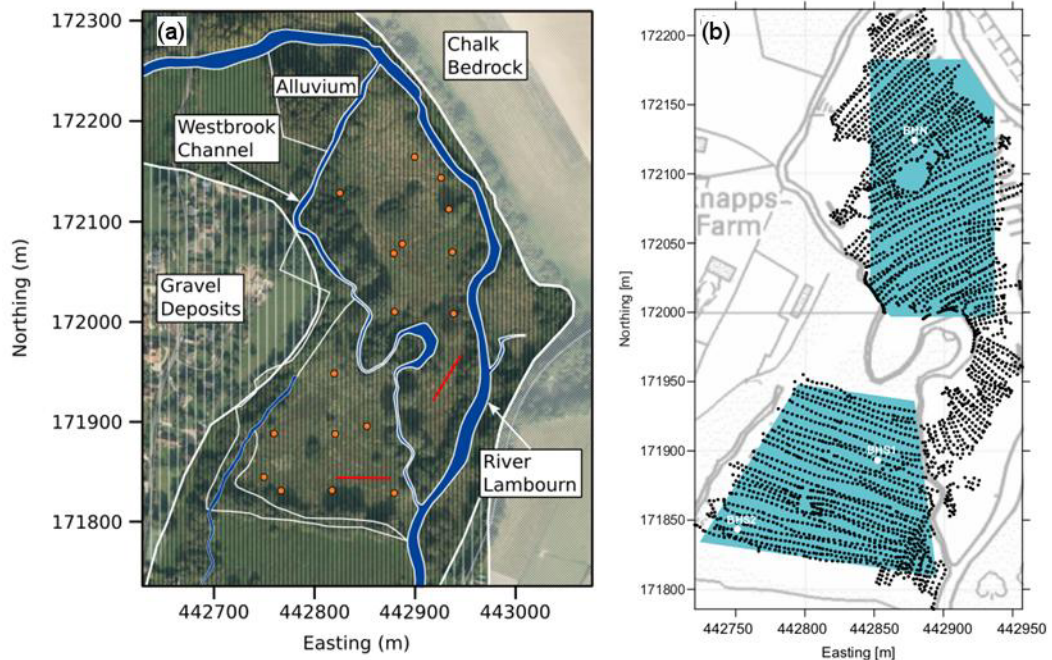
Figure 5.3: (a) Map of the Boxford field site. Orange dots indicate the positions of paired gravel and peat piezometers, red lines show the position of the two ERI transects used to calibrate EMI data. Transparent overlays indicate the extent of the underlying geology; white denotes the chalk bedrock, white vertical lines denote the gravel deposits and black vertical lines denote the alluvial deposits. (b) shows location of sampled peat locations (from Chambers et al., 2014). Axis coordinates are from the Ordinance Survey system,

The stratigraphy of the Boxford Wetland comprises alluvial peats and gravels deposited during the Late Pleistocene to Holocene, overlying Cretaceous chalks, see Fig. 5.3a. The chalk bedrock is characterised by a weathered putty chalk layer and deep channel scouring (Younger, 1989) which is thought to control the hydrology at the site (Chambers et al., 2014). The gravels can be divided into a lower unit of chalky gravels overlain by coarser flint gravels, with some of the upper gravels showing development of lateral accretion surfaces (Newell et al., 2015).

Several geophysical surveys have been conducted at the Boxford wetland, for instance Chambers et al. (2014) used a 3D grid of geophysical data to reveal the structure in the north and south

meadows, and Uhlemann et al. (2016) revealed temporal patterns using two 2D ERI monitoring transects. Furthermore, House et al. (2015) used a temperature survey to locate areas of GW upwelling. Similarly, Musgrave and Binley et al. (2008) used time-lapse ERI to monitor the suppression of season temperature fluctuations due to the presence of GW upwelling. The site therefore acts as an ideal test site to explore the EMI method.

5.3.2 Intrusive Data Collection

Peat samples were obtained at twenty four locations across the meadow using a soil auger. Sample locations were determined to ensure that samples were obtained from areas with a range of conductivity by discretising the wetland into areas with low, medium and high EMI measurements and obtaining eight samples from each area. Samples were split into 10 cm subsections in the field resulting in a total of one hundred and eighty six samples. Organic carbon content of each sample was determined by loss on ignition. Samples were oven dried at 100°C for one week to determine gravimetric water content, before being placed in crucibles and baked at 550°C for four hours to remove organic matter.

During the field campaign, from05-Mar-18 to 08-Mar-18, water levels of each piezometer were found to be stable. In addition to measuring water levels, the temperature and electrical conductivity of each sample was measured with a field conductivity meter (Cole-Parmer, Staffordshire, UK). Wells were purged and left to recover to ensure that samples were representative of pore water conditions. Water levels and pore water electrical conductivities were determined from 13 peat, 15 gravel and 1 chalk piezometers. Hydraulic conductivity measurements were obtained from 14 peat and 13 gravel piezometers using falling head tests. The locations of piezometers are shown in Fig. 5.3a.

As part of the work conducted by Chambers et al. (2014), the depth to the peat-gravel interface was determined intrusively using a simple 6 mm diameter steel rod during April 2012, See Fig. 5.3b. The gravel was assumed non-penetrable, in contrast to the penetrable peat, and the depth was determined from the maximum penetration depth that was achievable using the rod. This measurement was made at 2815 locations on an approximate grid with 5 x 5 m spacing. In six locations the peat depth was assumed to be 1.86 m, the maximum depth achievable using the rod. The position of each depth measurement was surveyed using a combination of real-time kinematic (RTK) GPS and Total Station.

5.3.3 Geophysical Data Collection

Prior to measurement the GF Explorer was left for 30 minutes to allow it to warm up. The device has a (manufacturer claimed) measurement accuracy of 4% at 50 mS/m and, as mentioned previously, uses a manufacturer calibration to convert quadrature to apparent electrical conductivity (GF-ECa). The VCP and HCP surveys of the south meadow were conducted in three portions and one portion, respectively. The VCP and HCP surveys of the north meadow were conducted in two portions and one portion, respectively. For each survey the device was carried at 1 m elevation and held perpendicularly to walking direction. Drift stations were used to assess, and correct for, any drift, whereas cross-over points were included to assess data quality. Cross-over points were locations of the survey area that were survey twice, this was achieved by including perpendicular transects in the survey path. Measurements were logged every second and paired with a location obtained from a Trimble GPS (Sunnyvale, California, US), approximately 20,000 VCP and 20,000 HCP measurements were obtained.

Two ERI transects were used to calibrate EMI measurements, one in each meadow, see Fig. 5.3a. Both transects were 47.5 m long and comprised 96 electrodes with 0.5 m spacing. Measurements were made using a dipole-dipole sequence and a Syscal Pro device (IRIS Instruments, Orleans, France). A full set of reciprocal measurements were collected to characterise errors to enable appropriate data weighting in the inversion. Prior to, and following, collection of ERI data, plastic pegs were used to mark the position of each transect to obtain EMI measurements in the same position as ERI measurements.

5.3.4 Filtering, Calibration and Interpolation of EMI Data

Measurements of poor quality were replaced by linearly interpolating from the nearest preceding and succeeding neighbour which had good quality. The GF Explorer does not provide a measure of data quality so measurements which differed by more than 5% from both neighbours were considered to be of poor quality and replaced via linear interpolation. Following this, data were binned based on their apparent conductivity and in-phase values into 16 equally spaced bins. Any bin that contained less than 0.5% of the data was considered an outlier and replaced via linear interpolation.

The ERI data were of good quality with average reciprocal error being in the order of 0.5%, for both transects. Data were inverted using R2 (see Binley and Kemna, 2005) to obtain a model with conductivity information to approximately 5 m (see Oldenburger and Li, 1999). Both transects were inverted on a quadrilateral mesh and were modelled allowing for 2% measurement error to

compensate for forward modelling error. Convergence of both transects was well behaved and both transects converged in four iterations.

The forward model response of both ERI models was calculated, in terms of quadrature, for each column of the ERI model between 0.25 and 47.25 m, using equations 5.1 and 5.2 for both north and south transects. Quadrature values were converted to LIN conductivity (LIN-ECa) values using the LIN approximation of McNeill (1980). The measurements for calibrating EMI measurements were obtained during the surveys, their locations, as obtained from the GPS, were converted into a distance along the transect and values were converted from GF-ECa values to LIN-ECa values.

The averages for EMI and ERI derived LIN-ECa values were calculated by grouping in terms of their position along each transect, i.e. groups for each metre interval along the transect. Due to the shallower depth of investigations at either end of each transect, data obtained in the first and last 5 m of each transect were removed and a linear regression was fitted to the remainder of the data for each coil orientation and separation. It is important to note that the influence of ERI sensitivity on the calibration of EMI data was not investigated in detail here, but could be an interesting direction for future work. Each survey file was then calibrated by converting the GF-ECa values to LIN-ECa values and then using the coefficients from the relevant linear regression.

As demonstrated with synthetic modelling, data collected at 1 m elevation are especially sensitive to errors, therefore it is important to assess the quality of data. Given that the GF Explorer does not provide a measurement error, errors were determined from cross-over points. The positions of cross-over points were determined in each survey file where transect directions were approximately perpendicular, and there was a minimum time-lag of 2 minutes between the measurements. Averages and errors for EMI measurements occurring within a 2 m radius of each cross-over point were then calculated. Errors were calculated at each step of data processing to assess whether any biases were introduced.

In order to build linear regression models and invert VCP and HCP EMI data together, measurements need to be collocated. To do this EMI values at the position of each peat depth measurement were estimated by averaging all EMI measurements within a 2 m radius. Of the 2,815 peat depth measurements 1,718 measurements had at least one EMI measurement within a 2 m radius. This value was chosen as a trade-off between lower correlational for larger spatial offsets and number of peat depth locations with at least one set of EMI measurements within the specified radius. Although this meant that 1,097 measurements were not used to build linear regression

models, it was found that the correlation of EMI data and peat depth was stronger for measurements made within 2 m of each other, than those made with a larger distance.

5.3.5 Correlation of ECa values and Intrusive Measurements

Prior to inverse modelling, the correlation of EMI measurements and the intrusively obtained peat depths were investigated. The six apparent conductivity values and six in-phase values collocated at the location of peat depth measurements were used to build a linear regression model using different numbers of sets of collocated measurements. This process was repeated with different numbers of points used in the linear regression in order to determine the minimum number of intrusive measurements required to obtain a robust prediction of peat depth from EMI measurements. Overall correlations were made using 20, 25, 30, 35, 45, 55, 65, 75, 85, 100, 150, 200, 250, 400 or 480 randomly sampled points; this was repeated 1,000 times for each number of points and the robustness was assessed by calculating the average RMSE of the predicted peat depth.

Similarly to the peat depths, linear regression models were built to link EMI measurements with the pore water conductivity, organic carbon content and hydraulic conductivity data. As with collocation of the EMI and peat depth data, the EMI values at the positions of these measurements were estimated by averaging the EMI measurements made within 2 m. Linear regression models were then built using the six averaged apparent conductivities at the location of the intrusive measurement using all of the data. For the organic matter data the correlation of was determined for data obtained from the same depths (e.g. all the organic matter values obtained from soil from the 0 to 10 cm interval). Depth ranges with less than seven organic matter values cannot be fitted with a linear regression model using six EMI measurements.

5.3.6 Inversion of EMI Data

The interpolated data set comprising of 1,718 measurements was inverted so as to allow for direct comparison with intrusively obtained peat depths. As noted, the Boxford wetland comprises three lithological layers, peat, gravel and chalk; to investigate whether the EMI data can be best represented by a two-layer or a three-layer model, calibrated data were inverted for both cases. However, given the instability of the inversion in the synthetic example shown in Fig. 5.1 and 5.2, data were also inverted whilst fixing the depth of the first layer for two and three-layer cases. In addition, non-calibrated data were inverted for the two and three-layer cases to assess the impact of calibration on model convergence.

5.4 Results

5.4.1 ERI and Calibration Results

Both ERI sections show a two-layer stratigraphy comprising a more conductive upper layer, Fig. 5.4. Furthermore, the measured peat depth coincides well with the ERI model; from these models it is evident that the peat has an average conductivity of 30–35 mS/m whereas the gravel has a conductivity of 7-10 mS/m. In comparison, Chambers et al. (2014) observed that the peat had a conductivity of 30 mS/m in the north meadow and 20 mS/m in the south meadow, whereas the gravel had a conductivity of around 4–5 mS/m in both meadows. Chambers et al. (2014) were also able to resolve a contrast between the gravel and the underlying chalk which had a conductivity of around 6–8 mS/m. The higher conductivities observed in the peat and gravel could be attributed to the different seasons in which the surveys were conducted. This survey was conducted in March as opposed to April for the north meadow and November for the south meadow. Furthermore, the arrays used by Chambers et al. (2014) had superior depth sensitivity, perhaps allowing them to better resolve subtle contrasts of gravel and chalk, which were not evident in these models.
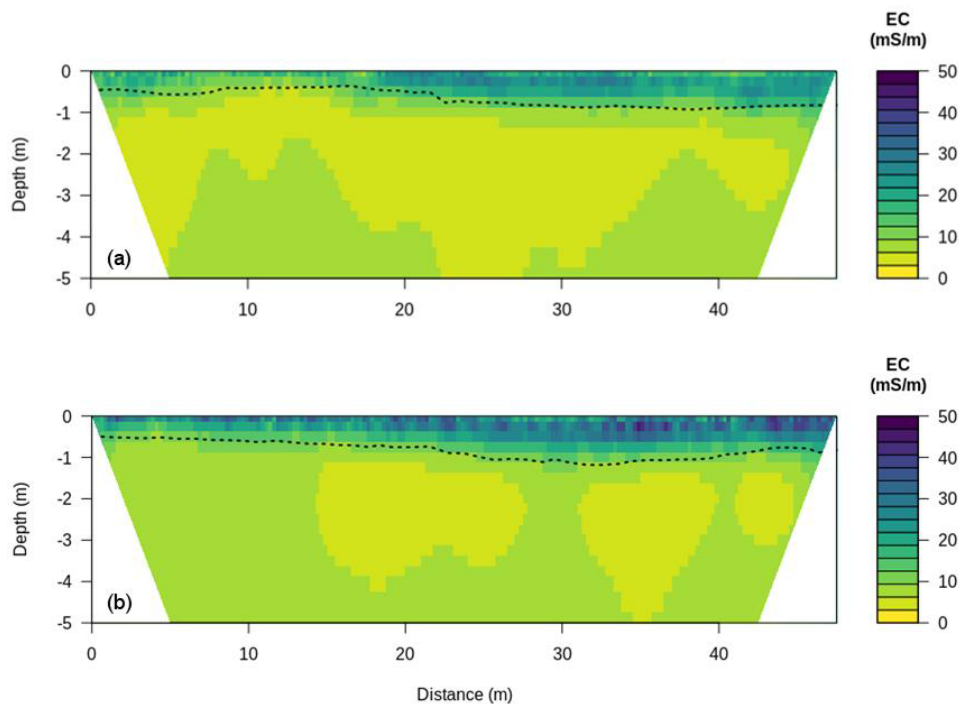
Figure 5.4: Electrical resistivity images of (a) north and (b) south meadow, dashed line shows intrusively obtained peat depths.
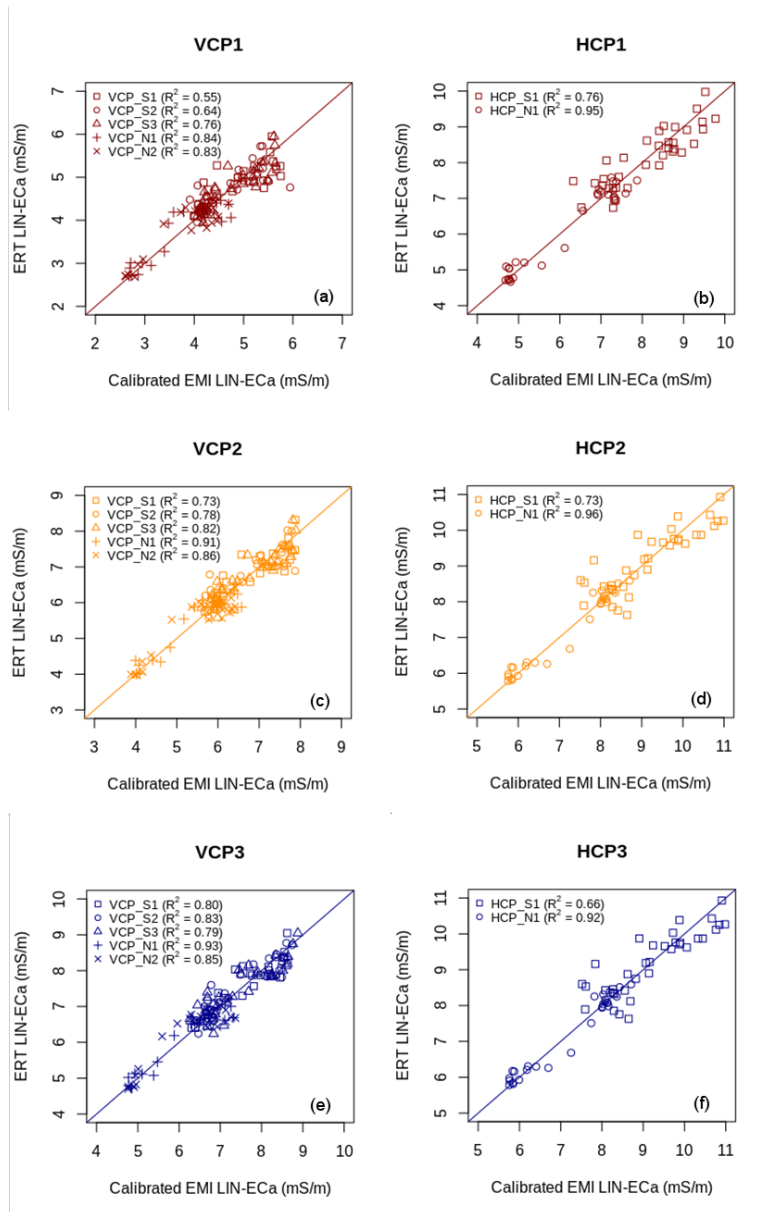
Figure 5.5: Calibration plots showing calibrated LIN-ECa data of VCP1, HCP1, VCP2, HCP2, VCP3 and HCP3 against ERI derived LIN-ECa values used for calibration.

The calibrated EMI apparent conductivities are shown alongside the apparent conductivities obtained from 1D forward modelling of the ERI models in Fig. 5.5. The linear calibration appears appropriate over these conductivity ranges, and the coefficients of determination, R^2, are high especially given that the measurements were obtained during the surveying. The correlations are generally stronger for the measurements with deeper depth sensitivity. This is expected given that these measurements are less sensitive to the air layer than measurements with a shallower depth of investigation which will have a lower signal to noise ratio when operated at 1 m elevation. The

shifts in apparent conductivity were different for each calibration file, indicating that the device calibration for each survey differed from each other. The calibration shift was the greatest for the shortest coil separations, sometimes in the order of 30%, furthermore, this shift is larger than possible bias introduced by the calibration.

5.4.2 Errors of EMI Data

The cross-over point errors for calibrated data calibration are presented in Fig. 5.6. The average errors for calibrated data (0.61, 0.32 and 0.37, and 0.48, 0.21 and 0.17 mS/m for VCP1–3 and HCP1–3, respectively), were lower than the errors for non-calibrated data (1.38, 0.51 and 0.55, and 0.62, 0.26 and 0.25 mS/m for VCP1–3 and HCP1–3, respectively), indicating that no additional biases were introduced by calibration. It is evident that measurements with lower depth sensitivity are prone to errors which are in agreement with the generally poorer correlation in the data calibration; e.g. errors of 4 mS/m and 7 mS/m were observed for VCP1 and HCP1 measurements, respectively. There also appears to be a slight proportional dependency of error on apparent conductivity in Fig. 5.6. This could be explained by the shifting of the instrument position during surveying, which was a common issue in areas of waterlogged ground. For instance, if the long axis of the device is not parallel to the ground, or the distance between the ground and device changes the relative contribution of signal from above and below ground is modified. This would be most noticeable when the contrast between ground and air conductivity is the highest, and when the depth sensitivity is the lowest, i.e. when ground conductivity is higher and in measurements made with the shortest coil separation.
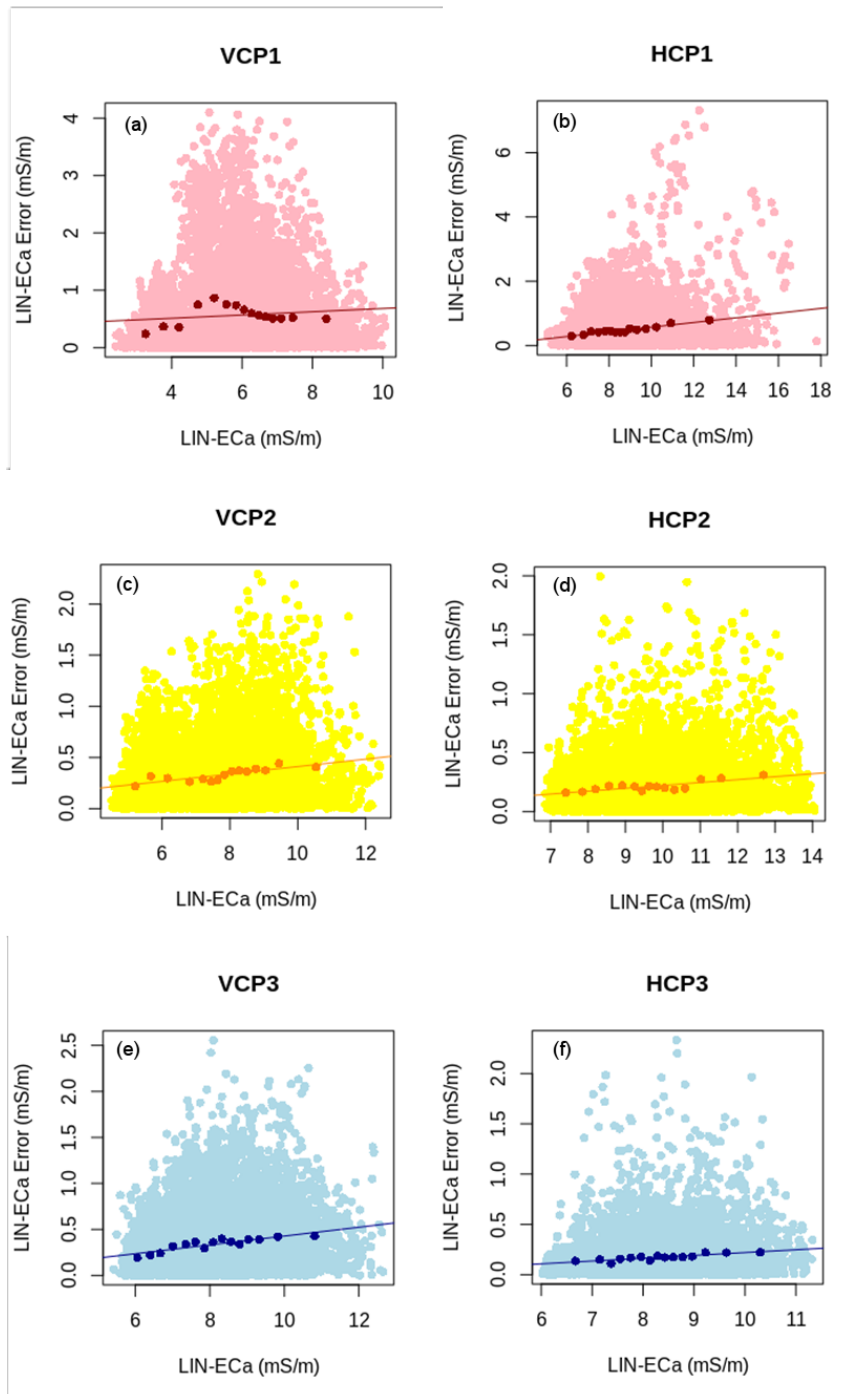
Figure 5.6: Cross-over error plots for the GF Explorer data obtained in both north and south meadows for measurements made in VCP and HCP orientation. Light coloured dots show all of the cross-over point mean apparent conductivities and their associated error, darker dots are the average error and the average apparent conductivities of 15 bins. The data are binned on the apparent conductivity values such that bins contain approximately equal numbers of data; a linear regression is then fitted to the binned data.

5.4.3 EMI Measurements

The individual correlation of each apparent conductivity and in-phase measurement with peat depth were determined for the entire data set of 1,718 collocated measurements. Although apparent conductivity had the best correlation with peat depth, it was evident that some information about the peat depth can be obtained from the in-phase component and it is not completely redundant. The predicted peat depth obtained from the linear regression model using 70 peat depth measurements is shown in Fig. 5.7, alongside the measured depth. The pattern of the peat channel is well resolved and the predicted depths match well with the measured depths, the average RMSE=0.18 m, although it is evident that the greater peat depths tend to be underestimated.
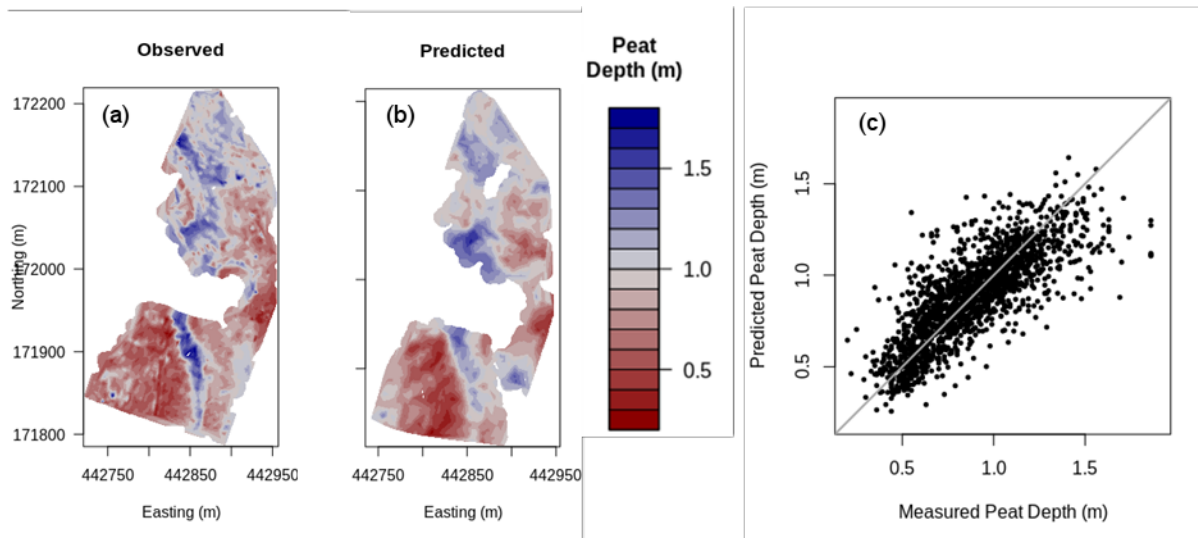
Figure 5.7: Maps of (a) measured, and (b) predicted peat depths, and (c) the scatter plot of predicted and measured peat depths.

Fig. 5.8 shows the number of points used in the linear regression model and the resultant RMSE for peat prediction. It is evident that accuracy of peat prediction is substantially improved if 50 collocated measurements are used, as opposed to 25. However, beyond 120 measurements the prediction is not improved substantially. It is also apparent that calibration of data does not improve correlation, although this is reasonable, given both relationships are linear; it would seem there was no significant calibration bias in the different survey files.
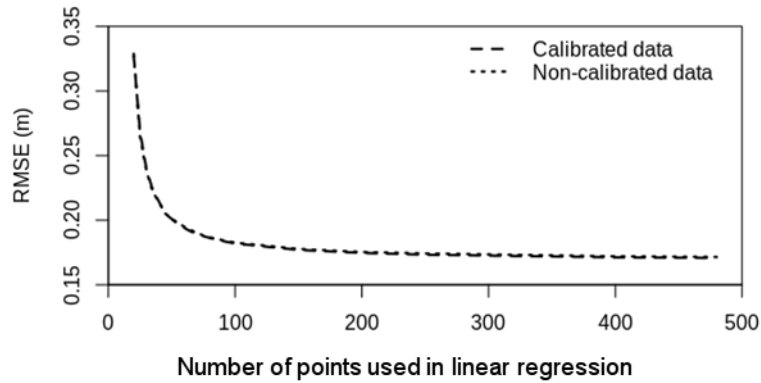
Figure 5.8: RMSE versus number of points used in linear regressions for calibrated and non-calibrated data.

5.4.4 Inversion of EMI Data

Distributions of the data misfit, as determined by equation 5.4, are shown in Fig. 5.9 for the two- and three-layer inversions of calibrated data without a fixed layer 1 depth, the two-layer inversions of calibrated data with a fixed layer 1 depth, and the two-layer inversions of non-calibrated data without a fixed depth. Several observations can be drawn from the misfit distributions; firstly the calibration of data significantly reduces data misfit and improves model confidence. Secondly, it is evident that the misfit for two and three-layer models are not significantly different, indicating that a two-layer model is appropriate for modelling the EMI data. However, as anticipated from Fig. 5.2, errors in the EMI data, e.g. from acquisition or calibration bias, both of these inversions produced models where the depth of layer 1 did not match the measured peat depth. Furthermore, the depth obtained from these inversions exhibited no coherent spatial pattern and the pattern of the peat channel, as seen in Fig. 5.7, and was visible in the conductivities of the inverted models indicating that data were fitted to the model conductivities, as opposed to the modelled depths. Thirdly, it can be seen that fixing the depth of layer 1 in the inversion does not increase the misfit substantially. This indicates the parameter space is relatively flat, and a number of models explain that data to an equal, or almost equal, extent.
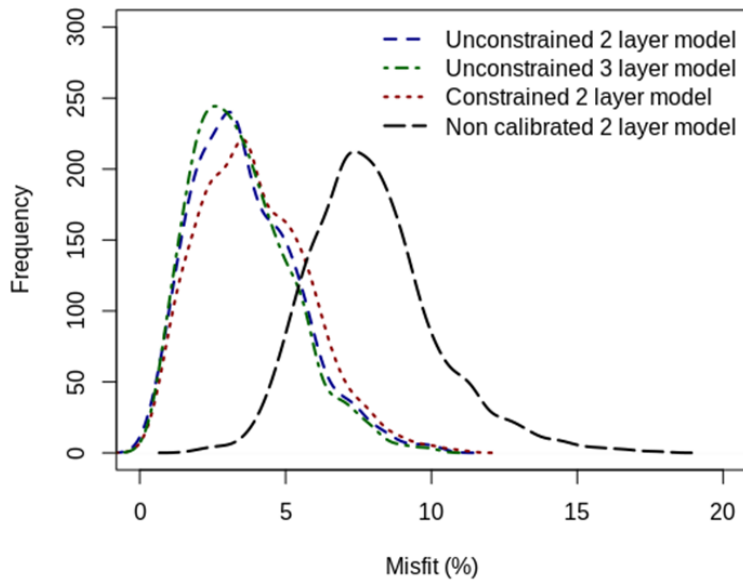
Figure 5.9: Model misfits for EMI inversions.

Given that the inverted layer 1 depths were inconsistent with the measured depths, it can be deduced that the inverted conductivities do not reflect the field site accurately. The conductivities of layer 1 and layer 2 obtained when the depth of layer 1 is fixed to the intrusively obtained peat depth are presented in 5.10. Furthermore, given the accuracy of the peat depth prediction shown in Fig. 5.7, the inversion was also conducted for a two-layer case where the depth of layer 1 is fixed at depths shown in Fig. 5.7b. The mean conductivity of the upper layer in both inversions, 28 mS/m in the south meadow and 33 mS/m in the north meadow is consistent with the ERI models presented in Fig. 5.4. In comparison, the mean conductivities of both inversions for the south and north meadow are more distinct. In the south meadow, the gravels have a mean conductivity of 7 mS/m, which is consistent with the ERI data, but the mean conductivity of the north meadow is 2 mS/m. This is likely due to poor calibration of EMI data, for instance artificially elevated VCP measurements will result in an elevated layer 1 EC, or vice versa where the HCP measurements are artificially minimised. The range in conductivities obtained when layer 1 depth is fixed to the predicted depth (Fig. 5.10a) is subdued in comparison to the layer 1 conductivities when the layer 1 depth is fixed at the measured depth (Fig. 5.10d) given that locations where the conductivity is higher will have a higher estimated depth. The maps of data misfit are similar showing increased misfit in the north meadow; this is mostly likely due to the more difficult terrain and higher vegetation that will influence the quality of the EMI measurements.

108
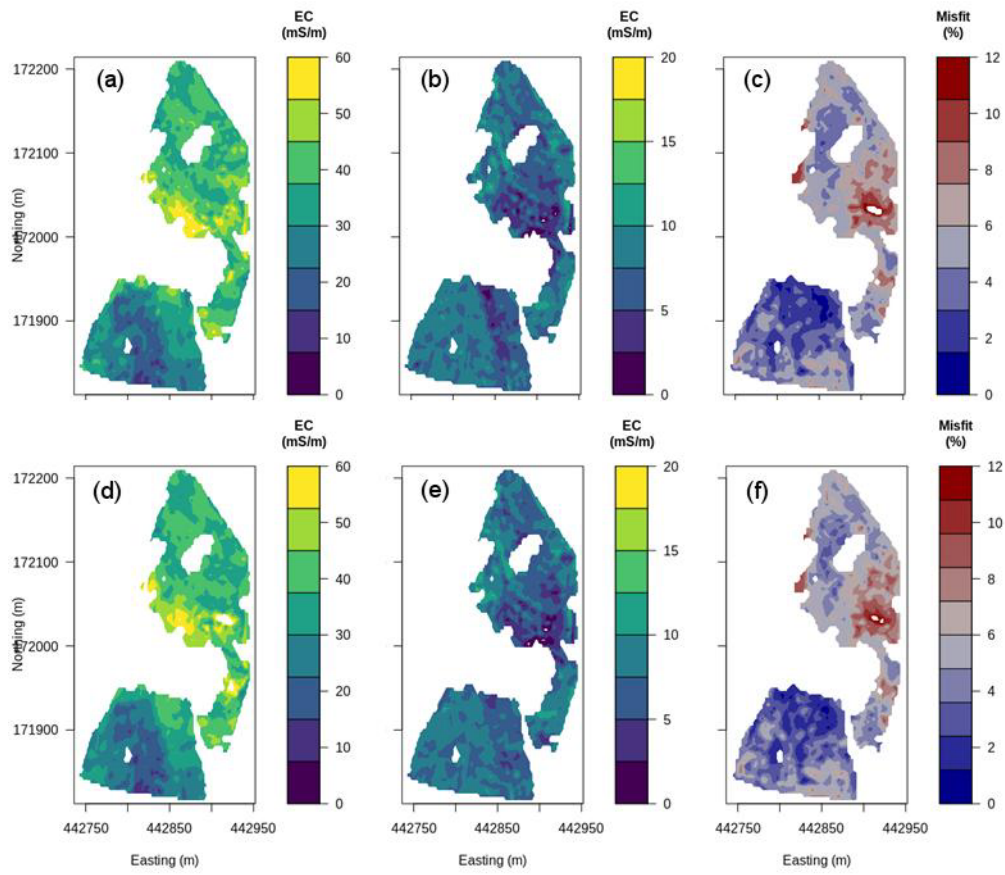
Figure 5.10: Maps of EC for inversion constrained with measured and predicted peat depths; measured depths, predicted depths, and data misfits for layer 1 are shown in (a), (b), and (c), respectively, and the same maps for layer 2 are shown in (d), (e), and (f), respectively. Different colour scales are used for layer 1 and layer 2 e.g. colour scales are different for (a, b) and (c, d).

5.4.5 Petrophysical Relationships

Similarly to the peat depths, linear regressions were used to link non-calibrated EMI measurements to the organic matter content, and water level, pore water conductivity and hydraulic conductivity of the peat and gravel. Due to the low sample numbers of intrusive data, linear regressions were based only on apparent conductivities and not in-phase measurements. No significant relationships for organic matter content, or for properties of the gravel and peat pore water conductivity (34 to 58 mS/m) were found; however significant relationships were observed between EMI measurements and both peat water level ($R^2 = 0.93$, p-value = 0.027) and peat hydraulic conductivity ($R^2 = 0.8$, p-value 0.020). A map of the predicted peat hydraulic conductivity is presented in Fig. 5.11.

The correlation of hydrological data with inverted conductivity was also assessed. As a single conductivity was obtained for the peat layer, they were not compared with the organic carbon data; however, given the poor correlations of apparent conductivity values, it is anticipated that correlation with multi-layer conductivity would also be poor. As with the apparent conductivities, significant relationships were only seen for peat water level and peat hydraulic conductivity; however, they were weaker (R^2 = 0.48, p-value = 0.026 and R^2 = 0.44, p-value = 0.080, respectively). Furthermore, the porosity of the saturated gravel can be estimated at 30-40% using Archie's law (1942) which is comparable to previous work (e.g. Newell et al., 2015).
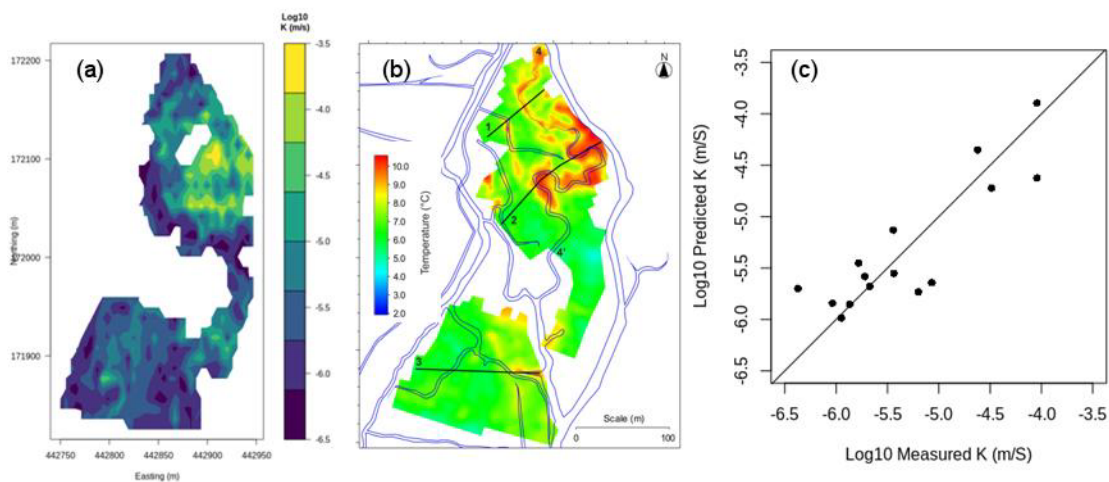
Figure 5.11: Maps of (a) predicted peat hydraulic conductivity, and (b) peat temperature 0.7 m below ground level (from House et al., 2015), and (c) scatter plot of measured and predicted hydraulic conductivity.

From, Fig. 5.11 it can be observed that the majority of the peat in the wetland has a predicted hydraulic conductivity of 10^{-5} to $10^{-6.5}$ m/s; however the north meadow appears to be characterised by a zone of reduced permeability. Moreover, this zone coincides well with the zones of GW upwelling, as determined from a temperature survey (House et al., 2015), Fig. 5.11b. The presence of these GW upwelling zones is thought to be related to the presence of drainage channels in the wetland. It is important to note that such temperature contrasts were not observed in the piezometer data during this work.

5.5 Discussion

5.5.1 Resolving Structure with EMI Methods

It was demonstrated using synthetic data that when the EMI instruments are operated at elevation, the result of the inversion becomes more susceptible to errors and the parameters of the synthetic model were not obtained in the inverse model. This was also seen in the field data in that depths obtained from the unconstrained inversion did not match with measured values. Previous work obtaining comparing inverted depths with intrusively obtained depths has included Frederiksen et al. (2017) who used a the Aarhus Workbench to produce vertically and laterally smoothed images of conductivity and extracted an iso-resistivity surface as the boundary between sand and clay; they were able to resolve the image with a RMSE of 1.04 m. Alternatively, Saey et al. (2014) operated their device at approximately ground level and inverted data using EM4Soil (http://emtomo.com) they were able to resolve well the structural pattern of deposit layers. The comparative poor performance of the inversion used here could be a result of the instability of the forward model when the device is operated above ground. However, it was shown that robust depth estimation can be obtained from a linear regression model and ~50 randomly sampled intrusive measurements; furthermore, the linear nature of this relationship is such that calibration is not necessary given the relatively narrow range of ECa values.

5.5.2 Best Approach for Inversion of Data

Despite the complications surrounding the inversion of data, it was evident that calibration of data significantly reduced data misfit of each model, indicating its importance in inverting EMI data. The difference between misfits obtained for the two and three-layer inversions were minimal, indicating that assumption of a sharply varying two-layer model was sufficient for describing the field site. However, it is anticipated that higher quality data would allow resolution of more complicated models. For instance, in reality, although the assumption of the fully saturated gravel being expressed as a homogenous layer is sufficient, the partial saturation of peat is such that a homogenous conductivity for the upper layer is perhaps insufficient. Moreover, obtaining depth

specific conductivity could permit correlation with depth specific organic matter (e.g. Huang et al., 2017). Furthermore, although a model of sharply varying electrical conductivity was deemed most valid for the context of this work, it is possible that production of smoothly varying conductivity models coupled with edge detection methods (e.g. steepest gradient or iso-conductivity methods) can be more successful.

5.5.3 EMI versus ERI

As noted, the wetland was previously characterised using 3D ERI by Chambers et al. (2014). They employed three different edge detection methods to extract the peat-gravel boundary from models of smoothing; they found that each method exhibited bias in depth prediction but an iso-resistivity method was able to predict the peat depth with the least bias. The iso-resistivity method used 996 measurements in the north meadow and 802 measurements in the south meadow. However, in addition to characterising the depth to the peat-gravel interface, Chambers et al. (2014) were able to resolve information about the gravel-chalk interface, and the extent of putty chalk. The use of EMI and ERI will depend on the requirements of the survey, e.g. in the case of the Boxford Wetland, whether characterisation of the peat-gravel interface is sufficient or not. For instance, whereas the geometry of the peat channel could be resolved adequately with 50 intrusive measurements and a VCP and a HCP EMI survey with reasonable spatial resolution would take 2 people working 2 days (15 hours), the ERI work conducted by Chambers et al. (2014) required 4 people working for 6 days (45 hours) however but would allow deeper characterisation.

5.5.4 Relating Geophysical and Hydrogeological Properties

In addition to structural characterisation, several applications have linked EMI measurements to hydrologically and lithologically relevant parameters, such as salinity, organic matter, pore water conductivity and pore water saturation, and have involved use of raw and inverted EMI data. In the context of wetlands, the principal properties of interest are organic carbon, hydraulic conductivity,

pore water conductivity and water content. It was found that the relationship between organic carbon and apparent conductivity were insignificant. Of the hydrological properties, the peat hydraulic conductivity and the water table displayed significance. The correlations of inverted conductivities and intrusive parameters were less significant when considering the meadow in its entirety, but when just the south meadow is considered, correlations were significant for peat hydraulic conductivity and gravel hydraulic conductivity.

5.6 Conclusions

EMI methods were used to characterise a riparian wetland; although the inversion of EMI data was complicated by measurements obtained at elevation and issues surrounding calibration, it was demonstrated that peat depths predicted from a multi-linear regression using apparent conductivity and in-phase measurements have a low RMSE. Furthermore, these can be used to constrain the two-layer inversion to give comparable results to when the measured depth is used in the inversion. A similar approach, where depths derived from another geophysical means, such as ground penetrating radar which have been successfully applied in wetland environments (e.g. Musgrave and Binley, 2011; Comas et al., 2017) could also be employed to make the obtained inverse model more robust. Although comparable conductivities to those obtained in the ERI models, the correlation of inverted conductivity and intrusive properties was not as strong the correlation between raw EMI measurements and intrusive properties. It is evident that although inversions of EMI data may be suitable for revealing structure and quantitative models of electrical conductivity in some areas, the use of apparent conductivities yields results that are of benefit to wetland management.

6 Assessing Electrical Resistivity and Induced Polarization Methods for Characterization of Riverbed Sediments

6.1 Introduction

Riverbed sediments play an active role in solute transfer between groundwater (GW) and surface water (SW); consequently they have implications for catchment-scale ecological health. Of particular interest are zones where GW and SW mix as they are characterized by unique biogeochemical conditions that permit the attenuation and transformation of nutrients and pollutants (Harvey and Gooseff, 2015). Properties of riverbeds such as hydraulic conductivity, surface area (SA) and cation exchange capacity (CEC) are important to characterize as they influence residence times of nutrients and pollutants, and the potential for their biogeochemical transformation. The significance of riverbed parameters has been recognized for several decades. For instance, Bencala et al. (1984) demonstrated that sand and gravel riverbeds were capable of sorbing cations and Triska et al. (1993) indicated that under specific oxidation conditions sorption could be more prevalent. Furthermore, although more recent studies have investigated how properties of riverbeds influence attenuation capabilities, e.g. Lansdown et al. (2015), they still rely on intrusive sampling; consequently, the spatial extent of information can be limited.

In recent years, geophysical applications have been used to target properties relevant to GW-SW interactions (McLachlan et al., 2017). For example, electrical resistivity (ER) methods have been used to reveal dynamic processes within the riverbed (Ward et al. 2010), characterize structure

(Crook et al., 2008; Orlando, 2013), and locate zones of GW up-welling (Mitchell et al., 2008; Gagliano et al., 2009). Additionally, induced polarization (IP) methods have been used for similar GW-SW interaction studies, for instance to characterize structure (e.g. Slater et al., 2010; Mwakanyamale et al., 2012), hydraulic conductivity (Benoit et al., 2018) and SA (Wang et al., 2020). It is important to note here that, as with the majority of geoelectrical methods, most applications targeting GW-SW interactions field based ER and IP studies use relative contrasts in electrical properties for interpretation, as opposed to obtaining quantitative information about hydrogeological and biogeochemical properties.

In addition, there has been significant work in the laboratory relating electrical properties to properties such as hydraulic conductivity, CEC and SA. Spectral IP (SIP) is commonly used to measure electrical properties across broad frequency ranges, e.g. 1 mHz to 1000 Hz. Slater (2007) provided an extensive review on efforts to link geoelectrical methods to hydraulic conductivity, commenting that IP methods may provide better estimates of hydraulic conductivity than ER methods. Furthermore, much of the SIP work demonstrate its sensitivity to CEC (e.g. Leroy et al., 2008; Revil and Florsch, 2010; Revil, 2012).

It is clear that a combination of field and laboratory IP methods has the potential to reveal relevant riverbed properties; furthermore, given the dependency of IP signals on cementation it has been proposed that IP characterization of unconsolidated sediments ought to be more effective in revealing quantitative properties than for sedimentary rocks (Weller et al., 2015). Despite this, such applications linking geoelectrical measurements and properties relevant to the GW-SW interface are rare, e.g. Benoit et al. (2018); however, this rarity also extends to land-based hydrogeological investigations, e.g. Hordt et al. (2007) and Binley et al. (2016). A key benefit of geoelectrical measurements for quantitative riverbed characterization is that it may permit large scale geoelectrical surveys (e.g. with towed electrodes) to infer information at scales larger than permitted by intrusive sampling.

However, it is important to note that aquatically-based ER and IP applications are more challenging than terrestrial applications due to the presence of a conductive water column overlying a more resistive riverbed. Several publications have addressed issues associated with aquatic ER surveys and their sensitivity (e.g. Snyder et al., 2002; Orlando 2013). For instance, although floating arrays are more efficient in towed surveys, they have poorer investigation depths than submerged arrays (Day-Lewis et al., 2006) and whilst bottom-towed arrays have been used to improve investigation depth (e.g. Wynn 1988; Kelly et al., 2009); equipment can become snagged on rough bed forms or vegetation. Consequently, most studies using submerged arrays have adopted fixed (anchored) arrays; this has the added benefit that reciprocal measurements can be obtained to assess data quality and improve inverse modelling. However, issues influencing the inversions have also been considered, e.g. Day-Lewis et al. (2006) demonstrated that erroneous fixing of water column properties in an inversion can lead to significant artefacts in ER images, but this has not previously been explored for IP images.

The principal aim of this work is therefore to determine the ability of both SIP and field-based IP to reveal bio-geochemically relevant properties of riverbeds. In addition, synthetic modelling was used to investigate some of the complications of inversion of IP data collected in the field: specifically (1) the sensitivity of geoelectrical measurements to the riverbed and riverbank; (2) the influence of fixing river properties on the inversion process, and (3) the influence of errors in geoelectrical data and river properties on the inversion process. In doing so, the potential of IP for characterization of the riverbeds can be assessed and several challenges related to IP imaging in aquatic environments can be explored. The investigation focuses on a well-characterized site; intrusive samples were obtained for SA, CEC and SIP measurements, and field IP data were collected.

6.2 Methods

6.2.1 Study Site

Fieldwork was conducted on the River Leith, see Fig. 6.1, a tributary of the River Eden (Cumbria, UK). The River Eden catchment is a fault-bound basin 50 km long and 5 to 15 km wide with Permian and Triassic sandstone bedrock (Allen et al., 2010). The catchment contains extensive Quaternary deposits comprising till, glacial-fluvial out-wash, and alluvial deposits. Much of the work conducted across the catchment has concerned the direction of GW flow paths and biogeochemical processes at the GW-SW interface have been shown to significantly mitigate river loading of legacy GW nitrate of agricultural origin (Heppell et al., 2014).
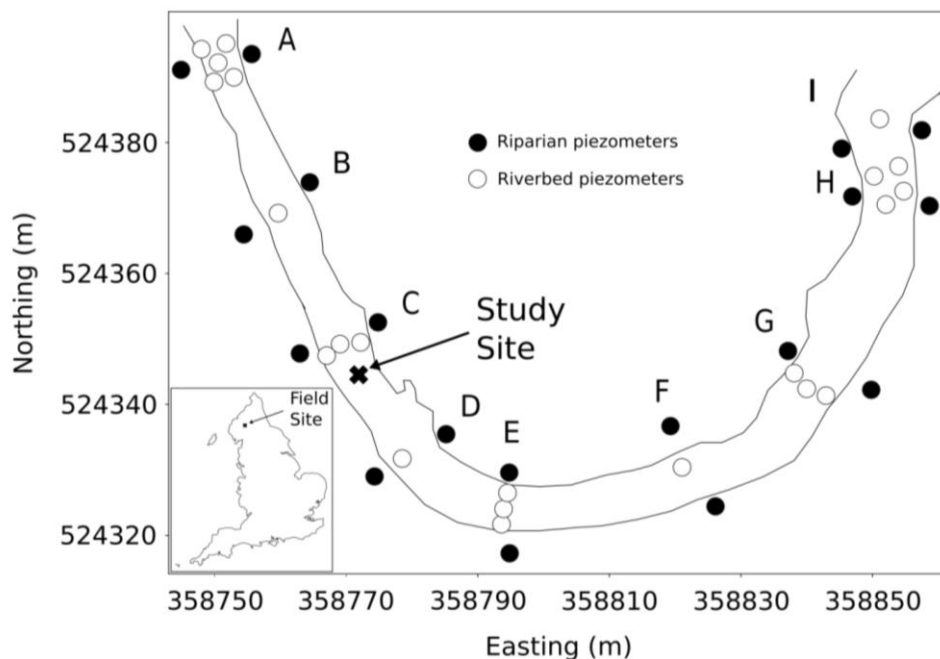

Figure 6.1: Location of study site within a 200 m meander of the River Leith. Inset shows position of field site in the north of England, the flow directions is from site A to site I. The circular symbols indicate the position of the riverbed and riparian piezometers used in the study of Binley et al. (2013), which provides additional analysis of site characteristics.

At the field site the riverbed comprises a mixture of alluvial pebbles, gravels and sands overlying unconsolidated red sands and silts, all underlain by the Penrith Sandstone aquifer (Allen et al., 2010). The riverbed is characterized by a series of riffle and pool sequences, and is predominantly GW fed; however, Käser et al. (2009) indicated the potential for SW down-welling at the site during storm events which was later confirmed experimentally by Dudley-Southern and Binley (2015). Most of the studies have focused on nitrate loading from the GW (e.g. Krause et al., 2009; Lansdown et al., 2011; 2015; Heppell et al., 2014). These studies have revealed evidence of heterogeneity in redox processes controlling nitrate delivery from regional GW, and demonstrated a clear need for measurement techniques to identify variation in the texture of riverbeds. The work presented here focused on an area just below site C (Fig. 6.1), which was shown to be a zone of regional GW up-welling, and therefore a zone of legacy nitrate loading to the river (Binley et al., 2013).

6.2.2 Field-Based Geoelectrical Measurements

Field-based frequency domain IP measurements were made using a Geolog2000 GeoTOM MK7E100 instrument (Augsburg, Germany). To aid with electrode positioning, twenty-four 6-mm-long stainless steel bolts were punched through rubber tree belting with 0.25 m spacing. Each electrode was wired using copper wire, hence they were non-shielded, and connected to the GeoTOM instrument. The array was placed onto the riverbed and electrodes were driven into the bed; rocks were placed between some of the electrodes to prevent the array from floating. A dipole-dipole sequence comprising 297 normal measurements, and 297 corresponding reciprocal measurements, was created. Current with a frequency of 2 Hz was injected with a range of 10 to 100 mA. Following the survey the river stage above each electrode was measured, as well as the electrical conductivity of the river water.

6.2.3 Data Quality and Error Modelling

Reciprocal measurements were used to calculate a mean transfer resistance and phase angle for each quadrupole, in addition, reciprocal errors were calculated from the difference between direct and reciprocal measurements. Transfer resistance measurements with > 10% error were removed, resulting in a total of 294 measurements with an average proportional error of 0.025; for the phase angle measurements, measurements with > 25% error were removed, resulting in 63 measurements with an average absolute error of 0.6 mrad. Due the discrepancy in measurement numbers following filtering, the resistance data were first inverted separately from the phase data. To model resistance errors for the inversion, measurements were grouped into 15 bins with equal size. The average error and resistance was determined for each bin and a linear model was fitted; the model exhibited an expected relationship of increasing error with increasing resistance magnitude. For phase errors it is common to find parabolic (e.g. Mwakanyemale et al., 2012), however, in this case no correlation was observed, instead a phase error of 0.6 mrad was assigned for weighting in the inversion.

6.2.4 Data Inversion

Data were inverted using the R2 and cR2 inversion algorithms that use a finite element grid to model the voltages resulting from a dipolar current injection. A triangular mesh was generated using Gmsh (Geuzaine and Remacle, 2009) to include an interface at the river-riverbed boundary, with finer elements close to the electrodes and coarser elements further away to accommodate far field boundary conditions. As noted by LaBreque et al. (1996), error models based solely on reciprocal errors typically lead to data over-fitting in the inversion as they do not consider forward modelling errors. To account for this forward modelling error was determined for the mesh used in the inversion with a homogeneous subsurface and added to error weights for both resistance and phase components. To prevent smoothing across the river and riverbed, the river was fixed to a resistivity of 20 ohm.m (conductivity = 50 mS/m) as measured in the field, and the phase angle was fixed at 0 mrad.

6.2.5 Intrusive Sampling

Seven 0.8 to 1.0 m core samples were extracted from the study site using a Cobra TT drill (Atlas Copco, Stockholm, Sweden) across an approximately 6 m longitudinal transect along the centre of the river. The transition of the alluvial gravels (ALV) and underlying red sands (RS) was abrupt allowing sub-sampling in the field. Samples were cut into approximately 10 cm sections and double bagged before storage in a refrigerator, in total forty-five samples were obtained. Samples were compressed during drilling but, by assuming a linear compression, the mean depth to the ALV-RS interface can be determined to be 0.35 m with a standard error (SE) of 0.04 m.

6.2.6 Laboratory SIP Measurements

SIP measurements were made using an Ontash and Ermac PSIP device (River Edge, New Jersey, USA) and a Zimmerman ZEL SIP device (see Zimmerman et al. 2008). For both, measurements were made at frequencies ranging from 10 mHz to 1 kHz, and several repeat samples were measured on both devices to ensure their agreement. Prior to SIP measurements, samples were rinsed several times using deionized water and saturated with 0.05 M sodium chloride solution for at least 12 hours. The sodium chloride concentration was selected to ensure that the electrical conductivity (~50 mS/m) was consistent with observed pore fluid conductivity at the site (Dudley-Southern and Binley, 2015). Samples were loaded into the holder and current was injected between two copper coil electrodes and potential was measured with two point electrodes (Fig. 6.2). The potential electrodes were positioned such that they were out of the electric field. For the ALV samples, measurements were made on samples sieved to < 4 mm and < 22.4 mm to match the criteria used in SA and CEC analysis and provide electrical values more relevant to field conditions.
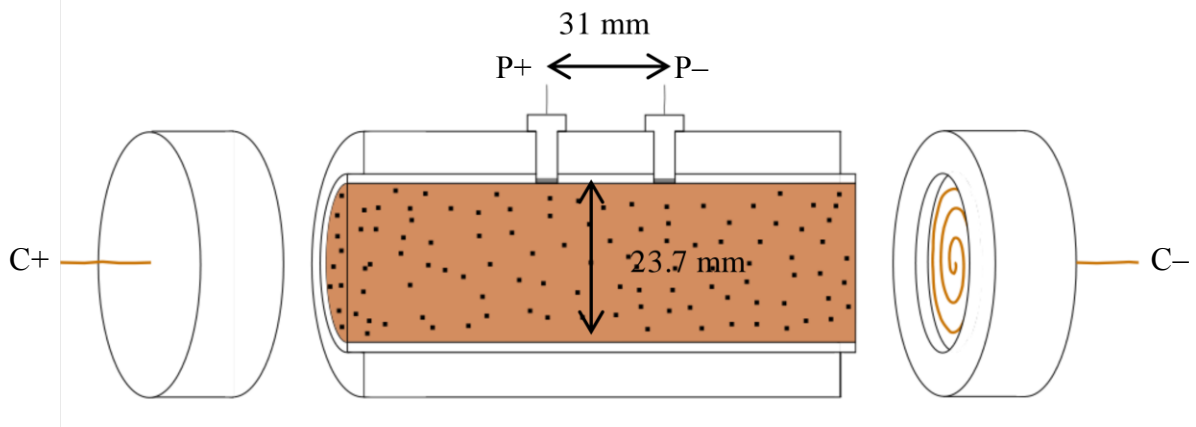
Figure 6.2: Schematic of sample holder used in SIP measurements, with the middle section shown as a cross section.

6.2.7 Sediment Laboratory Analysis

Nine ALV and eight RS samples were selected randomly for grain size distribution (GSD), SA and CEC analysis. ALV samples were dry sieved with the following size fractions: 45, 22.4, 11.2, 5.6, 4, 3.35, 2.8, 2.38, 1.7, 1.4, 1.18, and 1 mm. Sub-millimetre ALV samples and RS samples were analysed with a Beckman Coulter 13320 laser granulometer (Brea, California, USA). Laser granulometer data and sieving data were combined assuming a homogeneous density of grains.

SA was determined by nitrogen gas adsorption (Brunauer et al., 1938) using a Micrometrics Gemini VI 2385C instrument (Norcross, Georgia, USA). Samples were sieved to < 4 mm to fit the sample holder and 2 g of each sample were loaded into each holder prior to analysis. To ensure samples were representative the quartering method (Schumacher et al., 1990) was used and three replicates of an ALV sample and a RS sample were measured. As with SA, for CEC analysis samples were sieved to < 4 mm, quartered into 4 g samples and CEC values were obtained using the sodium acetate method (see Chapman, 1965) and a flame photometer.

6.3 Results

6.3.1 Laboratory Results

The spectral behaviour for RS, < 4 mm ALV and < 22.4 mm ALV are distinctive and display similar patterns for each sample type; the results of samples C2.2 (< 4 mm and < 22.4 mm) and C2.5 are shown in Fig. 6.3. It is important to note here that as the results are presented as conductivities the phase angles are positive, hence all of the figures presented here follow this convention. All samples showed the expected increasing conductivity with increasing frequency. The electrical conductivity of the RS samples was consistently higher than the < 22.4 mm ALV samples; however, in removing the > 4 mm particles, the ALV became less distinguishable from RS. In terms of phase angle, removal of coarser ALV fractions resulted in a slightly smaller phase angle and the contrasts between RS and ALV samples is greatest at higher frequencies (100-1000 Hz) and indistinguishable at lower frequencies (0.05 to 0.1 Hz). Given the higher conductivity and phase angle of RS samples, compared to ALV samples, there is clearly higher polarization in the RS samples. In many of the observed spectra, capacitive coupling was observed around and beyond 1000 Hz, as the interest here was to relate laboratory and field IP data, measurements beyond 1000 Hz were not considered in detail. However, it should be noted that the procedure presented by Wang et al. (2018) can be used to ensure more reliable measurements beyond 1000 Hz.
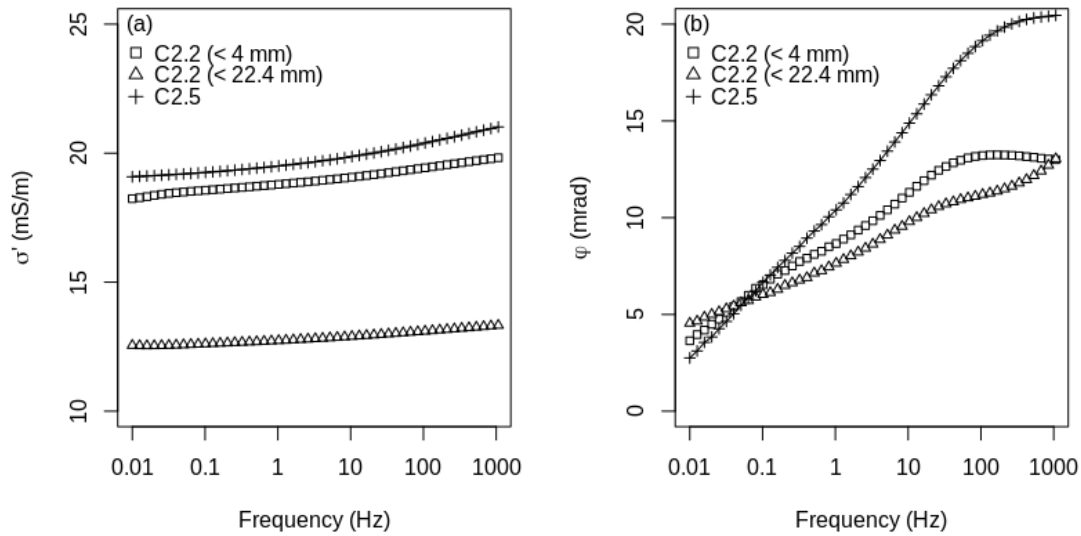
Figure 6.3: Laboratory based SIP spectra for RS, < 4 mm ALV and < 22.4 mm ALV for (a) conductivity and (b) phase angle.

The grain size data are shown in Fig. 6.4; the RS samples were well sorted and had a mean grain size of 0.255 (SE = 0.008) mm, whereas the ALV samples had significantly higher variability and a mean grain size of 4.792 (SE = 1.454) mm. For the ALV samples sieved to < 4 mm, the mean grain size was 0.413 (SE = 0.043) mm. The CEC, SA, complex conductivity and phase angles, at 2 Hz, for RS and < 4 mm samples are presented in Table 6.1. The measured SA of RS and < 4 mm ALV samples, expressed as specific surface per unit mass, were not significantly different from one another, 3.02 (SE = 0.15) m^2/g and 2.84 (SE = 0.34) m^2/g, respectively. Similarly the CEC values for RS and < 4 mm ALV were not significantly different, 2.87 (SE = 0.12) meq/100 g and 3.07 (SE = 0.24) meq/100 g, respectively.

Figure 6.4: Grain size distribution of (a) RS samples and (b) ALV samples.

Table 6.1: Laboratory data of < 4 mm ALV and RS samples, SIP measurements are for injected currents with a frequency of 2 Hz.

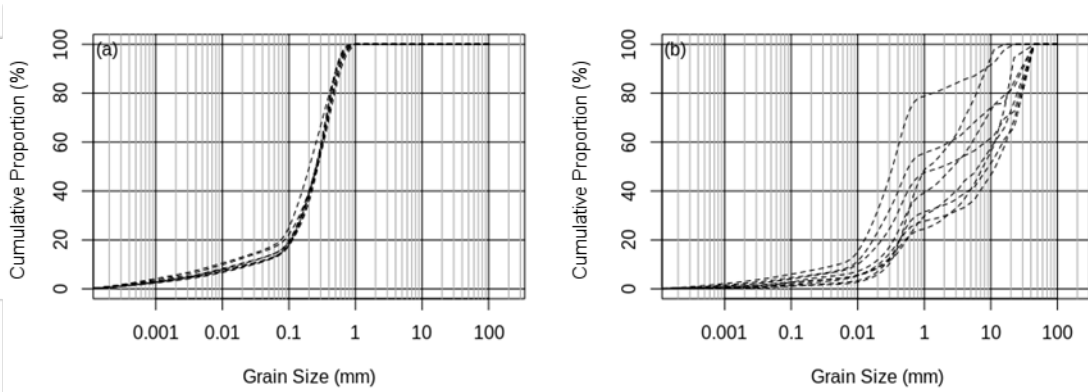| #	Type	SA (m²/g)	CEC (meq/g)	σ' (mS/m)	σ'' (mS/m)	φ (mrad)
C1.2	ALV (< 4 mm)	2.30	3.83	12.46	0.14	10.87
C1.3	ALV (< 4 mm)	2.92	2.83	21.88	0.24	10.92
C1.6	RS	3.09	2.78	20.48	0.24	11.47
C2.1	ALV (< 4 mm)	2.24	1.84	13.89	0.13	9.36
C2.2	ALV (< 4 mm)	4.95	4.10	18.86	0.18	9.33
C2.4	RS	2.7	2.94	20.22	0.24	12.35
C2.5	RS	3.45	3.28	19.59	0.23	11.55
C2.6	RS	2.65	2.40	19.08	0.23	11.95
C2.8	RS	2.62	2.46	20.01	0.16	8.02
C4.1t	ALV (< 4 mm)	2.83	3.39	19.47	0.16	6.97
C4.2t	ALV (< 4 mm)	3.64	4.37	20.59	0.27	13.11
C4.2b	RS	3.76	3.21	-	-	-
C5.7	RS	2.73	2.67	18.79	0.15	7.90
C6.1	ALV (< 4 mm)	1.64	1.55	19.47	0.1	5.27
C6.3	ALV (< 4 mm)	3.08	3.26	20.96	0.27	12.86
C6.7	RS	3.13	3.21	20	0.27	13.64
C7.2	ALV (< 4 mm)	1.88	2.01	17.69	0.13	7.45

The imaginary conductivity, σ'', is strongly correlated with SA, expressed as m²/g (see Fig. 6.5a); the SA measurement of C2.2 was excluded as it was deemed an outlier by Grubbs' outlier test, the resultant relationship had an R^2 of 0.74. It is important to note, however, that generally for σ'' and surface area relationships, pore normalized surface area, S_{por}, is used. Porosity was not measured directly, but samples were found to have low variability in estimating porosities from an assumed a

grain density of 2.65 g/cm^3 and measurements of sample mass and volume. In addition, although not as strong (R^2 = 0.34) σ'' is also positively correlated with CEC as expected (Fig. 6.5b).
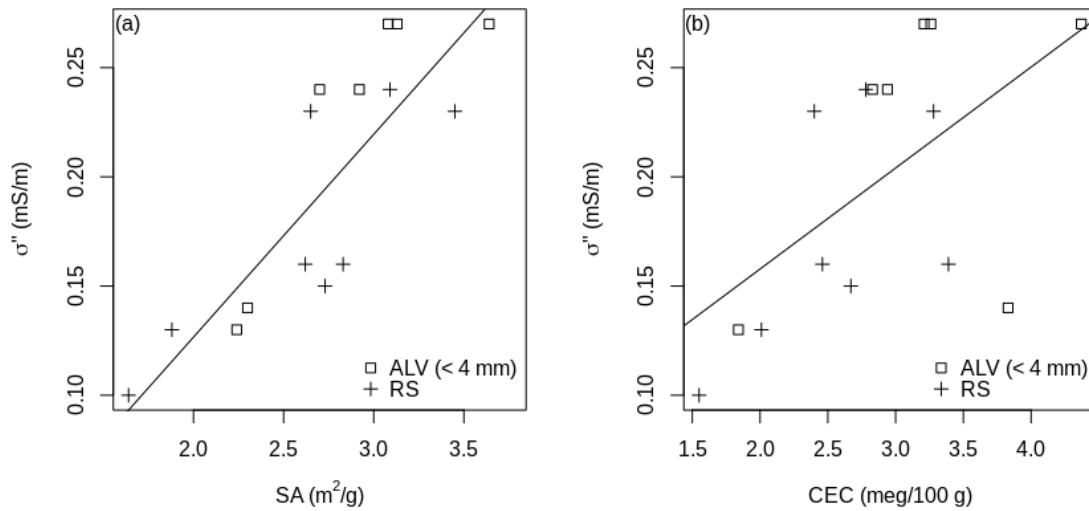
Figure 6.5: Linear relationship between surface area and imaginary conductivity (a), and linear relationship between cation exchange capacity and imaginary conductivity (b).

It is also possible to compare obtained *σ"* and estimated S$_{por}$ values from this work with published relationships. Firstly, if the > 4 mm ALV grains are considered spherical their SA, expressed in m^2/g, becomes negligible. In doing so an average *S$_{por}$* of 6.58 1/µm for < 22.4 mm ALV can be calculated, in comparison the average value for RS samples is of 18.08 1/µm. These values can be used to compare the results here with those obtained by Weller et al (2010) who present an empirical link between *S$_{por}$* and *σ"* following analysis of a large database of SIP measurements of sand and clay mixtures. Using pore fluids with conductivity of 100 mS/m and an excitation frequency of 1 Hz, they found that *σ" = 0.01 S$_{por}$* (with *σ"* expressed in mS/m and *S$_{por}$* expressed in 1/µm). Adjusting this relationship to account for the lower conductivity of the saturating fluid used here (following Weller et al., 2011), *σ"* (at 1 Hz) for the measured mean *S$_{por}$* equate to 20.21 1/µm and 50.51 1/µm for < 22.4 mm ALV and RS samples. Although these are higher than the actual *S$_{por}$*, these values fall within the data used by Weller et al. (2010) to fit their linear regression (see Fig. 2 of Weller et al., 2010).

6.3.2 Field Results

The inverted model for the field data, expressed in conductivity and phase angle, is shown in Fig. 6.6. Based on laboratory values obtained at 2 Hz, it was anticipated that the riverbed would be characterised with a two-layer nature with a conductivity of 14 mS/m, a phase angle of -8 mrad and a thickness of ~0.35 m overlying a layer with a conductivity of 20 mS/m and a phase angle of -11 mrad was expected. In contrast, the inverted conductivity model shows a broadly homogeneous subsurface with a mean conductivity of ~15 mS/m, and small areas of anomalies, up to a depth of 1.5 m below the water level where it becomes more resistive. In comparison, the phase angle model shows a two-layer structure that coincides well with the anticipated structure and comprises a slightly more polarizable upper layer. The opposite pattern was anticipated.
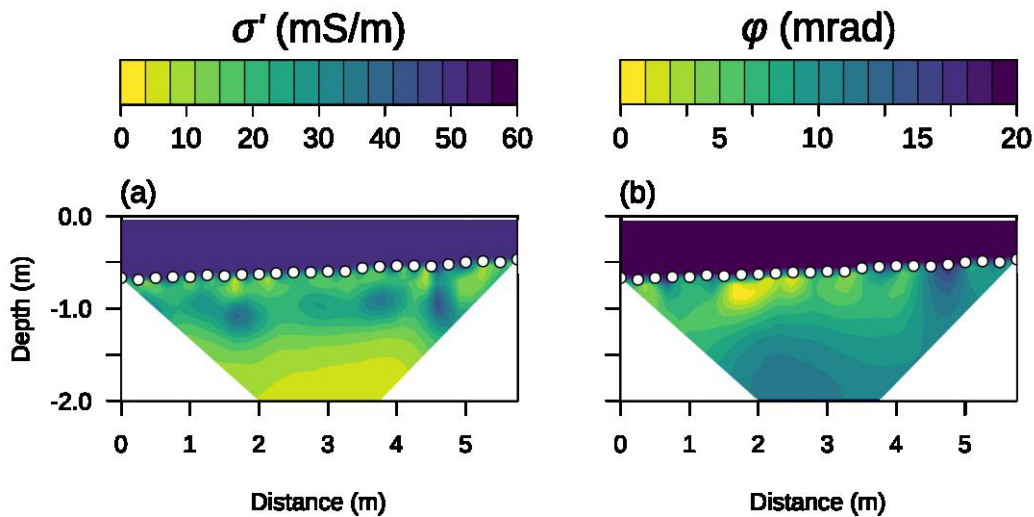
Figure 6.6: Inverted field data: (a) conductivity and (b) phase angle.

Whilst it is true that the anticipated contrasts expected in the field results would be subtle for measurements made at 2 Hz, it is important to assess the reliability of these images and determine necessary conditions to characterize these contrasts. The discrepancy between the obtained field results and the expected results can be attributed to either the laboratory and field measurements not being consistent with one another or errors associated with data collection. The former is

unlikely, for instance although it could be that loss of fine materials during sampling led to an underestimation of electrical properties in the laboratory, this is unlikely given that samples were collected in a plastic sheath. Moreover, it is more likely that larger particles are excluded due to the diameter of the drill and a significant portion of fine materials would need to be lost to explain the observed phase angles in the upper section of the phase angle image. There are, however, several sources of error that could introduce artefacts. To explore some of these complications the sensitivity of measurements to depth and lateral variation and the effect of fixing river properties was investigated. As each case was modelled in terms of complex resistivity the phase angles used were negative; however, as with Fig. 6.6 because the results are plotted as conductivity values the corresponding phase angle values are displayed as positive.

6.4 Synthetic Modelling

6.4.1 2D and 3D Measurement Sensitivity

Previous work (e.g. Orlando, 2013) demonstrated the influence of electrode separation on depth of investigation for ER measurements; however, this has not previously been done for IP measurements. Whilst it is intuitive that submerged arrays offer superior characterization of the riverbed (e.g. Day-Lewis, 2006) it is important to assess the influence of the water column height on observed IP measurements. Fig. 6.7 shows synthetic data generated for a two-layer model consisting of a river with stage, s, a 20 ohm.m resistivity (conductivity = 50 mS/m) and a 0 mrad phase angle, overlying an infinitely thick unit with a 75 ohm.m (conductivity = 13.33 mS/m) and a -8 mrad phase angle. The data were generated using cR2 for different dipole-dipole measurements with electrode spacing, a, and separation of the current and voltage dipoles, na, assuming the electrodes are located on the riverbed for three cases where $s = 0$ (i.e. no river present), $s = a$, and $s = 2a$. In order to illustrate the effect of the water column on the measurements a sensitivity, S, can be computed according to (see, for example Binley, 2015):

$$S(x,z) = \frac{\partial \log (\rho_a)}{\partial \log (\rho(x,z))}, \qquad (6.1)$$

where $\rho(x,z)$ is the resistivity at location (x,z) and ρ_a is the apparent resistivity. If $S(x,z)$ is integrated over a given depth z for all x, it can be shown as a vertical sensitivity profile. This is illustrated in Fig. 6.7(c) when $s = a$ and $s = 2a$ for $n = 1$.
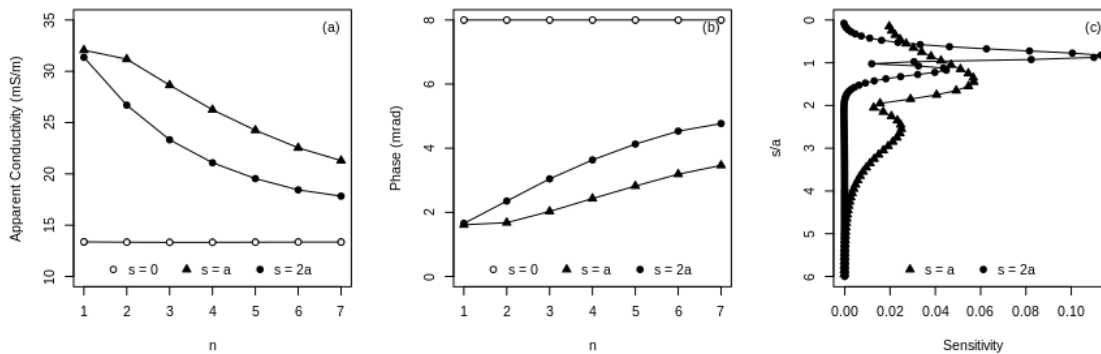
Figure 6.7: Response of dipole-dipole measurements to different river stages:

(a) apparent conductivity, (b) phase angle and (c) measurement sensitivity.

It is evident from the results in Fig. 6.7 that the water column suppresses the observed response, especially with regards to the phase angles. This effect may be amplified by the low signal-to-noise ratio and hence high error levels found in aquatic surveys. It can also be noted that when $n = 1$, the apparent conductivity and phase angle for $s = a$ and $s = 2a$ are almost identical, indicating that when $s \geq a$, river stage does not influence the response. However, these measurements do have some sensitivity to the riverbed, as indicated in Fig. 6.7c, but the majority of the signal is obtained from the river. It is also important to note that immediately at the river-riverbed interface there is a low sensitivity which could result in the anomalous conductivities and phase angles observed in the inverted field data (Fig. 6.6).

In addition to wider electrode separations providing enhanced signal penetration into the riverbed, it is also true that these measurements will have increased lateral sensitivity. Whilst it is typically justified to ignore off-axis effects, the presence of riverbanks may be problematic in longitudinal surveys, especially for narrow channels. To investigate the influence of the riverbanks, the response of dipole-dipole measurements with electrode separation, a, was generated from 3D models with different river widths using the 3D equivalent of cR2: cR3t. The river channel was assumed orthogonal with a depth of 0.5 m, the river was assigned a 20 ohm.m resistivity (conductivity = 50 mS/m) and a 0 mrad phase angle, the riverbed and bank were assigned a 75 ohm.m resistivity (conductivity = 13.33 mS/m) and a -8 mrad phase angle. Fig. 6.8 shows that when $a = 0.5$ m, bank effects begin to become evident in cases where river width is less than 4 m; given that the river was 7 m in this work the banks are unlikely to have an effect on the measurements in this case.
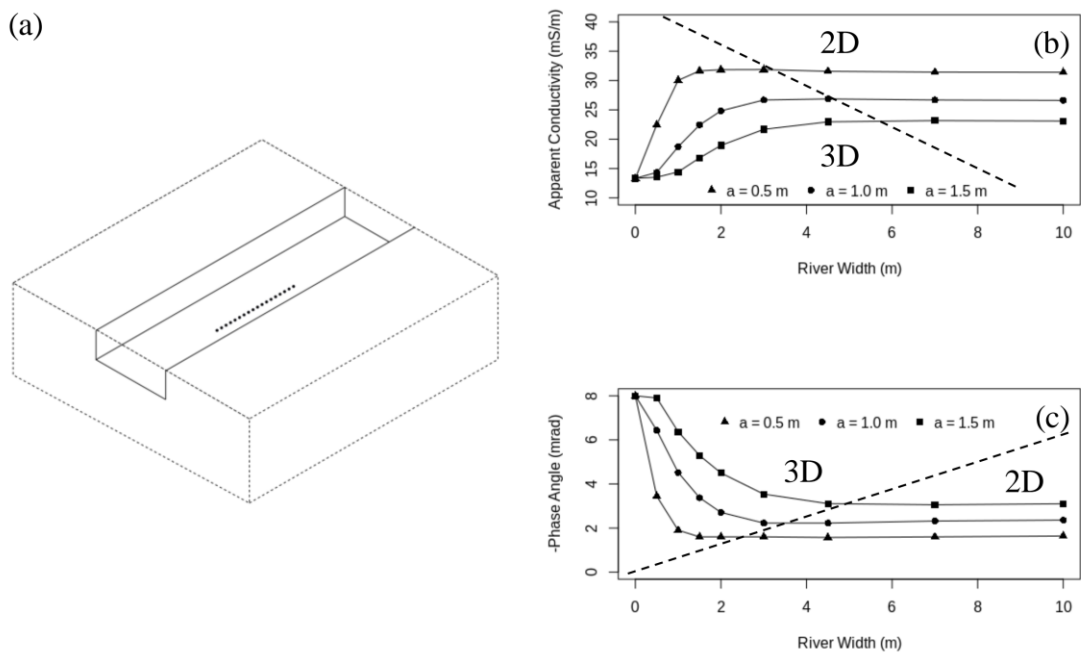
Figure 6.8: Response of dipole-dipole measurements to different river widths: (a) schematic showing central region of 3D mesh and electrode array, (b) apparent conductivity, and (c) phase angle.

6.4.2 Fixing the Properties of River Elements

To assess the necessity of fixing the properties of river elements in the inversion, a three-layer case was used to represent the field site. It comprised a 0.6 m thick layer with a 20 ohm.m resistivity (conductivity = 50 mS/m) and a 0 mrad phase angle, a 0.35 m thick layer with a 75 ohm.m resistivity (conductivity = 13.33 mS/m) and a -8 mrad phase angle, and an infinite layer with a 50 ohm.m resistivity (conductivity = 20 mS/m) and a -11 mrad phase angle (Fig. 6.9). Data were generated for the same sequence used in the field and then corrupted with Gaussian noise. Resistances were corrupted with 1% and 2.5% noise whereas phase angles were corrupted with 0.1 and 1 mrad absolute noise. Data with the lower noise levels were inverted allowing regularization across the riverbed, separate regularization in the river and riverbed, and fixed river elements. Data with the higher noise levels were inverted with fixed river elements.
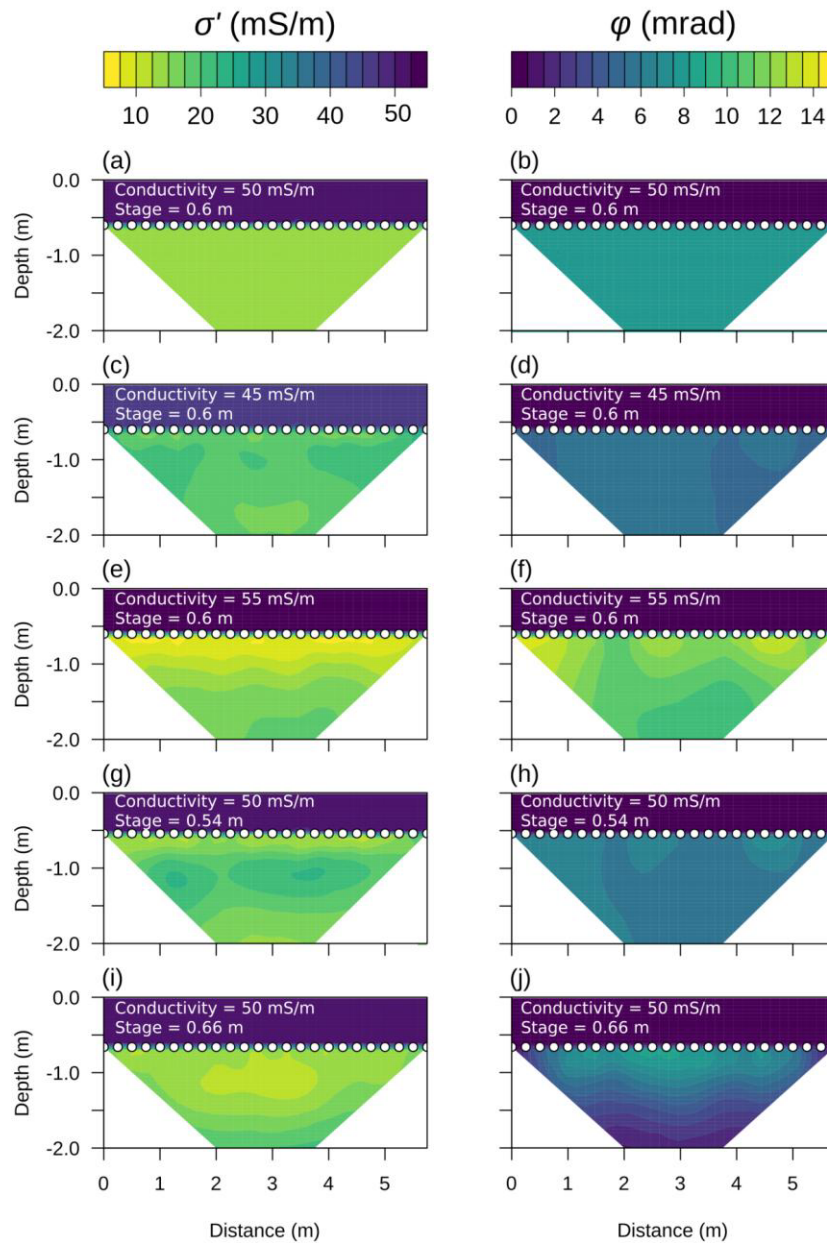
Figure 6.9: Models for regularized, blocked and fixed river element inversions. Synthetic models for conductivity are shown in (a) and (b). Inverse models for the lower noise case with regularization across the river-riverbed interface are shown in (c) and (d). Inverse models for the lower noise case with no regularization across the river-riverbed interface are shown in (e) and (f). Inverse models for the lower noise case with no regularization across the river-riverbed interface and fixed river element properties are shown in (g) an (h). Inverse models for the higher noise case with no regularization across the river-riverbed interface and fixed river element properties are shown in (i) an (j). The dashed lines indicate position of the 2nd and 3rd layer boundary and electrode positions are marked by white circles.

Allowing regularization across the river-riverbed interface gives a poorly resolved conductivity model (Fig. 6.9c) where the upper riverbed layer appears more conductive than the lower layer; a similar effect is seen for the phase angle model (Fig. 6.9d). Despite this, the river phase angles correspond to the values of the original model, and a stratified model with a broadly comparable depth as the synthetic model is apparent in both images. Adding the river-riverbed boundary (which can easily be measured) and enforcing a separation in the regularization results in the conductivity of the river being recovered more accurately, but the riverbed appears as a broadly homogeneous layer for both conductivity (Fig. 6.9e) and phase angle (Fig. 6.9f). This highlights that measurements are relatively insensitive to riverbed properties (see also Orlando, 2013) and that data can be fitted easily by modifying parameters within the river layer. When river values are fixed in the inversion, the inverse model is significantly improved and reveals a contrast in the two riverbed layers with a reasonable demarcation of the two units, particularly for the phase image (Fig. 6.9h). If data have higher noise levels, the contrast in the two units is weakened and demarcation of the lower unit is less obvious in the conductivity image (Fig. 6.9i) highlighting the importance of good quality data; this is especially pertinent for the phase data (Fig. 6.9j) given the poor quality of field data collected here and the difficulties surrounding collection of high quality data.

6.4.3 Accurate River Properties

In addition to errors in geoelectrical data, measurements of river conductivity and stage may be incorrect. Although not so relevant here, given that stage can be accurately measured, for larger-scale surveys the use of ultrasound or similar means of bathymetry determination may be prone to errors. Similarly, although it is reasonable to assume that for shallow cases the river conductivity is homogeneous, it is possible to obtain poor measurements from a faulty conductivity meter in all environments or have significant stratification in deeper environments (e.g. Dahlin and Loke, 2018). To investigate impact of inaccurate river properties on inverted ER and IP results, data were

generated from a two-layer model with a 0.6 m thick layer with a 20 ohm.m resistivity (conductivity = 50 mS/m) and a 0 mrad phase angle, and an infinite layer with a 75 ohm.m (conductivity = 13.33 mS/m) and a phase angle of -8 mrad. As before, resistances and phase angles were corrupted with 1% and 0.1 mrad Gaussian noise, respectively. Five scenarios were tested: (1) correct river depth and a resistivity of 20 ohm.m (conductivity = 50 mS/m); (2) a fixed river resistivity of 22.22 ohm.m (conductivity = 45 mS/m) with correct depth; (3) a fixed river resistivity of 18.18 ohm.m (conductivity = 55 mS/m) with correct depth; (4) a fixed river depth of 0.54 m with the correct river resistivity; (5) a fixed river depth of 0.66 m with the correct river resistivity (Fig. 6.10).

It is evident from Fig. 6.10 that erroneous fixing can have dramatic and misleading influence on the inverted models. Fixing the river conductivity to a value that is too low forces the inversion to compensate by resolving the riverbed as more conductive (Fig. 6.10c) and less polarizable (Fig. 10d) than it ought to be. The inverted phase angle is lower in this case because the synthetic data are less sensitive to the riverbed than is accounted for in the inversion, such that the riverbed appears less polarizable. Conversely, by setting the conductivity of the river too high, the inversion creates a non-existent low conductivity layer (Fig. 6.10e) and in the phase angle image the phase angles are elevated (Fig. 6.10f). Similar effects are also seen with erroneous depth fixing, underestimation of river depth results in a resistive artefact in the immediate vicinity of the riverbed followed by a more conductive layer (Fig. 6.10g). In comparison, overestimation of river stage results in an overly resistive upper riverbed with high phase angles, and overly conductive lower riverbed with low phase angles, Fig. 6.10i and 6.10j respectively.
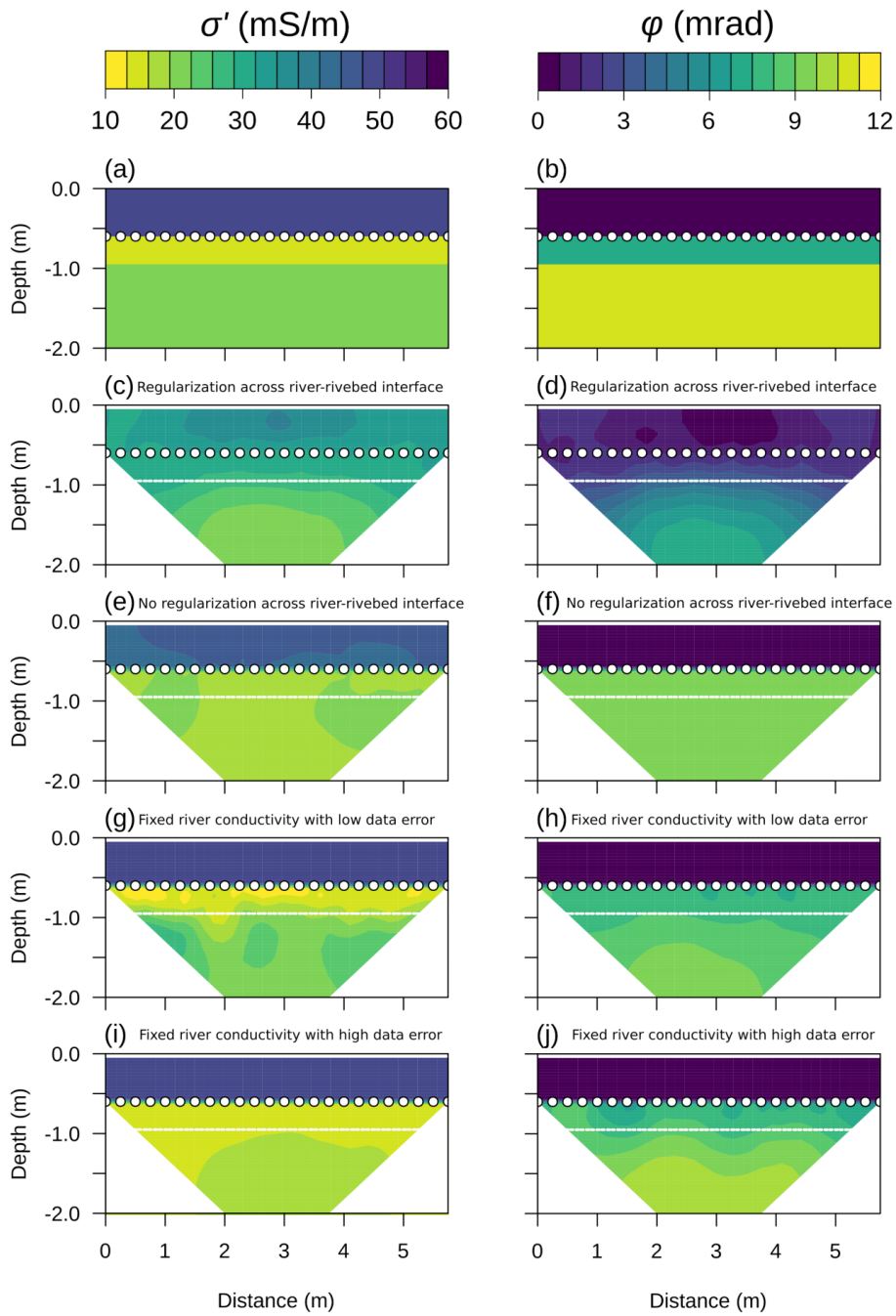
Figure 6.10: Inversion results with erroneous fixing of river conditions. Inverted models for when the river resistivity and river depth are correct are shown in (a) and (b). Inverted models when the river is fixed to 10% underestimation in conductivity are shown in (c) and (d). Inverted models when the in river is fixed to a 10% overestimation in conductivity are shown in (e) and (f). Inverted models with a 10% underestimation in river depth are shown in (g) and (h). Inverted models with a 10% overestimation in river depth are shown in (i) and (j).

6.4.4 Off-Axis Micro-Topography

Given that depth can be measured directly, inaccuracy of the river stage measurement by more than 10% is unlikely in field sites similar to this one. However, natural river channels, particularly in higher energy environments, are subject to micro-topographic variability. Hu et al. (2014) illustrated, for example, the existence of micro-forms at the study area using a high resolution topographic survey (Fig. 6.11). Moreover, although it was evident that 3D effects from the riverbank could reasonably be ignored (Fig. 6.8), natural rivers rarely conform to an orthogonal shape. Therefore, when inversions are carried out in 2D, topographical variation in the strike direction are ignored even though it is highly likely that this variation will have similar effects to fixing the river depth incorrectly.
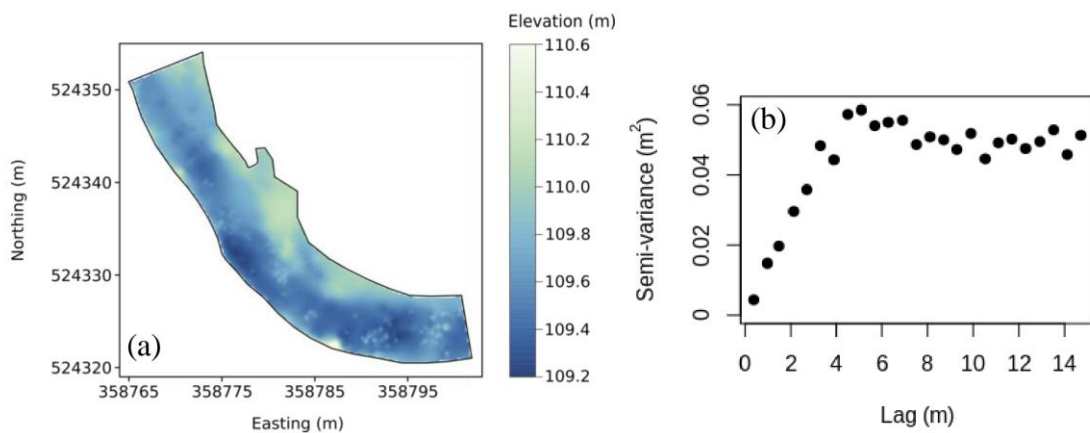
Figure 6.11: Evidence of micro-forms in the river Leith downstream of the survey area. (a) Riverbed topography of a 40 m sub-reach. (b) Variogram of topographic data. The survey includes the study site used here, spanning from site C to site E in Fig. 6.1.

To explore the influence of micro-topography, data were generated for a three-layer model comprising a 0.6 m thick layer with a 20 ohm.m resistivity (conductivity = 50 mS/m) and a 0 mrad phase angle, a 0.35 m thick layer with a 75 ohm.m resistivity (conductivity = 13.33 mS/m) and a -8 mrad phase angle, and an infinite layer with a 50 ohm.m resistivity (conductivity = 20 mS/m) and -

135

11 mrad phase angle, i.e. the same as shown in Fig. 6.9a and 6.9b. Data were generated for a flat riverbed and corrupted with 1% noise for the resistances and 0.1 mrad noise for the phase angles. River depths, and electrode positions, were perturbed by adding a depth error sampled from a normal distribution with a mean of 0 m and a standard deviation of 0.02 m. A finite element mesh was generated to represent the new bed geometry and the data were inverted. It can be seen that the conductivity image in Fig. 6.12 does not compare well with the corresponding image in Fig. 6.9; i.e. the three-layer structure is not visible and the images are characterized by discontinuous artefacts. The phase angle image (Fig. 6.12) is however more similar but the boundary is more undulating and diffuse than would be expected.
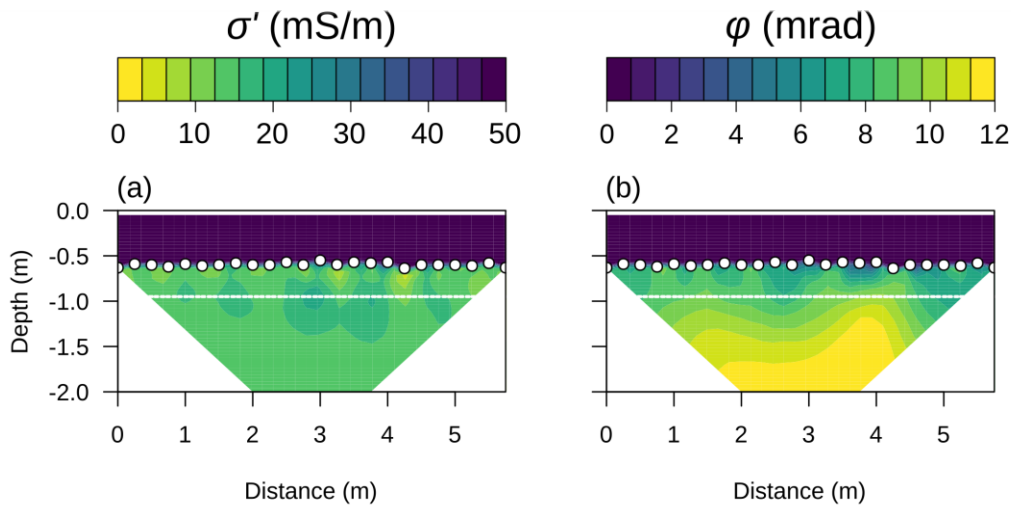
Figure 6.12: Effect of micro-topography on conductivity (a), and phase angle (b).

6.5 Discussion and Conclusions

The laboratory measurements indicate the potential of IP to characterize important properties of riverbed sediments. The SA for the RS samples were generally higher than the < 4 mm samples, and although there was significant overlap in values, the σ'' values coincided with the SA values (Fig. 6.5). Furthermore, the link between S_{por} and polarization follows published relationships for sands and sandstones (Weller et al., 2010), suggesting that IP may be used as a proxy for assessing

variation in S_{por}, and therefore has implications for characterizing reactive solute transport properties. It is worth noting, however, that although the empirical relationships work well at low frequencies, at higher frequencies contrasts were more distinct and therefore ought to be easier to resolve in the field, therefore the frequency for IP to be used is an important consideration, especially given the recent developments in field equipment for high frequency characterisation.

It was demonstrated that fixing river properties has both favourable and unfavourable outcomes. For instance, it is essential to prevent regularization across the river-riverbed interface, and fixing of the river conductivity enables accurate characterization of the riverbed properties, however, erroneous fixing led to significant artefacts that could lead to misinterpretation. Although it is possible that preventing regularization across the riverbed, but not fixing river conductivity, may work in areas with more significant contrasts in electrical properties, accurate characterization requires accurate knowledge of the river properties. This is a consequence of the contrasting sensitivities of the measurements to the river and riverbed, resulting in the inversion algorithm being less influenced by modification of riverbed electrical properties.

The formation of the artefacts seen in Fig. 6.9 is especially problematic in aquatic systems as the very nature of SW bodies and their underlying beds is that they comprise a horizontal conductor overlying a resistor. By fixing incorrect values of this upper conductive layer, significant horizontal artefacts are produced and can manifest themselves as a stratified inverse model, which could easily be interpreted, incorrectly, as sedimentary units. Furthermore, whilst it is possible to dampen these artefacts by increasing the error allowance in the inversion, this effect will merely be subdued and will still result in inaccurate determination of the riverbed electrical properties. These findings are in agreement with Orlando (2013), who stated that when the river is more conductive than the riverbed, artefacts can be created in the riverbed.

Collection of high quality data clearly improves the resolution of inverted images. However, the effect of noise on inverted models appears to be particularly detrimental in comparison to terrestrial

surveys due to the conductive river. For static surveys, error characterization is achievable using reciprocity checks. However, for towed ('streamer') surveys, assessment of data quality is more challenging and failure to do so may have consequences on the interpretation and reliability of inverted models. Furthermore, whilst the notion of using towed arrays to characterize extensive river reaches is an attractive one, it invokes many logistical complications, e.g. the need to characterize bathymetry beneath the array and off axis. Studies involving inversion of aquatic ER and IP data should be aware of the issues considered in this work, especially the tendency of artefacts to appear as horizontal anomalies which may easily be interpreted as sedimentary units.

It is important to note that use of geoelectrical methods to characterize riverbed sediments is not limited to standard 2D/3D inversion of geoelectrical data. For instance, Wang et al. (2020) use a complex conductivity analytical solution for a single quadrupole. Essentially this separates the contribution of the river and provides a measure of the apparent complex resistivity of the shallow riverbed. They successfully used this method to map complex conductivity at the same effective depth (i.e. consistent electrode separation) and locate areas of iron oxide precipitation. Nonetheless, if standard 2D/3D inversions are to be used, i.e. to quantitatively assess vertical variability in riverbeds, is clear that inversion needs to be approached carefully and validated with forward modelling to ensure coherence of petrophysical interpretation. Moreover, future work should also be concerned with using more elaborate survey designs or electrodes to obtain higher quality data and more accurate determination of riverbed electrical properties.

7 Electrical Resistivity Monitoring of River-Groundwater Interactions in a Chalk River and Neighbouring Riparian Wetland

7.1 Introduction

Rivers are often conceptualized as having gaining and losing sections, i.e. zones where the groundwater (GW) discharges into rivers and zones where the rivers recharge the GW. Moreover, in previous decades there has been significant interest in the biogeochemical cycling when GW and surface water (SW) mix in the subsurface (e.g. Hill et al., 1996; Prior et al., 2005; Johnes et al., 2020). GW-SW mixing regulates subsurface temperature and creates unique biogeochemical conditions. The coupled presence of mineral surfaces and microbes is such that biogeochemical cycling in the hyporheic and riparian zones can actively regulate the transfer of nutrients and pollutants, and consequently mitigate ecological degradation throughout the catchment (Kuusemets et al., 2001; Shabaga and Hill, 2010).

However, the importance of biogeochemical transformation may be misrepresented in catchment management literature due to the complex nature and variability of processes occurring in different settings. For instance, the efficiency of biogeochemical cycling is controlled by the sources and timing of water mixing, the substrate and organic matter content, and the microbial communities present, all of which can be drastically different between sites, even within the same catchment (Frei and Peiffer, 2016; Bernard-Jannin et al., 2017). Characterizing these parameters is not trivial and limited intrusive sampling may make it difficult to unravel complex interactions. It is clear that there is a need for methods to reveal properties and processes related to GW-SW interactions with high spatial and temporal resolution.

In recent years, there has been increasing application of geophysics to characterize GW-SW interactions (McLachlan et al., 2017). For example, electrical resistivity measurements obtained from electrical resistivity imaging (ERI) or electromagnetic induction methods have been used to

characterize riverbed structure (e.g. Crook et al., 2008) and to reveal zones of GW up-welling (e.g. Binley et al., 2013). Time-lapse ERI is particularly useful for monitoring GW-SW interactions because changes in resistivity can be interpreted in terms of changing saturation or changing pore-water conductivity. For example, time-lapse ERI has been used with saline tracers to monitor GW-SW interactions over several hours in the hyporheic zone (e.g. Ward et al. 2010; Toran et al., 2012). In addition, time-lapse ERI has also used natural electrical contrasts (e.g. from solute content or temperature) of water to monitor long term GW-SW interactions (e.g. Johnson et al., 2012, Wallin et al., 2013; Steelman et al., 2017).

In this work an ERI array was installed to characterize the timing and location of GW-SW interactions occurring beneath the River Lambourn and the adjacent riparian zone at the Boxford Wetland, West Berkshire, UK. The field site was investigated previously by Uhlemann et al. (2016) who revealed complex hydrological patterns involving a peat with two-layer behavior and the underlying gravel. Here, ERI data were collected diurnally over a one-year period to monitor electrical resistivity in both the riverbed and riparian zone and determine their relation to the changing stage and GW levels.

7.2 Methodology

7.2.1 Field Site

The River Lambourn, and its associated wetlands, is one of the least impacted Chalk river systems in the UK and it has been the subject of a number of publications to understand GW-SW interactions (e.g. Allen et al., 2010; Johnes et al., 2020). Furthermore, the Boxford Wetland, Fig. 7.1, is a Site of Special Scientific Interest (Natural England) and a Special Area of Conservation (EU Habitats Directive) owing to the habitat it provides for fauna and flora; particularly Desmoulin's whorl snail (*Vertigo moulinsiana*) and river-water crowfoot (*Ranunculetum fluitans*), which exhibits prolific growth during the spring-summer months. As part of the river management, this aquatic vegetation is cut during the year, primarily to maintain fish habitats for angling, and has been shown to significantly influence the river stage and GW levels (Old et al., 2014).
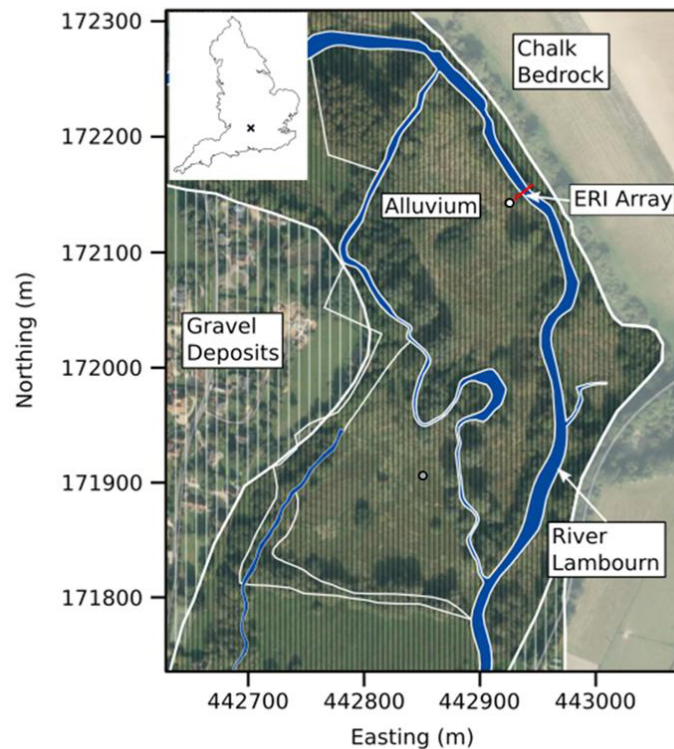
Figure 7.1: Spatial extent of geology at the field site and the location of the ERI monitoring array in relation to the Boxford Wetland. Locations of gravel and chalk piezometers are shown in white and grey, respectively.

Near the field site, the River Lambourn has a base flow index of 0.96 (Marsh and Hannaford, 2008); the river stage is therefore predominantly controlled by GW. The River Lambourn catchment, and wider Berkshire Downs area, is underlain by extensive, broadly horizontal, Upper Cretaceous Chalk up to 250 m thick in some areas. At Boxford, the Seaford Chalk Formation is characterized by variable degrees of weathering such that there is a well-developed, largely impermeable, putty layer in its upper sections. The presence of this putty layer is thought to govern the hydrology of the site; e.g. regions where this layer is poorly developed form zones of preferential groundwater discharge (Younger et al., 1989).

The extent of the putty chalk was investigated by Chambers et al. (2014) using 3D ERI, and locations of GW up-welling within the wetland were revealed by House et al. (2015) via a temperature survey. At the site, the chalk is overlain by Quaternary alluvial gravel and peat in the order of 3-7 m thick. The gravel exhibit braided structures, and the basal gravel are characterized by high proportions of reworked chalk, whereas the peat is interpreted to have accumulated during

141

a series of wet and dry periods, as evidenced by the predominance of organic matter sourced from terrestrial and aquatic plants (Newell et al., 2015; 2016).

From temporal resistivity patterns, Uhlemann et al. (2016) observed that the peat comprised two hydrologically distinct layers; in addition it was revealed with intrusive sampling that these layers were separated by a thin clay layer. Additionally, Musgrave and Binley (2011) used time-lapse ERI over a 12-month period in an adjacent wetland on the east side of the Lambourn, finding that seasonal temperature variation dominated the resistivity signal; they interpreted areas of low temporal variability to be sites where stable GW temperatures subdued seasonal temperature variations.

7.3 Site Selection

Prior to installation of the ERI array, a site of GW up-welling was identified from a riverbed temperature survey. A temperature probe was built by housing a thermocouple in a 1 cm diameter steel pipe, 2 mm holes were drilled in the vicinity of the thermocouple and the end of the pipe was flattened and sharpened to enhance riverbed penetration. The probe was driven into the upper 5-10 cm of the riverbed during winter (08-Jan-17); throughout the survey the river water temperature was 7°C and the GW was 10.5°C within the chalk piezometer (Fig. 7.1). Riverbed temperatures ranged from 7°C to 10.5°C, and locations with temperatures close to the temperature of chalk GW were interpreted to be areas of up-welling. The ERI array was installed to coincide with a zone of elevated riverbed temperature (Fig. 7.2), i.e. a zone of perceived GW-SW connectivity.
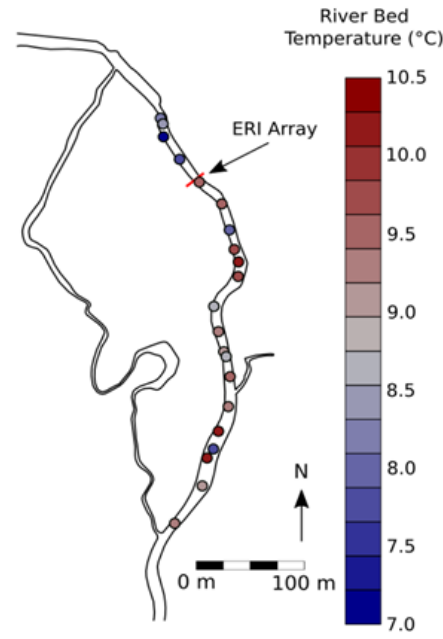
Figure 7.2: Riverbed temperature survey indicating areas of GW up-welling in relation to the ERI array.

7.3.1 ERI Acquisition

ERI data were collected using a PRIME ERI monitoring system (Huntley et al., 2019). The electrode array comprised thirty-two point electrodes each ~0.55 m apart; a larger spacing was used at either riverbank to prevent electrodes being periodically exposed to the air during low river stage (Fig. 7.3). Two electrodes were positioned in the east bank, eighteen on the riverbed, and twelve in the west bank; concrete slabs were used to prevent movement of the cable throughout the survey period. A dipole-dipole measurement sequence was selected as they provide good vertical and horizontal resolution (Chambers et al., 2002). A sequence with dipole lengths (a) of 1 to 5 and dipole separations (n) of 1a to 6a was used, resulting in a total of 438 measurements along with a full set of reciprocal measurements.

ERI data were collect diurnally from 16-Nov-17 to 30-Nov-18, at both 03:30 and 15:30 GMT. Two river loggers were housed in separate PVC pipes and installed in the river to monitor stage, temperature, and electrical conductivity; a series of temperature loggers were installed to correct the ERI inversions for seasonal temperature variations (Fig. 7.3). Additionally, the GW levels in the chalk and gravel piezometers (see Fig. 7.1) were monitored with pressure loggers, chalk level was

monitored from 11-Jan-18 and gravel level was logged from the start of the ERI monitoring period, with a logger error leaving a period from 08-Feb-18 to 27-Jun-18 absent from the record.
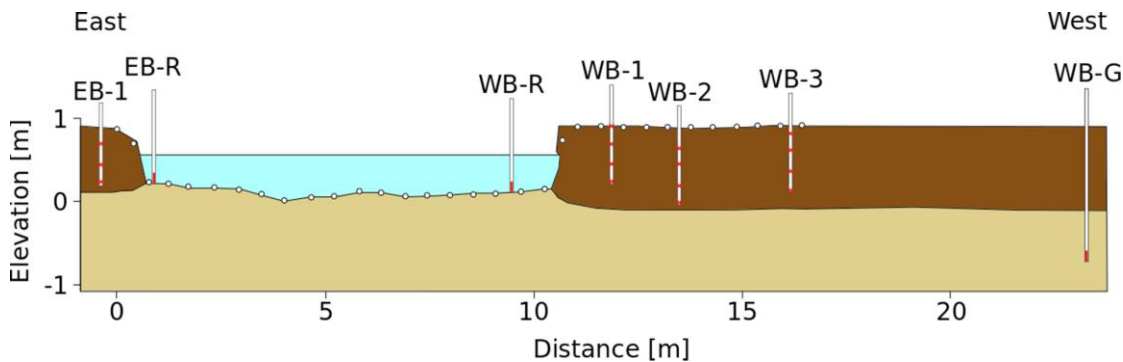
Figure 7.3: Positions of electrodes and data loggers, looking downstream. One set of temperature loggers was installed on the East bank (EB-1) and three were installed in the West bank (WB-1, 2, and 3). EB-R and WB-R were used to log the river level, temperature and electrical conductivity. WB-G was used to monitor the temperature of the gravel. Logger sets WB-1, 2, and 3 and EB-1 were installed < 0.5 m either site of the ERI transect, EB-R and WB-R were installed ~4 m downstream and ~1 m upstream, respectively.

7.3.2 Data Quality

Prior to inversion, data quality and general patterns within the ERI data were assessed. Reciprocal errors were calculated for each quadrupole from the difference between direct and reciprocal measurements; a mean resistance was also calculated to express reciprocal errors as a percentage. Apparent resistivity values were calculated for each of the measured resistances assuming a flat topography and an electrode spacing of 0.55 m to explore the pattern of data throughout the monitoring period. It is important to note that although this is invalid for modeling data, it is useful for obtaining information about the general resistivity patterns.

Data quality was good with most measurements having a reciprocal error < 0.5%. Measurements with reciprocal errors exceeding 10% or apparent resistivities greater than 400 ohm.m were discarded. To ensure that data sets had similar sensitivity patterns, data sets with fewer than 416 (95%) sets of direct and reciprocated measurements were discarded. This resulted in a total of 80 data sets out of 739 being discarded; this included a period of 25 days (between 02-Sep-18 and 26-

Sep-18) where high contact resistances of electrodes in the riparian zone gave data with high reciprocal errors.

7.4 ERI Inversion

7.4.1 Time-Lapse ERI Inversion

A number of inversion methods can be used for time-lapse ERI data; such as standard independent inversion of data collected at different times (e.g. Steelman et al., 2017). However, more elaborate methods have included inversions where data are constrained to a previous model. This can be done by inverting data with some penalty term for diverging from a prior model (e.g. Oldenborger et al., 2007), or difference inversions whereby the difference between two data sets is used to model deviations from a model obtained from one of those data sets (LaBrecque and Yang, 2001). For difference inversions, systematic noise, e.g. arising from poorly surveyed electrode positions, poor galvanic contact, and numerical measurement errors can be removed. This has the benefit of modeling data in cases where systematic errors dominate. However, as investigated by Lesparre et al. (2017), reciprocal errors contain information about both random and systematic errors and are therefore inappropriate for error characterization in difference inversion.

When large data sets are concerned, sequential inversions may be time-consuming; alternatively, data sets may be inverted simultaneously using some temporal regularization to link data sets (e.g. Johnson et al, 2012; Wallin et al., 2013). In this way data may be treated in parallel, which can be efficient for data sets collected over long periods or with high temporal resolution. Although these methods require a consistent mesh for each inversion, Wallin et al. (2013) demonstrated how inclusion of a zone of fine mesh elements could be used to prevent regularization across the water table and improve interpretation of dynamic GW-SW patterns.

7.4.2 Aquatic ERI Inversion

It is important to note that additional complications arise in aquatic ERI applications, in comparison to terrestrial applications, due to the abrupt transition between a conductive river and a more resistive riverbed. For example, McLachlan (2020) demonstrated by synthetic modeling that fixing the river resistivity in the inversion significantly improves riverbed characterization. However, the increased sensitivity of measurements to the river, in comparison to the riverbed, is such that erroneous fixing of river resistivity can lead to significant artifacts within the riverbed region of the inverted model. This issue becomes more problematic in time-lapse surveys, given

that erroneous fixing of river regions in models for sequential data sets could produce significant artificial changes through time, especially if river parameters (i.e. stage and conductivity) change.

Due to these complexities, in this work a new mesh was generated for each data set to account for the change in river stage, and inversions were conducted independently. Although it could be argued that an approach similar to Wallin et al. (2013) with consistent mesh and dynamic water table should be used, this would require incorporation of a layer with infinite resistivity to represent the air. Alternatively, an approach involving interpolation of prior inversions onto a new mesh for difference inversion could have been used, however, it was anticipated that, if present, resistivity changes related to GW-SW interactions would be revealed in independent inversions also. Finite element meshes were generated using Gmsh (Geuzaine and Remacle, 2009). Although the meshes for each data set were inherently different, they were generated using the same characteristic lengths to obtain similar finite element sizes and thus minimize substantial differences in forward modeling errors.

7.4.3 Error Modelling and Inversion

As noted, in this work reciprocal measurements were obtained to characterize errors. Reciprocal errors are sensitive to both systematic random components, e.g. arising from fluctuating contact between electrodes and soil, and the resultant modification of current pathways (Binley et al., 1995). In this work an error model is used to assign measurement error to ensure appropriate data weighting during the inversion. Reciprocal error (ε_{rec}) is proportional to the measured resistance (R) and is often expressed by the following relationship:

$$\varepsilon_{rec} = aR + b ,$$
(7.1)

where, a and b are fitting parameters. An envelope fit error model was used to encompass the majority of data (e.g. Slater et al., 2000). Log transformed mean resistances were sorted into bins of equal width and a linear model was fitted between the log of the sum of mean reciprocal error and twice the standard deviation of the reciprocal error, and the mean resistance. This meant that the error model encompassed 97% of the data.

7.4.4 ERI Inversion

Data were inverted using R2 (Binley, 2019), a robust and mature inversion algorithm. Through reduced local regularization, R2 permits blocking regularization across specified regions, e.g. the river-riverbed interface.

To begin with, each data set was inverted independently, with the reciprocal error model and a river resistivity fixed to the logged value. Several tests were also carried out whereby regularization between the river and riverbed was blocked but the inversion was able to modify the river resistivity. However, from experience, this led to unreliable results in that the river was modeled as having large ranges in resistivity, especially at the riverbanks. In addition, for reasons discussed below, data obtained from the riparian zone electrodes were inverted separately. Furthermore, to ensure smooth changes in modeled resistivity data were constrained to the prior inversion in R2 and inversions were conducted sequentially.

7.4.5 Temperature Correction

Given the influence of temperature on resistivity, inverted models were corrected for seasonal temperature variations. Using the procedure outlined by Chambers et al. (2014), temperature data collected from different depths within the peat and gravel were fitted to the following:

$$T_{z,t} = T_{air} + A e^{-\left(\frac{z}{d}\right)} sin\left(\omega t + \varphi - \frac{z}{d}\right), \tag{7.2}$$

where, $T_{z,t}$ is the average temperature of day t at depth z, T_{air} is the mean annual temperature of the air, A is the yearly amplitude of the air temperature variation, d is the depth by which the amplitude of the temperature variation reduced by 1/e, φ is a phase offset, and ω is the angular frequency. In this case, the obtained penetration depth for the monitoring period was 1.375 m.

Resistivity models were then corrected using the ratio model (Hayashi, 2004; Ma et al., 2010):

$$\rho_{corrected} = \rho_{model}\left[1 + \frac{c}{100}\left(T_{target}\right) - T_{model}\right], \tag{7.3}$$

where, $\rho_{corrected}$ and ρ_{model} are the corrected resistivity and the resistivity obtained from the inverse model, respectively, c is a correction factor, and T_{target} and T_{model}, is the target temperature and modeled temperature. Each inverse model was corrected to the mean annual temperature, 10.09 °C, and the c value used here, -2.95 °C^{-1}, was determined experimentally by Uhlemann et al. (2016) for the Boxford field site. The good fit for both the peat and gravel temperatures indicated that thermal diffusivities were similar. It is important to note that the corrections applied here are for laterally

averaged seasonal changes in temperature and are not correcting for diurnal temperature variations. For instance, the highest diurnal variations were observed in Mar-18 where diurnal variations of 4° C were observed at 0.5 m below the surface and diurnal variations of < 1 °C were observed at 1 m below the surface.

7.4.6 Time-Series Analysis

To aid with interpretation of the ERI models in the riparian zone, cross correlation metrics were used to assess the relationship between the changes in resistivity of each inversion element and the river stage. Summary statistics such as maximum absolute correlation and time lag to maximum absolute correlation offer a robust method for determining areas of the subsurface that exhibit similar behavior. Such analysis was employed by Johnson et al. (2012) and Wallin et al., (2013) to assess the infiltration of water due to the changing river stage of the River Columbia at the Hanford Nuclear Site, Washington, US.

It was anticipated that increasing river stage would result in an increase in the water content of the peat in the riparian zone, i.e. either from lateral infiltration from the river or vertical up-welling of GW, given the hydraulic connection between the river and GW. Consequently, a negative correlation between river stage and electrical resistivity was anticipated. However, it is also important to note that if conductive waters are replaced by more resistive waters, a positive correlation could be expected. In addition to obtaining maximum correlations, which give an indication of the connection of the subsurface to the changing river stage, the lag time to maximum correlation is related to pore water velocities. For example, areas with a short lag time could be used to indicate areas of higher pore water velocity and preferential flow.

Given that there is a gap in ERI coverage between 02-Sep-18 and 26-Sep-18, and that correlation analysis requires equally spaced data, only data from 16-Nov-17 to 02-Sep-18 were considered. Other gaps in the monitoring (< 3 days) were accounted for via linear interpolation from neighboring inverse models. The cross-correlation between river stage and bulk resistivity of each element was calculated using the Pearson correlation for different time lags, e.g.:

$$corr(t) = \frac{1}{N_k} \sum_{k=0}^{N_t-1} \left(\frac{\rho_{t+k} - \bar{\rho}}{\sigma_\rho} \right) \left(\frac{S_t - \bar{S}}{\sigma_S} \right), \qquad (7.4)$$

where, N_t is the number of stage and resistivity values in the time sequence, $N_k = N_{t-1}$, ρ_k is the bulk resistivity at time k, $\bar{\rho}$ is the mean resistivity of the time sequence, σ_R is the standard deviation

of the resistivity time sequence, $S_k, \bar{S}$ and σ_S are the corresponding river stage time-series, mean, and standard deviation.

7.5 Results

7.5.1 General ERI Data Patterns

Over the monitoring period, the river stage ranged from 90.7 to 91.1 m above sea level and rose steadily from mid-Dec-18 due to increasing water level in the chalk and growth of river water crowfoot, see Fig. 7.4a. The abrupt drop in stage on 20-Jun-18 coincides with removal of the river vegetation, furthermore this drop was also observed in the chalk water level (Fig. 7.4b). The specific conductivity of the river water (~55 mS/m) was stable throughout the year and matches the specific conductivity of the chalk GW. As a result, the electrical conductivity variation is predominantly dependent on river temperature variation, Fig. 7.4.

The mean apparent resistivity coincides with the river stage and drops abruptly following the aquatic vegetation cutting (Fig. 7.4d). Curiously, the aquatic vegetation cutting event results in different patterns of the maximum and minimum resistivities (Fig. 7.4c): the maximum resistivity coincides with abrupt increases following the cutting, whereas the minimum resistivity shows an abrupt reduction. The increase in maximum resistivity could be attributed to an increase in the resistivity of the largest quadrupole spacing given that the sensitivity patterns will be shifted significantly; the fall in minimum resistivity could be attributed to the bulk increase in the conductivity of the river, e.g. without the presence of plants or the increased sediment load following weed cutting (Old et al., 2014). Moreover, it can be seen that the mean reciprocal error also increased during the time immediately following the weed cutting; this was due to the increase in contact resistances of the riparian zone electrodes immediately following weed cutting, perhaps due to a reduction of moisture content in the uppermost riparian zone.
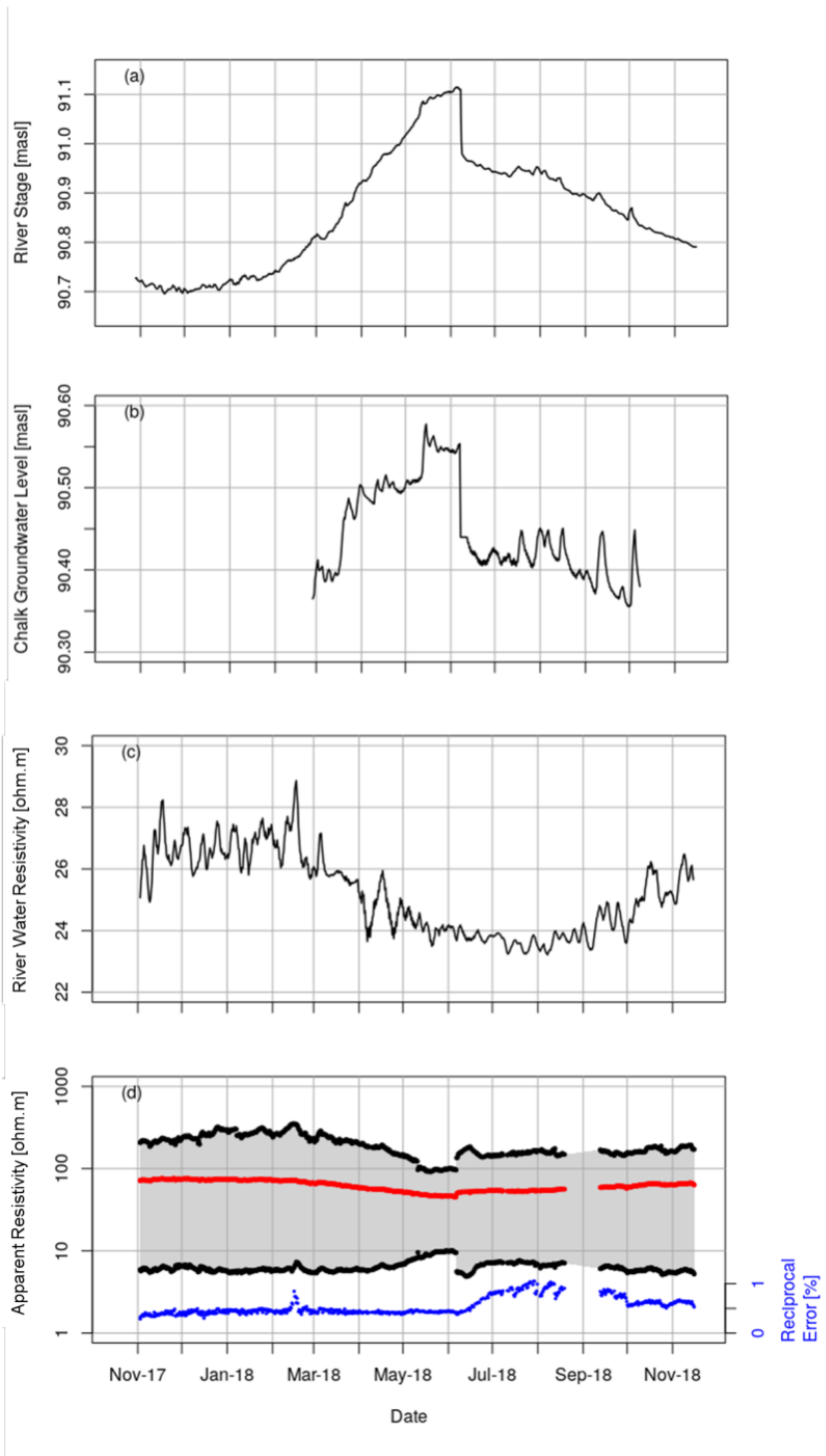
Figure 7.4: Seasonal patterns of river properties and ERI measurements: (a) river stage and (b) chalk GW level relative to sea level, (c) resistivity of river water, (c) mean (red line), maximum and minimum apparent resistivity of each data set, and reciprocal error as a percentage.

7.5.2 Background Resistivity

The resistivity model for the background data set (from 16-Nov-17) is displayed in Fig. 7.5. A clear two-layer structure can be observed in the resistivity model, which coincides well with the intrusively derived depths to the peat-gravel interface (white dashed line). The bulk resistivity of the peat layer is in the order of 15-40 ohm.m, which is in agreement with previous ERI studies conducted at the field site (e.g. Chambers et al., 2014; Uhlemann et al., 2016). Similarly, resistivities of 70-200 ohm.m for the gravels beneath the riparian zone and in the majority of the riverbed also agree with Chambers et al. (2014) and Uhlemann et al. (2016). However, immediately beneath the river, modeled resistivities were seen to exceed 1000 ohm.m, e.g. beneath electrode 5 and between electrodes 19 and 20. These extreme values are similar to those investigated by McLachlan (2020), and are likely to have arisen from a combination of reduced sensitivity in the upper portion of the riverbed and complications in fixing of river parameters in the inversion.
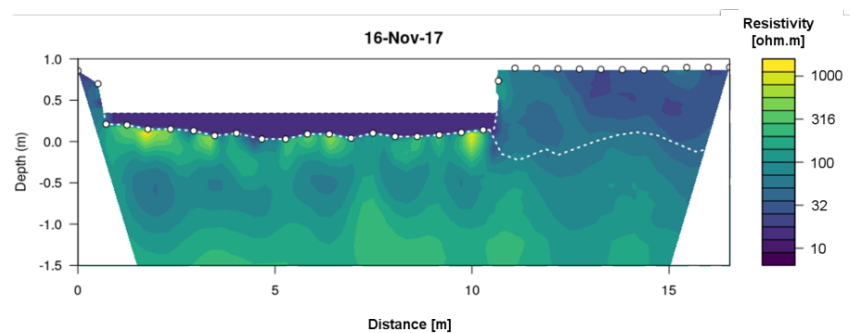
Figure 7.5: Background resistivity model collected on 16-Nov-17.

7.5.3 Temporal Resistivity Patterns

The extreme resistivity values beneath the riverbed are particularly noticeable when comparing data collected at two different times. For instance, comparing the background data set (16-Nov-17) and the data set collected the day prior to river vegetation cutting (19-Jun-18), changes exceeding ± 150% can be observed in the riverbed (Fig. 7.6b). Given the comparable specific conductivities of the GW and the river water, and the fact that changes due to temperature could only account for ~3% change in resistivity per °C, these patterns are likely to be artificial. As subtle changes in the riverbed resistivity dynamics are likely to be obscured by these inversion artefacts, the focus of the remainder of the paper will be characterizing the riparian zone dynamics.
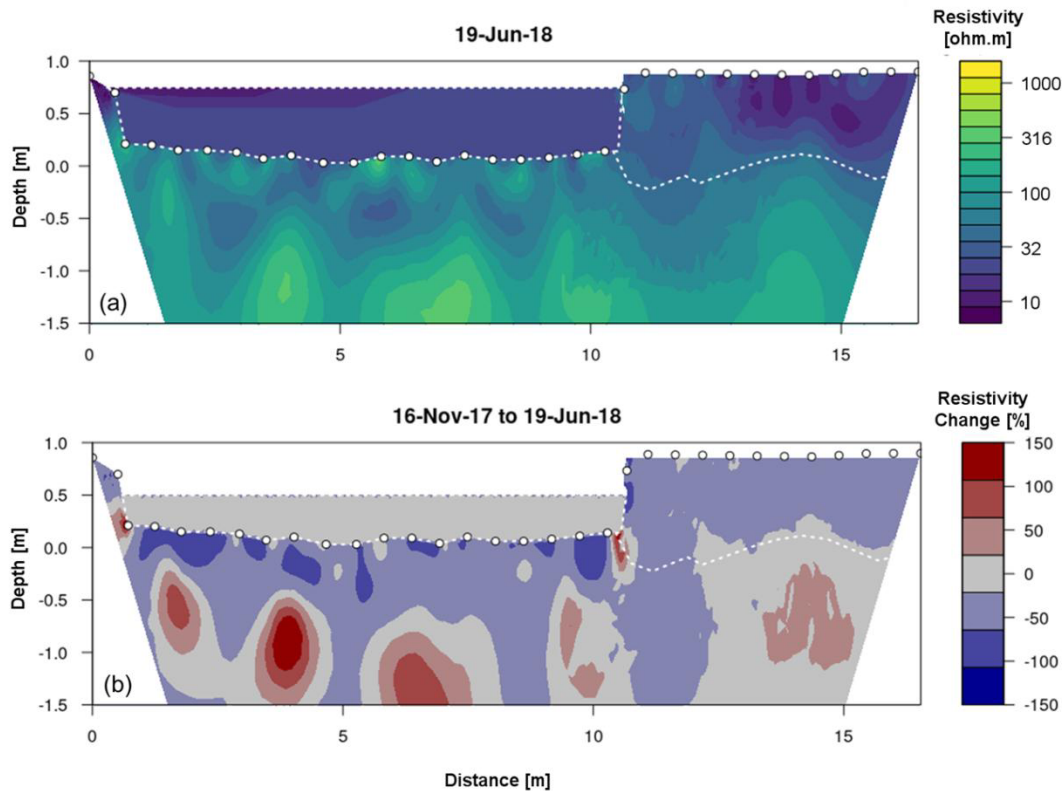
Figure 7.6: (a) Resistivity model obtained on 19-Jun-18 during the maximum stage. (b) Change in resistivity between 16-Nov-17 and 19-Jun-18.

7.5.4 Time-Series Analysis

Time-series analysis of the river stage and bulk resistivity for each mesh element of the riparian zone data was used to identify areas that exhibited similar behaviors. Plots of maximum absolute correlation with river stage and time to maximum absolute correlation with river stage are presented in Fig. 7.7, and several time-series from zones of interest are presented in Fig. 7.8.

The mean resistivity and coefficient of variation for the resistivity for each mesh element during the monitoring period were also calculated. The coefficient of variation gives an indication of the magnitude of changes and therefore an indication of the validity of the time-series metrics. The mean resistivity (Fig. 7.7a) of the entire monitoring period shows the same pattern as Fig. 7.5, i.e. a more conductive peat overlying a more resistive gravel layer. The highest variation in resistivity can be found in the upper portion of the peat; however, the gravel resistivity also demonstrates some variability (Fig. 7.7b). It is also important to note that although correlation analysis was done

152

using river stage data, it can be seen from Fig. 7.4a and b that the chalk water level and river stage are coincident with one another; river stage was used due its longer period of coverage.
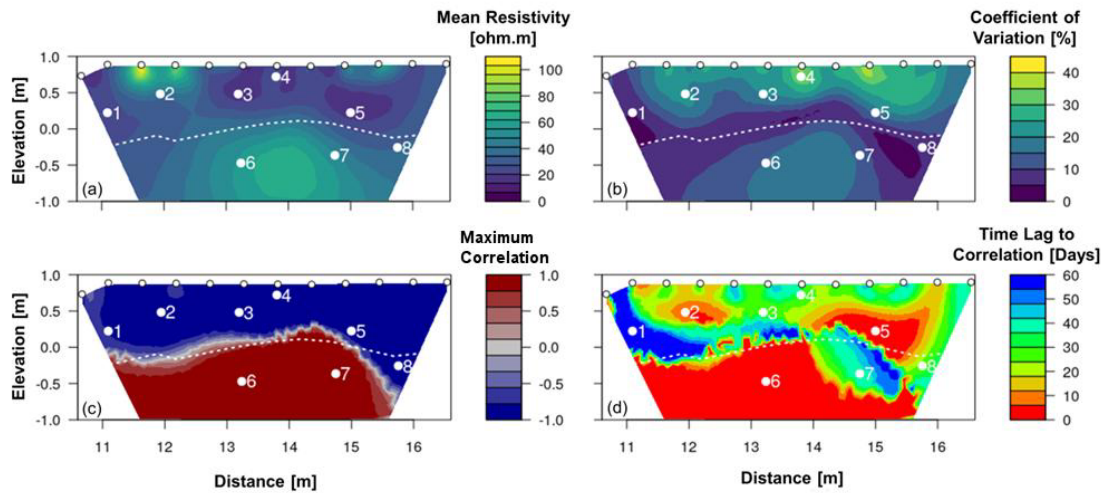
Figure 7.7: (a) mean resistivity, (b) coefficient of variation of resistivity, (c) maximum absolute correlation with river stage, and (d) lag time for maximum absolute correlation with river stage. The eight marked positions in each image are used for analysis in Fig. 7.8.

It is immediately apparent that the peat resistivity changes are negatively correlated with the changing river stage whereas the resistivity of the gravels are positively correlated (Fig. 7.7c). The lag to maximum absolute correlation also provides useful information about the behavior of the subsurface. In the gravels, the most common lag to maximum correlation was 0 days (Fig. 7.7d), indicating that the behavior of the gravel resistivity and river stage coincide well. However, a zone where lag time to maximum correlation is in the order of 30-40 days can be seen at the horizontal position of ~13.8 m. In comparison, the peat lag times are more disparate (0 to 60 days), with two prominent zones characterized by short lag times (< 5 days).

Given the anticipated high permeability of gravel and the zone characterized by lag times of 30-40 days it is important to explore what these metrics show in terms of the resistivity and stage time-series. To understand the patterns observed in Fig. 7.7, the normalized time-series of several inversion elements are displayed in Fig. 7.8. For instance, element 1 (Fig. 7.8a) exhibits a negative correlation (-0.785) and a large lag time to maximum absolute correlation (60 days); it is evident in comparing the time-series that the river stage does not coincide with the pattern of the resistivity well. In comparison, element 2 (Fig. 7.8b) is characterized by a negative correlation and a lag time to minimum correlation of 6.5 days. Complementary patterns are clearly evident, however, it is evident that the resistivity time-series is not simply shifted and the maximum stage and minimum

resistivity occur at similar times (Fig. 7.8b). Similarly, complementary bulk resistivity patterns are also evident for elements 3, and 4, but the time lag to maximum absolute correlation is substantially longer than the lag between the maximum stage and the minimum resistivity (Fig. 7.8c and 8d). Furthermore, although the stage drop following the river vegetation cutting coincides with an increasing resistivity in element 4, the change resistivity pattern during Nov-17 to Mar-18 behaves differently from the stage, indicating an additional control (Fig. 7.8d).
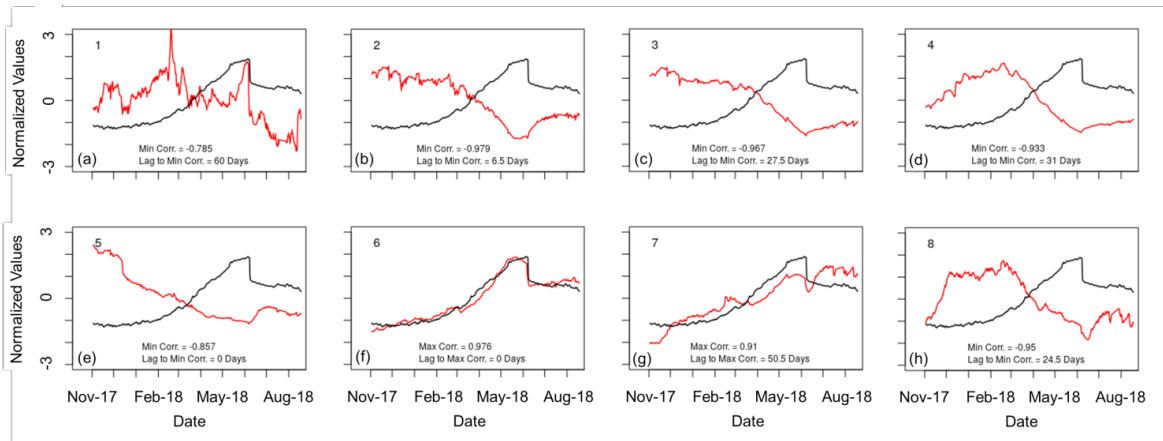
Figure 7.8: Normalized time-series of selected elements displayed in Fig. 7.7. Values are normalized by subtracting the mean value of the corresponding time-series and dividing by the standard deviation of the corresponding time-series, i.e. as is done in equation 4. Red lines are normalized resistivity and black lines are normalised stage.

Element 6 is characterized by a positive correlation (0.976) and lag of 0 days, and clearly follows the same pattern as the river stage (Fig. 7.8f). In comparison, element 7 is characterized by a similar positive correlation (0.935), but a longer lag to maximum correlation duration (Fig. 7.8g). On inspection of Fig. 7.8g it can be seen that following an initial drop in resistivity immediately after the vegetation cutting the resistivity increases above the pre-cutting value. This, again, gives evidence of additional controls on resistivity occurring in the riparian zone, other than the changing river stage. Lastly, although element 8 is located in the gravel according to intrusive measurements, it clearly behaves similarly to the peat. This could be because intrusive measurements were not made directly on the ERI line, due to presence of tree roots, or due to some additional 3D features.

7.6 Riparian Zone Dynamics

7.6.1 Resistivity Patterns in the Riparian Zone

Based on the cross correlation metrics discussed above, the subsurface was split into seven zones. Moreover, rather than using the intrusively derived depths, the peat was defined as any region of the subsurface that displayed a negative correlation with the river stage, and the gravel was defined as regions with a positive correlation with river stage. The thresholds used to discriminate between different zones are displayed in Table 7.1 and the respective zones are shown in Fig 7.9a. The geometric mean resistivity for each zone throughout the monitoring period was then calculated and is shown in Fig 7.9b.

Table 7.1: Summary of the different zones of the riparian zone as defined by cross-correlation metrics and coefficients of variation.

Zone Name	Maximum Abs. Correlation to River Stage	Time-Lag to Maximum Abs. Correlation to River Stage [Days]	Coefficient of Variation [%]	Horizontal Location [m]
P1	< -0.7	> 15 and < 50	> 20	-
P2	< -0.7	> 15 and < 50	< 20	-
P3	< -0.7	< 15	-	< 13.5
P4	< 0	< 15	-	> 13.5
P5	< 0 and > -0.5	> 50	-	-
G1	> 0.7	< 15	-	-
G2	> 0.7	> 15	-	-

From Fig 7.9b, it can be seen that the P1 resistivity gradually increased to its maximum resistivity from Nov-17 to Feb-18, following this, resistivity began to decrease. The resistivity of P1 responds to the vegetation cutting by exhibiting a sharp increase, and then from Jun-18 to Nov-18 it increases steadily with some rapid drops followed by gradual increases, which coincide with rainfall events, e.g. on the 14-Oct-18 and 10-Nov-18. In comparison, the resistivity of P2 increases slightly from Nov-17 through to Feb-17 where it begins to decrease to a minimum around the time of the vegetation cutting. The resistivity of P2 is also perturbed by the vegetation cutting, but is characterized by small drop in resistivity, immediately after the cutting. Following from this the resistivity increases, similarly to P2 and it also experiences sudden drops in resistivity on 14-Oct-18 and 10-Nov-18, albeit the signal is more subdued. Interestingly, the resistivity of P3 begins to increase in a period just before the vegetation cutting and immediately following the cutting it

decreases in resistivity. The bulk resistivity time-series for P4 is the most variable, however, the time-series becomes more stable as resistivity falls, probably due to increasing saturation; it generally follows the same patterns as the resistivity of P1. P5 shows a much less variable resistivity pattern; however, it is still affected by the vegetation cutting and shows a slight, and gradual, increase. In addition, P1, P2, P3 and P4 all show a sharp increase on 01-Mar-18, this does not appear to coincide with precipitation however it does precede a sudden increase in river stage and could be related to changing GW levels.
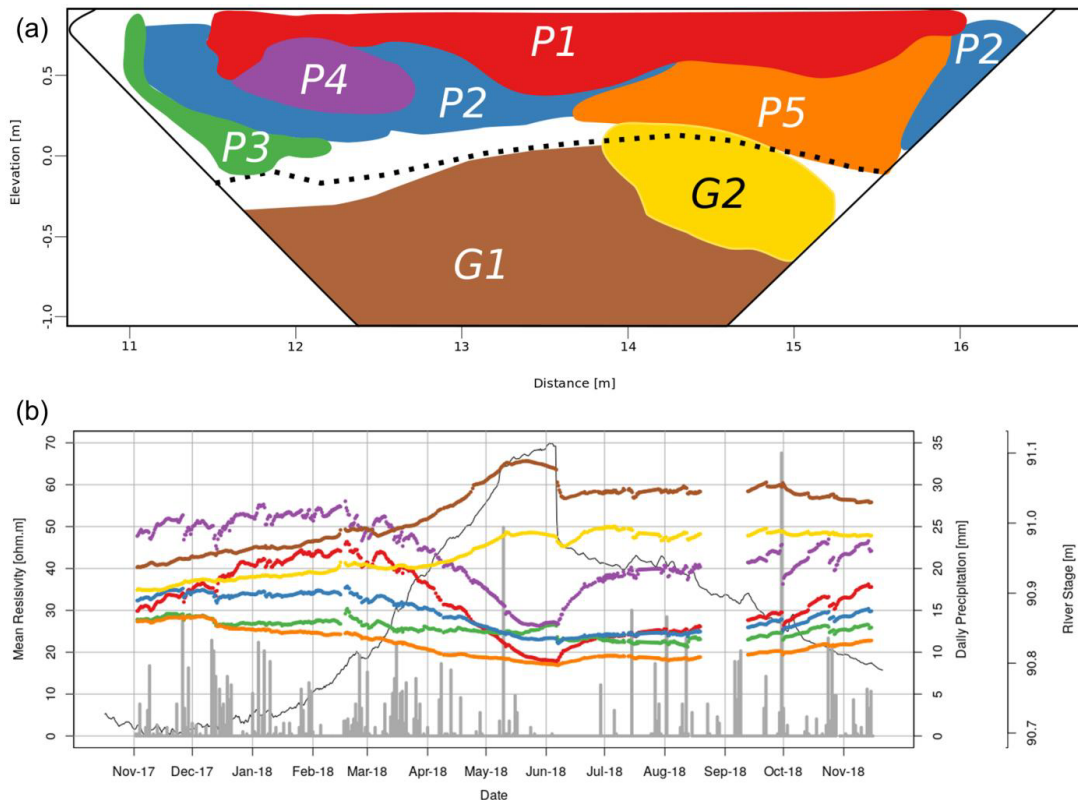
Figure 7.9: (a) Zonation of the riparian zone based on time-series summary statistics, (b) the geometric mean of resistivity dynamics of the zones and daily precipitation data from Deanwood golf course (5 km SE of field site).

The resistivity of G1 follows very closely the pattern of the rising stage and is characterized by a drop in resistivity immediately following the vegetation cutting, similarly to P3. From Jun-18 onward the resistivity of zone remains relatively stable, with a few perturbations around early to mid Oct-18. Similar resistivity patterns are seen in G2; however, the resistivity is both lower and does not vary as much. In addition, immediately following the vegetation cutting the resistivity of

the gravel layer increases to a value above the pre-vegetation-cutting level and following on from this the resistivity patterns broadly match those in G1.

7.6.2 Interpretation of Riparian Zone Hydrological Processes

P1 and P2 are comparable to the upper and lower peat zones identified by Uhlemann et al. (2016), with the upper peat zone being ~0.5 m thick. Although Uhlemann et al. (2016) observed a reduction in the resistivity of the upper peat layer in comparing resistivity models from Dec-12 and Apr-13, during the equivalent period in this work the P1 showed an increasing resistivity during Jan-18 and Feb-18 before returning to resistivity values similar to Dec-17 during Apr-18. Uhlemann et al. (2016) attributed the reducing resistivity of the upper peat layer during this time to an increase in pore-water conductivity as a result of increased activity of vegetation and microbes following the onset of increased temperatures. Although biological activity can explain the reducing resistivity from Feb-17 to Jun-17, the increasing resistivity from Nov-17 to Feb-18, here, is attributed to draining of waters from P1 into the lower zones. Additionally, Uhlemann et al. (2016) observed an increasing resistivity in the lower peat layer during the Dec-12 to Apr-13 period and attributed that to be the result of up-welling of more resistive GW. Here, the resistivity of P2 remains fairly stable from Nov-17 to Feb-18 indicating that this is probably not the case here and is line with the different chalk GW levels during the monitoring period considered here.

The increasing pore-water conductivity as a result of microbial and vegetation related processes in P1 from Mar-18 to Jun-18 agrees with the P2, G1 and G2 patterns in Fig. 7.9 where immediately following the vegetation cutting, their resistivity decreases. This is interpreted as being caused by an abrupt draining of high conductivity water from P1. The resistivity patterns in G1 and G2 following the vegetation cutting are also distinctive. While the resistivity of G1 remaining stable following its initial drop could be attributed to dilution of the conductive pore-waters obtained from P1, the increase of the resistivity of in G2 implies that there is focused up-welling of more resistive GW into this region, perhaps as GW levels equilibrate following vegetation cutting.

It is evident from Fig 7.9b, that the vegetation cutting dominates the resistivity dynamics of the riparian zone; however, patterns within the P1, P2, P3 and P4 indicate that precipitation influences the saturation of the upper peat layers when moisture content is low. For instance, the influence of precipitation is most evident during Nov-17 to Mar-18 and Oct-18 to Nov-18. Moreover, in comparing ERI models from 13-Oct-18 and 14-Oct-18 (Fig 7.10), it can be seen that reductions in resistivity are only in the shallowest peat layers and are due to infiltrating rainwater.
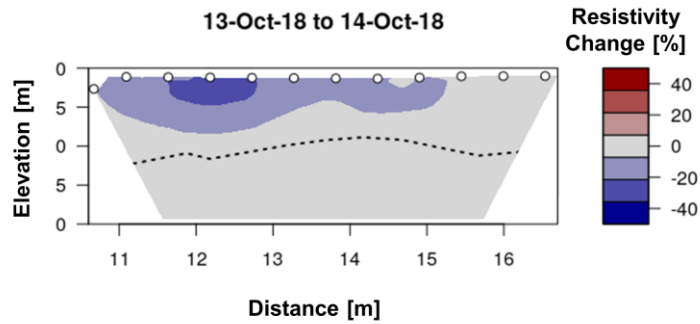
Figure 7.10: Comparison of resistivity models obtained on 13-Oct-18 and 14-Oct-18.

7.6.3 Determining Hydrological Properties of Different Zones

In addition to interpreting the patterns observed in each zone, the information about the hydrological properties of each can also be inferred. For instance, it is evident that P1 and P4 are closely connected given that they respond similarly to changes in the river stage and precipitation events. However, given the higher resistivity and greater changes in response to precipitation events it is anticipated that P3 is characterized by higher porosity. Furthermore, given that the resistivity of P3 is always higher both zones are unlikely to have ever been completely saturated during the monitoring period.

In comparison, the resistivity of P5 remains very stable during the monitoring period and whilst the effect of the vegetation cutting is seen on the resistivity, it is both subtle and prolonged (Fig 7.9b). This implies that this zone is not well-connected to the rest of the peat and pore-water velocities are low. This could be attributed to a higher clay content which would be in agreement with its low resistivity. P2 and P3 both show a decrease in resistivity following the vegetation cutting. This implies that although throughout the majority of the year there is limited connection between P1 and P4, with P2 and P3, when hydraulic gradients are high enough water can be moved between zones. Moreover, the increase in resistivity in P3 immediately before the vegetation cutting is worthy of mentioning and could be related to up-welling or infiltration of more restive water after some threshold level is surpassed.

Lastly, the different behaviors of the gravel zones G1 and G2 are distinct. The behavior of G1 is intuitive, i.e. resistivity increases due to up-welling of more resistive GW, it then drops following the vegetation cutting due to the draining of more conductive pore waters before its resistivity

158

stabilizes. In comparison, although G2 follows the same pattern it is less resistive than G1. Furthermore, whereas the resistivity drop following the vegetation cutting in G1 is abrupt, it is more gradual in G2. This coupled with the increasing resistivity following the initial post vegetation cutting drop could be a result of slower drainage from the overlying peat and then the up-welling of more resistive GW. It is anticipated that these differing patterns could be related to the depositional patterns and the braided structures described by Chambers et al. (2014) and Newell et al. (2015).

7.7 Conclusions

Time-lapse ERI was carried out in an attempt to reveal vertical and lateral exchanges of a river with the GW. Despite measures to appropriately account for the river stage and resistivity, resolution of processes in the riverbed was not possible. Furthermore, the localized nature of some artefacts, i.e. immediately next to the river, could arise from poorly positioned electrodes. Instead, analysis was focused on revealing patterns in the riparian zone.

Summary statistics proved useful for simplifying the large data set and identifying patterns and regions of the subsurface that behaved similarly. Resistivity of each element in the riparian zone was correlated with the river stage; however, it was clear that the changes in river stage behaved similarly to the GW levels. Although, it was apparent that there were additional controls of subsurface resistivity and non-linear relationships between bulk resistivity and river stage, cross-correlation metrics allowed grouping of distinctive hydrological units. Such identification of distinct hydrological behavior in the subsurface could provide a useful tool for locating areas of enhanced residence times or increased mixing, which may have important implications for catchment health.

It has been demonstrated that ERI monitoring provides a useful method for assessing the extent and timing of GW-SW interactions within the riparian zone. Future work could rely on more extensive installation of GW level and bulk conductivity loggers, which could help in interpreting patterns of electrical resistivity at a smaller scale. In addition, approaches aiming to characterize microbiological processes, alongside similar ERI installations, could help to quantify implications of GW-SW interactions for catchment scale health.

8 Discussion and Future Directions

8.1 Introduction

Given the usefulness of geophysical tools, the frequency of applications to characterise the groundwater-surface water (GW-SW) interactions will continue to increase. In the discussion of Chapter 2, the strengths, challenges, and future directions of geophysical methodologies were addressed. As Chapter 2 was written prior to the work conducted in Chapters 3 to 7 it offers a useful reference point to put the work conducted in these latter chapters into context. Chapter 2 highlighted that geophysical methods are useful for reconnaissance surveys, supplementing other data sets and monitoring dynamic processes. In comparison, the weaknesses of geophysics include model interpretation and data uncertainty, the presence of site-specific considerations, and the difficulties in extracting quantitative information about hydrogeological properties. In addition, several methodologies of interest discussed in Chapter 2: time-lapse electrical resistivity imaging (ERI), induced polarisation (IP), self-potential (IP), multi-coil frequency domain electromagnetic induction (EMI), and unmanned vehicles. It was also stressed in Chapter 2 that geophysical methods be used to answer hydrological problems, so it is important to assess the advances relevant to hydrological characterisation made here. In the section below, the thesis aims are considered in the context of the discussion of Chapter 2. Following this, advances in terms of hydrology are discussed and suggestions for future directions are provided.

8.2 Thesis Summary and Conclusions

The conclusions of the thesis are discussed in the context of the thesis aims presented in Section 1.2: (1) 'How best can EMI methods be used to reveal subsurface structure?', (2) 'Are electrical properties observed at lab scale resolvable at the field scale?', and (3) 'Can ERI be used to reveal GW-SW interactions between rivers and GW?'.

8.2.1 Using EMI Methods for Structural Characterisation

With regards to the first research aim, methods to model and process EMI data were developed as discussed in Chapter 4. In doing so, the performance of the cumulative sensitivity forward model was tested against a Maxwell based forward model. It was demonstrated that when data are collected with the device operated at 1 m elevation, the cumulative sensitivity forward model was inappropriate. However, it is important to note that when operated at ground level, the cumulative sensitivity function performs well for low conductivity and broadly homogenous subsurface. In addition, it was demonstrated in both Chapters 4 and 5 that when data are collected with the device operated at higher elevations, the effect of noise is more influential on the inversion results, and in some cases inverted data may not be useful.

In relation to the discussion of Chapter 2, the ability of EMI devices for quantitative determination of electrical conductivity was advocated strongly. However, in Chapter 5 it was demonstrated that characterising the peat depth with a linear regression linking peat depth and raw EMI measurements was more successful than inversion of the data. Upon reflection, it is evident that 'state of the art' methods do not necessarily yield better results and more traditional approaches can even offer superior results. For instance, in addition to correlating well with peat depths, raw EMI measurements were also found to be suitable for revealing the hydraulic conductivity of the peat across the field site, which was also shown to correlate with the perceived zones of groundwater upwelling mapped out by House et al. (2015).

With regards to the challenges of measurement uncertainty in geophysical applications, it is evident that data calibration improved the convergence of the EMI inversions. Furthermore, it was demonstrated how peat depths could be used to constrain the inversion and did not modify the total misfit of each model significantly. This implies that there are a number of models that appropriately describe the data. It was concluded that the poor performance of the EMI inversion was due to the increased uncertainty apparent in the parameter space when the device was operated

at 1 m elevation. This highlights that for EMI data with high measurement uncertainty deterministic methods may be inappropriate, especially for devices operated above the ground.

8.2.2 Linking Field and Laboratory IP

The second research aim was addressed by a study involving characterisation of riverbed sediments using field and laboratory based IP. It was noted that electrical characteristics of both the upper and lower riverbed were distinguishable in the laboratory, and the relationships between IP and textural properties followed published results. However, it was also found that the field results could not replicate the laboratory-based electrical properties. This issue is in line with the discussion in Chapter 2 about the ability of geophysics to provide quantitative information, for instance, although a number of convincing relationships have been built at the laboratory scale, it is evident that these may not translate well to the field site. Incorrect geoelectrical properties obtained either from artefacts due to erroneous fixing of river properties in the inversion, from overestimation/ underestimation of measurement error (which would act to subdue contrasts/create artefacts, respectively), or from not fixing resistivity of the river, would provide misleading information if they were translated using laboratory derived petrophysical models. Moreover, whilst similar synthetic modelling has been conducted for ERI (e.g. Orlando, 2013), here the investigations are more extensive and also focus on IP data.

In addition to the points considered in Chapter 2, it was also noted that the electrical properties were more distinctive at frequencies not typically used in the field. Measurements were made at higher frequencies in the field during this PhD, but the data are not included in this thesis. These higher frequency measurements were obtained using an Ontash and Ermac PSIP device (River Edge, New Jersey, USA); however, limitations in signal strength were such that phase values obtained from this device were inaccurate and far exceeded the values obtained in the lab. Nonetheless, it is clear that collection of data using multiple frequencies, or preliminary laboratory

tests on intrusive samples could be useful to identify frequencies that yield the most information about the subsurface, provided appropriate equipment is used.

8.2.3 Revealing GW-SW Exchanges Using Time-Lapse ERI

The third research aim was explored in Chapter 3 and Chapter 7, and built on similar themes established in Chapter 6. An ERI monitoring array was installed and left over a year-long period to assess changes in the resistivity structure of the riverbed and the adjacent riparian zone. To account for river stage, an inversion workflow was developed to handle the meshing, and inverse modelling of data. It was evident that similar problems with fixing the river resistivity, experienced in Chapter 6, resulted in artefacts occurring in the riverbed, making it not possible to reveal vertical exchanges between the river and riverbed. For instance, when the river level was low the riverbed was characterised by high resistivity regions, and when the river level was high the riverbed was characterised by low resistivity regions. This resulted in unrealistic temporal patterns in resistivity. It was, however, possible to observe patterns occurring in the riparian zone and time-series analysis was useful at condensing information and identifying regions of the subsurface that behaved similarly. This information could then be used to discretise the subsurface and explore, in detail, hydrological interactions occurring in the riparian zone.

Despite the assertion in Chapter 2 that methods ought to be used in association with supplementary data, device malfunctions were such that the additional information was minimal. Nonetheless, given that models were corrected for temperature, patterns could be interpreted with reasonable confidence. The demonstration here that ERI methods can be used to identify hydrofacies zones in the subsurface, indicates here that they could easily be used to supplement data collected by other more traditional methodologies such as biogeochemical sampling.

8.3 Relevance to Hydrology

Perhaps most importantly, the contribution of this work to hydrological applications ought to be assessed. For instance, geophysical studies ought to have broader relevance and application beyond technical challenges that need to be overcome. Given the technical nature of geophysics, it is a common pitfall that studies focus more heavily on the methods in which data are dealt with, and the broader implications and interpretations can sometimes be overlooked. Here, the wider implications of Chapters 3 to 7 to hydrological and environmental science are discussed objectively.

Chapters 3 and 4 focus on method development so their contribution is primarily technical. However, such tools to enable modelling of geophysical data remain an important step in the interpretation of geophysical data, therefore, by providing easy to use tools, the use of geophysics in multi-disciplinary studies can be facilitated. Furthermore, given the open source nature of these scripts and the presence of other R-based tools, e.g. MoisturEC (Terry et al., 2018) which estimates water content from electrical conductivity models, it is anticipated that they can easily be tailored for hydrological applications.

Chapter 5 demonstrated that raw measurement from EMI methods can be used to characterise the deposit architecture of peat with high accuracy. Such information is sufficient for providing additional information to employ in modelling studies, given the substantial hydrological differences between peat and gravel. Moreover, the strong correlation between raw measurements and hydraulic conductivity, even though these results are site specific, demonstrate how EMI methods can supplement traditional hydrological methodologies and provide crucial information to inform hydrological models.

Chapter 6 highlighted the complications of aquatic-based electrical surveys and demonstrated that relationships in the lab may not be applicable at the field scale. Other approaches could instead involve empirical relationships linking in situ hydrological measurements and electrical measurements, such as Benoit et al. (2019) who combined IP and slug tests to quantify hydraulic characteristics of a riverbed. However, the forward modelling presented in thesis show that caution should be employed when making hydrological interpretations of river based surveys.

There was also limited hydrological relevance of riverbed electrical measurements in Chapter 7, however, the results from the riparian zone were useful. It was clearly shown from the cross-correlation summary statistics that different regions of the subsurface had different hydrological responses. Such a method that enables detection of distinctive hydrological behaviour has clear relevance for determining conceptual understanding of field sites.

8.4 Future Directions

8.4.1 Obtaining Quantitative Information from EMI Methods

It was demonstrated that hydrogeological properties of the Boxford Wetland could be revealed sufficiently by using raw EMI measurements directly. Based on these findings it is evident that there are three principal avenues for future work: (1) using more suitable methods for data inversion, (2) using more appropriate methods for data acquisition, and (3) development of methods to use raw EMI results to directly predict properties of interest.

Firstly, although attempts were made to account for errors in EMI inversions by introducing an error weighting term into the objective function, this did not perform better than use of the L1 norm when applied to synthetic data. Future work could attempt to conduct an inversion with some form of lateral constraint to link neighbouring measurements; however, it would be necessary to prevent an inversion of anomalous data influencing the model obtained from good quality data, e.g. perhaps by inverting them simultaneously. Moreover, although the cumulative sensitivity functions offer a

useful tool for quick inversion of data; ideally EMI inversions should use the FS forward model, especially when devices are operated above ground level. For instance, applications using the cumulative sensitivity function for elevated data (e.g., Saey et al., 2016) should be avoided.

In addition to inverting data using classical optimisation methods, a method to model EMI data was developed in this PhD (not shown in this thesis) that used a neural network to link measurements with a two-layer model of electrical conductivity. The application of machine learning techniques to model geophysical data is not novel (e.g. El-Qady and Ushijima, 2001) but, until recently (Moghadas, 2020), they have not been employed for frequency domain EMI data. Using the Boxford data a neural network was trained using a set of EMI measurements and a corresponding two-layer model of electrical conductivity obtained from an inversion where the depth of layer 1 was constrained to the intrusive peat measurements. In this way the neural network effectively 'learns' a specific forward model which links EMI measurements and models of electrical conductivity. Once trained, this method was very quick and gave similar results to those obtained from a constrained inversion, without the need for additional intrusive data. However, a major disadvantage is that it required a lot of data for training. Furthermore, whilst it is true that the neural network could be trained on noisy synthetic data, these attempts generally gave results that differed significantly from the constrained inversion. Nonetheless, it is anticipated that machine learning methods to model EMI data and obtain quantitative models of electrical conductivity will become more apparent in the coming years.

In addition to developing new inversion methods, it may also be relevant to adapt acquisition methods. For instance, in this work it is assumed that poor performance of inversion of the field data was linked to measurement error and/or poor calibration. Despite the strong correlations between ERI and EMI measurements this correlation may not have been valid for the whole meadow, e.g. it was evident from Fig. 5.9 that a portion of the north meadow was characterised by a notable zone of higher misfits. However, it is also possible that this zone is characterised by

higher misfits because the device rotated along its long axis before it was noticed such that measurements made here were problematic or because of different vegetation coverage that may influence the measurements. Due to the vegetation at the site it was not possible to use a cart or a sled, however, perhaps a stretcher-type setup operated by two people would be more appropriate in similar settings in order to maintain a stable instrument. Furthermore, rather than conducting roaming surveys, perhaps EMI measurements could be made at isolated locations about the field site. This would allow the user to ensure correct device orientation and elevation. In addition, it would also allow for measurements to be made at multiple elevations, and hence provide additional measurements with different sensitivity patterns for inversion. However, it is important to note that such surveys would limit productivity.

With regards to developing methods to deal with raw EMI measurements, there is also potential in using machine leaning techniques to directly obtain information of hydrogeological interest, effectively bypassing the need for inversion. This would also be beneficial for hydrogeological characterisation and effectively skips the step where models of geophysical properties are obtained. For instance, neural networks could be used to combine large data sets of collocated geophysical and non-geophysical data. Although, as noted, neural networks require a large set of training data to be developed, it could be that future applications make more use of unmanned vehicles, as discussed in Chapter 2 for collection of both geophysical and hydrogeological data.

Moreover, the value of skipping the classical inversion step is such that it negates the need to calibrate geophysical data, and geophysical data sets that are not directly connected can be considered simultaneously. Furthermore, in addition to ground-based sensing methods an interesting application would perhaps be to combine airborne geophysical data with satellite data, geological mapping data, and/or ground-based data using similar techniques. For instance, it was highlighted in Chapter 2, although studies coupling geophysical data and remote sensing data are rare (e.g. Yoshikawa and Hinzman, 2003) the ability to relate the shallow subsurface with the surface at the catchment scale would surely yield informative results.

8.4.2 Characterising Riverbeds Using Geophysical Methods

The issue of fixing the river resistivity in an inversion was a key problem in Chapters 6 and 7. It was evident from the synthetic examples presented in Chapter 6 that fixing of the river resistivity was essential but Chapter 7 demonstrated that fixing of the river resistivity can lead to artefacts in the riverbed. Future methods to deal with this could include the use of different regularisation in the river and riverbed. For instance, instead of enforcing a single resistivity, or simply preventing smoothing across the boundary, perhaps an inversion method that uses a large smoothing factor in the river and a lower one in the riverbed could be employed. In this way it may be possible to obtain a river resistivity that is broadly homogenous but with regions having slight resistivity deviations. For instance, in the case of poorly surveyed riverbank topography, regions in the vicinity of the riverbank may be assigned a higher resistivity value which would prevent the forcing of artefacts just below the river. Moreover, it is anticipated that the measured river water conductivity may not be representative of the conductivity of the river, for instance if there is significant thermal stratification or dense in-stream vegetation.

It is also possible that waterborne electrical methods may be better suited to revealing lateral contrasts in qualitative electrical properties. For instance, Wang et al. (2018) extended an analytical solution of Keller and Frischknecht (1966) to deal with complex conductivity, as opposed to just real conductivity. The analytical solution can be used to explain cases where electrodes are located at the boundary of a finite upper layer and an infinite lower layer, if the electrical properties and stage of the river are known; the analytical solution can be used to remove the effect of the water column to obtain an apparent resistivity of the riverbed. For instance, the combined use of towed surveys and this analytical solution could be used to reveal lateral changes in the electrical characteristics of a riverbed.

8.4.3 Revealing Zones of Groundwater Upwelling Using EMI

There have been several applications that use waterborne EMI to reveal lateral contrasts in the apparent conductivity of riverbeds and link them to zones of groundwater upwelling (e.g. Butler et al., 2004; Binley et al., 2013; Steelman et al., 2017). However, rather than providing qualitative information about lateral changes in riverbed conductivity, it may be possible to link EMI measurements to quantitative estimates of groundwater upwelling. For instance, in areas where there is significant electrical contrast between groundwater and surface water it is possible to use vertical changes in electrical conductivity of the subsurface to groundwater discharge (e.g. Stieglitz et al., 2008). It is anticipated that waterborne EMI could be used to obtain estimates of groundwater discharge. For instance, a 1D inversion problem could be setup to provide a model comprising a river layer overlying a riverbed layer smoothly varying changes in vertical conductivity. Assuming the riverbed lithology is relatively homogenous, and without significant clay portions, it would be possible to translate riverbed electrical conductivity profiles into pore water conductivity values. In this way an EMI inversion could be formulated to obtain an estimate of groundwater upwelling from several EMI measurements.

8.4.4 Time-Lapse EMI

Lastly, although not investigated explicitly, some of the issues with time-lapse EMI were discussed in Chapter 4. For instance, it is evident that if repeat measurements are to be made with a device operated at 1 m elevation, slight changes in the height of the device could lead to underestimations, or overestimations, in the measured apparent conductivity, in the order of 5–10%. This would mean that significant changes in ground conductivity would be required in order for them to be detectable using the EMI device operated above ground. However, it could be that repeat measurements are made in the same location could be a viable method of employing EMI devices for time-lapse applications in environments where operation at ground level is not possible.

9 References

Abraham, J.D., Cannia, J.C., Bedrosian, P.A., Johnson, M.R., Ball, L.B., Sibray, S.S., 2012. Airborne Electromagnetic Mapping of the Base of Aquifer in Areas of Western Nebraska. 1–38. US Geological Survey Scientific Investigations Report 2011-5219. https://pubs.usgs.gov/sir/2011/5219/.

Aldiss, D., Newell, A., Marks, R., Hopson, P., Farrant, A., Royse, K., Aspden, J., Evans, D., Smith, N., Woods, M., Wilkinson, I., 2004. Geology of the Newbury district and part of the Abingdon district. British Geological Survey, Nottingham, UK.

Allen, D.A., 2007. Electrical conductivity imaging of aquifers connected to watercourses. Faculty of Science, University of Technology, Sydney. https://opus.lib.uts.edu.au/bitstream/2100/428/1/01front.pdf

Allen, D.J., Darling, W.G., Gooddy, D.C., Lapworth, D.J., Newell, A.J., Williams, A.T., Allen, D., Abesser, C., 2010. Interaction between groundwater, the hyporheic zone and a Chalk stream: a case study from the River Lambourn, UK. Hydrogeology Journal 18, 1125–1141. https://doi.org/10.1007/s10040-010-0592-2

Anderson, M.P., 2005. Heat as a Ground Water Tracer. Ground Water 43, 951–968. https://doi.org/10.1111/j.1745-6584.2005.00052.x

Anderson, N.L., Ismael, A.M., Thitimakorn, T., 2007. Ground-penetrating radar: a tool for monitoring bridge scour. Environmental and Engineering Geosciences. 13 (1), 1–10. http://pubs.er.usgs.gov/publication/70031991.

Andrade, F.C., Fischer, T., Valenta, J., 2016. Study of Errors in Conductivity Meters Using the Low Induction Number Approximation and How to Overcome Them. Presented at the Near Surface Geoscience 2016 - 22nd European Meeting of Environmental and Engineering Geophysics, Barcelona, Spain. https://doi.org/10.3997/2214-4609.201602080

Andrade, F.C., Fischer, T., 2018. Generalised relative and cumulative response functions for electromagnetic induction conductivity meters operating at low induction numbers: Relative and cumulative response functions. Geophysical Prospecting 66, 595–602. https://doi.org/10.1111/1365-2478.12553

Annan, A.P., 2005. GPR Methods for Hydrogeological Studies, in: Rubin, Y., Hubbard, S.S. (Eds.), Hydrogeophysics. Springer Netherlands, Dordrecht, 185–213. https://doi.org/10.1007/1-4020-3102-5_7

Archie, G.E., 1942. The Electrical Resistivity Log as an Aid in Determining Some Reservoir Characteristics. Transactions of the American Institute of Mining, Metallurgical and Petroleum Engineers. 146, 54–62. https://doi.org/10.2118/942054-G

Arora, T., Linde, N., Revil, A., Castermant, J., 2007. Non-intrusive characterization of the redox potential of landfill leachate plumes from self-potential data. Journal of Contaminant Hydrology 92, 274–292. https://doi.org/10.1016/j.jconhyd.2007.01.018

Aster, R., Borchers, B., Thurbur, C., 2005. Parameter Estimation and Inverse Problems, 2nd edition. Academic Press, New York, US.

Atekwana, E.A., Slater, L.D., 2009. Biogeophysics: A new frontier in Earth science research. Reviews of Geophysics 47, GR4004. https://doi.org/10.1029/2009RG000285

Auken, E., Doetsch, J., Fiandaca, G., Christiansen, A.V., Gazoty, A., Cahill, A.G., Jakobsen, R., 2014. Imaging subsurface migration of dissolved CO2 in a shallow aquifer using 3-D time-lapse electrical resistivity tomography. Journal of Applied Geophysics 101, 31–41. https://doi.org/10.1016/j.jappgeo.2013.11.011

Ball, L.B., Kress, W.H., Cannia, J.C., 2006. Determination of Canal Leakage Potential Using Continuous Resistivity Profiling Techniques in Western Nebraska and Eastern Wyoming, 2004. US Geological Survey Scientific Investigations Report 2006-5032, 1–53. https://pubs.water.usgs.gov/sir20065032.

Barker, R., 1992. A simple algorithm for electrical imaging of the subsurface. First Break, 10, 53–62.

Bechtold, M., Bechtold, M., Tiemeyer, B., Don, A., Altdorff, D., Van der Kruk, J., Huisman, J.A., 2013. Revealing spatial distribution of soil organic carbon contents and stocks of a disturbed bog relict by in-situ NIR and apparent EC mapping. Proceedings of the European Geosciences Union 2013 (EGU2013-13874-2).

Ben Hadj Miled, M.K., Miller, E.L., 2007. A projection-based level-set approach to enhance conductivity anomaly reconstruction in electrical resistance tomography. Inverse Problems 23, 2375–2400. https://doi.org/10.1088/0266-5611/23/6/007

Bencala, K.E., 1984a. Interactions of solutes and streambed sediment: 2. A dynamic analysis of coupled hydrologic and chemical processes that determine solute transport. Water Resources Research 20, 1804–1814. https://doi.org/10.1029/WR020i012p01804

Bencala, K.E., Kennedy, V.C., Zellweger, G.W., Jackman, A.P., Avanzino, R.J., 1984b. Interactions of solutes and streambed sediment: 1. An experimental analysis of cation and anion transport in a mountain stream. Water Resources Research 20, 1797–1803. https://doi.org/10.1029/WR020i012p01797

Benoit, S., Ghysels, G., Gommers, K., Hermans, T., Nguyen, F., Huysmans, M., 2019. Characterization of spatially variable riverbed hydraulic conductivity using electrical resistivity tomography and induced polarization. Hydrogeology Journal 27, 395–407. https://doi.org/10.1007/s10040-018-1862-7

Bianchin, M.S., Smith, L., Beckie, R.D., 2011. Defining the hyporheic zone in a large tidally influenced river. Journal of Hydrology 406, 16–29. https://doi.org/10.1016/j.jhydrol.2011.05.056

Binley, A., Ramirez, A., Daily, W., 1995. Regularised image reconstruction of noisy electrical resistance tomography data, in Beck, M. S., Hoyle, B. S., Morris, M. A., Waterfall, R. C., Williams, R. A. (Eds.). Process tomography: Proceedings, 4th Workshop of the European Concerted Action on Process Tomography, 401–410.

Binley, A., 2015. Tools and techniques: electrical methods. In: Schubert, G. (Ed.), 2nd ed.

Treatise on Geophysics 11. Elsevier, Oxford, UK, 233–259. https://doi.org/10.1016/B978-0-444-53802-4.00192-5.

Binley, A., Cassiani, G., Middleton, R., Winship, P., 2002. Vadose zone flow model parameterisation using cross-borehole radar and resistivity imaging. Journal of Hydrology 267, 147–159. https://doi.org/10.1016/S0022-1694(02)00146-4

Binley, A., Hubbard, S.S., Huisman, J.A., Revil, A., Robinson, D.A., Singha, K., Slater, L.D., 2015. The emergence of hydrogeophysics for improved understanding of subsurface processes over multiple scales: The Emergence of Hydrogeophysics. Water Resources Research 51, 3837–3866. https://doi.org/10.1002/2015WR017016

Binley, A., Kemna, A., 2005. DC Resistivity and Induced Polarization Methods, in: Rubin, Y., Hubbard, S.S. (Eds.), Hydrogeophysics. Springer Netherlands, Dordrecht, 129–156. https://doi.org/10.1007/1-4020-3102-5_5

Binley, A., Slater, L.D., Fukes, M., Cassiani, G., 2005. Relationship between spectral induced polarization and hydraulic properties of saturated and unsaturated sandstone. Water Resources Research 41, W12417. https://doi.org/10.1029/2005WR004202

Binley, A., Ullah, S., Heathwaite, A.L., Heppell, C., Byrne, P., Lansdown, K., Trimmer, M., Zhang, H., 2013. Revealing the spatial variability of water fluxes at the groundwater-surface water interface: Spatial Variability of Groundwater-Surface Water Fluxes. Water Resources Research 49, 3978–3992. https://doi.org/10.1002/wrcr.20214

Bloom, A.A., Palmer, P.I., Fraser, A., Reay, D.S., Frankenberg, C., 2010. Large-Scale Controls of Methanogenesis Inferred from Methane and Gravity Spaceborne Data. Science 327, 322–325. https://doi.org/10.1126/science.1175176

Boaga, J., 2017. The use of FDEM in hydrogeophysics: A review. Journal of Applied Geophysics 139, 36–46. https://doi.org/10.1016/j.jappgeo.2017.02.011

Boano, F., Harvey, J.W., Marion, A., Packman, A.I., Revelli, R., Ridolfi, L., Wörman, A., 2014. Hyporheic flow and transport processes: Mechanisms, models, and biogeochemical implications. Reviews of Geophysics 52, 603–679. https://doi.org/10.1002/2012RG000417

Boano, F., Revelli, R., Ridolfi, L., 2008. Reduction of the hyporheic zone volume due to the stream-aquifer interaction. Geophysical Research Letters 35. L09401. https://doi.org/10.1029/2008GL033554

Borner, F. D., Schon, J. H., 1991. A relation between the quadrature component of electrical conductivity and the specific surface area of sedimentary rocks, Log Analyst, 32, 612–613.
.

Boulton, A.J., Datry, T., Kasahara, T., Mutz, M., Stanford, J.A., 2010. Ecology and management of the hyporheic zone: stream–groundwater interactions of running waters and their floodplains. Journal of the North American Benthological Society 29, 26–40. https://doi.org/10.1899/08-017.1

Boulton, A.J., Findlay, S., Marmonier, P., Stanley, E.H., Valett, H.M., 1998. The functional significance of the hyporheic zone in streams and rivers. Annual Review of Ecology and Systematics 29, 59–81. https://doi.org/10.1146/annurev.ecolsys.29.1.59

Bridge, J.W. et al., 2005. High Resolution In-Situ Monitoring of Hyporheic Zone Biogeochemistry. UK Environment Agency Science Report SC030155/SR3, 1–44.

Bridgham, S. D., H. Cadillo-Quiroz, J. K. Keller, and Q. Zhuang (2013), Methane emissions from wetlands: Biogeochemical, microbial, and modeling perspectives from local to global scales, Global Change Biology, 19(5), 1325–1346.

Brosten, T.R., Day-Lewis, F.D., Schultz, G.M., Curtis, G.P., Lane, J.W., 2011. Inversion of multi-frequency electromagnetic induction data for 3D characterization of hydraulic conductivity. Journal of Applied Geophysics 73, 323–335. https://doi.org/10.1016/j.jappgeo.2011.02.004

Brunauer, S., Emmett, P. H., Teller, E., 1938. Adsorption of gases in multimolecular layers.vJournal of the American Chemical Society, 60, 309-19.

Brunet, P., Clément, R., Bouvier, C., 2010. Monitoring soil water content and deficit using Electrical Resistivity Tomography (ERT) – A case study in the Cevennes area, France. Journal of Hydrology 380, 146–153. https://doi.org/10.1016/j.jhydrol.2009.10.032

Brunke, M., Gonser, T., 1997. The ecological significance of exchange processes between rivers and groundwater. Freshwater Biology 37, 1–33. https://doi.org/10.1046/j.1365-2427.1997.00143.x

Buss, S. et al., 2009. The hyporheic handbook: a handbook on the groundwater-surface water interface and hyporheic zone for environment managers. Environment Agency, Bristol.

Butler, K.E., Nadeau, J.-C., Parrott, R., Daigle, A., 2004. Delineating Recharge to a River Valley Aquifer by Riverine Seismic and EM Methods. Journal of Environmental and Engineering Geophysics 9, 95–109. https://doi.org/10.4133/JEEG9.2.95

Byrd, R. H., Lu, P., Nocedal, J., Andzhu, C. 1995. A limited memory algorithm for boundconstrained optimization. Society for Industrial and Applied Mathematics, 16, 5, 1190 – 1208.

Cassiani, G., Ursino, N., Deiana, R., Vignoli, G., Boaga, J., Rossi, M., Perri, M.T., Blaschek, M., Duttmann, R., Meyer, S., Ludwig, R., Soddu, A., Dietrich, P., Werban, U., 2012. Non-invasive monitoring of soil static characteristics and dynamic states: a case study highlighting vegetation effects. Vadose Zone J. 11. http://dx.doi.org/10.2136/2011.0195

Chambers, J.E., Gunn, D.A., Wilkinson, P.B., Meldrum, P.I., Haslam, E., Holyoake, S., Kirkham, M., Kuras, O., Merritt, A., Wragg, J., 2014a. 4D electrical resistivity tomography monitoring of

soil moisture dynamics in an operational railway embankment. Near Surface Geophysics 12, 61–72. https://doi.org/10.3997/1873-0604.2013002

Chambers, J. E., Wilkinson, P.B., Uhlemann, S., Sorensen, J.P.R., Roberts, C., Newell, A.J., Ward, W.O.C., Binley, A., Williams, P.J., Gooddy, D.C., Old, G., Bai, L., 2014b. Derivation of lowland riparian wetland deposit architecture using geophysical image analysis and interface detection. Water Resources Research 50, 5886–5905. https://doi.org/10.1002/2014WR015643

Chambers, J.E., Meldrum, P.I., Wilkinson, P.B., Ward, W., Jackson, C., Matthews, B., Joel, P., Kuras, O., Bai, L., Uhlemann, S., Gunn, D., 2015. Spatial monitoring of groundwater drawdown and rebound associated with quarry dewatering using automated time-lapse electrical resistivity tomography and distribution guided clustering. Engineering Geology 193, 412–420. https://doi.org/10.1016/j.enggeo.2015.05.015

Chandler, I.D., Guymer, I., Pearson, J.M., van Egmond, R., 2016. Vertical variation of mixing within porous sediment beds below turbulent flows: POROUS BED MIXING. Water Resources Research 52, 3493–3509. https://doi.org/10.1002/2015WR018274

Chandra, S., Nagaiah, E., Reddy, D.V., Rao, V.A., Ahmed, S., 2012. Exploring deep potential aquifer in water scarce crystalline rocks. Journal of Earth System Science 121, 1455–1468. https://doi.org/10.1007/s12040-012-0238-y

Chen, J., Hubbard, S.S., Williams, K.H., Pride, S., Li, L., Steefel, C., Slater, L., 2009. A state-space Bayesian framework for estimating biogeochemical transformations using time-lapse geophysical data. Water Resources Research 45, W08420. https://doi.org/10.1029/2008WR007698

Chen, J., Hubbard, S.S., Williams, K.H., 2013. Data-driven approach to identify field-scale biogeochemical transitions using geochemical and geophysical data and hidden Markov models: Development and application at a uranium-contaminated aquifer. Water Resources Research 49, 6412–6424. https://doi.org/10.1002/wrcr.20524

Cheng, Q., Chen, X., Tao, M., Binley, A., 2019. Characterization of karst structures using quasi-3D electrical resistivity tomography. Environmental Earth Sciences 78, 285, 1-12. https://doi.org/10.1007/s12665-019-8284-2.

Christensen, B.N. and Sorensen, K., 1998. Surface and borehole electric and electromagnetic methods for hydrological investigation. European Journal of Environmental and Engineering Geophysics 3, 75-90.

Christiansen, A., Pedersen, J., Auken, E., Søe, N., Holst, M., Kristiansen, S., 2016. Improved Geoarchaeological Mapping with Electromagnetic Induction Instruments from Dedicated Processing and Inversion. Remote Sensing 8, 1022. https://doi.org/10.3390/rs8121022

Clémence, H., Marc, P., Véronique, D., Toihir, A., 2017. Monitoring an artificial tracer test within streambed sediments with time lapse underwater 3D ERT. Journal of Applied Geophysics 139, 158–169. https://doi.org/10.1016/j.jappgeo.2017.02.003

Colombero, C., Comina, C., Gianotti, F., Sambuelli, L., 2014. Waterborne and on-land electrical surveys to suggest the geological evolution of a glacial lake in NW Italy. Journal of Applied Geophysics 105, 191–202. https://doi.org/10.1016/j.jappgeo.2014.03.020

Comas, X., Slater, L., Reeve, A., 2007. In situ monitoring of free-phase gas accumulation and release in peatlands using ground penetrating radar (GPR). Geophysical Research Letters 34. https://doi.org/10.1029/2006GL029014

Constable, S.C., Parker, R.L., Constable, C.G., 1987. Occam's inversion: A practical algorithm for generating smooth models from electromagnetic sounding data. Geophysics 52, 289–300. https://doi.org/10.1190/1.1442303

Cook, P.G., Herczeg, A.L., 2000. Environmental Tracers in Subsurface Hydrology.

Springer, New York, US. https://link.springer.com/book/10.1007%2F978-1-4615-4557-6.

Corwin, D.L., Rhoades, J.D., 1982. An Improved Technique for Determining Soil Electrical Conductivity-Depth Relations from Above-ground Electromagnetic Measurements. Soil Science Society of America Journal 46, 517. https://doi.org/10.2136/sssaj1982.03615995004600030014x

Corwin, D.L., 2008. Past, present, and future trends in soil electrical conductivity measurements using geophysical methods. In: Allred, B.J., Daniels, J.J., Ehsani, M.R. (Eds.), Handbook of Agricultural Geophysics. CRC Press, Taylor and Francis Group, Boca Raton, Florida, 17–44.

Coscia, I., Greenhalgh, S.A., Linde, N., Doetsch, J., Marescot, L., Günther, T., Vogt, T., Green, A.G., 2011. 3D crosshole ERT for aquifer characterization and monitoring of infiltrating river water. Geophysics 76, G49–G59. https://doi.org/10.1190/1.3553003

Coscia, I., Linde, N., Greenhalgh, S., Vogt, T., Green, A., 2012. Estimating traveltimes and groundwater flow patterns using 3D time-lapse crosshole ERT imaging of electrical resistivity

fluctuations induced by infiltrating river water. Geophysics 77, E239–E250. https://doi.org/10.1190/geo2011-0328.1

Crook, N., Binley, A., Knight, R., Robinson, D.A., Zarnetske, J., Haggerty, R., 2008. Electrical resistivity imaging of the architecture of substream sediments. Water Resources Research 44. https://doi.org/10.1029/2008WR006968

Dahlin, T., Loke, M.H., 2015. Negative apparent chargeability in time-domain induced polarisation data. Journal of Applied Geophysics 123, 322–332. https://doi.org/10.1016/j.jappgeo.2015.08.012

Dahlin, T., Loke, M.H., 2018. Underwater ERT surveying in water with resistivity layering with example of application to site investigation for a rock tunnel in central Stockholm. Near Surface Geophysics 16, 230-237

Daily, W., Ramirez, A., Binley, A., 2004. Remote monitoring of leaks in storage tanks using electrical resistance tomography: application at the Hanford site. Journal of Environmental and Engineering Geophysics 9 (1), 11–24. http://dx.doi.org/10.4133/JEEG9.1.11.

Daily, W., Ramirez, A., Binley, A., LaBrecque, D., 2005. Electrical resistance tomography theory and practice. In: Butler, D.K. (Ed.), Near-Surface Geophysics. Society of Exploration Geophysicists, Oklahoma, US, 525–550. http://dx.doi.org/10.1190/1.9781560801719.

Day-Lewis, F.D., Lane, J.W., 2004. Assessing the resolution-dependent utility of tomograms for geostatistics. Geophysical Research Letters 31, https://doi.org/10.1029/2004GL019617

Day-Lewis, F.D., White, E.A., Johnson, C.D., Lane Jr., J.W., Belaval, M., 2006. Continuous resistivity profiling to delineate submarine groundwater discharge — examples and limitations. The Leading Edge 25 (6), 724–729.

De Smedt, P., Delefortrie, S., Wyffels, F., 2016. Identifying and removing micro-drift in ground-based electromagnetic induction data. Journal of Applied Geophysics 131, 14–22. https://doi.org/10.1016/j.jappgeo.2016.05.004

De Sosa, L.L., Glanville, H.C., Marshall, M.R., Schnepf, A., Cooper, D.M., Hill, P.W., Binley, A., Jones, D.L., 2018. Stoichiometric constraints on the microbial processing of carbon with soil depth along a riparian hillslope. Biology and Fertility of Soils 54, 949–963. https://doi.org/10.1007/s00374-018-1317-2

Delefortrie, S., De Smedt, P., Saey, T., Van De Vijver, E., Van Meirvenne, M., 2014. An efficient calibration procedure for correction of drift in EMI survey data. Journal of Applied Geophysics 110, 115–125. https://doi.org/10.1016/j.jappgeo.2014.09.004

Diaz, L., Herrero, J., 1992. Salinity estimates in irrigated sois using electromagnetic induction. Soil Science 154, 151–157. https://doi.org/10.1097/00010694-199208000-00009

Doetsch, J., 2012. Joint and constrained inversion of geophysical data for improved imaging of aquifer structure and processes. Geophysics 77, Z21–Z21. https://doi.org/10.1190/2012-0210-GEODIS.2

Doetsch, J., Linde, N., Pessognelli, M., Green, A.G., Günther, T., 2012a. Constraining 3-D electrical resistance tomography with GPR reflection data for improved aquifer characterization. Journal of Applied Geophysics 78, 68–76. https://doi.org/10.1016/j.jappgeo.2011.04.008

Doetsch, J., Linde, N., Vogt, T., Binley, A., Green, A.G., 2012b. Imaging and quantifying salt-tracer transport in a riparian groundwater system by means of 3D ERT monitoring. Geophysics 77, B207–B218. https://doi.org/10.1190/geo2012-0046.1

Doolittle, J.A., Brevik, E.C., 2014. The use of electromagnetic induction techniques in soils studies. Geoderma 223–225, 33–45. https://doi.org/10.1016/j.geoderma.2014.01.027

Doolittle, J., Zhu, Q., Zhang, J., Guo, L., Lin, H., 2012. Geophysical investigations of soil-landscape architecture and its impacts on subsurface flow. In: Lin, H. (Ed.), Hydropedology: Synergistic Integration of Soil Science and Hydrology. Academic Press, Elsevier, 413–447.

Dorn, C., Linde, N., Le Borgne, T., Bour, O., Baron, L., 2011. Single-hole GPR reflection imaging of solute transport in a granitic aquifer. Geophysical Research Letters 38, L08401. https://doi.org/10.1029/2011GL047152

Duan, Q.Y., Gupta, V.K., Sorooshian, S., 1993. Shuffled complex evolution approach for effective and efficient global minimization. Journal of Optimization Theory Applications 76, 501–521. https://doi.org/10.1007/BF00939380

Dudley-Southern, M., Binley, A., 2015. Temporal responses of groundwater-surface water exchange to successive storm events. Water Resources Research 51, 1112–1126. https://doi.org/10.1002/2014WR016623

Ekwe, A.C., Opara, A.I., 2012. Aquifer transmissivity from surface geo-electrical data: A case study of owerri and environs, southeastern Nigeria. Journal of the Geological Society of India 80, 123–128. https://doi.org/10.1007/s12594-012-0126-8

Edwards, R.T., 1998. The hyporheic zone. In: Naiman, R.J., Bilby, R.E. (Eds.), River Ecology and Management: Lessons from the Pacific Coastal Ecoregion. Springer-Verlag, New York, US, 399–429.

El-Qady, G., Ushijima, K., 2001. Inversion of DC resistivity data using neural networks. Geophys Prospect 49, 417–430. https://doi.org/10.1046/j.1365-2478.2001.00267.x

Elliott, H., Brooks, N.H., 1997. Transfer of nonsorbing solutes to a streambed with bedforms. Water Resources Research. 33 (1), 123–136.

Elwaseif, M., Robinson, J., Day-Lewis, F.D., Ntarlagiannis, D., Slater, L.D., Lane Jr., J.W., Minsley, B.J., Schultz, G., 2017. A matlab-based frequency-domain electromagnetic inversion code (FEMIC) with graphical user interface. Computers and Geosciences. 99, 61–71. https://doi.org/10.1016/j.cageo.2016.08.016.

EMTOMO, 2013. http://emtomo.com/

Erwin, K.L., 2009. Wetlands and global climate change: the role of wetland restoration in a changing world. Wetlands Ecology and Management 17, 71–84. https://doi.org/10.1007/s11273-008-9119-1

Everett, M.E., Meju, M.A., 2005. Electromagnetic induction. In: Rubin, Y., Hubbard, S.S. (Eds.), Hydrogeophysics 2. Springer, Netherlands, 157–183. https://doi.org/10.1080/00107516108202659

Findlay, S., Strayer, D., Goumbala, C., Gould, K., 1993. Metabolism of streamwater dissolved organic carbon in the shallow hyporheic zone. Limnology and Oceanography. 38 (7), 1493–1499. https://doi.org/10.4319/lo.1993.38.7.1493

Findlay, S., 1995. Importance of surface-subsurface exchange in stream ecosystems: the hyporheic zone. Limnology and Oceanography. 40 (1), 159–164. https://doi.org/10.4319/lo.1995.40.1.0159.

Fitterman, D.V., 2015. Tools and techniques: active-source electromagnetic methods. In: Schubert, G. (Ed.), 2nd ed. Treatise on Geophysics 11. Elsevier, Oxford, UK, 233–259. https://doi.org/10.1016/B978-0-444-53802-4.00193-7.

Fleckenstein, J.H., Krause, S., Hannah, D.M., Boano, F., 2010. Groundwater-surface water interactions: new methods and models to improve understanding of processes and dynamics.

Advances in Water Resources. 33 (11), 1291–1295. https://doi.org/10.1016/j.advwatres.2010.09.011.

Fletcher, R., Reeves, C.M., 1964. Function Minimization by Conjugate Gradients. Computer Journal, 7, 149-154. http://dx.doi.org/10.1093/comjnl/7.2.149

Flores-Orozco, A., Williams, K.H., Long, P.E., Hubbard, S.S., Kemna, A., 2011. Using complex resistivity imaging to infer biogeochemical processes associated with bioremediation of an uranium-contaminated aquifer. Journal of Geophysical Research: Biogeosciences. 116 (3), 1–17. https://doi.org/10.1029/2010JG001591.

Flores-Orozco, A., Gallistl, J., Bücker, M., Williams, K.H., 2016. Decay-Curve Analysis for the Quantification of Data Error in Time-Domain Induced Polarization Imaging.

Frederiksen, R.R., Christiansen, A.V., Christensen, S., Rasmussen, K.R., 2017. A direct comparison of EMI data and borehole data on a 1000 ha data set. Geoderma 303, 188–195. https://doi.org/10.1016/j.geoderma.2017.04.028

Freeze, R.A., Witherspoon, P.A., 1967. Theoretical analysis regional groundwater flow: 2. Effect of water-table configuration and subsurface permeability variation. Water Resources Research. 3 (2), 623–634. http://onlinelibrary.wiley.com/doi/10.1029/WR003i002p00623.

French, H., A. Binley, 2004, Snowmelt infiltration: monitoring temporal and spatial variability using time-lapse geophysics, Journal of Hydrology, 297, 174-186.

Frischknecht, F. C., Labson, V. F., Spies, B. R., Anderson, W. L., 1987. Profiling methods using small sources. In Nabighian, M. N. (Ed.) Electromagnetic methods in applied geophysics, vol. 2: SEG, 105–270.

Froese, D.G., Smith, D.G., Clement, D.T., 2005. Characterizing large river history with shallow geophysics: Middle Yukon River, Yukon Territory and Alaska. Geomorphology 67 (3–4), 391–406. https://doi.org/10.1016/j.geomorph.2004.11.011.

Gaffney, C., 2008. Detecting trends in the prediction of the buried past: a review of geophysical techniques in archaeology. Archaeometry, 50 (2), 313-336

Gagliano, M.P., Nyquist, J.E., Toran, L., Rosenberry, D.O., 2009. Assessment of Electrical Resistivity Method to Map Groundwater Seepage Zones in Heterogeneous Sediments, in: Symposium on the Application of Geophysics to Engineering and Environmental Problems 2009.

Presented at the Symposium on the Application of Geophysics to Engineering and Environmental Problems 2009, Environment and Engineering Geophysical Society, 815–823. https://doi.org/10.4133/1.3176773

Gallardo, L.A., Meju, M.A., 2011. Structure-coupled multiphysics imaging in geophysical sciences. Reviews of Geophysics 49. https://doi.org/10.1029/2010RG000330

Gandy, C.J., Smith, J.W.N., Jarvis, A.P., 2007. Attenuation of mining-derived pollutants in the hyporheic zone: A review. Science of the Total Environment 373, 435–446. https://doi.org/10.1016/j.scitotenv.2006.11.004

Garnier, S., 2018. https://cran.r-project.org/web/packages/viridisLite/viridisLite.pdf

Gebhardt, A., 2016. https://cran.r-project.org/web/packages/akima/akima.pdf

Geuzaine, C., Remacle, J. F., 2009. Gmsh: a three-dimensional finite element mesh generator with built-in pre- and post-processing facilities. International Journal for Numerical Methods in Engineering 79(11), 1309-1331.

Ghosh, D.P., 1971. The application of linear theory to the direct interpretation of geoelectrical resistivity sounding measurements. Geophysical Prospecting 19, 192–217. https://doi.org/10.1111/j.1365-2478.1971.tb00593.x

Glover, P.W.J., 2015. Geophysical Properties of the Near Surface Earth: Electrical Properties. In: Schubert, G. (Eds.)Treatise on Geophysics. Elsevier, 89–137. https://doi.org/10.1016/B978-0-444-53802-4.00189-5

Gomez-Velez, J.D., Harvey, J.W., 2014. A hydrogeomorphic river network model predicts where and why hyporheic exchange is important in large basins. Geophysical Research Letters 41, 6403–6412. https://doi.org/10.1002/2014GL061099

González-Pinzón, R., Ward, A.S., Hatch, C.E., Wlostowski, A.N., Singha, K., Gooseff, M.N., Haggerty, R., Harvey, J.W., Cirpka, O.A., Brock, J.T., 2015. A field comparison of multiple techniques to quantify groundwater–surface-water interactions. Freshwater Sciences 34 (1), 139–160. https://doi.org/10.1086/679738.

Gooseff, M.N., 2010. Defining hyporheic zones: advancing our conceptual and operational definitions of where stream water and groundwater meet. Geography Compass 4 (8), 945–955.

Gorham, E., 1995. The biogeochemistry of northern peatlands and its possible responses to global warming. In: Woodwell, G. M., Mackenzie, F. T. (eds.), Biotic Feedbacks in the Global Climate System: Will the Warming Feed the Warming? Oxford University Press, Oxford, UK, 169–186.

Grapes, T.R., Bradley, C., Petts, G.E., 2006. Hydrodynamics of floodplain wetlands in a chalk catchment: The River Lambourn, UK. Journal of Hydrology 320, 324–341. https://doi.org/10.1016/j.jhydrol.2005.07.028

Greswell, R.B., et al., 2005. High-resolution in situ monitoring of flow between aquifers and surface waters. Environment Agency, Bristol.

Griffiths, D.H., Turnbull, J., Olayinka, A.I., 1990. Two dimensional resistivity mapping with a computer-controlled array. First Break 8 (4), 121–129.

Gunther, T., Rucker, C., 2006. A New Joint Inversion Approach Applied to the Combined Tomography of DC Resistivity and Seismic Refraction Data, in: Symposium on the Application of Geophysics to Engineering and Environmental Problems 2006. Presented at the Symposium on the Application of Geophysics to Engineering and Environmental Problems 2006, Environment and Engineering Geophysical Society, 1196–1202. https://doi.org/10.4133/1.2923578

Hare, D.K., Briggs, M.A., Rosenberry, D.O., Boutt, D.F., Lane, J.W., 2015. A comparison of thermal infrared to fiber-optic distributed temperature sensing for evaluation of groundwater discharge to surface water. Journal of Hydrology 530, 153–166. https://doi.org/10.1016/j.jhydrol.2015.09.059

Harrington, G.A., Gardner, W.P., Munday, T.J., 2014. Tracking Groundwater Discharge to a Large River using Tracers and Geophysics. Groundwater 52, 837–852. https://doi.org/10.1111/gwat.12124

Harvey, J., Gooseff, M., 2015. River corridor science: Hydrologic exchange and ecological consequences from bedforms to basins. Water Resources Research 51, 6893–6922. https://doi.org/10.1002/2015WR017617

Harvey, J.W., Fuller, C.C., 1998. Effect of enhanced manganese oxidation in the hyporheic zone on basin-scale geochemical mass balance. Water Resources Research 34, 623–636. https://doi.org/10.1029/97WR03606

Harvey, J.W., Germann, P.F., Odum, W.E., 1987. Geomorphological control of subsurface hydrology in the creekbank zone of tidal marshes. Estuarine, Coastal and Shelf Science. 25, 677–691.

Harvey, J.W., Wagner, B.J., Bencala, K.E., 1996. Evaluating the Reliability of the Stream Tracer Approach to Characterize Stream-Subsurface Water Exchange. Water Resources Research 32, 2441–2451. https://doi.org/10.1029/96WR01268

Hatch, C.E., Fisher, A.T., Revenaugh, J.S., Constantz, J., Ruehl, C., 2006. Quantifying surface water-groundwater interactions using time series analysis of streambed thermal records. Water Resources Research 42. https://doi.org/10.1029/2005WR004787

Hayashi, M., Rosenberry, D.O., 2002. Effects of ground water exchange on the hydrology and ecology of surface water. Ground Water 40 (3), 309–316.

Hayashi, M. (2004), Temperature-electrical conductivity relation of water for environmental monitoring and geophysical data inversion, Environmental Monitoring and Assessment 96, 119–128.

Hayley, K., Bentley, L.R., Gharibi, M., Nightingale, M., 2007. Low temperature dependence of electrical resistivity: Implications for near surface geophysical monitoring. Geophysical Research Letters 34, L18402, 1-5. https://doi.org/10.1029/2007GL031124

Hayley, K., Pidlisecky, A., Bentley, L.R., 2011. Simultaneous time-lapse electrical resistivity inversion. Journal of Applied Geophysics 75, 401–411. https://doi.org/10.1016/j.jappgeo.2011.06.035

He, X., Koch, J., Sonnenborg, T.O., Jørgensen, F., Schamper, C., Christian Refsgaard, J., 2014. Transition probability-based stochastic geological modeling using airborne geophysical data and borehole data. Water Resources Research 50, 3147–3169. https://doi.org/10.1002/2013WR014593

Heppell, C., Heathwaite, L., Binley, A., Byrne, P., Ullah, S., Lansdown, K., Keenan, P., Trimmer, M., Zhang, H., 2014. Interpreting spatial patterns in redox and coupled water–nitrogen fluxes in the streambed of a gaining river reach. Biogeochemistry 117, 491–509. https://doi.org/10.1007/s10533-013-9895-4

Herckenrath, D., Fiandaca, G., Auken, E., Bauer-Gottwein, P., 2013. Sequential and joint hydrogeophysical inversion using a field-scale groundwater model with ERT and TDEM data. Hydrology and Earth System Sciences 17, 4043–4060. https://doi.org/10.5194/hess-17-4043-2013

Hering, D., Borja, A., Carstensen, J., Carvalho, L., Elliott, M., Feld, C.K., Heiskanen, A.S., Johnson, R.K., Moe, J., Pont, D., Solheim, A.L., van de Bund, W., 2010. The European water framework directive at the age of 10: a critical review of the achievements with recommendations for the future. Sci. Total Environ. 408 (19), 4007–4019. https://doi.org/10.1016/j.scitotenv.2010.05.031

Hestenes, M.R., Stiefel, E., 1952. Method of conjugate gradient for solving linear equations. Journal of Research National Bureau of Standards, 49, 409-436.

Hester, E.T., Cardenas, M.B., Haggerty, R., Apte, S.V., 2017. The importance and challenge of hyporheic mixing. Water Resources Research 53, 3565–3575. https://doi.org/10.1002/2016WR020005

Hester, E.T., Young, K.I., Widdowson, M.A., 2013. Mixing of surface and groundwater induced by riverbed dunes: Implications for hyporheic zone definitions and pollutant reactions. Water Resources Research 49 (9), 5221–5237. https://doi.org/10.1002/wrcr.20399

Hill, A.R., 1996. Nitrate removal in stream riparian zones. Journal of Environmental Quality, 25, 743–755.

Hinnell, A.C., Ferré, T.P.A., Vrugt, J.A., Huisman, J.A., Moysey, S., Rings, J., Kowalsky, M.B., 2010. Improved extraction of hydrologic information from geophysical data through coupled hydrogeophysical inversion. Water Resources Research 46 (4), 1–14. W00D40. https://doi.org/10.1029/2008WR007060

Hirsch, M., Bentley, L.R., Dietrich, P., 2008. A Comparison of Electrical Resistivity, Ground Penetrating Radar and Seismic Refraction Results at a River Terrace Site. Journal of Environmental and Engineering Geophysics 13, 325–333. https://doi.org/10.2113/JEEG13.4.325

Hohmann, G.W., 1982. Numerical modeling for electrical geophysical methods. Proceedings of the International Symposium for Applied Geophysics in Tropical Regions, 308–384.

Holliger, K., 2008. Groundwater geophysics: from structure and porosity towards permeability? In: Darnault, C.J.G. (Ed.), Overexploitation and Contamination of Shared Groundwater Resources: Management, (Bio)Technological, and Political Approaches to Avoid Conflicts. Springer, Dordrecht, Netherlands. https://doi.org/10.1007/978-1-4020-6985-7_4.

Hördt, A., Blaschek, R., Kemna, A., Zisser, N., 2007. Hydraulic conductivity estimation from induced polarisation data at the field scale — the Krauthausen case history. Journal of Applied Geophysics 62, 33–46. https://doi.org/10.1016/j.jappgeo.2006.08.001

House, A.R., Sorensen, J.P.R., Gooddy, D.C., Newell, A.J., Marchant, B., Mountford, J.O., Scarlett, P., Williams, P.J., Old, G.H., 2015. Discrete wetland groundwater discharges revealed with a three-dimensional temperature model and botanical indicators (Boxford, UK). Hydrogeology Journal 23, 775–787. https://doi.org/10.1007/s10040-015-1242-5

House, A.R., Thompson, J.R., Sorensen, J.P.R., Roberts, C., Acreman, M.C., 2016. Modelling groundwater/surface water interaction in a managed riparian chalk valley wetland: Modelling GW/SW Interaction in a Chalk Valley Wetland. Hydrological Processes 30, 447–462. https://doi.org/10.1002/hyp.10625

Hoversten, G.M., Cassassuce, F., Gasperikova, E., Newman, G.A., Chen, J., Rubin, Y., Hou, Z., Vasco, D., 2006. Direct reservoir parameter estimation using joint inversion of marine seismic AVA and CSEM data. Geophysics 71, C1–C13. https://doi.org/10.1190/1.2194510

Huang, J., Pedrera-Parrilla, A., Vanderlinden, K., Taguas, E.V., Gómez, J.A., Triantafilis, J., 2017. Potential to map depth-specific soil organic matter content across an olive grove using quasi-2d and quasi-3d inversion of DUALEM-21 data. Catena 152, 207–217. https://doi.org/10.1016/j.catena.2017.01.017

Huang, J., McBratney, A.B., Minasny, B., Triantafilis, J., 2017. Monitoring and modelling soil water dynamics using electromagnetic conductivity imaging and the ensemble Kalman filter. Geoderma 285, 76–93. https://doi.org/10.1016/j.geoderma.2016.09.027

Hubbard, S.S., Linde, N., 2011. Hydrogeophysics. In: Wilderer, P. (Ed.), Treatise on Water Science 2. Academic Press, Oxford, UK, pp. 401–432.

Huisman, J.A., Hubbard, S.S., Redman, J.D., Annan, A.P., 2003. Measuring Soil Water Content with Ground Penetrating Radar: A Review. Vadose Zone Journal 2, 476–491. https://doi.org/10.2113/2.4.476

Huisman, J.A., Rings, J., Vrugt, J.A., Sorg, J., Vereecken, H., 2010. Hydraulic properties of a model dike from coupled Bayesian and multi-criteria hydrogeophysical inversion. Journal of Hydrology 380, 62–73. https://doi.org/10.1016/j.jhydrol.2009.10.023

Hunt R.J., Krabbenhoft D.P., Anderson M.P., 1996. Groundwater inflow measurements in wetland systems. Water Resources Research, 32, 495–507.

Huntley, D, Bobrowsky, P Hendry, M, Macciotta, R, Elwood, D, Sattler, K, Best, M, Chambers, J, Meldrum, P, 2019. Application of multi-dimensional electrical resistivity tomography datasets to investigate a very slow-moving landslide near Ashcroft, British Columbia, Canada. Landslides, 16, 1033-1042.

Ingham, M., McConchie, J.A., Wilson, S.R., Cozens, N., 2006. Measuring and monitoring saltwater intrusion in shallow unconfined coastal aquifers using direct current resistivity traverses. Journal of Hydrology (New Zealand) 45 (2), 69–82.

Irvine, D.J., Lautz, L.K., 2015. High resolution mapping of hyporheic fluxes using streambed temperatures: recommendations and limitations. Journal of Hydrology 524, 137–146. https://doi.org/10.1016/j.jhydrol.2015.02.030.

Irvine, D.J., Cartwright, I., Post, V.E.A., Simmons, C.T., Banks, E.W., 2016. Uncertainties in vertical groundwater fluxes from 1-D steady state heat transport analyses caused by heterogeneity, multidimensional flow, and climate change. Water Resources Research 52, 813–826. https://doi.org/10.1002/2015WR017702.

Jackson, M.D., 2015. Tools and Techniques: self-potential methods. In: Schubert, G. (Ed.), 2nd ed. Treatise on Geophysics 11. Elsevier, Oxford, UK, pp. 261–293. https://doi.org/10.1016/B978-0-444-53802-4.00208-6.

Jacob, R.W., Hermance, J.F., 2004. Precision GPR measurements: assessing and compensating for instrument drift. In: Proceedings of the Tenth International Conference on Grounds Penetrating Radar. Delft, Netherlands, 159–162.

Jafar-Gandomi, A., Binley, A., 2013. A Bayesian trans-dimensional approach for the fusion of multiple geophysical datasets. Journal of Applied Geophysics 96, 38–54. https://doi.org/10.1016/j.jappgeo.2013.06.004

Jardani, A., Revil, A., Dupont, J.P., 2013. Stochastic joint inversion of hydrogeophysical data for salt tracer test monitoring and hydraulic conductivity imaging. Advances in Water Resources 52, 62–77. https://doi.org/10.1016/j.advwatres.2012.08.005

Johnes, P. J, Gooddy, D.C., Heaton, T.H.E., Binley, A., Kennedy, M.P., Shand, P., Prior H., 2020. Determining the Impact of Riparian Wetlands on Nutrient Cycling, Storage and Export in Permeable Agricultural Catchments, Water 12, 167.

Johnson, T.C., Versteeg, R.J., Hauang, H., Routh, P.S., 2009. Data-domain correlation approach for joint hydrogeologic inversion of time-lapse hydrogeologic and geophysical data. Geophysics 74 (6), F127–F140. http://library.seg.org/doi/abs/10.1190/1.3237087.

Johnson, T.C., Versteeg, R.J., Ward, A., Day-Lewis, F.D., Revil, A., 2010. Improved hydrogeophysical characterization and monitoring through parallel modeling and inversion of time-domain resistivity and induced-polarization data. Geophysics 75 (4), WA27–WA41.

Johnson, T.C., Slater, L.D., Ntarlagiannis, D., Day-Lewis, F.D., Elwaseif, M., 2012. Monitoring groundwater-surface water interaction using time-series and time-frequency analysis of transient three-dimensional electrical resistivity changes. Water Resources Research 48. https://doi.org/10.1029/2012WR011893

Johnson, T.C., Rucker, D.F., Glaser, D.R., 2015. Near-surface geophysics at the Hanford nuclear site, the United States. In: Schubert, G. (Ed.), 2nd edition. Treatise on Geophysics 11. Elsevier, Oxford, UK, pp. 571–595. https://doi.org/10.1016/B978-0-444-53802-4.00205-0.

Jørgensen, F., Scheer, W., Thomsen, S., Sonnenborg, T.O., Hinsby, K., Wiederhold, H., Schamper, C., Burschil, T., Roth, B., Kirsch, R., Auken, E., 2012. Transboundary geophysical mapping of geological elements and salinity distribution critical for the Syst. Sci. 16 (7), 1845–1862. https://doi.org/10.5194/hess-16-1845-2012.

Kaika, M., 2003. The Water Framework Directive: A New Directive for a Changing Social, Political and Economic European Framework. European Planning Studies 11, 299–316. https://doi.org/10.1080/09654310303640

Kalbus, E., Reinstorf, F., Schirmer, M., 2006. Measuring methods for groundwater-surface water interactions. Hydrology and Earth System Sciences 10, 873–887. https://doi.org/10.5194/hess-10-873-2006

Karaoulis, M., Revil, A., Werkema, D.D., Minsley, B.J., Woodruff, W.F., Kemna, A., 2011. Time-lapse three-dimensional inversion of complex conductivity data using an active time constrained (ATC) approach: Time-lapse complex conductivity imaging. Geophysical Journal International 187, 237–251. https://doi.org/10.1111/j.1365-246X.2011.05156.x

Käser, D.H., Binley, A., Heathwaite, A.L., Krause, S., 2009. Spatio-temporal variations of hyporheic flow in a riffle-step-pool sequence. Hydrol. Processes 23 (15), 2138–2149. https://doi.org/10.1002/hyp.

Käser, D., Binley, A.M., Heathwaite, A. L., 2013. On the importance of considering channel microforms in groundwater models of hyporheic exchange. River Res. Appl. 29 (4), 528–535. https://doi.org/10.1002/rra.

Kayranli, B., Scholz, M., Mustafa, A., Hedmark, Å., 2010. Carbon Storage and Fluxes within Freshwater Wetlands: a Critical Review. Wetlands 30, 111–124. https://doi.org/10.1007/s13157-009-0003-4

Kelly, B.F.J., Allen, D., Ye, K., Dahlin, T., 2009. Continuous electrical imaging for mapping aquifer recharge along reaches of the Namoi River in Australia. Near Surface Geophysics 7, 259–270. https://doi.org/10.3997/1873-0604.2009024

Kemna, A., Binley, A., Ramirez, A.L., Daily, W.D., 2000. Complex resistivity tomography for environmental applications. Chemical Engineering Journal 77, 11–18.

Kemna, A., Binley, A., Slater, L., 2004. Crosshole IP imaging for engineering and environmental applications. Geophysics 69, 97–107. https://doi.org/10.1190/1.1649379

Kemna, A., Binley, A., Cassiani, G., Niederleithinger, E., Revil, A., Slater, L., Williams, K., Flores-Orozco, A., Haegel, H., Kruschwitz, S., Leroux, V., Zimmermann, E., 2012. An overview of the spectral induced polarization method for near-surface applications. Near Surface Geophysics 10, 453–468. https://doi.org/10.3997/1873-0604.2012027.

Kennedy, C.D., Genereux, D.P., Corbett, D.R., Mitasova, H., 2009. Relationships among groundwater age, denitrification, and the coupled groundwater and nitrogen fluxes through a streambed. Water Resources Research 45, W09402, 1-15. https://doi.org/10.1029/2008WR007400

Kiel, B.A., Bayani Cardenas, M., 2014. Lateral hyporheic exchange throughout the Mississippi River network. Nature Geoscience 7, 413–417. https://doi.org/10.1038/ngeo2157

Kim, J. H., M. J. Yi, S. G. Park, . Kim, J. G., 2009, 4-D inversion of DC resistivity monitoring data acquired over a dynamically changing earth model. Journal of Applied Geophysics 68, 522–532

King, J.N., Mehta, A.J., Dean, R.G., 2009. Generalized analytical model for benthic water flux forced by surface gravity waves. Journal of Geophysical Research 114 (4), 1–14. C04004. https://doi.org/10.1029/2008JC005116.

Kinnear, J.A., Binley, A., Duque, C., Engesgaard, P.K., 2013. Using geophysics to map areas of potential groundwater discharge into Ringkøbing Fjord, Denmark. The Leading Edge 32, 792–796. https://doi.org/10.1190/tle32070792.1

Koestel, J., Kemna, A., Javaux, M., Binley, A., Vereecken, H., 2008. Quantitative imaging of solute transport in an unsaturated and undisturbed soil monolith with 3-D ERT and TDR. Water Resources Research 44. https://doi.org/10.1029/2007WR006755

Kowalsky, M.B., Finsterle, S., Peterson, J., Hubbard, S., Rubin, Y., Majer, E., Ward, A., Gee, G., 2005. Estimation of field-scale soil hydraulic and dielectric parameters through joint inversion of GPR and hydrological data. Water Resources Research 41 (11), 1–19. https://doi.org/10.1029/2005WR004237.

Krause, S., Heathwaite, L., Binley, A., Keenan, P., 2009. Nitrate concentration changes at the groundwater-surface water interface of a small Cumbrian river. Hydrological Processes 23, 2195–2211. https://doi.org/10.1002/hyp.7213

Krautblatter, M., Verleysdonk, S., Flores-Orozco, A., Kemna, A., 2010, Temperature-calibrated imaging of seasonal changes in permafrost rock walls by quantitative electrical resistivity tomography (Zugspitze, German/Austrian Alps). Journal of Geophysical Research 115, F02003.

Kuras, O., Pritchard, J.D., Meldrum, P.I., Chambers, J.E., Wilkinson, P.B., Ogilvy, R.D., Wealthall, G.P., 2009. Monitoring hydraulic processes with automated time-lapse electrical resistivity tomography (ALERT). Comptes Rendus Geoscience 341, 868–885. https://doi.org/10.1016/j.crte.2009.07.010

Kuras, O., Wilkinson, P.B., Meldrum, P.I., Oxby, L.S., Uhlemann, S., Chambers, J.E., Binley, A., Graham, J., Smith, N.T., Atherton, N., 2016. Geoelectrical monitoring of simulated subsurface leakage to support high-hazard nuclear decommissioning at the Sellafield Site, UK. Science of the Total Environment 566–567, 350–359. https://doi.org/10.1016/j.scitotenv.2016.04.212

Kuusemets, V., Mander, U., Lohmus, K., Ivask, M., 2001. Nitrogen and and assimilation in plants in complex riparian buffer zones. Water Science and Technology, 44, 615–622.

LaBrecque, D. J., M. Miletto, W. Daily, A. Ramirez, and E. Owen, 1996. The effects of noise on Occam's inversion of resistivity tomography data. Geophysics, 61, 538–548.

LaBrecque, D.J., Heath, G., Sharpe, R., Versteeg, R., 2004. Autonomous Monitoring of Fluid Movement Using 3-D Electrical Resistivity Tomography. Journal of Environmental and Engineering Geophysics 9, 167–176. https://doi.org/10.4133/JEEG9.3.167

LaBrecque, D. Yang, X., 2001. Difference Inversion of ERT Data: a Fast Inversion Method for 3-D in Situ Monitoring. Journal of Environmental and Engineering Geophysics 6, 2, 83-89.

LaBrecque, D., Daily, W., 2008. Assessment of measurement errors for galvanic-resistivity electrodes of different composition. Geophysics 73, 2 F55.

Lambot, S., Antoine, M., 2004. Electromagnetic Inversion of GPR Signals and Subsequent Hydrodynamic Inversion to Estimate Effective Vadose Zone Hydraulic Properties. Vadose Zone Journal 3, 10, 1071-1081.

Lambot, S., Slob, E.C., Vanclooster, M., Vereecken, H., 2006. Closed loop GPR data inversion for soil hydraulic and electric property determination. Geophysical Research Letters 33. https://doi.org/10.1029/2006GL027906

Lansdown, K., Heppell, C.M., Trimmer, M., Binley, A., Heathwaite, A.L., Byrne, P., Zhang, H., 2015. The interplay between transport and reaction rates as controls on nitrate attenuation in permeable, streambed sediments. Journal of Geophysical Research: Biogeosciences 120, 1093–1109. https://doi.org/10.1002/2014JG002874

Lansdown, K., Trimmer, M., Heppell, C.M., Sgouridis, F., Ullah, S., Heathwaite, A.L., Binley, A., Zhang, H., 2012. Characterization of the key pathways of dissimilatory nitrate reduction and their response to complex organic substrates in hyporheic sediments. Limnology and Oceanography 57, 387–400. https://doi.org/10.4319/lo.2012.57.2.0387

Larsen, L.G., Harvey, J.W., Maglio, M.M., 2014. Dynamic hyporheic exchange at intermediate timescales: Testing the relative importance of evapotranspiration and flood pulses. Water Resources Research 50, 318–335. https://doi.org/10.1002/2013WR014195

Lautz, L.K., Siegel, D.I., 2006. Modeling surface and ground water mixing in the hyporheic zone using MODFLOW and MT3D. Advances in Water Resources 29, 1618–1633. https://doi.org/10.1016/j.advwatres.2005.12.003

Lavoué, F., Van Der Kruk, J., Rings, J., André, F., Moghadas, D., Huisman, J.A., Lambot, S., Weihermüller, L., Vanderborght, J., Vereecken, H., 2010. Electromagnetic induction calibration using apparent electrical conductivity modelling based on electrical resistivity tomography. Near Surface Geophysics. 8 (6), 553–561.

Leroy, P., 2009. A mechanistic model for the spectral induced polarization of clay material. Journal of Geophysical Research 114, B10202.

Leroy, P., Revil, A., 2009. Spectral induced polarization of clays and clay-rocks. Journal of Geophysical Research 11 B10202.

Lesmes, D.P., Frye, K.M., 2001. Influence of pore fluid chemistry on the complex conductivity and induced polarization responses of Berea sandstone. Journal of Geophysical Research: Solid Earth 106 (B3), 4079–4090.

Lin, H., 2010. Earth's Critical Zone and hydropedology: concepts, characteristics, and advances. Hydrology and Earth Systems Science 21, 25–45.

Linde, N., Binley, A., Tryggvason, A., Pedersen, L.B., Revil, A., 2006. Improved hydrogeophysical characterization using joint inversion of cross-hole electrical resistance and ground-penetrating radar traveltime data. Water Resources Research 42. https://doi.org/10.1029/2006WR005131

Linde, N., Revil, A., 2007. Inverting self-potential data for redox potentials of contaminant plumes. Geophysical Research Letters 34. https://doi.org/10.1029/2007GL030084

Linde, N., Renard, P., Mukerji, T., Caers, J., 2015. Geological realism in hydrogeological and geophysical inverse modeling: a review. Water Resources Research 86, 86–90.

Loheide, S.P., Lundquist, J.D., 2009. Snowmelt-induced diel fluxes through the hyporheic zone. Water Resources Research 45. https://doi.org/10.1029/2008WR007329

Loke, M.H., Barker, R.D., 1996. Rapid least-squares inversion of apparent resistivity pseudosections using a quasi-Newton method. Geophysical Prospecting 44 (1), 131–152.

Loke, M.H., 2012. Tutorial: 2-D and 3-D Electrical Imaging Surveys. Geotomo Software, Malaysia.

Loke, M.H., Chambers, J.E., Rucker, D.F., Kuras, O., Wilkinson, P.B., 2013. Recent developments in the direct-current geoelectrical imaging method. Journal of Applied Geophysics 95, 135–156. https://doi.org/10.1016/j.jappgeo.2013.02.017

Loke, M. H., Wilkinson, P.B., Uhlemann, S.S., Chambers, J.E., Oxby, L.S., 2014. Computation of optimized arrays for 3-D electrical imaging surveys. Geophysical Journal International 199, 1751–1764. https://doi.org/10.1093/gji/ggu357

Loke, M.H., Wilkinson, P.B., Chambers, J.E., Strutt, M., 2014. Optimized arrays for 2D cross-borehole electrical tomography surveys: Arrays for 2D cross-borehole electrical tomography surveys. Geophysical Prospecting 62, 172–189. https://doi.org/10.1111/1365-2478.12072

Loke, M.H., Wilkinson, P.B., Chambers, J.E., Uhlemann, S.S., Sorensen, J.P.R., 2015. Optimized arrays for 2-D resistivity survey lines with a large number of electrodes. Journal of Applied Geophysics 112, 136–146. https://doi.org/10.1016/j.jappgeo.2014.11.011

Louie, J. N., 2001. Faster, better: Shear-wave velocity to 100 meters depth from refraction microtremor arrays. Bulletin of the Seismological Society of America 91, 2, 347–364

Ma, R., A. McBratney, B. Whelan, B. Minasny, Short, M., 2010. Comparing temperature correction models for soil electrical conductivity measurement. Precision Agriculture, 12, 1, 55–66.

Malard, F., Tockner, K., Dole-Olivier, M.-J., Ward, J.V., 2002. A landscape perspective of surface-subsurface hydrological exchanges in river corridors. Freshwater Biology 47, 621–640. https://doi.org/10.1046/j.1365-2427.2002.00906.x

Malzone, J.M., Anseeuw, S.K., Lowry, C.S., Allen-King, R., 2016. Temporal hyporheic zone response to water table fluctuations. Ground Water 54, 2, 274–285. https://doi.org/10.1111/gwat.12352.

Mansoor, N., Slater, L., 2007. Aquatic electrical resistivity imaging of shallow-water wetlands. Geophysics 72, F211–F221. https://doi.org/10.1190/1.2750667

Mansoor, N., Slater, L., Artigas, F., Auken, E., 2006. High-resolution geophysical characterization of shallow-water wetlands. Geophysics 71, B101–B109. https://doi.org/10.1190/1.2210307

Mares, R., Barnard, H.R., Mao, D., Revil, A., Singha, K., 2016. Examining diel patterns of soil and xylem moisture using electrical resistivity imaging. Journal of Hydrology 536, 327–338. https://doi.org/10.1016/j.jhydrol.2016.03.003

Marsh, T., Hannaford, J., 2008. UK Hydrometric register. Centre for Ecology and Hydrology, Wallingford, UK

Martinez, G., Vanderlinden, K., Ordóñez, R., Muriel, J.L., 2009. Can apparent electrical conductivity improve the spatial characterization of soil organic carbon? Vadose Zone Journal. 8 (3), 586–593.

Martini, E., Werban, U., Zacharias, S., Pohle, M., Dietrich, P., Wollschläger, U., 2017. Repeated electromagnetic induction measurements for mapping soil moisture at the field scale: validation with data from a wireless soil moisture monitoring network. Hydrology and Earth System Sciences 21, 495–513. https://doi.org/10.5194/hess-21-495-2017

Mary, B., Peruzzo, L., Boaga, J., Cenni, N., Schmutz, M., Wu, Y., Hubbard, S.S., Cassiani, G., 2019. Time-lapse monitoring of root water uptake using electrical resistivity tomography and Mise-à-la-Masse: a vineyard infiltration experiment. SOIL, 1–23. https://doi.org/10.5194/soil-2019-28

Marzadri, A., Dee, M.M., Tonina, D., Bellin, A., Tank, J.L., 2017. Role of surface and subsurface processes in scaling N_2O emissions along riverine networks. Proceedings of the National Academy of Sciences 114, 4330–4335. https://doi.org/10.1073/pnas.1617454114

Marzadri, A., Tonina, D., Bellin, A., 2013. Quantifying the importance of daily stream water temperature fluctuations on the hyporheic thermal regime: Implication for dissolved oxygen dynamics. Journal of Hydrology 507, 241–248. https://doi.org/10.1016/j.jhydrol.2013.10.030

McClymont, A.F., Roy, J.W., Hayashi, M., Bentley, L.R., Maurer, H., Langston, G., 2011. Investigating groundwater flow paths within proglacial moraine using multiple geophysical methods. Journal of Hydrology 399, 57–69. https://doi.org/10.1016/j.jhydrol.2010.12.036

McLachlan, P.J., Chambers, J.E., Uhlemann, S.S., Binley, A., 2017. Geophysical characterisation of the groundwater–surface water interface. Advances in Water Resources 109, 302–319. https://doi.org/10.1016/j.advwatres.2017.09.016

McNeill, J.D., 1980a. Electrical conductivity of soils and rock. Technical Note TN-5. Geonics Limited, Mississauga, Ontario, Canada.

McNeill, J.D., 1980b. Electromagnetic terrain conductivity measurement at low induction numbers. Technical Note TN-6Geonics Limited, Mississauga, Ontario, Canada.

Meier, P., Kalscheuer, T., Podgorski, J.E., Kgotlhang, L., Green, A.G., Greenhalgh, S., Rabenstein, L., Doetsch, J., Kinzelbach, W., Auken, Esben, Mikkelsen, P., Foged, N., Jaba, B.C., Tshoso, G., Ntibinyane, O., 2014. Hydrogeophysical investigations in the western and north-central Okavango Delta (Botswana) based on helicopter and ground-based transient electromagnetic data and electrical resistance tomography. Geophysics 79 (5), B201–B211. https://doi.org/10.1190/geo2014-0001.1.

Menichino, G.T., Ward, A.S., Hester, E.T., 2014. Macropores as preferential flow paths in meander bends. Hydrological Processes 28 (3), 482–495. https://doi.org/10.1002/hyp.9573.

Menichino, G.T., Hester, E.T., 2014. Hydraulic and thermal effects of in-stream structure-induced hyporheic exchange across a range of hydraulic conductivities. Water Resources Researcg. 50, 4643–4661. https://doi.org/10.1002/2013WR014758.

Menke, W., 2012. Geophysical Data Analysis: Discrete Inverse Theory, 3rd edition. Elsevier, Massachusetts, US.

Mermillod-Blondin, F., Winiarski, T., Foulquier, A., Perrissin, A., Marmonier, P., 2015. Links between sediment structures and ecological processes in the hyporheic zone: ground-penetrating radar as a non-invasive tool to detect subsurface biologically active zones. Ecohydrology 8 (4), 626–641. https://doi.org/10.1002/eco.1530.

Michot, D., Benderitter, Y., Doringny, A., Nicoullaud, B., King, D., Tabbagh, A., 2003. Spatial and temporal monitoring of soil water content with an irrigated corn crop cover using surface electrical resistivity tomography. Water Resources Research. 39 (5), 1–20. https://doi.org/10.1029/2002WR001581.

Miled, M.B.H., Miller, E.L., 2007. A projection-based level-set approach to enhance conductivity anomaly reconstruction in electrical resistance tomography. Inverse Problems 23 (6), 2375–2400. https://doi.org/10.1088/0266-5611/23/6/007.

Miller, R.B., Heeren, D.M., Fox, G.A., Halihan, T., Storm, D.E., Mittelstet, A.R., 2014. The hydraulic conductivity structure of gravel-dominated vadose zones within alluvial floodplains. Journal of Hydrology 513, 229–240. https://doi.org/10.1016/j.jhydrol.2014.03.046

Minsley, B., 2007. Modelling and Inversion of Self-Potential Data. Department of Earth, Atmospheric, and Planetary Sciences, Massachusetts Institute of Technology. https://dspace.mit.edu/bitstream/handle/1721.1/68023/Minsley_thesis2007.pdf?sequence=1

Mitchell, N., Nyquist, J.E., Toran, L., Rosenberry, D.O., Mikochik, J.S., 2008. Electrical Resistivity as a Tool for Identifying Geologic Heterogeneities Which Control Seepage at Mirror Lake, NH, in: Symposium on the Application of Geophysics to Engineering and Environmental Problems 2008. https://astro.temple.edu/~ltoran/docs/SAGEEP_2008_Paper_mirrorlake.pdf

Moghadas, D., 2020. One-dimensional deep learning inversion of electromagnetic induction data using convolutional neural network, Geophysical Journal International, available online: https://doi.org/10.1093/gji/ggaa161

Montaron, B., 2009. Connectivity theory – a new approach to modeling non-archie rocks. Petrophysics 50 (2), 102–115.

Moysey, S., Singha, K., Knight, R., 2005. A framework for inferring field-scale rock physics relationships through numerical simulation. Geophysical Researcg Letters 32 (8), 1–4. https://doi.org/10.1029/2004GL022152.

Musgrave, H., Binley, A., 2011. Revealing the temporal dynamics of subsurface temperature in a wetland using time-lapse geophysics. Journal of Hydrology 396, 258–266. https://doi.org/10.1016/j.jhydrol.2010.11.008

Musgrave, D.L., Reeburgh, W.S., 1982. Density-driven interstitial water motion in sediments. Nature 299 (5881), 331–334.

Muttil, N., Jayawardena, A.W., 2008. Shuffled Complex Evolution model calibrating algorithm: enhancing its robustness and efficiency. Hydrological Processes 22, 4628–4638. https://doi.org/10.1002/hyp.7082

Mwakanyamale, K., Day-Lewis, F.D., Slater, L.D., 2013. Statistical mapping of zones of focused groundwater/surface-water exchange using fiber-optic distributed temperature sensing: Statistical Mapping of Groundwater/Surface-Water Exchange. Water Resources Research 49, 6979–6984. https://doi.org/10.1002/wrcr.20458

Mwakanyamale, K., Slater, L., Binley, A., Ntarlagiannis, D., 2012. Lithologic imaging using complex conductivity: Lessons learned from the Hanford 300 Area. Geophysics 77, E397–E409. https://doi.org/10.1190/geo2011-0407.1

Ogilvy, R.D., Meldrum, P.I., Kuras, O., Wilkinson, P.B., Chambers, J.E., Sen, M., Pulido-Bosch, A., Gisbert, J., Jorreto, S., Frances, I., Tsourlos, P., 2009. Automated monitoring of coastal aquifers with electrical resistivity tomography. Near Surface Geophysics 7, 367–376. https://doi.org/10.3997/1873-0604.2009027

Nabighian, M.N., Macnae, J.C., 1991. Time-domain electromagnetic prospecting methods. In: Nabighian, M.N. (Ed.), Electromagnetic Methods in Applied Geophysics Theory 2. Society of Exploration Geophysicists, Oklahoma, US, pp. 427–520.

Nagorski, S.A., Moore, J.N., 1999. Arsenic mobilization in the hyporheic zone of a stream. Water Resources Research. 35 (11), 3441–3450. https://doi.org/10.1029/1999WR900204.

Naudet, V., Revil, A., Bottero, J., Bégassat, P., 2003. Relationship between self-potential (SP) signals and redox conditions in contaminated groundwater. Geophysical Research Letters. 30 (21), 1–4. https://doi.org/10.1029/2003GL018096.

Naudet, V., Revil, A., Rizzo, E., Bottero, J., Bégassat, P., 2004. Groundwater redox conditions and conductivity in a contaminant plume from geoelectrical investigations. Hydrological Earth Systems Science 8 (1), 8–22.

Nelder, J.A., Mead, R., 1965. A simplex method for function minimization. Computer Journal 7 (4), 308–313.

Nenna, V., Knight, R., 2013. Demonstration of a value of information metric to assess the use of geophysical data for a groundwater application. Geophysics 79 (1), E51–E60. https://doi.org/10.1190/geo2012-0474.1.

Newbold, J.D., O'Neill, R.V, Elwood, J.W., Van Winkle, W., 1982. Nutrient spiralling in streams: implications for nutrient limitation and invertebrate activity. American Naturalist 120 (5), 628–652.

Newell, A.J., Sorensen, J.P.R., Chambers, J.E., Wilkinson, P.B., Uhlemann, S.S., Roberts, C., Gooddy, D.C., Vane, C.H., Binley, A., 2015. Fluvial response to late Pleistocene and Holocene environmental change in a Thames chalkland headwater: the Lambourn of southern England. Proceedings of Geological Association 126 (6), 683–697. https://doi.org/10.1016/j.pgeola.2015.08.008.

Newell, A.J., Vane, C.H., Sorensen, J.P.R., Moss-Hayes, V., Gooddy, D.C., 2016. Long-term Holocene groundwater fluctuations in a chalk catchment: Evidence from Rock-Eval pyrolysis of riparian peats. Hydrological Processes, 30, 4556–4567.

Nyquist, J.E., Freyer, P., Toran, L., 2008. Stream bottom resistivity tomography to map ground water discharge. Ground Water 46 (4), 561–569. https://doi.org/10.1111/j.1745-6584.2008.00432.x.

Oldenborger, G.A., Logan, C.E., Hinton, M.J., Pugin, A.J.M., Sapia, V., Sharpe, D.R., Russell, H.A.J., 2016. Bedrock mapping of buried valley networks using seismic reflection and airborne electromagnetic data. Journal ofApplied Geophysics 128, 191–201. https://doi.org/10.1016/j.jappgeo.2016.03.006.

Oldenburg, D.W., Li, Y., 1999. Estimating depth of investigation in dc resistivity and IP surveys. Geophysics 64 (2), 403. https://doi.org/10.1190/1.1444545.

Orlando, L., 2013. Some considerations on electrical resistivity imaging for characterization of waterbed sediments. Journal of Applied Geophysics 95, 77–89. https://doi.org/10.1016/j.jappgeo.2013.05.005

Packman, A.I., MacKay, J.S., 2003. Interplay of stream-subsurface exchange, clay particle deposition, and streambed evolution. Water Resources Research 39, 4, 1097. https://doi.org/10.1029/2002WR001432

Parsekian, A.D., Comas, X., Slater, L., Glaser, P.H., 2011. Geophysical evidence for the lateral distribution of free phase gas at the peat basin scale in a large northern peatland. Journal of Geophysical Research 116, G03008. https://doi.org/10.1029/2010JG001543

Parsekian, A.D., Singha, K., Minsley, B.J., Holbrook, W.S., Slater, L., 2015. Multiscale geophysical imaging of the critical zone: Geophysical Imaging of the Critical Zone. Reviews of Geophysics 53, 1–26. https://doi.org/10.1002/2014RG000465

Pastick, N.J., Jorgenson, M.T., Wylie, B.K., Minsley, B.J., Ji, L., Walvoord, M.A., Smith, B.D., Abraham, J.D., Rose, J.R., 2013. Extending airborne electromagnetic surveys for regional active layer and permafrost mapping with remote sensing and ancillary data, Yukon Flats Ecoregion, Central Alaska. Permafrost and Periglacial Processes 24 (3), 184–199.

Phelps, G., Ippolito, C., Lee, R., Spritzer, J., Yeh, Y., 2014. Investigations into Near-real time surveying for Geophysical Data Collection Using an Autonomous Ground Vehicle. US Geological Survey Open File Report 2014-1013, 1–12.

Pidlisecky, A., Singha, K., Day-Lewis, F.D., 2011. A distribution-based parametrization for improved tomographic imaging of solute plumes: Distribution-based parametrizations. Geophysical Journal International 187, 214–224. https://doi.org/10.1111/j.1365-246X.2011.05131.x

Power, G., Brown, R.S., Imhof, J.G., 1999. Groundwater and fish–insights from northern North America. Hydrol. Process. 13 (3), 401–422.

Prendergast, L.J., Gavin, K., 2014. A review of bridge scour monitoring techniques. Journal of Rock Mechanics and Geotechnical Engineering 6, 138–149. https://doi.org/10.1016/j.jrmge.2014.01.007

Prior, H.; Johnes, P.J. 2002, Regulation of surface water quality in a Chalk catchment, UK: An assessment of the relative importance of instream and wetland processes. Science of the Total Environment, 282–283, 159–174.

R Core Team, 2018. R: A language and environment for statistical computing. R Foundation for Statistical Computing, Vienna, Austria. https://www.R-project.org/.

Rabbel, W., 2010. Seismic methods, in Groundwater Geophysics: A Tool for Hydrogeology, edited by R. Kirsch, pp. 23–84, Springer, Berlin.

Rayner S.F., Bentley L.R., Allen D.M., 2007. Constraining aquifer architecture with electrical resistivity imaging in a fractured hydrogeological setting. Journal of Environmental and Engineering Geophysics 12(4), 323–335.

Refsgaard, J.C., Auken, E., Bamberg, C.A., Christensen, B.S.B., Clausen, T., Dalgaard, E., Effersø, F., Ernsten, V., Gertz, F., Hansen, A.L., He, X., Jacobsen, B.H., Jensen, K.H., Jørgensen, F., Jørgensen, L., F., Koch, J., Nilsson, B., Peterson, C., De Schepper, G., Schamper, C., Sørensen, K.I., Therrien, R., Thirup, C., Viezzoli, A., 2014. Science of the total environment nitrate reduction in geologically heterogeneous catchments – a framework for assessing the scale of predictive capability of hydrological models. Science of the Total Environment. 468–469, 1278–1288. https://doi.org/10.1016/j.scitotenv.2013.07.042

Revil, A., 2005. Self-potential signals associated with preferential ground water flow pathways in a buried paleo-channel. Geophysical Research Letters 32 (7), L7401. https://doi.org/10.1029/2004GL022124

Revil, A., Atekwana, E., Zhang, C., Jardani, A., Smith, S., 2012a. A new model for the spectral induced polarization signature of bacterial growth in porous media. Water Resources Research 48. https://doi.org/10.1029/2012WR011965

Revil, A., Gevaudan, C., Lu, N., Maineult, A., 2008. Hysteresis of the self-potential response associated with harmonic pumping tests. Geophysical Research Letters 35, 16402.. https://doi.org/10.1029/2008GL035025

Revil, A., Karaoulis, M., Johnson, T., Kemna, A., 2012b. Review: Some low-frequency electrical methods for subsurface characterization and monitoring in hydrogeology. Hydrogeology Journal 20, 617–658. https://doi.org/10.1007/s10040-011-0819-x

Revil, A., Mendonça, C.A., Atekwana, E.A., Kulessa, B., Hubbard, S.S., Bohlen, K.J., 2010. Understanding biogeobatteries: Where geophysics meets microbiology. Journal of Geophysical Research 115. https://doi.org/10.1029/2009JG001065

Richards, L.A., Magnone, D., van Dongen, B.E., Polya, D.A., 2017. High resolution profile of inorganic aqueous geochemistry and key redox zones in an arsenic bearing aquifer in Cambodia. Science of the Total Environment. 590–591, 540–553. https://doi.org/10.1016/j.scitotenv.2017.02.217

Rizzo, E., Suski, B., Revil, A., 2004. Self-potential signals associated with pumping tests experiments. Journal of Geophysical Research: Solid Earth 109, B10203. https://doi.org/10.1029/2004JB003049.

Robinson, D.A., Binley, A., Crook, N., Day-Lewis, F.D., Ferré, T.P.A., Grauch, V.J.S., Knight, R., Knoll, M., Lakshmi, V., Miller, R., Nyquist, J., Pellerin, L., Singha, K., Slater, L., 2008. Advancing process-based watershed hydrological research using near-surface geophysics: a vision for, and review of, electrical and magnetic geophysical methods. Hydrological Processes 22, 3604–3635. https://doi.org/10.1002/hyp.6963

Robinson, D.A., Abdu, H., Lebron, I., Jones, S.B., 2012. Imaging of hill-slope soil moisture wetting patterns in a semi-arid oak savanna catchment using time-lapse electromagnetic induction. Journal of Hydrology. 416–417, 39–49. https://doi.org/10.1016/j.jhydrol.2011.11.034.

Rosenberry, D.O., LaBaugh, J.W., 2008. Field techniques for Estimating Water Fluxes Between Surface Water and Ground Water Techniques and Methods. US Geological Survey Techniques and Methods 4–D2, 1–128. http://pubs.usgs.gov/tm/04d02/.

Rubin, Y., Hubbard, S.S. (Eds.), 2005. Hydrogeophysics. Springer, Netherlands.

Rucker, D.F., Crook, N., Winterton, J., McNeill, M., Baldyga, C.A., Noonan, G., Fink, J.B., 2014. Real-time electrical monitoring of reagent delivery during a subsurface amendment experiment. Near Surface Geophysics 12, 151–163. https://doi.org/10.3997/1873-0604.2013017

Rucker, C., Gunther, T., Wagner, F.M., 2017, pyGIMLi: An open-source library for modelling and inversion in geophysics, Computers and Geosciences. 109, 106-123.

Russell, H.A.J., 2016. Bedrock mapping of buried valley networks using seismic reflection and airborne electromagnetic data. Journal of Applied Geophysics. 128, 191–201. https://doi.org/10.1016/j.jappgeo.2016.03.006.

Saey, T., De Smedt, P., Delefortrie, S., Van De Vijver, E., Van Meirvenne, M., 2015. Comparing one- and two-dimensional EMI conductivity inverse modeling procedures for characterizing a two-layered soil. Geoderma 241–242, 12–23. https://doi.org/10.1016/j.geoderma.2014.10.020

Saey, T., Van Meirvenne, M., De Smedt, P., Neubauer, W., Trinks, I., Verhoeven, G., Seren, S., 2013. Integrating multi-receiver electromagnetic induction measurements into the interpretation of the soil landscape around the school of gladiators at Carnuntum. European Journal of Soil Science. 64, 716–727.

Saey, T., Verhegge, J., De Smedt, P., Smetryns, M., Note, N., Van De Vijver, E., Laloo, P., Van Meirvenne, M., Delefortrie, S., 2016. Integrating cone penetration testing into the 1D inversion of multi-receiver EMI data to reconstruct a complex stratigraphic landscape. Catena 147, 356–371. https://doi.org/10.1016/j.catena.2016.07.023

Saneiyan, S., Ntarlagiannis, D., Ohan, J., Lee, J., Colwell, F., Burns, S., 2018. Induced polarization as a monitoring tool for in-situ microbial induced carbonate precipitation (MICP) processes. Ecological Engineering 172, 36-47.

Sassen, D.S., Hubbard, S.S., Bea, S.A., Chen, J., Spycher, N., Denham, M.E., 2012. Reactive facies: An approach for parameterizing field-scale reactive transport models using geophysical methods. Water Resources Research 48, W10526. https://doi.org/10.1029/2011WR011047

Sato, M., Mooney, H.M., 1960. The electrochemical mechanism of sulfide self-potentials. Geophysics 25 (1), 226–249. https://doi.org/10.1190/1.1438689.

Schmadel, N.M., Ward, A.S., Lowry, C.S., Malzone, J.M., 2016. Hyporheic exchange controlled by dynamic hydrologic boundary conditions. Geophys. Res. Lett. 43, 4408–4417. https://doi.org/10.1002/2016GL068286.

Schmitt, D.R., 2015. Geophysical properties of the near surface earth: seismic properties. In: Schubert, G. (Ed.), Treatise on Geophysics 11. Elsevier, Oxford, UK, 43–87.

Schumacher, B.A., Shines, K.C., Burton, J.V., Papp, M.L., 1990. A Comparison of Soil Sample Homogenization Techniques, Environmental Science. 54, 4 1187-1190.

Seigel, H. O., 1959. Mathematical formulation and type curves for induced polarization. Geophysics 24(3), 547–565.

Shabaga, J.A.; Hill, A.R., 2010. Groundwater-fed surface flow path hydrodynamics and nitrate removal in three riparian zones in southern Ontario, Canada. Journal of Hydrology, 388, 52–64.

Shanahan, P.W., Binley, A., Whalley, W.R., Watts, C.W., 2015. The use of electromagnetic induction to monitor changes in soil moisture profiles beneath different wheat genotypes. Soil Science Society of America Journal 79, 459–466.

Singha, K., Day-Lewis, F.D., Johnson, T., Slater, L.D., 2015. Advances in interpretation of subsurface processes with time-lapse electrical imaging. Hydrological Processes 29, 1549–1576. https://doi.org/10.1002/hyp.10280

Sri Niwas, and Singhal, D.C., 1981. Estimation of Aquifer Transmissivity from Dar Zarrouk Parameters in Porous Media. Journal of Hydrology. 50, 393–399.

Skoein, J. O., 2018. https://cran.r-project.org/web//packages/rtop/rtop.pdf

Slater, L., Binley, A. M., Daily, W., Johnson, R., 2000. Cross-hole electrical imaging of a controlled saline tracer injection. Journal of Applied Geophysics 44, 85-102.

Slater, L., D. Ntarlagiannis, N. Yee, M. O'Brien, C. Zhang, Williams, K. H., 2008. Electrodic voltages in the presence of dissolved sulfide: Implications for monitoring natural microbial activity. Geophysics, 73(2), F65-F70.

Slater, L.D. Atekwana, E.A., 2011. Biogeophysics. In: Gupta, H. K. (Ed.), Encyclopedia of Solid Earth Geophysics. Springer, Netherlands, 25–28.

Slater, L., Binley, A., Brown, D., 1997. Electrical Imaging of Fractures Using Ground-Water Salinity Change. Ground Water 35, 436–442.

Slater, L., Binley, A., 2006. Synthetic and field-based electrical imaging of a zerovalent iron barrier: Implications for monitoring long-term barrier performance. Geophysics 71, B129–B137. https://doi.org/10.1190/1.2235931

Slater, L., Ntarlagiannis, D., Personna, Y.R., Hubbard, S., 2007. Pore-scale spectral induced polarization signatures associated with FeS biomineral transformations. Geophysical Research Letters 34, L21404. https://doi.org/10.1029/2007GL031840

Slater, L.D., Lesmes, D., 2002. IP interpretation in environmental investigations. Geophysics 67, 77–88. https://doi.org/10.1190/1.1451353

Slater, L.D., Ntarlagiannis, D., Day-Lewis, F.D., Mwakanyamale, K., Versteeg, R.J., Ward, A., Strickland, C., Johnson, C.D., Lane, J.W., 2010. Use of electrical imaging and distributed temperature sensing methods to characterize surface water-groundwater exchange regulating uranium transport at the Hanford 300 Area, Washington. Water Resources Research 46, W10533. https://doi.org/10.1029/2010WR009110

Snyder, D.D., Wightman, W.E., 2002. Application of continuous resistivity profiling to aquifer characterization. In: Proceedings of the 15th Symposium on the Application of Geophysics to Engineering and Environmental Problems. Las Vegas, Nevada, USA

Sonkamble, S., Sahya, A., Jampani, M., Ahmed, S., Amerasinghe, P., 2019. Hydro-geophysical characterization and performance evaluation of natural wetlands in a semi-arid wastewater irrigated landscape. Water Research 148, 176–187. https://doi.org/10.1016/j.watres.2018.10.040

Sophocleous, M., 2002. Interactions between groundwater and surface water: the state of the science. Hydrogeology Journal 10, 52–67. https://doi.org/10.1007/s10040-001-0170-8

Soueid Ahmed, A., Jardani, A., Revil, A., Dupont, J.P., 2014. Hydraulic conductivity field characterization from the joint inversion of hydraulic heads and self-potential data. Water Resources Research 50, 3502–3522. https://doi.org/10.1002/2013WR014645

Soueid Ahmed, A., Jardani, A., Revil, A., Dupont, J.P., 2016. Joint inversion of hydraulic head and self-potential data associated with harmonic pumping tests. Water Resources Research 52 (9), 6769–6791.

Stanford, J.A., Ward, J.V., 1988. The hyporheic habitat of river ecosystems. Nature 335 (6185), 64–66. https://doi.org/10.1038/335064a0.

Stanford, J.A., Ward, J.V., 1993. An Ecosystem Perspective of Alluvial Rivers: Connectivity and the Hyporheic Corridor. Journal of the North American Benthological Society 12, 48–60. https://doi.org/10.2307/1467685

Steelman, C.M., Kennedy, C.S., Capes, D.C., Parker, B.L., 2017. Electrical resistivity dynamics beneath a fractured sedimentary bedrock riverbed in response to temperature and groundwater–surface water exchange. Hydrological and Earth Systems Science 21, 3105–3123. https://doi.org/10.5194/hess-21-3105-2017

Steeples, D.W., 2005. Shallow seismic methods. In: Rubin, Y., Hubbard, S.S. (Eds.), Hydrogeophysics 2. Springer, Netherlands, 215–251.

Stieglitz, T., Rapaglia, J., Bokuniewicz, H., 2008. Estimation of submarine groundwater discharge from bulk ground electrical conductivity measurements. Journal of Geophysical Research 113, C08007. https://doi.org/10.1029/2007JC004499

Stoll, J.B., 2013. Unmanned aircraft systems for rapid near surface geophysical measurements. International Archives of the Photogrammetry, Remote Sensing and Spatial Information Sciences. UAV-g2013, Rostock, Germany, pp. 391–394 XL-1/W2.

Stonedahl, S.H., Harvey, J.W., Packman, A.I., 2013. Interactions between hyporheic flow produced by stream meanders, bars, and dunes. Water Resources Research 49, 5450–5461. https://doi.org/10.1002/wrcr.20400

Stonedahl, S.H., Harvey, J.W., Wörman, A., Salehin, M., Packman, A.I., 2010. A multiscale model for integrating hyporheic exchange from ripples to meanders. Water Resources Research 46. https://doi.org/10.1029/2009WR008865

Stonestrom, D.A., Constantz, J., 2003. Heat as a Tool for Studying the Movement of Ground Water Near Streams. US Geological Survey Circular 1260, 1–96. https://doi.org/SBN0-607-94071-9.

Sudduth, K.A., Kitchen, N.R., Myers, D.B., Drummond, S.T., 2010. Mapping Depth to Argillic Soil Horizons Using Apparent Electrical Conductivity. Journal of Environmental and Engineering Geophysics 15, 135–146. https://doi.org/10.2113/JEEG15.3.135

Sudduth, K.A., Kitchen, N.R., Wiebold, W.J., Batchelor, W.D., Bollero, G.A., Bullock, D.G., Clay, D.E., Palm, H.L., Pierce, F.J., Schuler, R.T., Thelen, K.D., 2005. Relating apparent electrical conductivity to soil properties across the north-central USA. Computers and Electronics in Agriculture 46, 263–283. https://doi.org/10.1016/j.compag.2004.11.010

Sudduth, K.A., Myers, D.B., Kitchen, N.R., Drummond, S.T., 2013. Modeling soil electrical conductivity–depth relationships with data from proximal and penetrating ECa sensors. Geoderma 199, 12–21. https://doi.org/10.1016/j.geoderma.2012.10.006

Sudduth, K., Drummond, S.T., Kitchen, N., 2001. Accuracy issues in electromagnetic induction sensing of soil electrical conductivity for precision agriculture. Computers and Electronics in Agriculture 31, 239–264

Supper, R., Ottowitz, D.. Jochum, B., Römer, A., Pfeiler, S., Kauer, S., Keushnig, M., Ita, A., 2014. Geoelectrical monitoring of frozen ground and permafrost in alpine areas: Field studies and considerations towards an improved measuring technology. Near Surface Geophysics 12, 93–115.

Swarzenski, P.W., Simonds, F.W., Paulson, T., Kruse, S., 2007. Geochemical and geophysical examination of submarine groundwater discharge and associated nutrient loading estimates into Lynch Cove, Hood Canal, WA. US Geol. Surv. Environtal Science and Technology 41 (20), 7022–7029. http://pubs.er.usgs.gov/publication/70031439.

Tan, X., Mester, A., von Hebel, C., van der Kruk, J., Zimmerman, E., Vereecken, H., van Waasen, S., 2017. https://meetingorganizer.copernicus.org/EGU2017/EGU2017-2902-1.pdf

Tarantola, A., 2005. Inverse Problem Theory and Methods For Model Parameter Estimation. Society for Industrial And Applied Mathematics. [online] Available at: http://www.ipgp.fr/~tarantola/Files/Professional/Books/InverseProblemTheory.pdf [Accessed September 2019].https://doi.org/10.1137/1.9780898717921

Telford, W.M., Geldart, R.E., Sheriff, R.E., 2010. Applied Geophysics. Cambridge University Press, Cambridge, UK.

Terry, N., Day-Lewis, F.D., Robinson, J.L., Slater, L.D., Halford, K., Binley, A., Lane, J.W., Werkema, D., 2017. Scenario Evaluator for Electrical Resistivity Survey Pre-modeling Tool. Ground Water 55, 885–890. https://doi.org/10.1111/gwat.12522

Terry, N., Day-Lewis, F.D., Werkema, D. and Lane, J.W., Jr (2018), MoisturEC: A New R Program for Moisture Content Estimation from Electrical Conductivity Data. Ground Water, 56: 823-831

Tonina, D., Buffington, J.M., 2007. Hyporheic exchange in gravel bed rivers with pool-riffle morphology: laboratory experiments and three-dimensional modeling. Water Resources Research 43, 1–16. https://doi.org/10.1029/2005WR004328.

Tonina, D., Buffington, J.M., 2009. Hyporheic exchange in mountain rivers I: mechanics and environmental effects. Geography Compass 3 (3), 1063–1086.

Topp, G.C., Davis, J.L., Annan, A.P., 1980. Electromagnetic determination of soil water content: Water Resources Research 16(3), 574–582. https://doi.org/10.1029/WR016i003p00574.

Toran, L., Nyquist, J.E., Fang, A.C., Ryan, R.J., Rosenberry, D.O., 2013a. Observing lingering hyporheic storage using electrical resistivity: variations around stream restoration structures, Crabby Creek, PA. Hydrological Processes 27, 1411–1425. https://doi.org/10.1002/hyp.9269

Toran, L., Hughes, B., Nyquist, J., Ryan, R., 2013b. Freeze core sampling to validate time-lapse resistivity monitoring of the hyporheic zone. Ground Water 51 (4), 635–640. https://doi.org/10.1111/j.1745-6584.2012.01002.x.

Toran, L., Hughes, B., Nyquist, J., Ryan, R., 2012. Using hydrogeophysics to monitorchange in hyporheic flow around stream restoration structures. Environmental and Engineering Geoscience 18 (1), 83–97. https://doi.org/10.2113/gseegeosci.18.1.83.

Tóth, J., 1963. A theoretical analysis of groundwater flow in small drainage basins. Journal of Geophysical Research 68 (16), 4795–4812.

Travelletti, J., Sailhac, Malet, J. P., Grandjean, G., Ponton, J., 2012. Hydrological response of weathered clay-shale slopes: Water infiltration monitoring with time-lapse electrical resistivity tomography. Hydrological Processes 26, 2106–2119.

Triantafilis, J., Lesch, S. M., 2005. Mapping clay content variation using electromagnetic induction techniques. Computers and Electronics in Agriculture 46, 203–237.

Triska, F.J., Duff, J.H., Avanzino, R.J., 1993. The role of water exchange between a stream channel and its hyporheic zone in nitrogen cycling at the terrestrial-aquatic interface . Hydrobiologia 251, 167–184.

Triska, F.J., Kennedy, V.C., Avanzino, R.J., Zellweger, G.W., Bencala, K.E., 1989. Retention and Transport of Nutrients in a Third-Order Stream in Northwestern California: Hyporheic Processes. Ecology 70, 1893–1905. https://doi.org/10.2307/1938120

Tso, C.-H.M., Kuras, O., Wilkinson, P., Uhlemann, S., Chambers, J., Meldrum, P., Graham, J., Sherlock, E., Binley, A., 2017. Improved characterisation and modelling of measurement errors in electrical resistivity tomography (ERT) surveys. Journal of Applied Geophysics 146, 103-119. https://doi.org/10.1016/j.jappgeo.2017.09.009.

Turner, R., 2019. [online] Available at: https://mran.revolutionanalytics.com/web/packages/deldir/deldir.pdf [Accessed on September 2019].

Uhlemann, S.S., Sorensen, J.P.R., House, A.R., Wilkinson, P.B., Roberts, C., Gooddy, D.C., Binley, A.M., Chambers, J.E., 2016. Integrated time-lapse geoelectrical imaging of wetland hydrological processes. Water Resources Research 52, 1607–1625. https://doi.org/10.1002/2015WR017932

Uhlemann, S., Kuras, O., Richards, L.A., Naden, E., Polya, D.A., 2017. Electrical resistivity tomography determines the spatial distribution of clay layer thickness and aquifer vulnerability, Kandal Province, Cambodia. Journal of Asian Earth Sciences 147, 402-414. https://doi.org/10.1016/j.jseaes.2017.07.043.

Valett, H.M., Hakenkamp, C.C., Boulton, A.J., 1993. Perspectives on the Hyporheic Zone: Integrating Hydrology and Biology. Journal of the North American Benthological Society 12, 40–43. https://doi.org/10.2307/1467683

van der Kruk, J., 2015. Tools and Techniques: Ground-Penetrating Radar. In: Schubert, G. (Ed.) Treatise on Geophysics. Elsevier, pp. 209–232. https://doi.org/10.1016/B978-0-444-53802-4.00195-0

Viezzoli, A., Tosi, L., Teatini, P., Silvestri, S., 2010. Surface water-groundwater exchange in transitional coastal environments by airborne electromagnetics: the Venice Lagoon example. Geophysical Research Letters. 37 (1), 1–6. L01402. https://doi.org/10.1029/2009GL041572.

Vinegar, H.J., Waxman, M.H., 1984. Induced polarization of shaly sands. Geophysics 49 (8), 1267–1287. https://doi.org/10.1190/1.1441755.

von Gunten, H. R., Lienert, C., 1993. Decreased metal concentrations in ground water caused by controls of phosphate emissions. Nature 364, 220-222.

von Hebel, C., Rudolph, S., Mester, A., Huisman, J.A., Kumbhar, P., Vereecken, H., van der Kruk, J., 2014. Three-dimensional imaging of subsurface structural patterns using quantitative large-scale multiconfiguration electromagnetic induction data. Water Resources Research 50, 2732–2748. https://doi.org/10.1002/2013WR014864

Wait, J.R., 1982. Geo-Electromagnetism. Academic Press, New York.

Wallin, E.L., Johnson, T.C., Greenwood, W.J., Zachara, J.M., 2013. Imaging high stage river-water intrusion into a contaminated aquifer along a major river corridor using 2-D time-lapse surface

electrical resistivity tomography. Water Resources Research 49, 1693–1708. https://doi.org/10.1002/wrcr.20119

Wang, C., Slater, L., 2019. Extending accurate spectral induced polarization measurements into the kHz range: modelling and removal of errors from interactions between the parasitic capacitive coupling and the sample holder. Geophysical Journal International. 218, 2, 895–912.

Voytek, E.B., Rushlow, C.R., Godsey, S.E., Singha, K., Science, H., Program, E., 2016. Identifying hydrologic flowpaths on arctic hillslopes using electrical resistivity and self-potential. Geophysics 81 (1), 1–31. https://doi.org/10.1190/GEO2015-0172.1.

Ward, S.H., 1990. Resistivity and induced polarization methods. In: Ward, S.H. (Ed.), Geotechnical and Environmental Geophysics. Investigations in Geophysics No. 5. Society of Exploration Geophysicists, US, 147–190.

Ward, A.S., 2016. The evolution and state of interdisciplinary hyporheic research: The evolution and state of interdisciplinary hyporheic research. Wiley Interdisciplinary Reviews: Water 3, 83–103. https://doi.org/10.1002/wat2.1120

Ward, A.S., Fitzgerald, M., Gooseff, M.N., Voltz, T.J., Binley, A.M., Singha, K., 2012. Hydrologic and geomorphic controls on hyporheic exchange during base flow recession in a headwater mountain stream. Water Resources Research 48, W04513. https://doi.org/10.1029/2011WR011461

Ward, A.S., Gooseff, M.N., Singha, K., 2013a. How Does Subsurface Characterization Affect Simulations of Hyporheic Exchange? Ground Water 51, 14–28. https://doi.org/10.1111/j.1745-6584.2012.00911.x

Ward, A.S., Gooseff, M.N., Singha, K., 2010a. Imaging hyporheic zone solute transport using electrical resistivity. Hydrological Processes 24, 948–953. https://doi.org/10.1002/hyp.7672

Ward, A.S., Gooseff, M.N., Singha, K., 2010b. Characterizing hyporheic transport processes — Interpretation of electrical geophysical data in coupled stream–hyporheic zone systems during solute tracer studies. Advances in Water Resources 33, 1320–1330. https://doi.org/10.1016/j.advwatres.2010.05.008

Ward, A.S., Gooseff, M.N., Voltz, T.J., Fitzgerald, M., Singha, K., Zarnetske, J.P., 2013b. How does rapidly changing discharge during storm events affect transient storage and channel water balance in a headwater mountain stream? Water Resources Research 49, 5473–5486. https://doi.org/10.1002/wrcr.20434

Waxman, M. H., Smits, L. J. M., 1968. Electrical Conductivities in Oil-Bearing Shaly Sands. Society of Petroleum Engineers Journal 8, 107–122.

Webb, D.J., Anderson, N.L., Newton, T., Cardimona, S., 2000. Bridge Scour: Application of Ground Penetrating Radar. [online] Transportation.mst.edu. Available at: https://transportation.mst.edu/media/research/transportation/documents/scour.pdf [Accessed September 2019].

Webster, I.T., Norquay, S.J., Ross, F.C., Wooding, R.A., 1996. Solute Exchange by Convection Within Estuarine Sediments. Estuarine, Coastal and Shelf Science 42, 171–183. https://doi.org/10.1006/ecss.1996.0013

Weller, A., Slater, L., Binley, A., Nordsiek, S., Xu, S., 2015a. Permeability prediction based on induced polarization: Insights from measurements on sandstone and unconsolidated samples spanning a wide permeability range. Geophysics 80, D161–D173. https://doi.org/10.1190/geo2014-0368.1

Weller, A., Slater, L., Huisman, J.A., Esser, O., Haegel, F.-H., 2015b. On the specific polarizability of sands and sand-clay mixtures. Geophysics 80, A57–A61. https://doi.org/10.1190/geo2014-0509.1

Weller, A., Slater, L., Nordsiek, S., 2013. On the relationship between induced polarization and surface conductivity: Implications for petrophysical interpretation of electrical measurements. Geophysics 78, D315–D325. https://doi.org/10.1190/geo2013-0076.1

Weller, A., Slater, L.D., 2015. Induced polarization dependence on pore space geometry: Empirical observations and mechanistic predictions. Journal of Applied Geophysics 123, 310–315. https://doi.org/10.1016/j.jappgeo.2015.09.002

Whitehead, K., Hudenholtz, C.H., 2014a. Remote sensing of the environment with small unmanned aircraft systems (UASs) part 1: a review of progress and challenges. Journal of Unmanned Vehicles and Systems 2 (3), 69–85.

Whitehead, K., Hugenholtz, C.H., Myshak, S., Brown, O., LeClair, A., Tamminga, A., Barchyn, T.E., Moorman, B., Eaton, B., 2014b. Remote sensing of the environment with small unmanned aircraft systems (UASs) part 2: scientific and commercial applications. Journal of Unmanned Vehicles and Systems 2 (3), 86–102.

Wilkinson, P.B., Meldrum, P.I., Chambers, J.E., Kuras, O., Ogilvy, R., 2006. Improved strategies for the automatic selection of optimized sets of electrical resistivity tomography measurement configurations. Geophysical Journal International 167 (3), 1119–1126.

Wilkinson, P.B., Meldrum, P.I., Kuras, O., Chambers, J.E., Holyoake, S.J., Ogilvy, R.D., 2010. High-resolution Electrical Resistivity Tomography monitoring of a tracer test in a confined aquifer. Journal of Applied Geophysics 70, 268–276. https://doi.org/10.1016/j.jappgeo.2009.08.001

Wilkinson, P.B., Loke, M.H., Meldrum, P.I., Chambers, J.E., Kuras, O., Gunn, D.A., Ogilvy, R.D., 2012. Practical Aspects of Applied Optimised Survey Design for Electrical Resistivity Tomography. Geophysical Journal International 189, 428–440. https://doi.org/10.1111/j.1365-246X.2012.05372.x/pdf

Williams BG, Baker GC (1982) An electromagnetic induction technique for reconnaissance surveys of soil salinity hazards. Australian Journal of Soil Research 20, 107-118

Williams, B.A., Thompson, M.D., Miller, S.F., 2012a. Integrated Surface Geophysical Investigation Results at Liquid Effluent Retention Facility, 200 East Area, Hanford. CH2MHill Plateau Remediation Company, Richland, Washington.

Williams, B.A., Thompson, M.D., Miller, S.F., 2012b. Interpretation and Integration of Seismic Data in the Gable Gap. CH2MHill Plateau Remediation Company, Richland, Washington.

Williams, B.A., Thompson, M.D., Miller, S.F., 2012c. Land Streamer and Gimbaled Geophones Phase II-200 Areas: High-Resolution Seismic Reflection Survey At the Hanford Site. CH2MHill Plateau Remediation Company , Richland, Washington.

Williams, B.A., Thompson, M.D., Miller, S.F., 2012d. Seismic Reflection Investigation At the Liquid Effluent Retention Facility, 200 East Area, Hanford Site. CH2MHill Plateau Remediation Company, Richland, Washington.

Williams, K.H., Ntarlagiannis, D., Slater, L.D., Dohnalkova, A., Hubbard, S.S., Banfield, J.F., 2005. Geophysical Imaging of Stimulated Microbial Biomineralization. Environmental Science and Technology 39, 7592–7600. https://doi.org/10.1021/es0504035

Wilson, J., Coxon, C., Rocha, C., 2016. A GIS and remote sensing based screening tool for assessing the potential for groundwater discharge to lakes in Ireland. Biology and Environment: Proceedings of the Royal Irish Academy 116B (3), 265–277. https://doi.org/10.3318/bioe.2016.15.

Winter, T., 1976. Numerical Simulation Analysis of the Interaction of Lakes and Groundwater. US Geological Survey Professional Paper 1001, 1–45. https://pubs.er.usgs.gov/publication/pp1001.

Winter, T.C., Harvey, J.W., Franke, O.L., Alley, W.M., 1998. Ground Water and Surface Water: A Single Resource. US Geological Survey Circular 1139, 1–79.

Wishart, D.N., Slater, L.D., Gates, A.E., 2006. Self-potential improves characterization of hydraulically-active fractures from azimuthal geoelectrical measurements. Geophysical Research Letters 33 (17), 2–6. https://doi.org/10.1029/2006GL027092.

Wishart, D.N., Slater, L.D., Gates, A.E., 2008. Fracture anisotropy characterization in crystalline bedrock using field-scale azimuthal self-potential gradient. Journal of Hydrology 358 (1–2), 35–45. https://doi.org/10.1016/j.jhydrol.2008.05.017.

Woessner, W.W., 2000. Stream and fluvial plain ground water interactions: rescaling hydrogeological thought. Ground Water 38 (3), 423–429.

Wojnar, A.J., Mutiti, S., Levy, J., 2013. Assessment of geophysical surveys as a tool to estimate riverbed hydraulic conductivity. Journal of Hydrology 482, 40–56. https://doi.org/10.1016/j.jhydrol.2012.12.018

Wondzell, S.M., Gooseff, M.N., McGlynn, B.L., 2010. An analysis of alternative conceptual models relating hyporheic exchange flow to diel fluctuations in discharge during baseflow recession. Hydrological Processes 24, 686–694. https://doi.org/10.1002/hyp.7507

Worrall, L., Munday, T.J., Green, A.A., 1999. Airborne electromagnetics – providing new perspectives on geomorphic process and landscape development in regolith-dominated terrains. Physics and Chemistry of the Earth 24 (10), 855–860. https://doi.org/10.1016/S1464-1895(99)00127-1.

Wynn, J.C., Sherwood, S.I., 1986. The self-potential (SP) method: an inexpensive reconnaissance and archaeological mapping tool. Journal of Field Archaeology 11 (2), 195–204. https://doi.org/10.1179/jfa.1984.11.2.195.

Xie, Y., Cook, P.G., Shanafield, M., Simmons, C.T., Zheng, C., 2016. Uncertainty of natural tracer methods for quantifying river–aquifer interaction in a large river. Journal of Hydrology 535, 135–147. https://doi.org/10.1016/j.jhydrol.2016.01.071

Yoshikawa, K., Hinzman, L.D., 2003. Shrinking thermokarst ponds and groundwater dynamics in discontinuous permafrost near Council, Alaska. Permafrost and Periglacial Processes 14 (2), 151–160. https://doi.org/10.1002/ppp.451.

Younger, P.L., 1989. Devensian periglacial influences on the development of spatially variable permeability in the Chalk of southeast England. Quarterly Journal of Engineering Geology and Hydrogeology 22, 343–354. https://doi.org/10.1144/GSL.QJEG.1989.022.04.07

Zarroca, M., Linares, R., Rodellas, V., Garcia-Orellana, J., Roqué, C., Bach, J., Masqué, P., 2014. Delineating coastal groundwater discharge processes in a wetland area by means of electrical resistivity imaging, 224Ra and 222Rn. Hydrological Processes 28 (4), 2382–2395. https://doi.org/10.1002/hyp.9793

Zhang, J., Revil, A., 2015. 2D joint inversion of geophysical data using petrophysical clustering and facies deformation. Geophysics 80 (5), M69–M88. https://doi.org/10.1190/geo2015-0147.1

Zhou, B., Greenhalgh, S.A., 2000. Cross-hole resistivity tomography using different electrode configurations. Geophysical Prospecting 48 (5), 887–912. https://doi.org/10.1046/j.1365-2478.2000.00220.x.

Zhou, J., Revil, A., Karaoulis, M., Hale, D., Doetsch, J., Cuttler, S., 2014. Image-guided inversion of electrical resistivity data. Geophysics Journal International 197 (1), 292–309. https://doi.org/10.1093/gji/ggu001.

Zimmer, M.A., Lautz, L.K., 2014. Temporal and spatial response of hyporheic zone geo-chemistry to a storm event. Hydrological Processes 28 (4), 2324–2337. https://doi.org/10.1002/hyp.9778.

Zarif, F., Kessouri, P., Slater, L., 2018. Recommendations for Field-Scale Induced Polarization (IP) Data Acquisition and Interpretation. Journal of Environmental and Engineering Geophysics 22(4), 395–410.

Zarroca, M., Linares, R., Rodellas, V., Garcia-Orellana, J., Roqué, C., Bach, J., Masqué, P., 2014. Delineating coastal groundwater discharge processes in a wetland area by means of electrical resistivity imaging, [224]Ra and [222]Rn. Hydrological Processes 28, 2382–2395. https://doi.org/10.1002/hyp.9793

Zhou, B., Dahlin, T., 2003. Properties and effects of measurement errors on 2D resistivity imaging surveying. Near Surface Geophysics 1, 105–117. https://doi.org/10.3997/1873-0604.2003001

Zohdy, A.A.R., Jackson, D.B., 1969. Application of deep electrical soundings for ground-water exploration in Hawaii. Geophysics 34 (4), 584–600.

10 Appendix 1 – R Functions for Filtering Electrical Data and Facilitating Inverse Modelling via R2 and cR2

The codes used to produce the case study figures in Chapter 3 are shown in figures below. In addition the names of the R functions for filtering and modelling resistivity and induced polarisation data, their required inputs and a brief description are shown in Table A1.1. The codes used are available to access and download at https://1drv.ms/u/s!AkZoCSS-z-n_g7JOxTR0ztDz8HjVVw?e=QOCgam.

```
pretty.tri(xyz_df=inv_mod_df2[,c(1,2,3)], ylim=c(-20,20), elec_df=elec_df, zones=zones, crop_end=T,
zlab='Resistivity\n(Ohm.m)',zlim=c(0,1400))
```
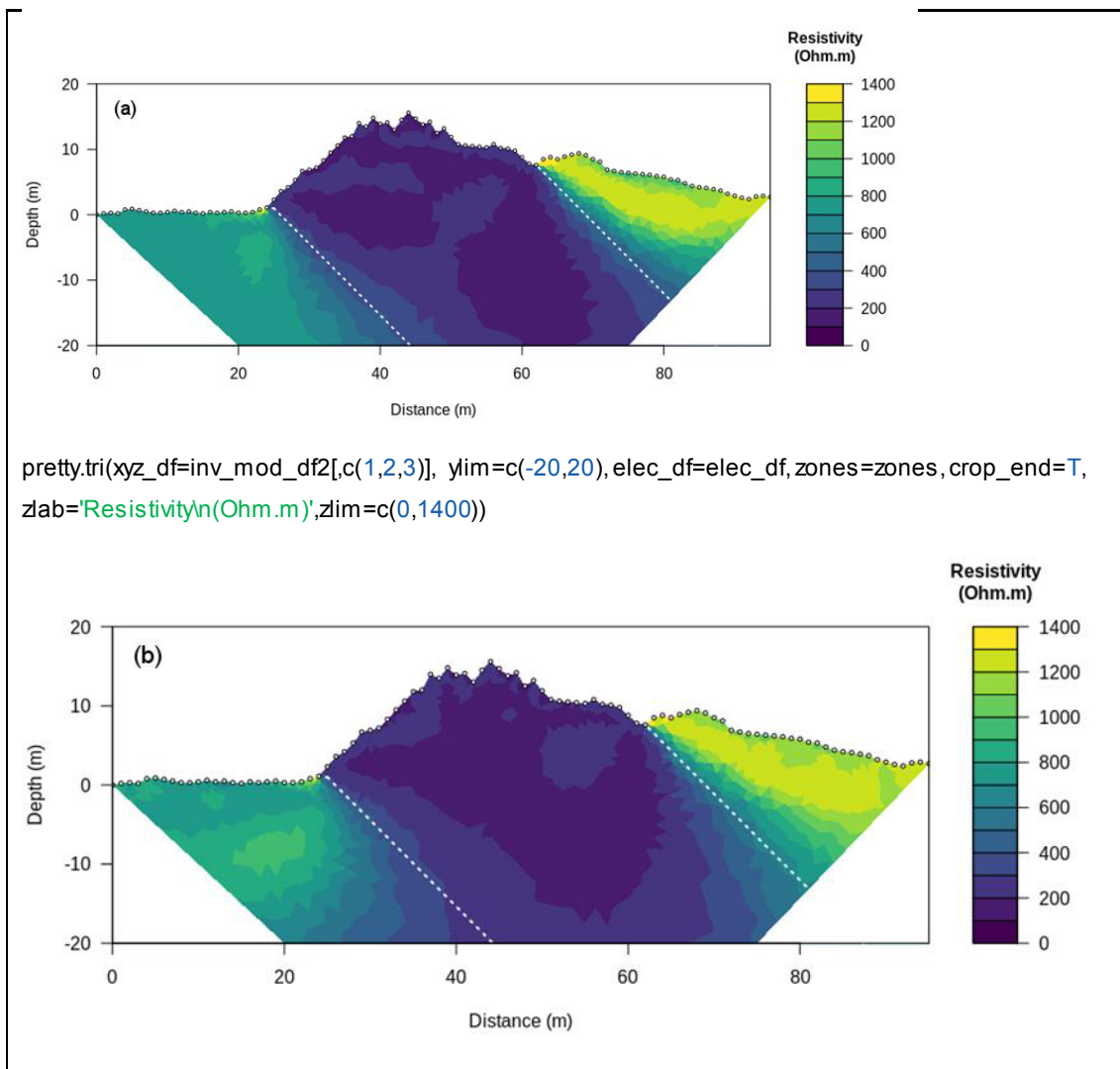

Figure 10.1: R script for Case 1, generating and inverting synthetic data for (a) a dipole-dipole, and (b) a Schlumberger array. White circles indicate electrode positions.

```r
#import functions
source('/home/R_ELEC.R')

#import electrode positions
x <- seq(0,17.5,0.5)
z <- c(0.6,0.6,0.7,0.64,0.7,0.75,0.7,0.66,0.7,0.72,0.7,0.6,
       0.0,-0.8,-1.3,-1.35,-1.4,-1.44,-1.4,-1.35,-1.3,-1.3,-1.2,-0.8,
       0.65,0.7,0.7,0.75,0.7,0.8,0.75,0.8,0.7,0.8,0.72,0.8)

buried <- c(rep(T, 13), rep(F, 11), rep(T, 12)))
elec_df <- cbind(x, z, buried)

#write mesh and create zones for starting model
write.tri.mesh(elec_df=elec_df,cl1=0.05,cl2=2, doi=6, topo_points_df=cbind(c(6.25, 11.55), c(-0.5, -0.5)))

zones <- list(list(x=c(-10,0,2,4,6,8,10,12,14,16,18,28,28,-10),
                   y=c(-0.8,-1.2,-1.0,-1.1,-1.2,-1.3,-1.2,-1.1,-1,-1.1,-1.2,-1, -10,-10), res=200),
             list(x=c(6.25,11.55,11.5,11,10.5,10,9.5,9,8.5,8,7.5,7,6.5),
                   y=c(-0.5,-0.5,-0.8,-1.2,-1.3,-1.3,-1.35,-1.4,-1.44,-1.4,-1.35, -1.3,-0.8), res=20))

#create dipole-dipole array synthetic data and write to protocol.dat file
write.seq(elec_df, a=1:4, n=1:8, typ='dpdp')
synth_data_df <- return.synth.data(elec_df=elec_df, prog='R2', zones=zones, bg_res=50)
synth_data_df2 <- add.noise(synth_data_df, res_err=0.02)
write.protocol.dat(res_data_df=synth_data_df2)

#write coarser mesh and invert dipole-dipole array synthetic data with and without blocked river
write.tri.mesh(elec_df,cl1=0.1,cl2=4, doi=4, topo_points_df=cbind(c(6.25,11.55),c(-0.5,-0.5)))

inv_mod_df1 <- return.inv.mod(elec_df=elec_df, res_err=0.02)

block.mesh(zones[2], fixed=F)
inv_mod_df2 <- return.inv.mod(elec_df=elec_df, res_err=0.02)

block.mesh(zones[2], fixed=T)
inv_mod_df3 <- return.inv.mod(elec_df=elec_df, res_err=0.02)

#load synthetic model and plot results
pretty.tri(xyz_df=inv_mod1[,c(1,2,3)],  ylim=c(-4,1), elec_df=elec_df, zones=zones,  crop_end=T,
zlab='Resistivity\n(Ohm.m)', zlim=c(0,220), topo_points_df=cbind(c(6.25, 11.55), c(-0.5,-0.5)))
```
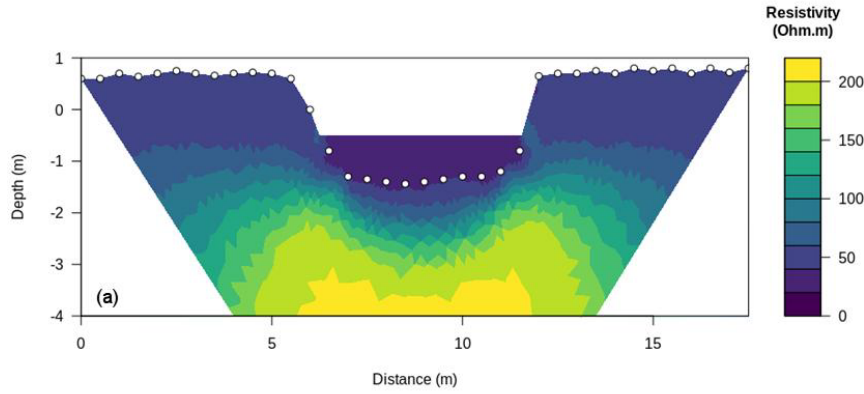
```
pretty.tri(xyz_df=inv_mod2[,c(1,2,3)], ylim=c(-4,1), elec_df=elec_df, zones=zones, crop_end=T,
zlab='Resistivity\n(Ohm.m)', zlim=c(0,220), topo_points_df=cbind(c(6.25, 11.55), c(-0.5,-0.5)))
```
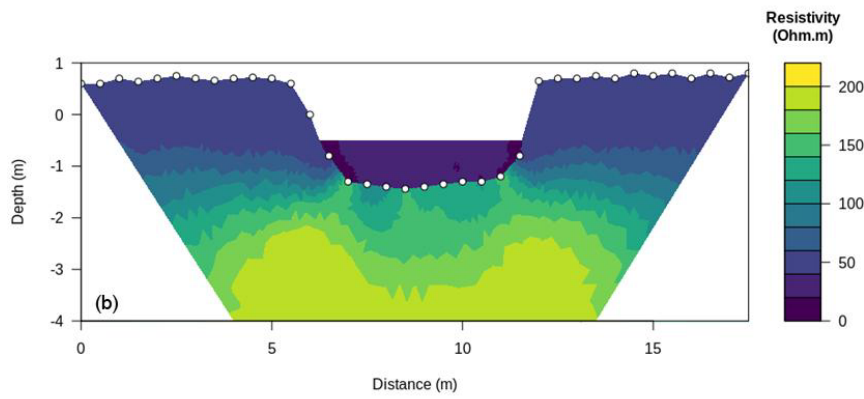


```
pretty.tri(xyz_df=inv_mod3[,c(1,2,3)], ylim=c(-4,1), elec_df=elec_df, zones=zones, crop_end=T,
zlab='Resistivity\n(Ohm.m)', zlim=c(0,220), topo_points_df=cbind(c(6.25,11.55), c(-0.5,-0.5)))
```
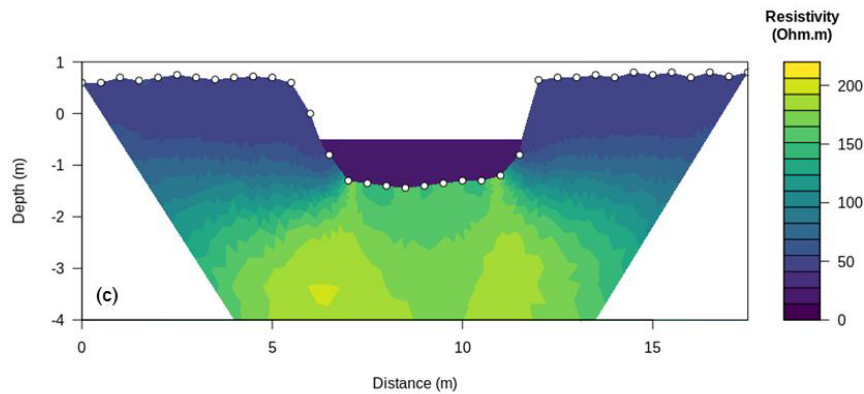

Figure 10.2: Code to replicate Case 2 in Chapter 3, (a) modelled resistivity with no regularisation block, (b) modelled resistivity with separate regularisation in river, and bed-riparian zone, and (c) fixed river resistivity.

216

```
#import functions
source('/home/R_ELEC.R')


#import electrode positions
elec_df <- cbind(seq(0, 23.5, 0.5), rep(0, 24), c(rep(T, 24)))
ip_data_df <- read.delim('case3_ip_data.dat', sep="")


#filter ip data based on decay curves, pair measurements, plot pseudo-sections and fit error models
t <- seq(480, 3520, 160)
ip_data_df <- filt.decay.curves(ip_data_df=ip_data_df, t=t, min_r_sq=0.9, plt=T)
```
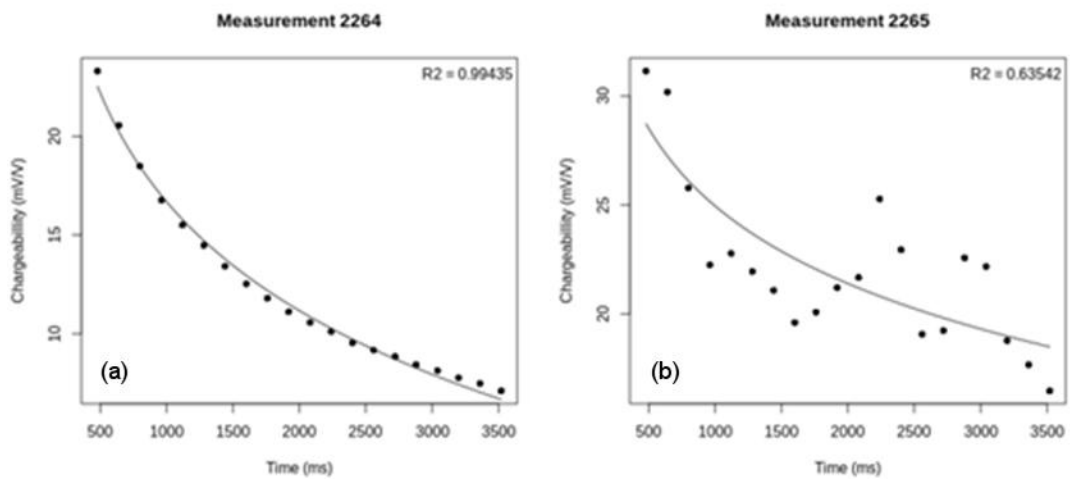


```
res_data_df <- pair.meas(res_dat_df=ip_data_df, phase=T)
plot.pseudo(res_data_df, plt='AppRes', elec_spa=0.5)
```
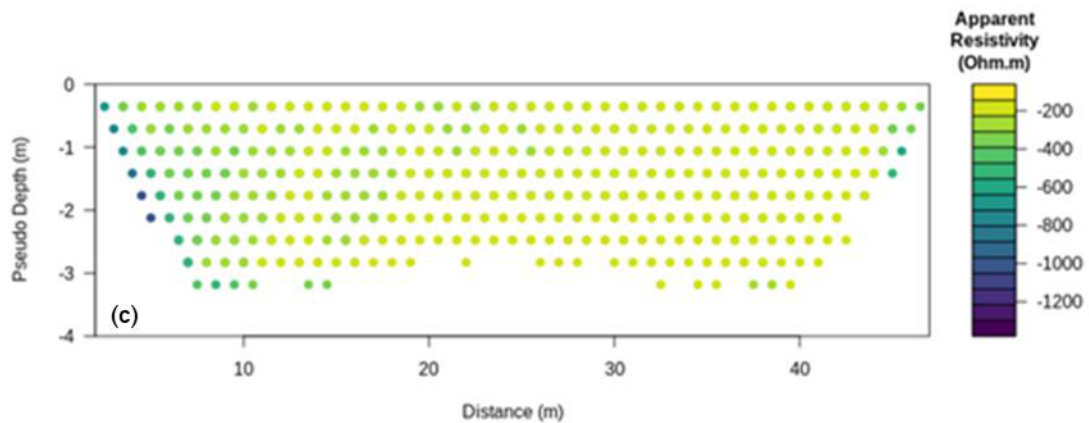
```
plot.pseudo(res_data_df, cols=inferno(256), plt='Phase')
```
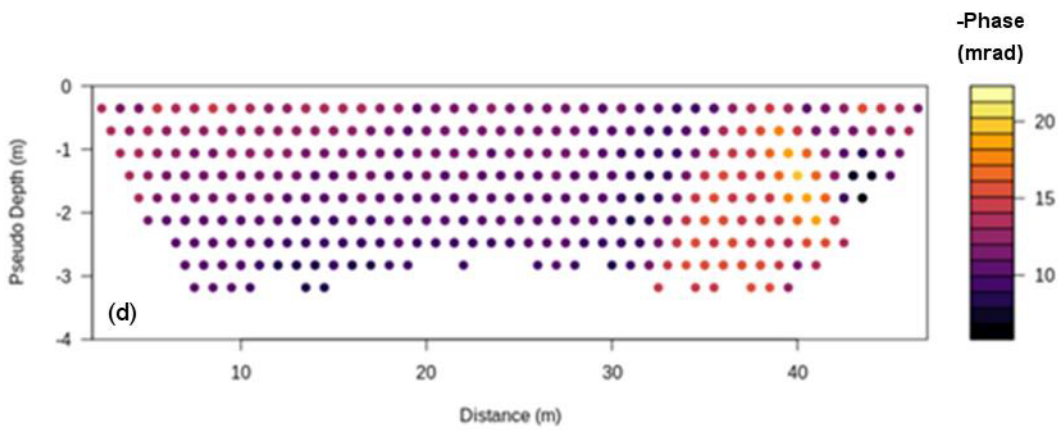


```
err.mod(res_data_df=res_data_df, nbins=15, plt=T, res_err_mod='powerlaw', phase_err_mod='')
```
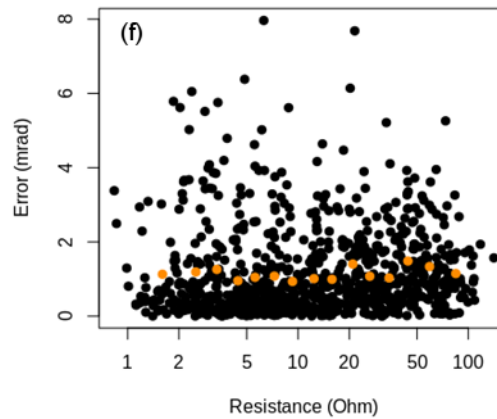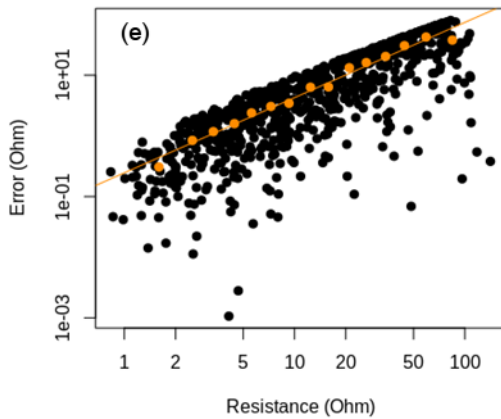


```
#write files for cR2 inversion and run cR2.exe
write.protocol.dat(res_data_df=res_data_df)
inv_mod_df <- return.inv.mod(elec_df=elec_df, prog='cR2', res_err=0.02,
phase_err=0.5, start_res=100, start_phase=-5)

#plot resistivity and phase models
pretty.tri2(xyz_df=inv_mod_df1[,c(1,2,5)], elec_df=elec_df, ylim=c(4,0), zlab='Resistivity\n(Ohm.m)')
```

```
pretty.tri2(xyz_df=inv_mod_df1[,c(1,2,4)], elec_df=elec_df,cols=inferno(256),ylim=c(-4,0),zlab='-
Phase\n(mrad)')
```
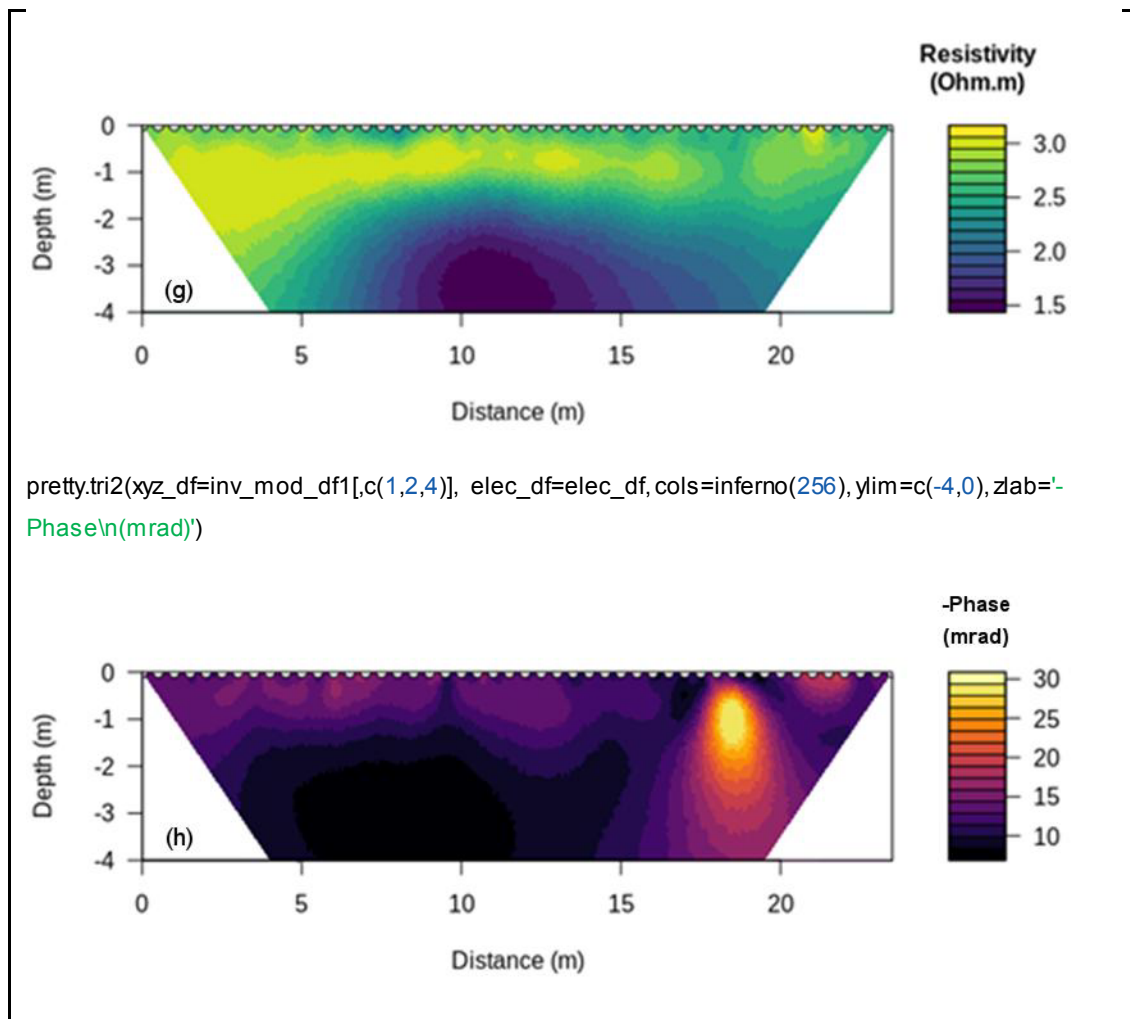

Figure 10.3: Code to replicate Case 3 in Chapter 3, (a) acceptable decay curve, (b) rejected decay curve, (c) apparent resistivity pseudo-section, (d) phase pseudo-section, (e) resistance errors, (f) phase errors, (g) inverted resistivity model, and (h) inverted phase model.

Table 10.1: Data-related functions for geoelectrical data.

Function Name	Input Parameters	Description
filt.decay.curves()	**ip_data_df** - induced polarisation data frame comprising A, B, M, N, transfer resistance, chargeability and integral chargeabilities. **t** - vector pf time windows. **min_r_sq** - minimum allowable R^2 of decay curve. **plt** - True or False value to determine if decay curves are plotted or not. **m** - coefficient by which to multiply chargeabilities by to convert to phase values. Default value **m=-1.**	Filters time domain IP data
pair.meas()	**res_dat_df** - resistance data frame comprising A, B, M, N, transfer resistance and phase values (optional) of both direct and reciprocal measurements. **phase** - True or false value determining whether averages and	Pairs direct and reciprocal measurements, calculates resistance

219

	errors should be calculated for phase values.	and phase averages and errors
err.mod()	**res_dat_df** - resistance data frame comprising A, B, M, N, transfer resistance, phase values (optional), transfer resistance errors and phase errors (optional). **nbins** - number of bins used in building error model. **res_err_mod ('lin', 'powerlaw', 'envelope', 'lme', 'log_lme')** - error model to fitted to resistance values. **min_bin_num** - minimum number of data points required in each bin for it to be used in regression fitting. **plt** - True or false value of whether to plot error model(s) or not.	Fits error models to resistance and phase data
add.noise()	**synth_dat_df** - data frame of synthetic data comprising A, B, M, N, transfer resistance and phase values (optional). **res_err** - percentage error to be added to transfer resistances. **phase_err** - absolute error to be added to phase values.	Adds Gaussian noise to synthetic data

Table 10.2: R2- and cR2-related functions for modelling geoelectrical data.

write.seq.dat()	**elec_df** - data frame defining the x position and z positions of each electrode in addition to a column indication whether an electrode is a surface electrode (True) or a non surface electrode, i.e. a buried electrode, (False). **typ ('dipole-dipole', 'Wenner' and 'Schlumberger')** - type of array geometry to be used. **a** - separation of electrodes (a in Figure 3.2). **n** - separation multiplier (n in Figure 3.2).	Writes measurement sequence to file for forward modelling
write.protocol.dat()	**res_dat_df** - resistance data frame comprising A, B, M, N, transfer resistance, phase values (optional), transfer resistance errors (optional) and phase errors (optional). **fwd_err** - orward modelling error can also be added, however this is optional. **diff_inv (0 or 1)** - whether standard of difference inversion is to be carried out. If **diff_inv=1** a second resistance data frame must also be supplied.	Writes measurement sequence and values to 'protocol.dat' file
write.cR2.in()	**elec_df** - data frame defining the x position and z positions of each electrode in addition to a column indication whether an electrode is a surface electrode (True) or a non surface electrode, i.e. a buried electrode, (False). **prob_type ('inv' or 'fwd')** - whether the problem is inverse or forward modelling. **start_res** - starting resistivitity to be used in the inversion can be set to any positive numeric value, or 'res0.dat' which will read from a previously created starting model. **phase_start** - starting phase to be used in the inversion can be set to a numeric value if **res_err** is set to 'res0.dat' then this value will be ignored. **min_err** - minimum error allowed. **res_err** - percentage resistance error, a value of 0 will use error values from the '**protocol.dat**' file. **phase_err** - phase error, a value of 0 will use error values from the '**protocol.dat**' file.	Writes cR2.in file to be read by cR2.exe
write.R2.in()	**elec_df** - data frame defining the x position and z positions of each electrode in addition to a column indication whether an	Writes R2.in file to be read by R2.exe

	electrode is a surface electrode (True) or a non surface electrode, i.e. a buried electrode, (False). Type of problem, i.e. whether to do forward or inverse, **prob_typ ('fwd', 'inv').** **prob_type ('inv' or 'fwd')** - whether the problem is inverse or forward modelling. **start_res** - starting resistivitiy to be used in the inversion can be set to any positive numeric value, or 'res0.dat' which will read from a previously created starting model. **time_lapse (0, 1, 2)** - type of inversion to do, independent inversion, regularisation to 'res0.dat', or a difference inversion.	
run.cR2.exe()	No input parameters	Runs cR2 executable
run.R2.exe()	No input parameters	Runs R2 executable
return.fwd.err()	**elec_df** - data frame defining the x position and z positions of each electrode in addition to a column indication whether an electrode is a surface electrode (True) or a non surface electrode, i.e. a buried electrode, (False).	Returns the forward error for a given postion of electrodes, 'protocol.dat' and 'mesh.dat' must have previously been generated
return.synth.data()	**elec_df** - data frame defining the x position and z positions of each electrode in addition to a column indication whether an electrode is a surface electrode (True) or a non surface electrode, i.e. a buried electrode, (False). **prog** - whether the progtam used should be R2 or cR2. **zones** - zones indicating the resistiviy and phase values (optional) of the subsurface. Individual zones comprise a list of x position, y position a resistiviy and a phase value (optional), the x and z coordinates need to be sequential either in a clockwise or countor clockwise directions. **bg_resistivity** - background resistivity for any area of the mesh lying outwith any of the zones. **bg_phase** - background phase for any area of the mesh lying outwith any of the zones.	Nested function which creates a 'res0.dat' file and uses *write.R2.in()* or *write.cR2.in()* followed by *run.R2.exe()* or *run.cR2.exe().*

Table 10.3: Mesh-related functions for modelling geoelectrical data.

write.mesh.dat()	**elec_df** - data frame defining the x position and z positions of each electrode in addition to a column indication whether an electrode is a surface electrode (True) or a non surface electrode, i.e. a buried electrode, (False). **cl1** - characteristic length 1. **cl2** - characteristic length 2. **doi** - depth of investigation indication the depth of the fine region.	Creates mesh.dat file using Gmsh
msh.to.dat()	**plt** - True or false value of whether to plot error model(s) or not.	Rewrites Gmsh output file as R2/cR2 compatible file
write.res0.dat()	**elec_df** - data frame defining the x position and z positions of each electrode in addition to a column indication whether an electrode is a surface electrode (True) or a non surface electrode, i.e. a buried	Writes 'res0.dat' file

	electrode, (False). **prog ('R2' or 'cR2') - w**hether to write starting model for resistance or resistance and phase. **zones** - nested lists of x, z, resistivity and phase (optional) of different zones. **bg_res** - resistivity values to assign to mesh elements outside of the provided zones. **bg_phase** - phase values to assign to mesh elements outside of the provided zones.	
in.zone()	**x** - vector of element centre x values. **y** - vector of element centre y values. **zone** - zone of prescribed resistivity and phase values.	Determines if points are inside or outside of a polygon
block.mesh()	**zone** - zone of prescribed resistivity and phase values. **fixed (True or False)** - whether the elements in that zone should be fixed or just a distinct region.	Separates zones within mesh to prevent smoothing in inversion
return.elem.centre()	Does not have any input parameters	Returns data frame of element centres

Table 10.4: Plot-related functions used for processing geoelectrical data.

pretty.scatter()	**xyz_df** - data frame containing x and y positions and z values of something. **xlim** - limits of the x axis. **ylim** - limits of the y axis. **zlim** - limits of the z axis. **num_bins** - number of bins used to bin z values. **cols (c('colour1','colour2', 'colour3'…)** - colours to be used, default values use the viridis colour scheme. **asp** - aspect ratio of plot. **cex** - size of text. **xlab** - label for x axis. **ylab** - label for y axis. **zlab** - label for z axis. **main**, plot title.	Plots xyz scatter plot
plot.pseudo()	**res_data_df** - data frame of resisitivity data. **plt ('Res', AppRes, 'AbsErr', 'LogAppRes', 'Phase)** - which variable to plot. **elec_spa**, electrode spacing. **cols (c('colour1','colour2', 'colour3'…)** - colours to be used, default values use the viridis colour scheme. **xlim** - limits of the x axis. **ylim** - limits of the y axis. **zlim** - limits of the z axis.	Calculates pseudo-depths and plots pseudo-section using *pretty.scatter()*
pretty.tri()	**xyz_df** - data frame containing x and y positions and z values of something. **elec_pos**, data frame with electrode positions. **xlim** - limits of the x axis. **ylim** - limits of the y axis. **zlim** - limits of the z axis. **num_bins** - number of bins used to bin z values. Colours to be used, default values use the viridis colour scheme, **cols (c('colour1','colour2', 'colour3'…).** **asp** - aspect ratio of plot. **cex** - size of text.	Plots inverted sections with elements as triangular polygons

	xlab - label for x axis. **ylab** - label for y axis. **zlab** - label for z axis. **main**, plot title. **crop_ends** - whethet to crop ends at a 45 degree angle or not to prevent plotting of zones with low sensitivity.	
pretty.contour()	**xyz_df** - data frame containing x and y positions and z values of something. **elec_pos**, data frame with electrode positions. **xlim** - limits of the x axis. **ylim** - limits of the y axis. **zlim** - limits of the z axis. **num_bins** - number of bins used to bin z values. Colours to be used, default values use the viridis colour scheme, **cols (c('colour1','colour2', 'colour3'…).** **asp** - aspect ratio of plot. **cex** - size of text. **xlab** - label for x axis. **ylab** - label for y axis. **zlab** - label for z axis. **main**, plot title. **crop_ends** - whethet to crop ends at a 45 degree angle or not to prevent plotting of zones with low sensitivity.	Plots inverted sections with elements contour plots
pretty.start()	**xyz_df** - data frame containing x and y positions and z values of something. **elec_pos**, data frame with electrode positions. **xlim** - limits of the x axis. **ylim** - limits of the y axis. **zlim** - limits of the z axis. **num_bins** - number of bins used to bin z values. Colours to be used, default values use the viridis colour scheme, **cols (c('colour1','colour2', 'colour3'…).** **asp** - aspect ratio of plot. **cex** - size of text. **xlab** - label for x axis. **ylab** - label for y axis. **zlab** - label for z axis. **main**, plot title. **crop_ends** - whethet to crop ends at a 45 degree angle or not to prevent plotting of zones with low sensitivity.	Plot zones of starting model

11 Appendix 2 – R Functions for Filtering and Modelling Electromagnetic Induction Data

The names of the R functions for filtering and modelling electromagneric induction data, their required inputs and a brief description, as discussed in Chapter 4 are shown in Table A2.1. The R functions are available to access and download from https://1drv.ms/u/s!AkZoCSS-z-n_g7MMitUScheArG0dlw?e=RJ8UsY.

```r
#import functions, and store Hankel weights, lambda and mu_0 values
source('/home/EM_TOOLS.R')

#create synthetic data for operation of GF Explorer at 0 and 1 m elevation
synth_data0_df <- array(dim=c(48, 9))
synth_data1_df <- array(dim=c(48, 9))

x <- 0:47
y <- approx(x=c(x[1],x[48]),y=c(0.2,2),  xout=x)$y

seps <- c(1.48, 2.82, 4.49, 1.48, 2.82, 4.49)
orients <- c(rep('vcp', 3), rep('hcp', 3))
for(i in 1:48)
{
   synth_data0 <- fwd.eca.fs3(sigmas=c(50,5), depths=c(0,y[i]), seps=seps,
orients=orients, height=0, freq=10000))

   synth_data0_df[,i] <- c(i-1, 0, 0, synth_data0)

   synth_data1 <- fwd.eca.fs3(sigmas=c(50,5), depths=c(0,y[i]), seps=seps,
                  orients=orients, height=1, freq=10000))

   synth_data1_df[,i] <- c(i-1, 0, 0, synth_data1)
}

#invert synthetic data using cumulative sensitivity and full Maxwell solution inversion
cs_mod0_df <- all.inv.eca.cs2.3(synth0_df, depth_lims=c(0, 3), runs=100, num_layers=2,
                  seps=seps, orients=orients, height=0, maxit=100)[,1:6]

fs_mod0_df <- all.inv.eca.fs3.3(synth0_df, depth_lims=c(0, 3), runs=100, num_layers=2,
seps=seps, orients=orients, height=0, freq=10000, maxit=100)[,1:6]

cs_mod1_df <- all.inv.eca.cs2.3(synth0_df, depth_lims=c(0, 3), runs=100, num_layers=2,
seps=seps, orients=orients, alpha=0, maxit=100)[,1:6]

fs_mod1_df <- all.inv.eca.fs3.3(synth1_df, depth_lims=c(0,3), runs=100, num_layers=2,
seps=seps, orients=orients, height=1, freq=10000, maxit=100)[,1:6]

#plot results
zones <- list(list(x,-y))
pretty.quad1(cs_mod0_df, zones=zones, zlim=c(0, 40), ylim= c(-2, 0), nbins=10)
pretty.quad1(fs_mod0_df, zones=zones, zlim=c(0, 40), ylim= c(-2, 0), nbins=10)
```

```
pretty.quad1(cs_mod1_df, zones=zones, zlim=c(0, 40), ylim= c(-2, 0), nbins=10)
pretty.quad1(fs_mod1_df, zones=zones, zlim=c(0, 40),  ylim= c(-2, 0), nbins=10)
```
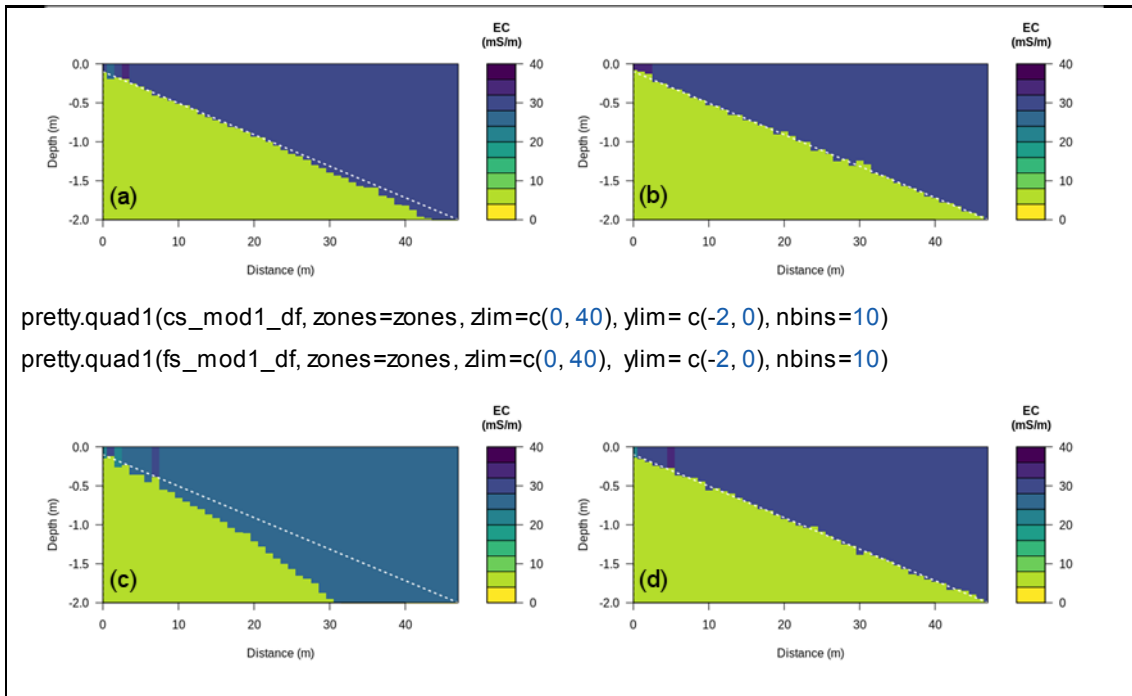
Figure 11.1: R scripts for Case 1 in Chapter 4 detailing importing the functions, generating data, inverting data and plotting results. (a) data generated at ground level and inverted using CS forward model, (b) data generated at ground level and inverted using FS forward model, (c) data generated at 1m and inverted using CS forward model and, (d) data generated at 1m and inverted with FS forward model.

```r
#import functions, and store Hankel weights, lambda and mu_0 values
source('/home/EM_TOOLS.R')
#create synthetic data for operation of GF Explorer at 0 and 1 m elevation
x <- 0:47
y <- c(rep(c(0.5, 0.55, 0.6, 0.65, 0.7, 0.75, 0.8, 0.75, 0.7, 0.65, 0.55, 0.5), 4))

synth0_df1 <- array(dim=c(48, 9))
synth0_df2 <- array(dim=c(48, 9))
synth1_df1 <- array(dim=c(48, 9))
synth1_df2 <- array(dim=c(48, 9))
seps <- c(1.48, 2.82, 4.49, 1.48, 2.82, 4.49)
orients <- c(rep('vcp', 3), rep('hcp', 3))

for(i in 1:48)
{
  depths <- c(0, y[i])
  synth0_eca1 <- fwd.eca.fs3(c(30, 5), depths, seps=seps, orients=orients, height=0,
```

```
freq=10000)


  synth0_eca2 <- rnorm(6, 1, 0.02) * synth0_eca1
  synth0_df1[i,] <- c(i-1, 0, 0, synth0_eca1)
  synth0_df2[i,] <- c(i-1, 0, 0, synth0_eca2)


  synth0_eca1 <- fwd.eca.fs3(c(30, 5), depths, seps=seps, orients=orients, height=1, freq=10000)


  synth1_eca2 <- rnorm(6, 1, 0.02) * synth1_eca1
  synth1_df1[i,] <- c(i-1, 0, 0, synth1_eca1)
  synth1_df2[i,] <- c(i-1, 0, 0, synth1_eca2)
}


#invert synthetic data using cumulative sensitivity and full Maxwell solution inversion
fs_mod0_df1 <- all.inv.eca.fs3.3(synth0_df1, seps=seps, depth_lims=c(0, 3), runs=100,
num_layers=2, orients=orients, height=0, maxit=100, freq=10000)[,1:6]


fs_mod0_df2 <- all.inv.eca.fs3.3(synth0_df2, seps=seps, depth_lims=c(0, 3), runs=100,
num_layers=2, orients=orients, height=0, maxit=100, freq=10000)[,1:6]


fs_mod1_df1 <- all.inv.eca.fs3.3(synth1_df1, seps=seps, depth_lims=c(0, 3), runs=100,
num_layers=2, orients=orients, height=0, maxit=100, freq=10000)[,1:6]


fs_mod1_df2 <- all.inv.eca.fs3.3(synth1_df2, seps=seps, depth_lims=c(0, 3), runs=100,
num_layers=2, orients=orients, height=0, maxit=100, freq=10000)[,1:6]


#plot results
zones <- list(list(c(0, x, 48), c(0, -y, 0)))
pretty.quad1(fs_mod0_df1, zones=zones, zlim=c(0, 40), ylim= c(-2, 0), nbins=10)
pretty.quad1(fs_mod0_df2, zones=zones, zlim=c(0, 40), ylim= c(-2, 0), nbins=10)
```



```
pretty.quad1(fs_mod0_df1, zones=zones, zlim=c(0, 40), ylim= c(-2, 0), nbins=10)
pretty.quad1(fs_mod0_df2, zones=zones, zlim=c(0, 40), ylim= c(-2, 0), nbins=10)
```
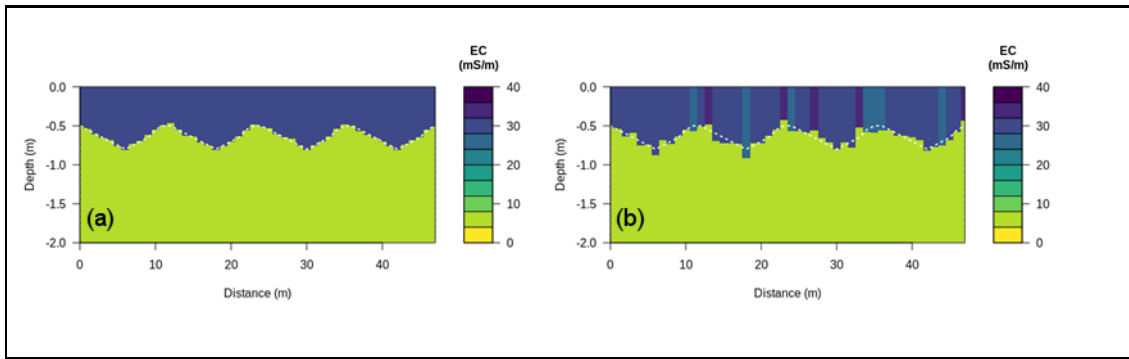
227
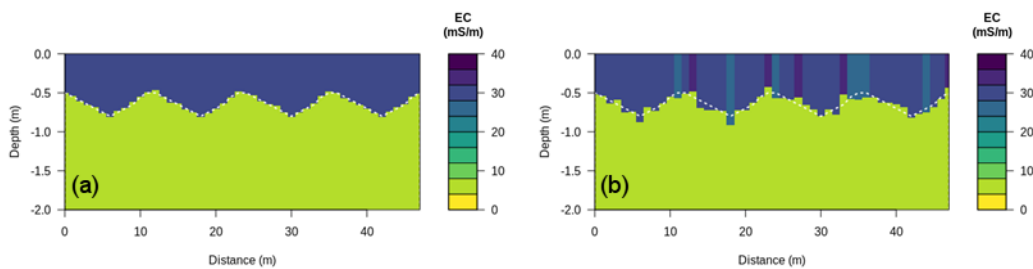
Figure 11.2: R scripts used for Case 2 in Chapter 3 detailing importing the functions, generating data, adding noise, inverting data using the FS forward model and plotting results: (a) shows the model for error free data generated at ground level, (b) shows the model for data with 2% noise generated at ground level, (c) shows the model for noise free data generated at 1 m and, (d) shows the model for data with 2% noise generated at 1 m. White dashed line shows the true depth of the interface.

Table 11.1: Data-related functions used for processing calibrating electromagnetic induction data.

Function Name	Input parameters	Description
filt.data.emi()	**emi_dat_df** - data frame of EMI data comprising measurement number, easting, northing, elevation, time, ECa1, phase1, ECa2, phase2, ECa3 and phase3. **max_err** - maximum allowable difference between sequential measurements, default value is 0.1 (10%),. **nbins** - number of bins used to bin data based on their EC and phase values. **threshold** - proportion threshold above which the number of data in each bin must exceed to be considered inlier data.	Replaces noisy and outlier data with values interpolated from sequential measurements.
run.ave()	**emi_dat_df** - data frame of EMI data comprising measurement number, easting, northing, elevation, time, ECa1, phase1, ECa2, phase2, ECa3 and phase3. **num_points** - number of points across which to calculate a running average.	Calculates running average of measurements.
cross.over.points()	**emi_dat_df** - data frame of EMI data comprising measurement number, easting, northing, elevation, time, ECa1, phase1, ECa2, phase2, ECa3 and phase3. **min_lag_time** - minimum time lag between two groups of measurements in order to be considered a cross-over point. **max_dist** - maximum radius from cross-over point used to calculate measurement average and error. **nbins** - number of bins used to fit linear error model.	Locates cross-over points, average and error values for measurements obtained at cross-over point and fits a linear error model.
change.calib.values()	**emi_dat_df** - data frame of EMI data comprising measurement number, easting, northing, elevation, time, ECa1, phase1, ECa2, phase2, ECa3 and phase3. **em_calib_df** - data frame of EMI measurements made a locations along resistivity transect comprising measurement number, easting, northing, distance, ECa1, ECa2 and ECa3.	Replaces ECa values in calibration file with processed ECa values.

	xy_tol - allowable distance in m between measurements in measurement data frame and calibration data frames.	
ert.to.eca1()	**ert_mod_df** - data frame of electrical resistivity obtained on a quadrilateral grid comprising x position, z position and resistivity. **seps** - coil separations of the EMI device in m. **orients ('vcp' or 'hcp')** - coil orientations of the EMI device. **freq** - frequency of EMI device in Hz. **height** - height which the EMI device is operated at in metres.	Calculates forward response in LIN-ECa for a given resistivity model.
calibrate.emi()	**ert_mod_df** - data frame of electrical resistivity obtained on a quadrilateral grid comprising x position, z position and resistivity. **em_calib_df** - data frame of EMI measurements made at locations along resistivity transect comprising measurement number, easting, northing, distance, ECa1, ECa2 and ECa3. **seps** - coil separations of the EMI device in m. **orients ('vcp' or 'hcp')** - coil orientations of the EMI device. **freq** - Frequency of EMI device in Hz. **height** - height which the EMI device is operated at in m. **crop_dist** - distance at either end of the resistivity model to discount.	Calibrates EMI data using model of electrical resistivity and *ert.to.eca1()*.

Table 11.2: Forward model-related functions used for modelling electromagnetic induction data.

return.cs()	**depths** - the upper depth of each layer as a positive integer in m, starting at 0 m. **seps** - coil separations of the EMI device in m. **orients ('vcp' or 'hcp')** - coil orientations of the EMI device. **height** - height which the EMI device is operated at in m.	Returns the cumulative sensitivities for a set of depths
return.R0()	**sigmas** - EC of each layer in mS/m. **depths** - the beginning depth of each layer as a positive integer in m, starting at 0 m. **freq** - frequency of EMI device in Hz. **height** - height which the EMI device is operated at in m.	Returns the refelection coefficient for the air layer.
return.Rn()	**sigmas** - EC of each layer in S/m. **depths** - the upper depth of each layer as a positive integer in m, starting at 0 m. **freq** - frequency of EMI device in Hz. **height** - height which the EMI device is operated at in m.	Returns reflection coefficient for all layers.
return.Hankel()	**sigmas** - EC of each layer in S/m. **depths** - the upper depth of each layer as a positive integer in m, starting at 0 m. **seps** - coil separations of the EMI device in m. **orients ('vcp' or 'hcp')** - coil orientations of the EMI device. **freq** - frequency of EMI device in Hz. **height** - height which the EMI device is operated at in m.	Returns Hankel transform
return.Q2()	**sigmas** - EC of each layer in S/m. **depths** - the upper depth of each layer as a positive integer in m, starting at 0 m. **seps** - coil separations of the EMI device in m. **orients ('vcp' or 'hcp')** - coil orientations of the EMI device. **freq** - frequency of EMI device in Hz. **height** - height which the EMI device is operated at in m.	Returns Q using for VCP and HCP orientations
return.Q3()	**sigmas** - EC of each layer in S/m. **depths** - the upper depth of each layer as a positive integer in m, starting at 0 m. **seps** - coil separations of the EMI device in m. **orients ('vcp' or 'hcp')** - coil orientations of the EMI device. **freq** - frequency of EMI device in Hz.	Returns Q of homogenous model using analytical solutions of McNeill (1980)

	height - height which the EMI device is operated at in m.	
fwd.eca.cs()	**sigmas** - EC of each layer in S/m. **depths** - the upper depth of each layer as a positive integer in m, starting at 0 m. **seps** - coil separations of the EMI device in m. **orients ('vcp' or 'hcp')** - coil orientations of the EMI device. **freq** - frequency of EMI device in Hz. **height** - height which the EMI device is operated at in m.	Calculates forward response using cumulative sensitivity equations.
fwd.eca.fs1()	**sigmas** - EC of each layer in S/m. **depths** - the upper depth of each layer as a positive integer in m, starting at 0 m. **seps** - coil separations of the EMI device in m. **orients ('vcp' or 'hcp')** - coil orientations of the EMI device. **freq** - frequency of EMI device in Hz. **height** - height which the EMI device is operated at in m.	Calculates forward response using *Q.to.eca1()* and *rtn.Q2()*.
fwd.eca.fs2()	**sigmas** - EC of each layer in S/m. **depths** - the upper depth of each layer as a positive integer in m, starting at 0 m. **seps** - coil separations of the EMI device in m. **orients ('vcp' or 'hcp')** - coil orientations of the EMI device. **freq** - frequency of EMI device in Hz. **height** - height which the EMI device is operated at in m.	Calculates forward response using *Q.to.eca2()* and *rtn.Q2()*.
fwd.eca.fs3()	**sigmas** - EC of each layer in S/m. **depths** - the upper depth of each layer as a positive integer in m, starting at 0 m. **seps** - coil separations of the EMI device in m. **orients ('vcp' or 'hcp')** - coil orientations of the EMI device. **freq** - frequency of EMI device in Hz. **height** - height which the EMI device is operated at in m.	Calculates forward response using *Q.to.eca3()* and *rtn.Q2()*.

Table 11.3: ECa and Q conversion functions for electromagnetic induction data.

GF.eca.to.Q()	**meas_eca** - measured ECa obtained with GF Instruments Explorer. **seps** - coil separations of the EMI device in m. **orients ('vcp' or 'hcp')** - coil orientations of the EMI device. **height** - height which the EMI device is operated at in m.	Converts GF-ECa to Q.
eca1.to.Q()	**meas_eca** - measured ECa obtained with GF Instruments Explorer. **seps** - coil separations of the EMI device in m. **orients ('vcp' or 'hcp')** - coil orientations of the EMI device.	Converts LIN-ECa to Q.
Q.to.eca1()	**meas_Q** - measured Q values. **seps** - coil separation of the EMI device in m. **orients ('vcp' or 'hcp')** - coil orientation of the EMI device. **freq** - frequency of EMI device in Hz.	Converts quadrature to apparent EC to LIN-ECa
Q.to.eca2()	**meas_Q** - measured Q values. **seps** - coil separation of the EMI device in m. **orients ('vcp' or 'hcp')** - coil orientation of the EMI device. **freq** - frequency of EMI device in Hz.	Converts Q to ECa using optimization procedure of Andrade et al. (2016), Q is obtained using *rtn.Q2()*.
Q.to.eca3()	**meas_Q** - measured Q values. **seps** - coil separation of the EMI device in m. **orients ('vcp' or 'hcp')** - coil orientation of the EMI device. **freq** - frequency of EMI device in Hz.	Converts Q to ECa using optimization procedure of Andrade et al. (2016), Q is obtained using *rtn.Q3()*.

Table 11.4: Inversion functions used for modelling electromagnetic induction data.

homo.eca.cs()	**meas_eca** - measured ECa. **depths** - the upper depth of each layer as a positive integer in m, starting at 0 m. **seps** - coil separation of the EMI device in m. **orients ('vcp' or 'hcp')** - coil orientation of the EMI device. **height** - height which the EMI device is operated at in m. **sigma_lim** - range of expected EC in mS/m. **algo (1 or 2)** - whether to use L1 or L2 norm in objective function.	Finds best homogenous starting model using *fwd.eca.cs()*.
homo.eca.fs3()	**meas_eca** - measured ECa. **depths** - the upper depth of each layer as a positive integer in m, starting at 0 m. **seps** - coil separation of the EMI device in m. **orients ('vcp' or 'hcp')** - coil orientation of the EMI device. **height** - height which the EMI device is operated at in m. **sigma_lim** - range of expected EC in mS/m. **algo (1 or 2)** - whether to use L1 or L2 norm in objective function. **freq** - frequency of EMI device in Hz.	Finds best homogenous starting model using *fwd.eca.fs3()*.
homo.Q()	**meas_Q** - measured Q values. **depths** - the beginning depth of each layer as a positive integer in m, starting at 0 m. **seps** - coil separation of the EMI device in m. **orients ('vcp' or 'hcp')** - coil orientation of the EMI device. **height** - height which the EMI device is operated at in m. **sigma_lim** - range of expected EC in mS/m. **algo (1 or 2)** - whether to use L1 or L2 norm in objective function. **freq** - frequency of EMI device in Hz.	Finds best homogenous starting model using *return.Q()*.
emi.rmse()	**meas_val** - measured values. **pred_val** - predicted values. **meas_err** - measurement error. **algo (1 or 2)** - whether to use L1 or L2 norm in objective function.	Calculate misfit of measured and predicted values.
inv.eca.cs2.1()	**meas_eca** - measured ECa. **depths** - the upper depth of each layer as a positive integer in m, starting at 0 m. **seps** - coil separation of the EMI device in m. **orients ('vcp' or 'hcp')** - coil orientation of the EMI device. **height** - height which the EMI device is operated at in m. **alpha** - smoothing term to determine weight of model misfit term in the objective function. **err_eca** - measurement error. **maxit** - maximum number of iterations for Nelder-Mead, conjugate gradient and L-BFGS-B methods, not for Shuffled Complex Evolution methods. **optim_method ('Nelder-Mead', 'CG', 'L-BFGS-B' and 'SCE)** - optimisation method to be used. **start_sigma** - EC value for homogenous starting model in mS/m. **fix_inf_sigma** - fix EC of infinite layer to ensure reasonable values. **algo (1 or 2)** - whether to use L1 or L2 norm in objective function. **sigma_lims** - EC limits for L-BFGS-B methods and SCE optimisation methods.	Inverts data using *fwd.eca.cs()* forward model, requires a set of depths and produces a smooth model of EC.
inv.eca.cs2.2()	**meas_eca** - measured ECa.	Inverts data using

231

	depths - the upper depth of each layer as a positive integer in m, starting at 0 m. **seps** - coil separation of the EMI device in m. **orients ('vcp' or 'hcp')** - coil orientation of the EMI device. **height** - height which the EMI device is operated at in m. **alpha** - smoothing term to determine weight of model misfit term in the objective function. **err_eca** - measurement error. **maxit** - maximum number of iterations for Nelder-Mead, conjugate gradient and L-BFGS-B methods, not for Shuffled Complex Evolution methods. **optim_method ('Nelder-Mead', 'CG', 'L-BFGS-B' and 'SCE)** - optimisation method to be used. **start_sigma** - EC value for homogenous starting model in mS/m. **start_depth** - starting depth for bottom depth of layer 1. **algo (1 or 2)** - whether to use L1 or L2 norm in objective function. **sigma1_lims** - EC limits for layer 1 when L-BFGS-B or SCE optimization methods are used. **sigma2_lims** - EC limits for layer 2 when L-BFGS-B or SCE optimization methods are used. **depth1_lims** - depth limits for bottom depths of layer 1 when L-BFGS-B or SCE optimization methods are used.	*fwd.eca.cs()* forward model, produces a two-layer model with a sharp boundary.
inv.eca.cs2.3()	**meas_eca** - measured ECa. **num_layers** - number of layers in model. **seps** - coil separation of the EMI device in m. **orients ('vcp' or 'hcp')** - coil orientation of the EMI device. **height** - height which the EMI device is operated at in m. **alpha** - smoothing term to determine weight of model misfit term in the objective function. **err_eca** - measurement error. **maxit** - maximum number of iterations for Nelder-Mead, conjugate gradient and L-BFGS-B methods, not for Shuffled Complex Evolution methods. **optim_method ('Nelder-Mead', 'CG', 'L-BFGS-B' and 'SCE)** - optimisation method to be used. **start_sigma** - EC value for homogenous starting model in mS/m. **algo (1 or 2)** - whether to use L1 or L2 norm in objective function. **runs** - number of values of random depths to run. **sigma_lims_df** - data frame of EC limits with column of maximum and minimum EC, and the number of rows equaling the number of layers. **depth_lims** - depth limits for bottom depths of each layer when L-BFGS-B or SCE optimisation methods.	Inverts data using *fwd.eca.cs()* forward model, produces a multiple layer model with a sharp boundary.
inv.eca.fs3.1()	**meas_eca** - measured ECa. **depths** - the upper depth of each layer as a positive integer in m, starting at 0 m. **seps** - coil separation of the EMI device in m. **orients ('vcp' or 'hcp')** - coil orientation of the EMI device. **height** - height which the EMI device is operated at in m. **freq** - frequency of EMI device in Hz. **alpha** - smoothing term to determine weight of model misfit term in the objective function. **err_eca** - measurement error. **maxit** - maximum number of iterations for Nelder-Mead,	Inverts data using *fwd.eca.fs3()* forward model, requires a set of depths and produces a smooth model of EC.

	conjugate gradient and L-BFGS-B methods, not for Shuffled Complex Evolution methods. **optim_method ('Nelder-Mead', 'CG', 'L-BFGS-B' and 'SCE)** - optimisation method to be used. **start_sigma** - EC value for homogenous starting model in mS/m. **fix_inf_sigma** - fix EC of infinite layer to ensure reasonable values. **algo (1 or 2)** - whether to use L1 or L2 norm in objective function. **sigma_lims** - EC limits for L-BFGS-B methods and SCE optimisation methods.	
inv.eca.fs3.2()	**meas_eca** - measured ECa. **depths** - the upper depth of each layer as a positive integer in m, starting at 0 m. **seps** - coil separation of the EMI device in m. **orients ('vcp' or 'hcp')** - coil orientation of the EMI device. **height** - height which the EMI device is operated at in m. **freq** - frequency of EMI device in Hz. **alpha** - smoothing term to determine weight of model misfit term in the objective function. **err_eca** - measurement error. **maxit** - maximum number of iterations for Nelder-Mead, conjugate gradient and L-BFGS-B methods, not for Shuffled Complex Evolution methods. **optim_method ('Nelder-Mead', 'CG', 'L-BFGS-B' and 'SCE)** - optimisation method to be used. **start_sigma** - EC value for homogenous starting model in mS/m. **start_depth** - starting depth for bottom depth of layer 1. **algo (1 or 2)** - whether to use L1 or L2 norm in objective function. **sigma1_lims** - EC limits for layer 1 when L-BFGS-B or SCE optimization methods are used. **sigma2_lims** - EC limits for layer 2 when L-BFGS-B or SCE optimization methods are used. **depth1_lims** - depth limits for bottom depths of layer 1 when L-BFGS-B or SCE optimization methods are used.	Inverts data using *fwd.eca.fs3()* forward model, produces a two-layer model with a sharp boundary.
inv.eca.fs3.3()	**meas_eca** - measured ECa. **num_layers** - number of layers in model. **seps** - coil separation of the EMI device in m. **orients ('vcp' or 'hcp')** - coil orientation of the EMI device. **height** - height which the EMI device is operated at in m. **freq** - frequency of EMI device in Hz. **alpha** - smoothing term to determine weight of model misfit term in the objective function. **err_eca** - measurement error. **maxit** - maximum number of iterations for Nelder-Mead, conjugate gradient and L-BFGS-B methods, not for Shuffled Complex Evolution methods. **optim_method ('Nelder-Mead', 'CG', 'L-BFGS-B' and 'SCE)** - optimisation method to be used. **start_sigma** - EC value for homogenous starting model in mS/m. **algo (1 or 2)** - whether to use L1 or L2 norm in objective function. **runs** - number of values of random depths to run. **sigma_lims_df** - data frame of EC limits with column of maximum and minimum EC, and the number of rows equaling the number of layers.	Inverts data using *fwd.eca.fs3()* forward model, produces a multiple layer model with a sharp boundary.

	depth_lims - depth limits for bottom depths of each layer when L-BFGS-B or SCE optimisation methods.	
inv.eca.fs3.4()	**meas_eca** - measured ECa. **num_layers** - number of layers in model. **seps** - coil separation of the EMI device in m. **orients ('vcp' or 'hcp')** - coil orientation of the EMI device. **height** - height which the EMI device is operated at in m. **freq** - frequency of EMI device in Hz. **alpha** - smoothing term to determine weight of model misfit term in the objective function. **err_eca** - measurement error. **sigma_lims_df** - data frame of EC limits with column of maximum and minimum EC, and the number of rows equaling the number of layers. **depth_lims** - depth limits for bottom depths of each layer when L-BFGS-B or SCE optimisation methods.	Inverts data using *fwd.eca.fs3()* forward model and shuffled complex evolution algorithm (Duan et al., 1993), produces a multiple layer model with a sharp boundary.
inv.Q1()	**meas_Q** - measured Q. **depths** - the upper depth of each layer as a positive integer in m, starting at 0 m. **seps** - coil separation of the EMI device in m. **orients ('vcp' or 'hcp')** - coil orientation of the EMI device. **height** - height which the EMI device is operated at in m. **freq** - frequency of EMI device in Hz. **alpha** - smoothing term to determine weight of model misfit term in the objective function. **err_Q** - measurement error. **maxit** - maximum number of iterations for Nelder-Mead, conjugate gradient and L-BFGS-B methods, not for Shuffled Complex Evolution methods. **optim_method ('Nelder-Mead', 'CG', 'L-BFGS-B' and 'SCE)** - optimisation method to be used. **start_sigma** - EC value for homogenous starting model in mS/m. **fix_inf_sigma** - fix EC of infinite layer to ensure reasonable values. **algo (1 or 2)** - whether to use L1 or L2 norm in objective function. **sigma_lims** - EC limits for L-BFGS-B methods and SCE optimisation methods.	Inverts data using *fwd.Q()* forward model, requires a set of depths and produces a smooth model of EC.
inv.Q2()	**meas_Q** - measured Q. **depths** - the upper depth of each layer as a positive integer in m, starting at 0 m. **seps** - coil separation of the EMI device in m. **orients ('vcp' or 'hcp')** - coil orientation of the EMI device. **height** - height which the EMI device is operated at in m. **freq** - frequency of EMI device in Hz. **alpha** - smoothing term to determine weight of model misfit term in the objective function. **err_Q** - measurement error. **maxit** - maximum number of iterations for Nelder-Mead, conjugate gradient and L-BFGS-B methods, not for Shuffled Complex Evolution methods. **optim_method ('Nelder-Mead', 'CG', 'L-BFGS-B' and 'SCE)** - optimisation method to be used. **start_sigma** - EC value for homogenous starting model in mS/m. **start_depth** - starting depth for bottom depth of layer 1. **algo (1 or 2)** - whether to use L1 or L2 norm in objective	Inverts data using *fwd.eca.Q()* forward model, produces a two-layer model with a sharp boundary.

	function. **sigma1_lims** - EC limits for layer 1 when L-BFGS-B or SCE optimization methods are used. **sigma2_lims** - EC limits for layer 2 when L-BFGS-B or SCE optimization methods are used. **depth1_lims** - depth limits for bottom depths of layer 1 when L-BFGS-B or SCE optimization methods are used.	
inv.Q3()	**meas_Q** - measured Q. **num_layers** - number of layers in model. **seps** - coil separation of the EMI device in m. **orients ('vcp' or 'hcp')** - coil orientation of the EMI device. **height** - height which the EMI device is operated at in m. **freq** - frequency of EMI device in Hz. **alpha** - smoothing term to determine weight of model misfit term in the objective function. **err_Q** - measurement error. **maxit** - maximum number of iterations for Nelder-Mead, conjugate gradient and L-BFGS-B methods, not for Shuffled Complex Evolution methods. **optim_method ('Nelder-Mead', 'CG', 'L-BFGS-B' and 'SCE)** - optimisation method to be used. **start_sigma** - EC value for homogenous starting model in mS/m. **algo (1 or 2)** - whether to use L1 or L2 norm in objective function. **runs** - number of values of random -depths to run. **sigma_lims_df** - data frame of EC limits with column of maximum and minimum EC, and the number of rows equaling the number of layers. **depth_lims** - depth limits for bottom depths of each layer when L-BFGS-B or SCE optimisation methods.	Inverts data using *fwd.eca.Q()* forward model, produces a multiple layer model with a sharp boundary.
inv.Q4()	**meas_Q** - measured Q. **seps** - coil separation of the EMI device in m. **orients ('vcp' or 'hcp')** - coil orientation of the EMI device. **height** - height which the EMI device is operated at in m. **freq** - frequency of EMI device in Hz. **alpha** - smoothing term to determine weight of model misfit term in the objective function. **err_Q** - measurement error. **maxit** - maximum number of iterations for Nelder-Mead, conjugate gradient and L-BFGS-B methods, not for Shuffled Complex Evolution methods. **optim_method ('Nelder-Mead', 'CG', 'L-BFGS-B' and 'SCE)** - optimisation method to be used. **start_sigma** - EC value for homogenous starting model in mS/m. **algo (1 or 2)** - whether to use L1 or L2 norm in objective function. **fixed_cond1** - fixed layer 1 EC value. **fixed_cond2** - fixed layer 2 EC value. **fixed_depth1** - fixed layer 1 depth value.	Inverts data using *fwd.eca.Q()* forward model and shuffled complex evolution algorithm (Duan et al., 1993), produces a multiple layer model with a sharp boundary.
inv.Q5()	**meas_Q** - measured Q. **seps** - coil separation of the EMI device in m. **orients ('vcp' or 'hcp')** - coil orientation of the EMI device. **height** - height which the EMI device is operated at in m. **freq** - frequency of EMI device in Hz. **alpha** - smoothing term to determine weight of model misfit term in the objective function. **err_Q** - measurement error. **maxit** - maximum number of iterations for Nelder-Mead,	Inverts data using *fwd.eca.Q()* forward model and shuffled complex evolution algorithm (Duan et al., 1993), produces a two-

	conjugate gradient and L-BFGS-B methods, not for Shuffled Complex Evolution methods. **optim_method ('Nelder-Mead', 'CG', 'L-BFGS-B' and 'SCE)** - optimisation method to be used. **start_sigma** - EC value for homogenous starting model in mS/m. **sigma_lims_df** - data frame of EC limits with column of maximum and minimum EC, and the number of rows equaling the number of layers. **algo (1 or 2)** - whether to use L1 or L2 norm in objective function. **fixed_cond1** - fixed layer 1 EC value. **fixed_cond2** - fixed layer 2 EC value. **fixed_depth1** - fixed layer 1 depth value.	layer model with a sharp boundary. In addition a fixed value for the layer 1 EC, layer 2 EC or depth can be supplied.
all.inv.eca.cs2.1()	**meas_eca_df** - meas_eca is replaced by data frame of x, y and z position and ECa values. **num_cores** - number of cores to use. For all other parameters see *inv.eca.cs.2.1()*	Parallel version of all.inv.eca.cs2.1()
all .inv.eca.cs2.2()	**meas_eca_df** - meas_eca is replaced by data frame of x, y and z position and ECa values. **num_cores** - number of cores to use. For all other parameters see *inv.eca.cs.2.2()*	Parallel version of all.inv.eca.cs2.2()
all inv.eca.cs2.3()	**meas_eca_df** - meas_eca is replaced by data frame of x, y and z position and ECa values. **num_cores** - number of cores to use. For all other parameters see *inv.eca.cs.2.3()*	Parallel version of all.inv.eca.cs2.3()
all inv.eca.fs3.1()	**meas_eca_df** - meas_eca is replaced by data frame of x, y and z position and ECa values. **num_cores** - number of cores to use. For all other parameters see *inv.eca.fs.3.1()*	Parallel version of all.inv.eca.fs3.1()
all inv.eca.fs3.2()	**meas_eca_df** - meas_eca is replaced by data frame of x, y and z position and ECa values. **num_cores** - number of cores to use. For all other parameters see *inv.eca.fs.3.2()*	Parallel version of all.inv.eca.fs3.2()
all inv.eca.fs3.3()	**meas_eca_df** - meas_eca is replaced by data frame of x, y and z position and ECa values. **num_cores** - number of cores to use. For all other parameters see *inv.eca.fs.3.3()*	Parallel version of all.inv.eca.fs3.3()
all inv.eca.fs3.4()	**meas_eca_df** - meas_eca is replaced by data frame of x, y and z position and ECa values. **num_cores** - number of cores to use. For all other parameters see *inv.eca.fs.3.4()*	Parallel version of all.inv.eca.fs3.4()
all inv.Q1()	**meas_eca_df** - meas_Q is replaced by data frame of x, y and z position and ECa values. Number of cores to use, **num_cores**. For all other parameters see *inv.Q.1()*	Parallel version of *all.inv.eca.Q1()*
all inv.Q2()	**meas_eca_df** - meas_Q is replaced by data frame of x, y and z position and ECa values. Number of cores to use, **num_cores**. For all other parameters see *inv.Q.2()*	Parallel version of *all.inv.eca.Q2()*
all inv.Q3()	**meas_eca_df** - meas_Q is replaced by data frame of x, y and z position and ECa values. Number of cores to use, **num_cores**. For all other parameters see *inv.Q.3()*	Parallel version of *all.inv.eca.Q3()*
all.inv.Q4()	**meas_eca_df** - meas_Q is replaced by data frame of x, y and z position and ECa values. Number of cores to use, **num_cores**.	Parallel version of *all.inv.eca.Q4()*

	For all other parameters see *inv.Q.4()*	

Table 11.5: Plotting functions for electromagnetic induction data.

pretty.quad1()	**xlim** - limits of x. **ylim** - limits of y. **zlim** - limits of z. **nbins** - number of bins. **num_layers** - number of layers. **cols** - colours. **xlab** - label of x axis. **ylab** - label of y axis. **zlab** - label of z axis. **main** - main plot label.	Plot inverted models of EC.
plot.misfit()	**mod_cons** - model of inverted conductivities. **meas_eca** - measured apparent conductivities.	Plots scatter plot of measured and predicted ECa values